UNIVERSIDAD COMPLUTENSE DE MADRID

FACULTAD DE CIENCIAS FÍSICAS
Departamento de Física de Materiales

TESIS DOCTORAL

Solid-solid phase transformations in a metastable stainless steel: microestructural control and mechanical properties

Transformaciones de fase en estado sólido en un acero inoxidable metaestable : control microestructural y propiedades mecánicas

MEMORIA PARA OPTAR AL GRADO DE DOCTOR

PRESENTADA POR

Carola Alonso de Celada Casero

Director
David San Martín Fernández

Madrid, 2016

UNIVERSIDAD COMPLUTENSE DE MADRID
FACULTAD DE CIENCIAS FÍSICAS
Departamento de Física de Materiales

Solid-solid Phase Transformations in a Metastable Stainless Steel: Microstructural Control and Mechanical Properties

Transformaciones de Fase en Estado Sólido en un Acero Inoxidable Metaestable: Control Microestructural y Propiedades Mecánicas

Tesis Doctoral

Carola Alonso de Celada Casero

Director:

Dr. D. David San Martín Fernández

Grupo de investigación Materalia
Departamento de Metalúrgia Física
Centro Nacional de Investigaciones Metalúrgicas (CENIM)
Consejo Superior de Investigaciones Científicas (CSIC)

La presente memoria constituye la Tesis Doctoral de Dña. Carola Alonso de Celada Casero, presentada en el Departamento de Física de Materiales de la Facultad de Ciencias Físicas de la Universidad Complutense de Madrid, para optar al grado de Doctor en Ciencias Físicas.

Este trabajo ha sido realizado en el Grupo Materalia del Departamento de Metalurgia Física del Centro Nacional de Investigaciones Metalúrgicas (CENIM-CSIC), bajo la dirección del Dr. D. David San Martín Fernández, Científico Titular del CSIC.

GLOSARY OF ABBREVIATIONS

AC	Alternating current
ADF	Annular dark field
AGS	Austenitic Grain Size
ASS	Austenitic Stainless Steel
BCC	Body Centred Cubic
BF	Bright Field
CG	Coarse grain
CR	Cold-Rolled
DC	Direct current
DF	Dark Field
BSE	Backscattered Electrons
EBSD	Electron Backscatter Diffraction
EDS	Energy Dispersive X-Ray Spectroscopy
EPMA	Electron Probe Microanalysis
FCC	Face Centred Cubic
FEG	Field Emission Gun
FFT	Fourier Fast Transform
FG	Fine grain
HCP	Hexagonal Close Packed
HAADF	High angle annular dark field
HRTEM	High Resolution Transmission Electron Microscopy
HV	Hardness Vickers
IC	Integrated Circuit
IFFT	Inverse Fourier Fast Transform
KS OR	Kurdjumov-Sachs Orientation Relationship
L-B	Lichtenegger-Blöch
LOM	Light Optical Microscopy
ND	Normal Direction
RD	Rolling Direction
SAED	Selected Area Electron Diffraction
SE	Secondary Electrons
SEM	Scanning Electron Microscopy
SG	Submicron Grained
SIM	Strain-Induced Martensite
SQUID	Superconducting Quantum Interference Device
SS	Stainless Steel

STEM	Scanning Transmission Electron Microscopy
TEM	Transmission Electron Microscopy
TEP	Thermoelectric Power
TD	Transverse Direction
TRIP	Transformation-Induced Plasticity
TWIP	Twinning-Induced Plasticity
XRD	X-Ray Diffraction
UFG	Ultra-Fine Grain
WDS	Wavelength Dispersive Spectrometer
WDXRF	Wavelength dispersive X-ray fluorescence spectrometer

NOMENCLATURE

a	Lattice parameter [Å]
A_F	Martensite (α') to austenite (γ) phase transformation finish temperature [°C]
A_S	Martensite (α') to austenite (γ) phase transformation start temperature [°C]
$f_{\alpha'}$	Volume fraction of the α'-martensite phase
f_γ	Volume fraction of the austenite phase
f_χ	Volume fraction of the chi-phase
$\Delta G^{\gamma\rightarrow\alpha'}$	Chemical free-energy difference between austenite and α'-martensite phases [J/mol]
$\Delta G_{M_S}^{\gamma\rightarrow\alpha'}$	Chemical free-energy difference between austenite and α'-martensite phases at M_S temperature [J/mol]
$\Delta G_{T_0}^{\gamma\rightarrow\alpha'}$	Chemical free-energy difference between austenite and α'-martensite phases at T_0 temperature [J/mol]
M_S	Martensite start temperature on cooling [° C]
M_d	Temperature above which the austenite is stable (no martensite transformation occurs), even when plastic strain is applied [° C]
M_S^σ	Maximum temperature at which the martensite transformation occurs by elastic stress [° C]
$M_{sat}^{\alpha'}$	Magnetization saturation of a 100 % martensitic phase
M_{sat}	Magnetization saturation
Q	Activation energy [kJ/mol]
U'	Mechanical driving force [J/mol]
T	Temperature [° C]
T_0	Temperature at which austenite and martensite phases are in thermodynamic equilibrium
$T_{\gamma 1}, T_{\gamma 2}$	Reaustenitization temperatures [° C]
V	Voltage [Volts]
α	Ferrite phase
α'	Martensite phase
χ	Magnetic susceptibility
χ-phase	Intermetallic phase $Fe_{36}Cr_{12}Mo_{10}$
ε	Engineering strain
ε_{un}	Uniform elongation

ε_t	Total elongation or elongation to fracture
ε_T	True strain
$\dot{\varepsilon}$	Strain rate [s^{-1}]
γ	Austenite phase
μ_r	Relative magnetic permeability
σ	Engineering stress [GPa]
$\sigma_{y0.2}$	Yield strength [GPa]
σ_{UTS}	Ultimate tensile strength [GPa]
σ_T	True stress [GPa]

TABLE OF CONTENTS

ABSTRACT

In this thesis work the processing-microstructure-mechanical properties relationship has been studied in a cold-rolled semi-austenitic metastable stainless steel of composition (in wt. %): 12Cr-9Ni-4Mo-2Cu-1Ti-0.5Mn-0.4Al. Due to its good corrosion resistance, good ductility in the annealed state, high strength in martensitic state and its ability to precipitation harden, this material is especially suitable for complicated designs that still have high requirements on the strength of the final product. However, the complex thermo-mechanical behavior of this steel is difficult to understand and limits its applications. Therefore, and in view of its good properties, it is worth investing time in studying the phase transformations that the material may undergo during the thermo-mechanical processing and the microstructure-properties interlink. In this way, it is possible to gain insight about the parameters controlling the thermal and mechanical stability and to propose new processing routes that lead to the adequate final properties depending on the application.

The pronounced chemical banding present in the cold-rolled as-received state has turned up to be a thorny and difficult-to-solve problem that influences the stability and the microstructure of the material. The combination of techniques such as transmission electron microscopy (TEM), electron probe microanalysis (EPMA), magnetization, micro-hardness Vickers and thermoelectric power (TEP) measurements have allow to perform a detailed characterization of the the $\alpha' \rightarrow \gamma$ transformation under continuous heating (0.1, 1 and 10 °C/s). It was found to occur in two steps due to the chemical banding, in a wide range of temperatures and through an

interface-controlled mechanism for all heating rates. The isochronal heating allows the precise control of the microstructure and very fine submicrometer size (0.35-0.41 μm) dual (α'/γ) and austenitic microstructures can be obtained. The mechanical behavior of these microstructures was studied by tensile testing, magnetization measurements and TEM and it was found In consequence the mechanical properties can be varied from ultimate tensile strengths and elongations of about 1.20 GPa and 25 % to 2.20 GPa and 3 %, respectively. The main factors affecting the mechanical behavior in this steel are the mechanical stability of the austenite, the balance of austenite/martensite volume fractions, the presence of strengthening second-phase nano-particles and the chemical banding. Due to its metastability, the austenite is susceptible of transforming into martensite under applied uniaxial tensions (so-called TRIP effect), which results in outstanding work-hardening rates and enhanced mechanical properties.

Finally, the ability of precipitation hardening of this steel was thoroughly investigated in the cold-rolled state for aging temperatures of 300-550 °C and times up to 72 h. The hardening rate during aging has been characterized using hardness and TEP measurements; and nano-precipitates formed have been analyzed by TEM and HRTEM. A semi-empirical model has been used to estimate the activation energy of the process. The mechanical behavior of selected microstructures aged at 400, 450 and 500 °C has been also characterized and discussed based on the nanometric size, the formation of austenite after long aging treatments and the coarsening of the precipitates.

RESUMEN

Este trabajo de tesis se centra fundamentalmente en entender la relación procesado-microestructura-propiedades mecánicas en un acero inoxidable semi-austenítico metaestable y endurecible por precipitación. El acero inoxidable estudiado presenta una composición 12Cr-9Ni-4Mo-2Cu-1Ti-0.5Mn-0.4Al y se fabrica por colada continua seguido de varias etapas de laminado en caliente y frío hasta que se obtienen planchas de 0.45 mm de espesor. Este material presenta muy buena ductilidad en estado recocido austenítico (elongaciones de 0.20-0.30), y ultra-alta resistencia en su estado martensítico endurecido por precipitación (límite elástico de 1.50-1.80 GPa, resistencia máxima de hasta 2 GPa y dureza de 450-650 Hv10). Estas características le hacen atractivo para un gran número de aplicaciones que requieran resistencia a la corrosión, buena formabilidad y ultra-alta resistencia, como son algunos componentes de cabezales de maquinillas eléctricas de afeitar, instrumental quirúrgico o material deportivo. Sin embargo, su complejo comportamiento termo-mecánico limita en muchos casos su aplicación. Se ha observado que pequeñas variaciones de composición tienen una gran influencia en la estabilidad térmica y mecánica de la austenita.

Las posibilidades que ofrece este acero y sus extraordinarias propiedades mecánicas justifican un estudio en profundidad para desentrañar su complejo comportamiento. Para ello, es necesario estudiar las transformaciones de fase que puede sufrir este material durante su procesado termo-mecánico, determinar los parámetros que afectan a su estabilidad térmica y mecánica y estudiar la relación microestructura-propiedades

para así poder proponer nuevas rutas de procesado que permitan alcanzar las prestaciones finales adecuadas dependiendo de la aplicación.

Para alcanzar estos objetivos, el trabajo se ha dividido fundamentalmente en cuatro paquetes de trabajo que se explican a continuación:

1. Caracterización de la microestructura inicial

La caracterización del estado recibido (laminado en frío) se ha llevado a cabo mediante microscopía óptica (MO), electrónica de barrido (MEB-EDS), electrónica de transmisión (MET), difracción de rayos-X y microsonda electrónica de barrido (EPMA). La microestructura inicial consiste principalmente en martensita (α') inducida por deformación y severamente deformada ($fv_{\alpha'}\sim0.97$), pequeñas pequeñas cantidades de austenita (γ) y ferrita-δ retenidas ($fv_{\gamma+\delta}\sim0.01$-0.02) y precipitados de fase-χ ($fv_{\chi}\sim0.02$). Se ha observado que el ataque químico con el reactivo Lichtenegger-Blöch (L-B) no solo revela las fases, sino también la presencia de bandeado químico (segregación de los elementos de aleación) a lo largo de la sección transversal de las planchas. Este bandeado químico es resultado del modo de solidificación del acero y del proceso de laminación. Cálculos termodinámicos realizados con el software ThermoCalc, usando la base de datos TCFE6 (versión 6.2), predicen que la solidificación ocurre primero con la formación de ferrita-δ y, depués, de γ. El reactivo L-B colorea las bandas dependiendo de los elementos segregados. Los mapas 2D realizados con EPMA han demostrado que los elementos Ni, Cu y Ti segregan juntos en bandas, mientras que el Cr presenta un comportamiento opuesto y el Mo un comportamiento mixto. La comparación entre las imágenes de MO y los mapas de EPMA ha permitido establecer una relación directa entre la concentración de elementos de aleación y el contraste de color obtenido tras el ataque con L-B.

2. Transformaciones de fase en calentamiento continuo

Uno de los objetivos fundamentales de este apartado ha sido entender la evolución microestructural y los procesos que ocurren en calentamiento continuo en el acero considerado: precipitación, recuperación de la microestructura inicial, el mecanismo de reaustenización (transformación de α'→γ) y el crecimiento de grano austenítico. Para ello, se estudiaron diferentes velocidades de calentamiento (Vc: 0.1, 1 y 10 °C/s) y se emplearon diferentes técnicas, como MO, MEB, MET, micro-durezas Vickers, EPMA, medidas de magnetización, poder termoeléctrico (PTE) y difracción de electrones retrodispersados (EBSD). Se ha observado que todas las temperaturas críticas se desplazan a mayores temperaturas cuanto más rápida es la Vc, lo cual es característico de procesos difusionales. El calentamiento hasta temperaturas comprendidas entre 300 y 550 °C da lugar a un incremento significativo de la dureza del material (de hasta 285 Hv) debido a la nano-precipitación de $Ni_3(Ti,Al)$ en la matriz martensítica. El inicio de la reaustenización produce la disolución de los nano-precipitados, perdiéndose el efecto endurecedor a medida que aumenta la fv_γ. Las temperaturas críticas de inicio y fin (A_S-A_F) de la transformación α'→γ se detectaron en 600-825°C, 650-900°C y 690-950°C para las velocidades de 0.1, 1 y 10 °C/s, respectivamente. Independientemente de la Vc, la transformación ocurre mediante un mecanismo difusional de corto alcance, sin partición, en un amplio rango de temperaturas y en dos etapas. El calentamiento hasta A_F resulta en la obtención de microestructuras-γ de tamaño de grano (TGA) ultrafino (280-440nm) con fracciones de volumen de fase-χ en el rango 0.10 - 0.02 para Vc=0.1 10 °C/s. Se ha demostrado que la morfología tipo celda de dislocaciones de la α' inicial juega un papel fundamental en el afino de grano, ya que proporciona un elevado número de sitios de nucleación para la fase austenita. El calentamiento por encima de A_F da lugar al crecimiento del grano y la consecuente disminución de estabilidad térmica de estas microestructuras austeníticas.

3. Comportamiento mecánico de microestructuras reaustenizadas

Para establecer la relación entre microestructura, ruta de procesado y propiedades mecánicas, se estudió el comportamiento mecánico a tracción a temperatura ambiente de microestructuras parcial (α'/γ) y completamente reaustenizadas en calentamiento continuo (Vc=0.1, 1 y 10°C/s). Para microestructuras-γ submicrométricas y duales

(α'/γ), la resistencia máxima (Rm) y la elongación total (ε_T) varían entre 2.10-1.2GPa y 3-25% dependiendo del balance α'/γ, la presencia de nano-precipitados $Ni_3(Ti,Al)$ y la estabilidad mecánica de la austenita (efecto TRIP o formación de α' inducida por deformación). En microestructuras-γ la Rm puede bajar hasta 0.87 GPa y la ε_T incrementar hasta 44 % al aumentar el TGA de 0.44 a 6.50 µm. La deformación plástica en estas microestructuras ocurre vía formación de bandas de Lüders previo endurecimiento por deformación. La estabilidad de la austenita se estudió mediante medidas de magnetización post-mortem en muestras ensayadas a tracción y se observó que esta disminuye al aumentar la fracción de volumen de austenita en la microstructura. La formación de α' inducida por deformación empieza con la formación de bandas de Lüders, que se propagan por la sección calibrada de las probetas de tracción previo endurecimiento y deformación homogénea. El efecto TRIP juega un papel fundamental en microestructuras-γ o duales con altas $fv_\gamma \sim 0.70 - 0.98$, ya que produce un incremento significativo del ritmo de endurecimiento por deformación, dando lugar a un aumento simultaneo de resistencia y ductilidad.

4. Estudio de los procesos de endurecimiento por precipitación

Este apartado se centra en la optimización de la etapa de endurecimiento por precipitación con vistas a implementarlo en una línea de procesado industrial. Por este motivo, se ha estudiado la respuesta al envejecimiento del acero bajo estudio en un amplio rango de temperaturas donde ocurre la precipitación (T_{env}=300 - 550°C) y tiempos no superiores a 72 horas. Combinando técnicas de caracterización como MET, PTE, micro-dureza Vickers y ensayos de tracción se ha observado que a mayor T_{env} más rápida es la respuesta endurecedora del material. La dureza y resistencia máxima a la tracción más altas (710 Hv y 2.7 GPa, respectivamente) se alcanzan tras un tratamiento de 72 h entre 425 - 475°C. Medidas de magnetización y caracterización microestructural revelaron que envejecimientos de 24 h o más a T_{env} mayores de 500 - 550°C inducen la formación de fase austenita, lo que resulta en un ablandamiento del material. Los nano-precipitados se caracterizaron por TEM y TEM de alta resolución como $Ni_3(Ti,Al)$. Se observó que crecen en forma de barra de una longitud no superior a 30 nm y con una relación de orientación con la matriz $(1\bar{1}0)_{\alpha'} \| (0001)_{Ni_3(Ti,Al)}$ y $[1\bar{1}1]_{\alpha'} \| [11\bar{2}0]_{Ni_3(Ti,Al)}$. Envejecimientos entre 400 y 475 °C producen un aumento continuo de la dureza, incluso tras 72 h. La ultra-alta resistencia de este acero tras tiempos largos de envejecimiento (24 – 72 h) se atribuye a la resistencia a engrosar que presentan los precipitados.

Chapter 1

Introduction

This chapter goes briefly through the history of the discovery of “stainlessness” and gives an overview on the various types of stainless steels, their general classification based on microstructures and the effect of different alloying elements. Since the stainless steel under investigation belongs to the semi-austenitic metastable and precipitation hardening group, a more extensive description is given about them, highlighting their main features such as metastability or precipitation hardening ability, whose combination makes this kind of steels versatile for a wide range of applications. This thesis work mainly focuses on understanding the three-links chain (processing-microstructure-properties) paradigm of the steel under investigation to enhance its high performance. For this reason, it is convenient to introduce the main strengthening mechanisms in steels, in order to review some important concepts that will appear frequently throughout the thesis work.

1.1 Introduction to stainless steel

Iron and the most common iron alloy, steel, are relatively poor materials from a corrosion viewpoint since they rust in air, corrode in acids and scale in high temperature furnace atmospheres. In spite of this, there is a group of iron-base alloys, with minimum chromium (Cr) content of 12 wt. % and often with nickel (Ni) additions that are able to resist the corrosion and are known as stainless steels. Chromium plays a determining role in making the steel corrosion resistant. In relatively benign environments chromium can form a thin an adherent chromium oxide (Cr_2O_3) passive surface film, which protects it of staining, rusting or corroding in environments where normal steels are susceptible (for instance, in relatively pure, dry air). However, to prevent pitting and rusting in more hostile environments or depending on the type of stainless steels under consideration other alloying elements are required. In addition to their stainlessness, stainless steel does not discolor in a normal atmospheric environment and keeps a shiny surface [1].

The discovery of stainless steels is generally thought to happen in Europe about a century ago, although, there is controversy over its ‘birthplace’. It is incontrovertible; however, that stainless steel is a remarkable achievement of modern metallurgy and has contributed significantly to the wellbeing of humankind. The use of stainless steels ranges from the low-end products such as water buckets or cutlery, to the very high-end ones, such as the spacecraft propellers and casings, constructions or surgical implants. The ubiquity of stainless steels in our daily life makes it impossible to enumerate all their applications [2].

Stainless steels also outperform ordinary steels on high-temperature mechanical properties. Stainless steels are much better in terms of fire resistance and retention of strength and stiffness at elevated temperatures compared with carbon steels. Steel is frequently the ‘gold-standard’ against which emerging structural materials are compared. Steel remains the most successful and cost-effective of all materials, with more than a billion tones being consumed annually in improving the quality of life. One reason for the overwhelming dominance is the endless variety of microstructures and properties that can be generated by solid-state transformation and processing.

1.2 The effect of alloying elements

Traditionally, the effects of different alloying elements on phase balance have been quantified by using the nickel and chromium equivalent numbers, Ni_{eq} and Cr_{eq}, respectively. These coefficients consider the difference between ferrite (BCC structure) stabilizing elements (Cr_{eq}), and austenite (FCC structure) stabilizing elements (Ni_{eq}) to predict the solidification path that the molten steel follows and, thus, the phases that will constitute the microstructure. The Cr and Ni equivalent numbers suggested by Schaeffler and DeLong are as follows, respectively. Afterwards, subsequent researchers have incorporated the effects of more elements in such expressions [3].

$$Cr_{eq} = \%Cr + \%Mo + 1.5\%Si + 0.5\%Nb$$

$$Ni_{eq} = \%Ni + 30\%C + 30\%N + 0.5\%Mn$$

One commonly used tool to predict the microstructure of high-alloy steels at room temperature is the Schaeffler-DeLong diagram, (Figure 1.1). By studying this diagram, it is observed that high Ni_{eq} numbers are required to maintain an austenitic (FCC) structure. Therefore, the Ni_{eq} number is used as a yardstick for assessing the stability of austenitic stainless steels against the martensitic transformation.

The different alloying elements have specific effects on the properties of the stainless steel, and it is their combined effect together with the heat treatment and to some extent, the impurities, which determines the properties of a certain steel grade. In order to understand their effects on the microstructure and properties, a brief overview is given of the main alloying elements [4].

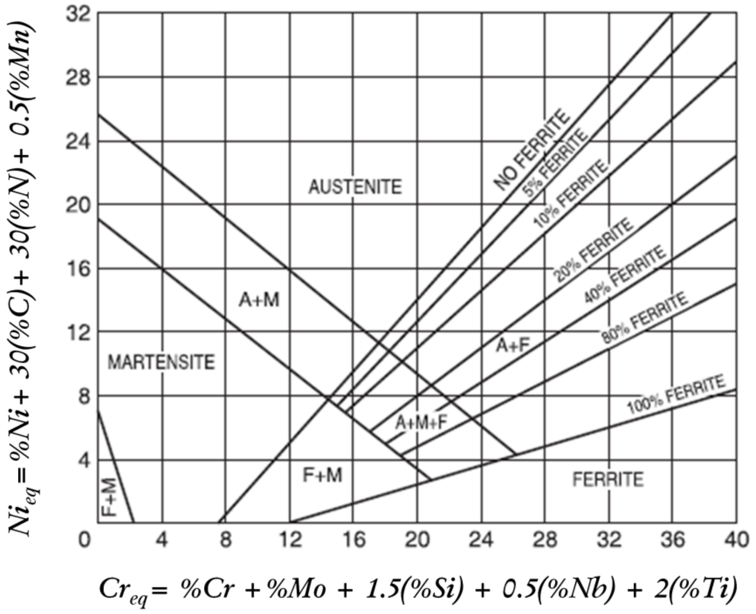

Figure 1.1. Schaeffler-DeLong diagram predicting the phase structure for different chemical compositions in stainless steel.

Carbon (C): Carbon is an important alloying element in all ferrous metal based materials, since it is a very strong austenite stabilizing element and increases the strength of steel. In austenitic, ferritic, and duplex stainless steels, it is kept to low levels (typically 0.005 - 0.03 wt. % C in low carbon grades) to retain the desired mechanical properties. In martensitic stainless steels, carbon is added in amounts varying from 0.15 wt. % to 1.2 wt. % to make these alloys heat treatable by quenching and tempering to develop the martensite phase and, thus, to increase both the strength and hardness. The principal effect of carbon on corrosion resistance is determined by the way in which it exists in the alloy. If it is combined with Cr as carbide, it may have a detrimental effect on corrosion resistance by removing some of the Cr from solid solution in the alloy and, thus, reducing the amount of Cr available to ensure corrosion resistance. Moreover, upon certain heat treatments, the precipitation of Cr-carbides takes place at grain boundaries, leading to localized corrosion, i.e. intergranular corrosion, referred to as sensitization [5].

Chromium (Cr): This is the most important alloying element since it makes steel stainless. All stainless steels have a Cr content of at least 12 wt.% and the corrosion resistance increases with its content. Its effectiveness stems from its high degree of reactivity, which leads to the formation of an adherent, insoluble and very fine layer (1 – 2 nm) of chromium oxide that shields the metal from uniform and localized attack. Besides, Cr also increases the resistance to oxidation at high temperatures and promotes a ferritic microstructure.

Nickel (Ni): It has no direct influence on the passive layer but exerts a beneficial effect, particularly in sulphuric acid environments. Ni additions promote an austenitic microstructure and thanks to it Fe-Cr-Ni(Mo) alloys exhibit a wide range of mechanical properties. Generally, it increases ductility and toughness and is a moderate strengthener. In precipitation hardening steels, it is used to form intermetallic compounds that increase the strength. In martensitic grades Ni addition combined with lowered carbon content improves the weldability.

Molybdenum (Mo): Mo is used in stainless steels in amounts up to 8 wt. % and most commonly in the range from 2 - 4 wt.%. Even such relatively small percentages of Mo have powerful effects in improving the resistance to pitting in chloride environments and uniform corrosion. Mo decrease the tendency of previously formed passive films to break down. It somewhat increases the mechanical strength and strongly promotes a ferritic microstructure. However, Mo also enhances the risk for the formation of deleterious secondary phases in ferritic, duplex and austenitic steels, which cause embrittlement.

Copper (Cu): Copper enhances the corrosion resistance in certain acids and promotes an austenitic microstructure. It can also be added to decrease work hardening in grades for improved machinability. It may also be added to improve formability. Moreover, it has been also found that stainless steel is strengthened by clusters of Cu produced during aging, which also act as nucleation sites for Ni-rich intermetallic compounds.

Titanium (Ti): Titanium is a highly reactive element. In low alloy steels, Ti has a strong desire to unite with carbon, nitrogen and oxygen. When dissolved in steel, Ti is believed to increase hardenability; however, the carbide-forming tendency of this element is so strong that it is frequently in the steel structure as undissolved carbides and in this way decreases hardenability.

Aluminum (Al): If added in substantial amounts, Al improves oxidation resistance and is used in certain heat-resistant grades for this purpose. In precipitation hardening steels, Al is used to form the intermetallic compounds that increase the strength in the aged condition.

Silicon (Si): In small amounts, silicon confers mild hardenability on steels. Small amounts of silicon and copper are usually added to the austenitic stainless steels containing molybdenum to improve corrosion resistance in sulphuric acid. Silicon is commonly added to stainless steels as a ferrite stabilizer. In austenitic stainless steels, high-silicon content also prevents the formation of carbides at elevated temperatures.

Manganese (Mn): Mn is usually found as an alloying element in all types of steel to assist the deoxidation of the steel and to prevent the formation of iron sulphide inclusions, which may cause hot cracking problems, by forming MnS. Moreover, the presence of Mn increases the hardenability of the steel and, in large additions (12 to 15 wt.%), makes the steel austenitic at room temperature.

1.3 Classification of stainless steels

Conventionally, stainless steels are classified in five groups as function of the microstructure they exhibit. These are: 1) ferritic stainless steels, 2) austenitic stainless steels, 3) martensitic stainless steels, 4) duplex stainless steels and 5) precipitation hardening stainless steels [1].

Ferritic stainless steels (FSSs): FSSs are iron-chromium alloys that have the same structure as pure iron at room temperature, body centered cubic (bcc) ferrite (α) phase. Therefore, the solubility of carbon is rather limited and most of the carbon forms carbides such as $(Cr,Fe)_7C_3$ and $(Cr,Fe)_{23}C_6$. Their corrosion resistance and toughness is moderate, however, they are affordable due to the low content of alloying elements.

Austenitic stainless steels (ASSs): ASSs have superior corrosion resistance and toughness and are the most weldable of the stainlesses. This group can be divided rather loosely into five sub-groups: Cr-Mn grades (also referred to as “200-series” grades), Cr-Ni grades (sometimes referred as 18-8 SS, indicating the approximate content in Cr and Ni, respectively), Cr-Ni-Mo grades, high performance austenitic grades and high temperature austenitic grades, for use at temperatures exceeding 550 °C. Their alloying elements content allows ASSs the retention of the high temperature face centered cubic (FCC) austenite (γ) phase at room temperature. They are the most common stainless steels, constituting the 80 % of the total production. They are frequently used in kitchen sinks, chemical industry or food processing. ASSs have a face-centered cubic structure. Though generally very weldable, some grades can be prone to sensitization of the weld heat-affected zone and weld metal hot cracking.

Martensitic stainless steels (MSSs): MSSs as types 403, 410, 410NiMo and 420, have relatively high carbon content, but contain a balance of C and Ni versus Cr and Mo that promote the phase transformation from the high temperature parent phase (austenite) into the body centered tetragonal (BCT) martensite (α’) phase. The tetragonality of the martensite phase depends on the carbon content of the alloy, being referred to as BCC for C concentrations up to 0.6 wt % [6]. Thus, MSSs are hardenable through the γ→ α’ transformation. Their corrosion resistance is moderate, and by adding some Ni and reducing the carbon content the rather poor weldability can be improved.

Duplex stainless steels (DSSs): DSSs have a ferritic-austenitic microstructure. Their strength is higher and their common usage is in petrochemical industry. DSSs typically contain approximately 22-25 Cr and 2-7 Ni with Mo and N (in wt. %), so they offer good resistance to corrosion. Although duplex and some austenitic SS do have similar alloying elements, the former ones have higher yield strength and greater stress corrosion cracking resistance to chloride than austenitic SS.

Precipitation hardening stainless steels

Precipitation-hardening stainless steels (PHSSs) are commonly classified as austenitic, semi-austenitic and martensitic [7-17]. The stainless steel studied in this thesis work belongs to the semi-austenitic PHSSs group, and for this reason, a more detailed description is given below.

1.4 Semi-austenitic precipitation hardening stainless steels

1.4.1 Stable and metastable phases

After solution treatment or annealing, semi-austenitic PHSSs exist predominantly in the austenitic (γ) state with small amounts of retained phases such as α-ferrite and δ-ferrite. Therefore, under this condition they exhibit good ductility and formability.

The retention of austenite at room temperature does not imply that it is the most thermodynamically stable phase at this temperature. Indeed, martensite (α’) is the stable phase. However, with a carefully balanced addition of austenite and ferrite stabilizers, it is possible to obtain austenite phase at room temperature with an adequate grade of metastability. Under certain conditions and processes, such as thermo-mechanical treatments, the martensitic transformation ($\alpha' \rightarrow \gamma$) can be triggered [1]. Particularly, for the steel under investigation, it has been shown that the metastable austenite transforms into martensite phase either under the application of stresses/strains due to the Transformation Induced Plasticity (TRIP) effect, or isothermally when subjected to cryogenic treatments [18; 19]. In addition, San Martin *et al* have recently found that the transformation can be accelerated by applying external magnetic fields. [20; 21]. Due to its importance for this work, some concepts regarding the martensitic transformation are reviewed below.

A) The martensitic transformation

The formation of martensite involves a diffusionless, shear transformation, where a coordinated and rapid movement of atoms (1100 ms^{-1}) takes place. This results in a change in the crystalline structure (FCC → BCT/BCC) and in a deformation in shape, known as invariant plane strain that causes shear and a volume expansion of the transformed region. The transformation is highly crystallographic in character because it is generated by a specific deformation of the austenite. Thus, the interface between austenite and martensite (α'/γ) will be intimately related by a reproducible orientation relationship such as the well-known Kurdjumov-Sachs (KS), Nishiyama-Wassermann (NW) or Greninger-Troiano (GT) orientation relationships [22].

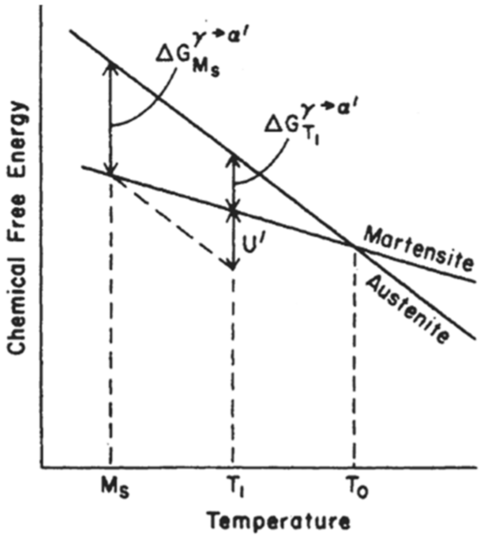

Figure 1.2. Schematic diagram showing the free energy change for a martensitic transformation, adapted from Wayman *et al.* [23].

Kinetically, iron based alloys can undergo martensitic transformation either under an *athermal* or *isothermal* mechanism. The *athermal martensite* transforms during cooling as a function of temperature only, whereas the *isothermal martensite* forms as a function of both temperature and time, and an incubation time is needed for the transformation to start. In this sense, for an adequate semi-austenitic metastable stainless steel, it is important the temperature at which the austenite and martensite are in thermodynamic equilibrium (T_0), at which the free energies of both phases are equal ($G_{T_0}^{\gamma} = G_{T_0}^{\alpha'}$). An increase in the content of γ-stabilizers, lowers the T_0 and, thus, reduces the driving force for the γ → α' transformation ($\Delta G^{\gamma\rightarrow\alpha'}$), being possible to "trap" the material in a metastable austenitic state at room temperature [22].

Figure 1.2 shows schematically the change in chemical free energies of martensite and austenite (parent phase) with temperature. M_S is the martensitic transformation temperature, at which the γ → α' transformation occurs spontaneously upon cooling (athermally). The difference in free energies between austenite and martensite ($\Delta G_{M_S}^{\gamma\rightarrow\alpha'}$) at M_S is the critical chemical driving force for the onset of the martensitic transformation [23]. However, the transformation can occur also at the temperature T_1 ($> M_S$), if a sufficient mechanical driving force *U'* is available, so that:

$$\Delta G_{T_1}^{\gamma\rightarrow\alpha'} + U' = \Delta G_{M_S}^{\gamma\rightarrow\alpha'} \qquad [1.1]$$

Therefore, if a critical mechanical driving force (*U'*) is applied, the austenite will transform into martensite at T_1. Since this martensite is originated by an applied stress, it is known as stress-induced martensite. Figure 1.2 suggests that the driving force of the martensitic transformation ($\Delta G^{\gamma\rightarrow\alpha'}$) decreases linearly with increase in temperature above M_S. Olson and Cohen [24] demonstrated this linear relation to be valid up to the stress level corresponding to the yield strength of the austenite (σ_y), which is illustrated in Figure 1.3. Bolling and Richman [25] defined the corresponding temperature as the M_S^{σ} temperature. Below M_S^{σ}, the yielding can occur by means of the martensitic transformation, whereas at higher temperatures the transformation can take place only after the plastic deformation of the austenite phase. Olson and Cohen [24] established the concepts of *stress-assisted* and *strain-induced martensitic transformations*. The former one occurs below the yield strength of the austenite phase with the aid of the applied stress, and the latter only after plastic deformation of the austenite phase, being its upper limit defined by M_d or temperature above which the chemical driving force becomes so small that nucleation of martensite cannot be mechanically induced, even in the plastic strain regime [23]. Besides, the strain level at which austenite begins to transform to martensite is also influenced by the carbon content and the size of the austenite grains [26; 27].

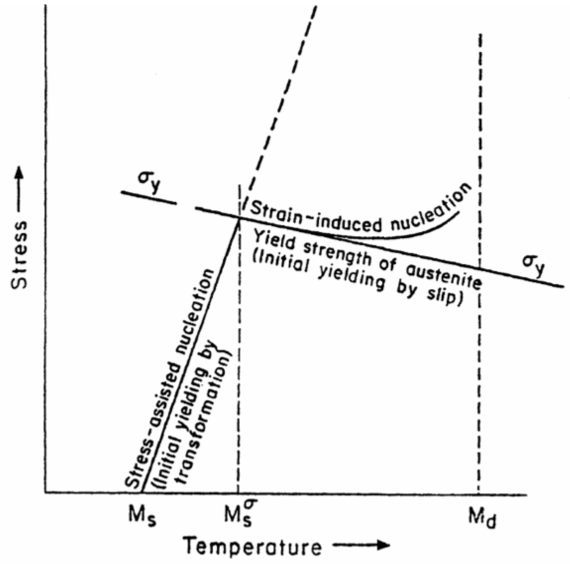

Figure 1.3. Schematic stress-temperature diagram showing the critical stress to initiate the formation of martensite as a function of the temperature [24].

It was also suggested by Olson and Cohen [24] that depending on the residual stress level and the amount of martensite, the strain-induced transformation may turn into stress-assisted transformation after deformation. When the formation of martensite is constrained by its surroundings, it forms as thin plates or laths in order to minimize the strain energy due to deformation, as shown by San Martin *et al.* [20] (Figure 1.4). The deformation of the austenite aids the transformation by the formation of energetically favorable nucleation sites for the martensite.

In ASSs, martensitic nucleation sites involve the intersections of shear bands, consisting of bundles of overlapping stacking faults that result in the formation of a close-packed hexagonal (HCP) ε-martensite phase. Although this phase is in equilibrium only at high pressure [28], it is often observed in ASSs at ambient temperature and pressure as an intermediate phase between austenite and α'-martensite during plastic deformation [6; 29; 30].

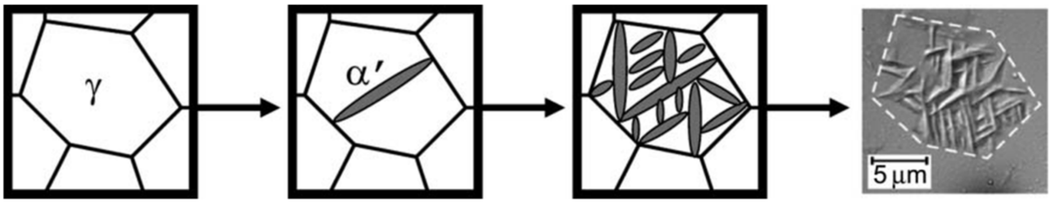

Figure 1.4. Schematic view of the microstructure evolution during the isothermal transformation from austenite (γ) to martensite (α') and optical micrograph of the surface roughening resulting from the transformation, after San Martin *et al.* [20]. The dashed line outlines the original austenite grain boundary.

Sandvik Nanoflex ® does not transform athermally into martensite but only isothermally [31]; therefore, the M_S could be only defined in this steel as the temperature at which isothermal martensite is thermodynamically favorable, which seems to be around room temperature (although kinetics might be too slow).

B) Implications of the martensitic transformation

It is well known that the martensite phase has a higher flow stress ($R_{e\alpha'}$ = 700 N/mm^2) than the austenite phase ($R_{e\gamma}$=200 N/mm^2) [32]. Therefore, the martensite itself along with the subsequent accumulation of stresses and dislocations in the α'/γ-interface resulting from the martensitic transformation give rise to an increased strength in the material. This effect of extra hardening associated to the strain-induced martensite, leads to a greater attainable strain during plastic deformation since the necking is delayed, which in turn results in an improvement of strength, ductility and toughness of steels [33].

Therefore, the metastability of the austenite in semi-austenitic PHSSs allows taking advantage of the material in its soft condition for forming and, simultaneously, to increase its strength due to the martensitic transformation. The steels that exploited these effects are known as transformation-induced plasticity (TRIP) steels [34].

However, it has to be borne in mind that the interstitial solid solution of carbon plays the major strengthening factor in martensite, since it leads to dynamic interactions with dislocations that, in turn, result in high rates of strain hardening during deformation [22; 35; 36]. Therefore, if carbon is eliminated from the steel, the resulting hardening effect is much lower. In this case, as in low-carbon SS, the strengthening comes from the high dislocation density of the martensite and the martensitic block size[1] [35; 37]. Alternatively, low-carbon SS may contain alloying elements that will form strengthening particles in the matrix under the adequate heat treatment to enhance the final mechanical properties, as is the case of the steel under investigation. The combination of both effects: (1) the metastability of the austenite phase and (2) the possibility of further strengthening by precipitation, make semi-austenitic PHSSs versatile for a wide range of applications [32; 38].

1.4.2 The precipitation hardening ability

Steels combining properties of ultrahigh strength, good ductility and corrosion resistance are of great importance in the industry. PHSSs can attain high strengths without seriously compromising corrosion resistance and ductility as in other classes of stainless steels. In particular, lath martensite has been widely accepted to be a very efficient matrix for precipitate strengthened ultra-high strength (UHS) steels, and is employed and investigated in various commercial grades such as PH 17-4 [7-11], PH 15-5 [12; 13] or PH 13-8 [14; 16; 17]. On the other hand, the PHSSs whose strengthening mechanism is associated with, first, the formation of martensite and, second, the precipitation of strengthening particles induced by an aging treatment are known as maraging steels, and their aging behavior has been thoroughly investigated [39-47]. Maraging and PH stainless steels differ mainly in terms of the nature of precipitates that form due to aging, consequence of the different carbon content, which may be almost an order of magnitude lower in the maraging type.

Table 1.1. Secondary phases present in stainless steels [48-50].

---

[1] A martensitic block consists of martensitic laths with the same crystallographic orientations [36].

Phase	Symbol	Type	Formula	T range, °C	Structure	Lattice constant, nm
Carbide	–	M_7C_3	$(Cr,Fe,Mo)_7C_3$	950-1050	Orthorhombic	$a=0.452$; $b= 0.699$; $c= 1.211$
Carbide	–	$M_{23}C_6$	$(Cr,Fe,Mo)_{23}C_6$	600-950	Cubic fcc	$a=1.057$-1.068
Carbide	–	M_6C	$(Cr,Fe,Mo,Cb)_6C$	700-950	Cubic diamond	$a=1.093$-1.128
Nitride	–	M_2N	$(Cr,Fe)_2N$	650-950	Hexagonal	$a=0.478$; $c= 0.446$
Nitride	Z	MN	(Nb,Cr)N	700-1000	Tetragonal	$a=0.303$; $c= 0.737$
Nitride	π	–	$Fe_7Mo_{13}N_4$	550-600	Cubic	$a=0.647$
Carbo-nitride	–	MC	Ti(CN)	700-1400	Cubic fcc	$a=0.432$-0.424
Carbo-nitride	–	MC	Nb(CN)	700-1350	Cubic fcc	$a=0.442$-0.438
Sigma	σ	AB	(Fe,Ni,Cr,Mo)	550-1050	Tetragonal	$a=0.886$-0.892; $c= 0.454$
Chi	χ	$A_{48}B_{10}$	$Fe_{36}Cr_{12}Mo_{10}$	600-900	Cubic fcc	$a=0.886$-0.4892
Alpha prime	α'	–	CrFe(Cr61-83%)	350-550	Cubic fcc	$a=0.2877$
Beta	β	AB	NiAl	<600	Cubic	$a=0.2887$
Laves	η	A_2B	$(Fe,Cr)_2(Mo,Nb,Ti,Si)$	550-900	Hexagonal	$a=0.473$-0.482; $c= 0.726$-0.785
Inermetallic	η	A_3B	$Ni_3(Ti,Al)$	300-550	Hexagonal	$a=0.5109$-0.5115 $c=0.8299$-0.8304
Intermetallic	γ'	A_3B	$(Ni,Co,Fe,Cr)_3(Ti,Al)$	300-550	Cubi fcc	$a=0.3565$-0.3601
Mu	μ		$(Cr,Fe)_7(Mo)_2$		Rhombohedral	$a=0.4762$; $c=2.5015$
R	*R*	–	(Fe,Mo,Cr,Ni)	550-650	Hexagonal	$a=1.0903$; $c= 1.9347$
Tau	τ	–	–	551 - 650	Orthorhombic	$a=0.05$; $b= 0.484$; $c= 0.286$
G	*G*	$A_{16}B_6D_7$	$Ni_{16}(Nb,Ti)_6Si_7$	500 - 850	Cubic fcc	$a=1.12$

For the purpose of precipitation, most PHSSs contain alloying additions such as C, Cr, Ti, Al, Cu, Mo, V, Mn, Nb, Co, W, Si, etc., that upon aging form carbides, intermetallics and other strengthening particles. Table 1.1 shows a summary of possible precipitate phases detected in stainless steels. For example, 17-7 PH and PH 15-7 Mo have about a 1 wt. % Al addition, and 17-4 PH and 15-5 PH have a 3 – 5 wt. % Cu [47]. Servant *et al.* [7] studied the PH 17-4 stainless steel (17Cr-4Ni-1Mo, in at. %) and found that various carbides (TiC, Mo_2C, $M_{23}C_6$ and M_7C_3) form at different aging temperatures while a hardening peak related to the Mo_2C carbide was observed for aging close to 400 °C. Steel grades based on intermetallic precipitates, only contain a small amount of C in order to avoid the formation of carbides or carbonitrides. Different precipitation phases have been identified, including γ-Ni_3Mo, η-Ni_3Ti, Laves-Fe_2Mo, σ-FeMo, μ-Fe_7Mo_6, FeTi and Fe_2Ti. A well-known example of steel strengthened by intermetallics is the PH 13-8 grade, as Seetharaman and co-authors [14] observed. This steel is significantly hardened by the formation of nano-sized (1 - 6 nm) intermetallic β-NiAl in the range 400 – 550 °C. Viswanathan *et al.* [8] reported the formation of pure copper precipitates in the 17-4 PH steel at about 400 °C, and phases like $Ni_3(Ti,Mo)$ and the Fe_2Mo have been seen to form aging at temperature of about 500 °C in 18 wt.% Ni maraging steel [40; 42]. The formation of pure copper particles or clusters has been identified in several PHSS. Habibi *et al.* [13] identified two stages of hardening in a PH15-5 associated, initially, to the formation of Cu-clusters and, the second stage, to the formation of another type of Cu precipitates, spherical and semi-coherent. Other authors have also detected the early formation of Cu-clusters upon aging, which later act as nucleation sites for other Ni-rich intermetallic precipitates [51-53].

In addition to the homogeneous intragranular or intralath precipitates in the matrix, the formation of intergranular precipitates, such as MX carbides (Ti,Nb,V)(C,N) along prior austenitic grain boundaries during the heat-treatment may also be beneficial in increasing the toughness since they pin the movement of grain boundaries, hindering the grain growth. However, the formation of undesirable phases that limit the strength and the toughness, such as $M_{23}C_6$, M_6C, M_7C_3, μ-phase, χ-phase should be prevented during the design of the alloy by ensuring that only the desired phases are thermodynamically stable.

1.5 Strengthening mechanisms in steels

Austenitic stainless steels (ASSs) present an excellent combination of properties and corrosion resistance, which makes them good candidates for a great number of applications [32; 38]. However, their lack of high strength precludes their wide spread use in an important number of these applications. For this reason, the development of stainless steels (SSs) with high strength-high ductility combinations is a subject of significant interest. There are many ways of strengthening steels, which is why they are able to offer such a wide range of properties. It is also possible to combine several strengthening mechanism, and in such circumstances it is often difficult to quantify the variety of contributions to the overall strength. In principle, the strength of steel is contributed by a number of strengthening mechanisms as follows:

$$\sigma_y = \sigma_0 + \sigma_{ss} + \sigma_{gs} + \sigma_{dis} + \sigma_{ppt} \qquad [1.2]$$

Where σ_y is the yield strength, σ_0 is the friction stress for pure iron and has been estimated to be ~ 219 MPa for pure annealed iron [54], and σ_{ss}, σ_{ppt}, σ_{gs} and σ_{dis} are the contributions to the strengthening due to the solid solution, the precipitation, the grain size and the dislocations, respectively. However, as demonstrated by Queyreau *et al.* [55], the expression in Eq. [1.2] might overestimate the dislocation forest and precipitation hardening terms, since they arise from similar density and strength obstacles. Thus, their contribution to the overall strengthening must obey a quadratic mixture law, resulting a modified expression that is often used in plasticity modeling of multiphase alloys [56]:

$$\sigma_y = \sigma_0 + \sigma_{ss} + \sigma_{gs} + \sqrt{\sigma_{dis}^2 + \sigma_{ppt}^2} \qquad [1.3]$$

In the following sections different strengthening mechanism will be presented and discussed in detail.

1.5.1 Solid solution strengthening

Solid solution strengthening occurs when the strain fields around misfitting solutes interfere with the motion of dislocations as they move through the lattice causing plastic flow. The factors behind the solid solution strengthening seem to be the size difference and the shear module difference between solvent (iron) and solute atoms (atoms that substitute iron), that cause local expansions or contractions and, thus, lattice strain. These strains are isotropic and therefore can only interact with the hydrostatic components of the strain fields of dislocations. In contrast, an interstitial atom (carbon or nitrogen) located in the irregular octahedron interstice in ferrite causes a tetragonal distortion, which has a powerful interaction with the shear, the dominant component of a dislocation strain field. This is why interstitial solid solution strengthening is so potent in ferrite. The corresponding interstitial site in austenite is a regular octahedron. An interstitial atom in austenite therefore behaves like a substitutional solute, with only hydrostatic strains surrounding it. This is why carbon is much less effective in strengthening austenite [57].

Generally, the solid solution strengthening can be described as a function of the atomic concentration of solutes. The following formula has shown the best agreement with experimental results for binary BCC-iron systems [58-61]. Their linear dependence model yields:

$$\sigma_{ss} = \sum_{i} K_i C_i \qquad [1.4]$$

Where K_i is the strengthening coefficient for 1 wt.% of alloying element i and C_i is the concentration of the alloying element i in the solution in weight per cent. The strengthening factor combines both size misfit and modulus misfit effect and is generally determined from experiments. Table 1.2 shows K_i values for some alloying elements [60; 62].

Kim *et al.* [60] detected increments between 148 and 219 MPa associated to high (2.3 wt.%), medium (1.7 wt.%) and low (1.4 wt.%) Si content alloys. According to Misra *et al.* [61], simultaneous additions of 0.3 wt.% Cu and 0.15 wt.% Ni can further enhance yield strength by 32.4 MPa in a 690 MPa grade steel.

Table 1.2. Strengthening factor (K_i) values of some alloying elements in ferritic matrix [58; 60; 62].

Element	C, N	Ni	Ti	Mo	Al	Co	V	Mn	Si	W
K_i (MPa/at.%)	1103.45	19.2	17.9	15.9	9	2.1	2	16.9	25.8	31.8

1.5.2 Dislocation strengthening

In the absence of strong pinning points, plastic deformation is dominated by dislocation-dislocation interactions, which impede their own motion. The intersection of a dislocation with other dislocations threading its glide plane results in the formation of crystal defects (jogs and kinks) and more dislocation. Moreover, dislocations may also interact with grain boundaries, which act as barriers in length sufficiently strong to sustain dislocation pile-ups, which not only stops the source producing dislocations, but also generates internal stress, both leading to hardening. Thus, increasing the dislocation density in a metal increases its yield strength. Work hardening is an important strengthening process in steel, particularly in obtaining high strength levels in rods, wires or sheets, both in plain carbon and alloy steels. However, the hardening can reach saturation once the defect creation and annihilation rates balance [63].

Work hardening has an important consequence on ductility. During tensile testing, the sample will inevitably contain features which cause a concentration of stress and hence the initiation of necking. The reduced cross-sectional area at the neck increases the stress in the necked region. In the absence of work hardening to help resist local deformation, the neck becomes unstable and the sample fractures with poor overall ductility. To encourage uniform elongation, the work hardening rate must raise the yield strength at a rate greater than the increase in stress due to the reduced area at the neck. Therefore, microstructures in which the dislocation density does not substantially increase during deformation should lack ductility, as is the case of extremely fine grains [57]. Figure 1.5 demonstrates how the strength-elongation ratio of the austenitic stainless steels can be adjusted within a wide range by work hardening [64].

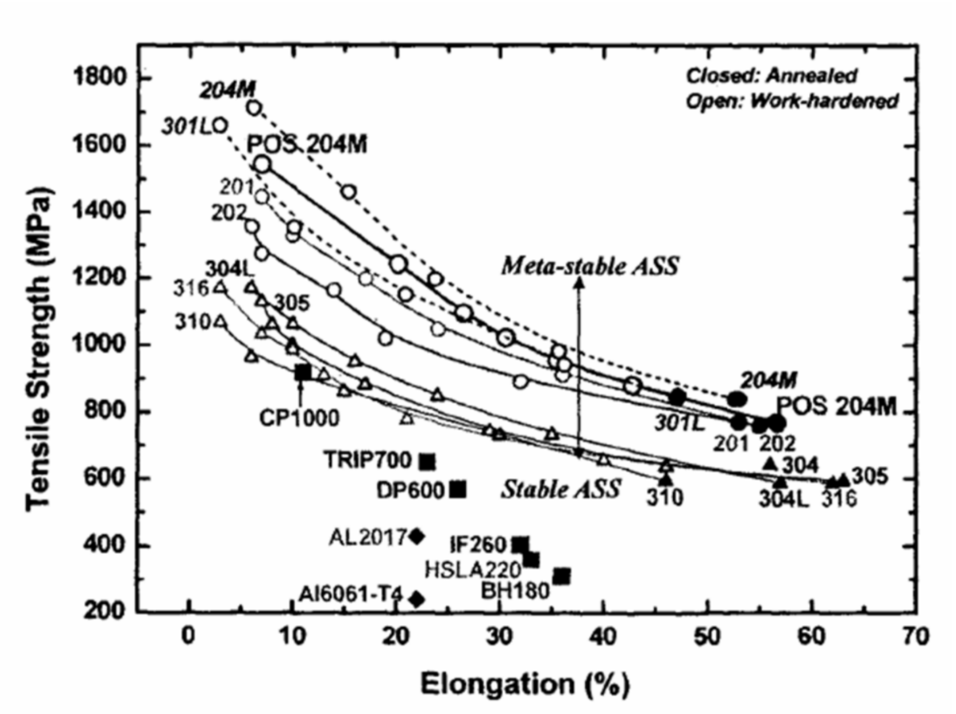

Figure 1.5. Elongation versus tensile strength of various austenitic stainless steel grades in annealed and work-hardened condition compared to carbon steels and aluminium alloys, after Kim *et al.* [64].

The relationship between dislocation density and strength increment can be described as expression in Eq. [1.5], where M is the Taylor factor (taken to be 3), α is a constant (α=0.25), b is the Burgers vector; G is the shear modulus and ρ is the dislocation density.

$$\sigma_\rho = M\alpha Gb\sqrt{\rho} \qquad [1.5]$$

Dislocation density is often evaluated by means of neutron or X-ray diffraction [65-67], since the peak broadening of a particular line, corresponding to an interplanar d spacing can be considered related only to the elastic microstrains, ε_{micro}. Christen *et al.* derived an expression for the dislocation density [67]:

$$\rho = \frac{3E}{Gb^2(1 + 2\nu^2)}\varepsilon_{micro}^2 \qquad [1.6]$$

Where E is the Young's modulus and v the Poisson's ratio. Typically reported values for ρ in martensitic steels are of the order of magnitude ~10^{15} m^{-2} [65; 67]. Table 1.3 shows typical values of parameters used for strengthening calculations in steels.

Table 1.3. Physical meaning and values of different symbols used in the strengthening mechanism calculations [33; 68; 69].

Symbol	Meaning	Value	Unit
a	Lattice constant	$a_{bcc} = 0.286$ $a_{fcc} = 0.356$	nm nm
b	Magnitude of the Burgers vector	$b_{bcc} = a_{bcc}\sqrt{3/2} = 0.249$ $b_{fcc} = a_{fcc}\sqrt{2/2} = 0.254$	nm nm
M	Taylor factor	3.06 for fcc polycrystalline matrix	—
G	Shear modulus	80 Gpa	GPa
α	Constant	0.25	—
E	Young's modulus	200 ± 15	GPa
υ	Poisson ratio	0.3	—

1.5.3 Precipitation strengthening

Precipitation strengthening effect by the precipitates relies on their interaction with dislocations. Essentially, precipitation strengthening is achieved by producing a dispersion of second phase particles induced by a precipitation process. These particles dispersed in the matrix acts as obstacles to dislocation movement, increasing the yield strength or critical resolved shear stress (CRSS) of the material, in other words, the shear stress at which permanent plastic deformation first occurs in an annealed single crystal. The degree of strengthening obtained not only is highly dependent upon the volume fraction and the size of particles, but also on the structure of the particle (whether it is an ordered particle or not) and the nature of the dislocation-particle interaction [70].

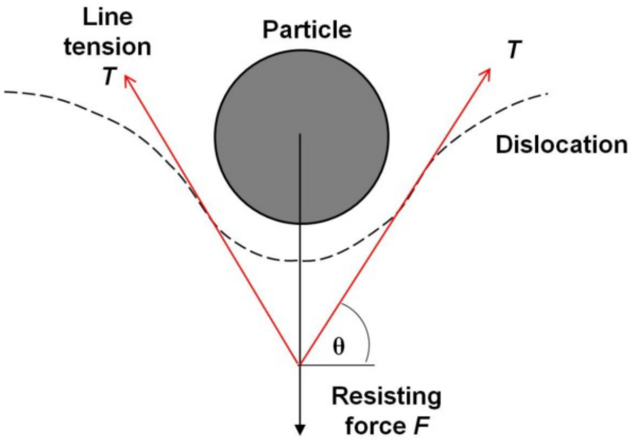

Figure 1.6. Balance of forces acting during particle resistance to dislocation movement. Adapted from Gladman [71].

The forces acting on a mobile dislocation in a stressed metal containing a dispersion of second phase particles is shown schematically in Figure 1.1. Considering the balance of forces between the dislocation line tension T and the resistance force F exerted by the precipitate: $F = 2Tsin\theta$. As F increases, so does the bowing of the dislocation that is given by the angle θ. In this way, dislocation line tension is maximum (T_{max}) for $sin\,\theta = 1$. Now, there are two possible dislocation-particle interactions as a function of the particle nature and are illustrated in Figure 1.2:

A) Impenetrable particles

The particle is hard and exerts a resistance force F greater than $2T_{max}$. Then, the dislocation will avoid the particle by the well-known Orowan looping mechanism, by cross-slipping or climbing and the particle will remain unchanged. In this case the actual strength of the particle is irrelevant since the bypassing operation depends only upon the interparticle spacing.

a) Impenetrable particles

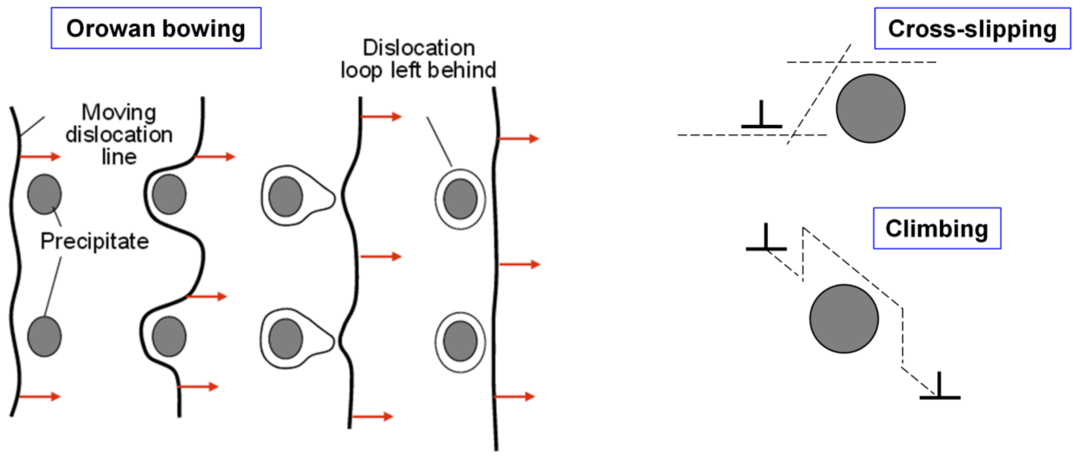

b) Penetrable particles

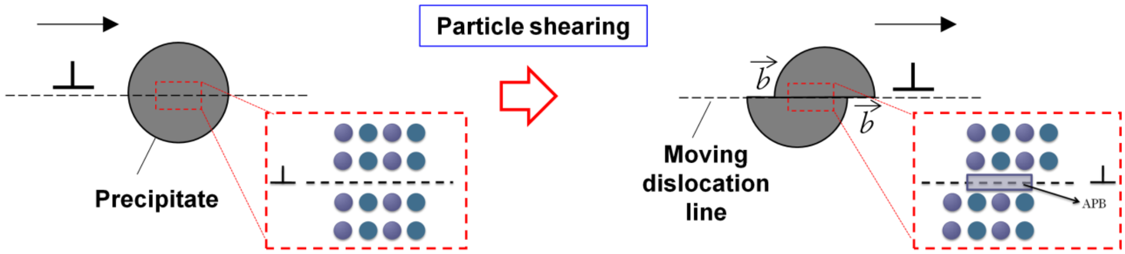

Figure 1.7. Schematic illustration of the main interactions between particles and dislocations during plastic deformation: (a) Interaction with impenetrable particles may by Orowan bowing or by-passing, cross-slipping, or climbing mechanisms; (b) Interaction of glide dislocations with penetrable ordered particles by shearing or cutting mechanism generates new interfaces and an anti-phase boundary (APB) [70].

Impenetrable particles are those whose interface has very different atomic configuration with the matrix and, therefore, the misfit between their interatomic distances (ε_{misfit}) may be larger than 25 %. Since incoherent particles are characterized by a high interfacial energy (~500-1000 mJ/m^2) their equilibrium shape will be roughly spherical. The contribution to the strengthening provided by the looping of dislocations, assuming spherical precipitates can be approximated by employing the Ashby-Orowan equation [71]:

$$\sigma_{ppt} = \left(\frac{0.538Gb\sqrt{V_f}}{X}\right) ln\left(\frac{X}{2b}\right) \qquad [1.7]$$

Where G is the shear modulus (MPa), b is the Burger vector (mm), V_f is the volume fraction of precipitates and X is the particle mean diameter (mm).

B) Penetrable particles

If the strength of the particle is such that the maximum resistance force F is attained before $sin\theta = 1$, then particles will be sheared and the dislocation will pass through the particle (Figure 1.7b). When a dislocation shears a particle, it passes from the matrix into the particle due to the continuity of slip planes across the matrix/particle interface. This situation can only arise when the precipitate/matrix interface is fully coherent or semi-coherent and, thus, there is no or little misfit ($\varepsilon_{misfit} < 25$ %) between the lattices.

Table 1.4. Factors contributing to the increase in the yield strength for the shearing mechanism, where M, G, b and r are listed in Table 1.3; $\alpha_\varepsilon = 2.6$ for fcc metals; $m = 0.85$; ΔG and $\Delta\gamma_{sf}$ are the modulus and stacking fault energy mistmatches between the matrix (M) and the precipitate (P), respectively; ε_c is the constrained lattice parameter misfit; f is the volume fraction of the precipitates; and γ_{apb} is the anti-phase boundary free energy of the precipitate [72; 73].

Strengthening mechansim	Meaning	Descriptive equation
Modulus hardening	Difference in the shear modulus G between M and P	$\sigma_{ms} = M0.0055(\Delta G)^{\frac{3}{2}} \left(\frac{2f}{G}\right)^{\frac{1}{2}} \left(\frac{r}{b}\right)^{\frac{3m}{2}-1}$
Coherency strg.	Elastic interaction between the strain fields of the coherent misfitting precipitate and the dislocation	$\sigma_{cs} = M\alpha_\varepsilon (G\varepsilon_c)^{\frac{3}{2}} \left(\frac{rf}{0.5Gb}\right)^{\frac{1}{2}}$
Order strg.	A mobile dislocation shears an ordered P and creates an APB on the slip plane	$\sigma_{os} = M0.81 \frac{\gamma_{apb}}{2b} \left(\frac{3\pi f}{8}\right)^{\frac{1}{2}}$
Chemical strg.	New P-M interface is produced. There is a surface energy associated with this new interface	$\sigma_{cc} = \left(\frac{12\gamma_s^3 f}{\pi G b r^2}\right)^{\frac{1}{2}}$
Stacking-fault strg.	Different SFE between M and P impedes the motion of dislocations since the separation of partial dislocation varies depending on the phase.	$\sigma_{sf} = (\Delta\gamma_{sf})^{\frac{3}{2}} \frac{1}{b^2} \left(\frac{3\pi^2 fr}{16G}\right)^{\frac{1}{2}}$

Whereas the strengthening after Ashby-Orowan is only dependent on the volume fraction and the diameter of the particle, the strength increment from dislocation shearing is influenced by the intrinsic material properties and crystal structure. There are five factors, listed in Table 1.4, that contribute to increase the yield strength, being the three first the most important.

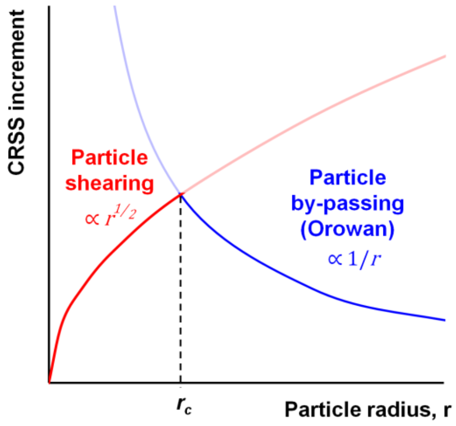

Figure 1.8. Critical resolved shear stress (CRSS) versus particle size for particle shearing and particle by-passing by glide dislocation. Adapted from J.W. Martin [70].

To estimate the strength increment from precipitates, the operative mechanism must be first identified, although it may also change. Usually, at early stages of the precipitation sequence, particles nucleate coherent with the matrix, since it is energetically more favorable than the creation of an incoherent interface, enhancing a particle shearing mechanism. However, as the particles grow with increasing the aging time, they tend to become semi-coherent and incoherent as the energy of the strained coherent interface becomes greater than that for an incoherent interface. This loss of coherency occurs when the particle reaches its critical radius (r_c), which is of the order of 10 nm, and results in a change in the mechanism from shearing to Orowan by-passing (Figure 1.8).

1.5.4 Grain size refinement strengthening

Grain size refinement is one of the predominant strengthening methods for improvement of strength and toughness in steels, as well as in other metals. The well-known Hall-Petch equation (Eq. [1.8]) describes the strengthening due to boundaries and states that the strength is inversely proportional to the square root of the mean grain size (d) and proportional to the Hall-Petch coefficient (k_{HP}). This microstructure-properties dependency has been validated for a wide range of grain sizes in austenitic stainless steels [74-81], although the limit appears to be at about 20 nm of mean grain size, value beyond which the strengthening decreases. In the case of martensitic SS, the size of the crystallographic coherent block, which may be the packet size or block size, is accepted [60].

$$\sigma_y = \sigma_0 + k_{HP} d^{-1/2} \tag{1.8}$$

The refinement of the microstructure is hold as a unique mechanism for improving strength and toughness, and one of the key methods to achieve it is through thermo-mechanically controlled processing (TMCP), which involves controlling the hot-deformation processes such as rolling, controlled-cooling and direct-quenching, in order to change its shape and refine the microstructure. The deformation leads to a breaking down of the original coarse microstructure by repeated recrystallization of the steel. However, it is difficult to obtain nano-grained/ultrafine-grained (NG/UFG) ASSs by conventional TMCP [82]. Nowadays, these limitations can be overcome by equal channel angular pressing (ECAP) [83; 84], accumulative roll bonding (ARB) [85], high pressure torsion (HPT) [86], multiple compression [87], hydrostatic extrusion [88] or cold rolling [78; 89-91].

1.6 Literature review of the steel under investigation

The material under investigation, Sandvik Nanoflex®, exhibits an excellent ductility in the austenitic annealed state (γ), it transforms to martensite (α') phase either under the application of stresses/strains or isothermally, when subjected to cryogenic treatments [18; 19]. This steel does not transform athermally [31], so that, the M_S could be only defined as the temperature at which isothermal martensite is thermodynamically favorable, which seems to be around room temperature (although kinetics might be too slow). However, it has been shown recently that the γ→α' transformation can be accelerated by applying external magnetic fields [20; 21]. Finally, after its transformation to martensite, the mechanical strength can be substantially increased by precipitation hardening of nano-intermetallic phases [52], after which the steel will meet the requiring good corrosion resistance, high strength and good ductility of the previously mentioned applications [32].

This material was originally designed for surgical needles, but its main application has been focused on the caps of water-proof electrical razors. However, the complex thermo-mechanical behavior of this material has hindered many times its application. Therefore, the few works found in the literature are focused on simulating multi-stage metal-forming processes under certain conditions to study how they influence the final shape of the product for this application [92] as well as on the investigation of the stress-assisted and strain-induced transformation and the hardening that takes place during plastic deformation for the same end [18]. On the other hand, some more work is found concerning the precipitation hardening of the steel, although it has been always focused on the aging at very specific conditions. Thuvander, Stiller or Hättestrand have been mainly dedicated to the investigation of the evolution of the chemical composition of the precipitates formed in the martensitic matrix after heating to 475 °C for aging times as long as 1000 h [51; 52; 93-95]. They found that the precipitation sequence in this steel is rather complex, involving many phases that form in direct contact to others. Besides, it was also observed that very long aging times induce the formation of the quasicrystalline *R'* phase. There are not researches that, rather than focusing on one single temperature for very long aging times, have focused on a wider temperature range for times which are more valuable from an industrial point of view.

Chapter 2

Motivation and objectives

Versatile, recyclable, extremely durable, rust, corrosion resistant are some key features that make stainless steel a good and attractive candidate for different industries such as nuclear, chemical, automotive, construction and aerospace. This thesis work focuses on the study of a specific type of stainless steel known as Sandvik Nanoflex (ASTM A693): a semi-austenitic metastable (transformable to martensite) and hardenable by precipitation in the martensitic state. This steel has showed an excellent corrosion resistance, good ductility and formability in annealed state and ultra-high strength after precipitation hardening. However, the current lack of understanding of many aspects of its complex thermo-mechanical behavior precludes in many cases its application. Small variations in composition and processing route have been observed to influence the thermal and mechanical stability of the austenite phase significantly. Indeed, a remarkable behavior differences have been observed from one sample to another within the same steel sheet. Besides the presence of a microstructural banding along the transversal section has been referenced by other researchers, but its origin has not been clarified yet. As it has been exposed in *Section 1.6*, the research published and concerned with this steel has been focused on three main aspects: 1) microstructural (precipitate) evolution during ageing at selected temperatures (mainly 475 °C); 2) The isothermal martensitic transformation that takes place at cryogenic temperatures and 3) the modelling and characterization of the mechanical behavior of the steel in the annealed industrial state.

The study of this complex alloy, in which different transformations may take place and overlap in time/temperature depending on the processing route: austenite formation; isothermal, stress assisted and strained induced martensite (TRIP) formation, delta ferrite formation, precipitation hardening (Cu-clusters+Ni_3Ti) at 300-550 °C; sensitization (χ-phase) up to 1050 °C; suppose a challenge for any materials scientist. However, it is believed that the outstanding properties of this material has exhibited in the past justify its further study and the need of gaining knowledge concerning alternative processing annealing routes, deeper understanding of solid-solid phase transformations and unveil what microstructural parameters affect the mechanical and thermal stability of dual phase ($\alpha'+\gamma$) or fully austenitic (γ) microstructures. Therefore, the matter of this thesis should be of interest both to industry and to materials scientists in the field.

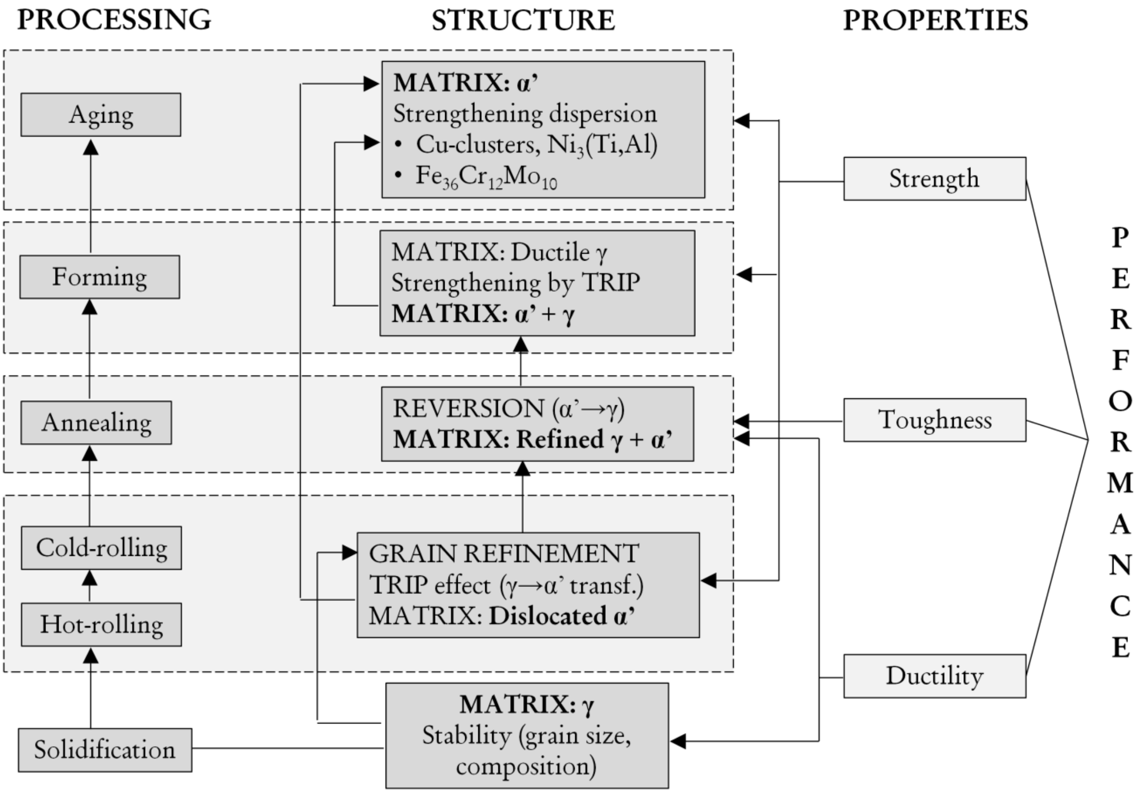

Figure 2.1. Flow chart of the materials science and engineering paradigm (relationship between processing, microstructure and properties) is established for the steel under investigation.

Figure 2.1 represents a flow chart of the thermo-mechanical processing undergone by this steel from the manufacturing down to the last forming and finishing steps generally applied to this steel at industrial scale. Processes that take place within the microstructure linked of these processing routes are also summarized based on the results of this thesis. Some mechanical properties evaluated in this research have been also highlighted.

In the following paragraphs, the objectives and work carried out and described in each chapter of this thesis are briefly outline.

- Chapter 3 gives a detailed description of the heat-treatments carried out in this thesis work. Besides, this chapter goes through the different experimental techniques used, describing the fundamental basis of the techniques, the working methodology and conditions as well as some problems and limitations found during the development of the investigation.
- Chapter 4 focuses on the microstructural characterization of the as-received (cold-rolled) microstructure; describing with detail what phases are present in the microstructure, and characterizing the chemical banding and how it influences the phase transformations that occur in subsequent annealing processing steps under investigation in this work. Based on two-dimensional electron probe microanalysis (EPMA) maps and the different contrast obtained after etching the steel with the Lichtenegger-Blöch color chemical reagent, a rapid methodology to characterize the chemical banding in this steel has been developed.
- The industrial annealing of the cold-rolled material (1050 °C for 10 min) results in austenitic microstructures (with grain sizes of 5 – 10 μm). In recent years nano- and ultrafine-grained austenitic structures with enhanced properties than their coarse-grained counterparts have been obtained in some stainless steels by controlling the annealing step of cold-strained microstructures. In Chapter 5, isochronal annealing treatments of the initial cold-rolled microstructure have been carried out at different heating rates. Very fine sub-micrometer size austenitic microstructures have been

obtained (0.35 – 0.41 μm). Moreover, the microstructural evolution during these routes is thoroughly characterized by transmission electron microscopy (TEM) and high-resolution TEM, with emphasis on the reaustenitization process (the martensite to austenite phase transformation), i.e. nucleation and growth of austenite and its dependence with the heating rate. It will be discussed the interplay between processes that occur simultaneously during heating, i.e. recovery, precipitation and reaustenitization, control the austenite grain size and the thermal stability of these microstructures.

- In Chapter 6 the mechanical behavior of the microstructures obtained in Chapter 5 using different isochronal annealing routes has been investigated. By combining tensile testing and magnetization measurements, it will be revealed and discussed how the mechanical behavior of this material is affected by the mechanical stability of the austenite, the balance of austenite/martensite volume fractions, the presence of strengthening second-phase nano-particles and the chemical banding. Due to its metastability, the austenite is susceptible of transforming into martensite under applied uniaxial tensions (so-called TRIP effect), which results in outstanding work-hardening rates and enhanced mechanical properties.
- Finally, in Chapter 7 the precipitation hardening behavior that the steel displays in its martensitic state during ageing will be thoroughly investigated in a wide range of temperatures between 300 and 550 °C for holding times up to 72 h. The hardening rate during aging has been characterized using hardness and thermoelectric power measurements; and nano-precipitates formed have been analyzed by TEM and HRTEM. A semi-empirical model has been used to estimate the activation energy of the process. The mechanical behavior of selected microstructures aged at 400, 450 and 500 °C has been also characterized and discussed based on the nanometric size, the formation of austenite after long aging treatments and the coarsening of the precipitates.

Chapter 3

Material and experimental procedure

In this chapter a detailed description of the different heat-treatments carried out in this thesis work is given. Besides, this chapter goes through the different experimental techniques used, explaining the fundamental basis of the techniques, the working methodology and conditions. Finally, the experimental limitations and problems found during the development of the investigation are commented as well as their influence on the results and conclusions.

3.1 Material

The material under investigation, Sandvik Nanoflex®, is a semi-austenitic metastable and precipitation hardening stainless steel developed by Sandvik AB, Sweden. Table 3.1 shows its chemical composition. Due to its importance for this work, several methods were used to determine the chemical composition of the steel. An accurate quantitative determination of the main alloying elements was done using different techniques: the Ni content was obtained by gravimetric analysis, the Cr content by volumetric analysis, and the Mo, Cu, Ti and Al contents were determined by atomic absorption spectrometry (VARIAN, SpectrAA 220 FS). The analytical results are the ones indicated in Table 3.1 and correspond to the mean value of two independent measurements of each alloying element. On the other hand, a semi-quantitative analysis of Si and Mn has been done by using a "Bruker" (S8 TIGER ECO) Wavelength dispersive X-ray fluorescence spectrometer (WDXRF).

Table 3.1. Chemical composition of the studied stainless steel (wt. %).

Cr	Ni	Mo	Cu	Ti
12 ± 0.09	8.87 ± 0.05	4.05 ± 0.02	1.91 ± 0.01	1.35 ± 0.02

Al	Si	Mn	C+N	Fe
0.39 ± 0.01	0.36 ± 0.04	0.33 ± 0.03	< 0.01	Balance

Nanoflex® is highly suitable for products requiring good corrosion resistance, high strength and good ductility in the final product, combined with high formability in the 'as delivered' condition. It is especially suitable for complicated designs that still have high requirements on the strength of the final product. It was initially conceived for a customer that needed surgical tools for eye and coronary surgery (Figure 3.1); materials needed for this application have to fulfil very strict regulations. The material had to be hard and sharp enough to cut through human tissue; tensile enough as to not break inside the tissue; and ductile to take on many different shapes At that moment, around

20 years ago, Sandvik did not have a material with this specifications and developed Nanoflex. In addition to surgical needles it can be used for dental drills and as it is bio-compatible. However, the bulk of business comes from the Philips shavers where it has extended the use of water-proof electrical razors (Figure 3.1). It is also used, but to a lesser extent in sports (golf clubs, climbing gears, bicycles, rackets). The exceptional strength and toughness of this steel can lead to a reduced weight in lightweight structures compared to titanium and aluminium alloys. However, the lack of significant investigation regarding the optimization of its thermomechanical processing hampers its applicability to a wider number of applications like in construction/building, automotive and aerospace industries.

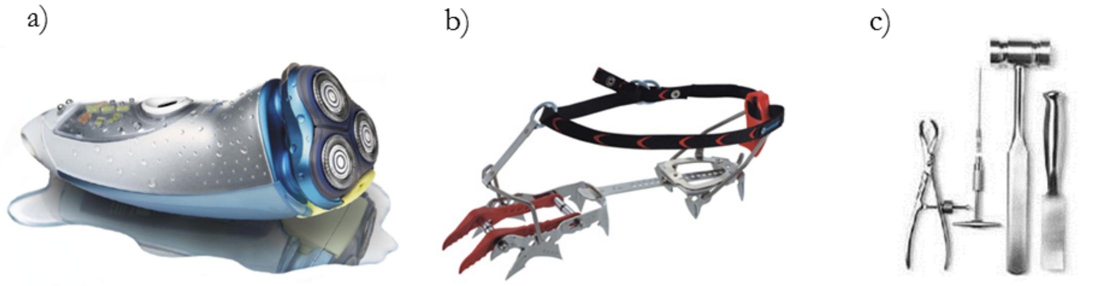

Figure 3.1. Examples of applications of Sandvik Nanoflex ®. (a) Electrical shaver heads; (b) Climbing crampons and (c) surgical needles.

The manufacturing process consists of a continuous casting followed by a hot-rolling and subsequent cold-rolling. Different finishing thicknesses are available. In this project the starting materials has been received in the form of sheets of 310 mm width and 0.45 mm thickness are obtained.

Due to its importance for this work, several methods were used to determine the chemical composition of the steel. An accurate quantitative determination of the main alloying elements was done using different techniques: the Ni content was obtained by gravimetric analysis, the Cr content by volumetric analysis, and the Mo, Cu, Ti and Al contents were determined by atomic absorption spectrometry (VARIAN, SpectrAA 220 FS). The analytical results are the ones indicated in Table 3.1 and correspond to the mean value of two independent measurements of each alloying element. On the other hand, a semi-quantitative analysis of Si and Mn has been done by using a "Bruker" (S8 TIGER ECO) Wavelength dispersive X-ray fluorescence spectrometer (WDXRF).

3.2 Microstructural characterization techniques

With the aim of studying which phases are present in the initial microstructure as well as potential microsegregation problems, the metallographic characterization was carried out on the cross section of the steel sheet (perpendicular to the rolling direction). Steel samples were cut with their axial length perpendicular to the rolling direction and were heat-treated. In addition, for XRD, EPMA and SEM inspection a polished to a colloidal silica finish was required.

3.2.1 Light optical microscopy (LOM)

For the inspection with the light optical microscope a Nikon Epiphot 200 optical microscope was used. First, samples were mounted in bakelite and then their surface was ground and polished using standard metallographic preparation procedures, finishing with 1μm diamond paste. To reveal the microstructure for its inspection the samples were etched using different chemical solutions, summarized in Table 3.2.

Table 3.2. Etching solutions employed to reveal the microstructure

Method	Name	Composition	Conditions
Electrolytic	Oxalic acid	10 g oxalic acid + 100 mL distilled water	Etching at room temperature and 15 V dc for 6 s
Electrolytic	Sodium hydroxide	10 g NaOH + 100 mL distilled water	Etching at room temperature and 15 V dc for 10 s
Standard chemical etching by immersion	Lichtenegger-Blöch (L-B)	20 g NH4F·HF (ammonium difluoride) + 0.5 g K2S2O5 (potassium metabisulfite) + 100 mL of distilled water	Etching at 60 °C for times between 10 s and 1 min 45 s

After metallographic preparation and etching, optical micrographs have been used for grain size measurements and the volume fraction of χ-phase quantification. The grain size was revealed with the hot L-B color etching solution at 60 °C. Several cycles of polishing and etching for times of about 1 min and 45 s were needed to disclose the grain boundaries. The grain size was determined by manually tracing grain boundaries using an image-editing software (Corel) to create a skeleton outline of the boundaries. Then, by using an image analyzer (Image Tool), the grain area and the corresponding equivalent diameter (assuming spherical grains) was calculated. This process was done over more than 300 grains in each case. Regarding the estimation of the volume fraction of χ-phase, it was determined by the manual point-counting method in more than five representative micrographs.

3.2.2 Scanning Electron Microscopy (SEM)

As for the inspection with LOM, SEM characterization was also undertaken on as-delivered and heat treated samples. The metallographic preparation and etching solutions employed to reveal the microstructure are the same as described for LOM. Two different field emission gun scanning electron microscopes (FEG-SEM) were used: a FEG-SEM Hitachi S4800 and a FEG-SEM Jeol J8M6500, both equipped with secondary electron (SE) and backscattered electron (BSE) detectors, as well as an Oxford INCA energy dispersive X-ray microanalysis system. For imaging, an accelerating voltage of 7 kV has been used. SEM micrographs were used to determine grain size and volume fraction of χ-phase using the same procedure described for LOM. In addition the amount of phases such as delta ferrite and retained austenite was also carried out using SEM images.

3.2.3 Electron Backscatter Diffraction (EBSD)

This technique, also known as backscatter Kikuchi diffraction (BKD), is an SEM based microstructural-crystallographic technique to measure the crystallographic orientation. In EBSD a beam of electrons is directed at a point of interest on a tilted crystalline sample approximately 70° relative to the normal incidence of the electron beam (to enhance the collection of backscattered electrons) and the diffracted electrons form a set of paired large angle cones corresponding to each diffracting plane. When used to form an image on the fluorescent screen the regions of enhanced electron intensity between the cones produce the characteristic Kikuchi bands of the electron backscatter diffraction pattern. This pattern is characteristic of the crystal structure and orientation of the sample region from which it was generated. It provides the absolute crystal orientation with sub-micron resolution. It is a very powerful tool for microstructural characterization since it can index and identify the seven crystal systems. Therefore, typical EBSD measurements include crystal orientation, misorientation, grain size, texture, recrystallized fraction, grain boundary characterization, strain analysis, phase identification, phase distribution, etc. In this work, EBSD was used for grain size determination of fully austenitic microstructures obtained after continuous heating at 0.1 and 10 °C/s up to 900 and 1000 °C, respectively. Gran sizes were determined from the image quality (IQ) or band contrast (BC) maps in the same manner as explained for optical micrographs.

The EBSD patterns were acquired using a FEG-SEM Jeol JSM-6500F microscope located at CENIM-CSIC. The metallographic preparation of the samples was performed in the same way as for LOM/SEM observations, but finishing with OPS colloidal silica to obtained a much finer polishing. All measurements were done with the Channel 5 system (Oxford Instrument), operated at an accelerating voltage of 20 kV. The step size used varied between 0.01 and 0.03 μm.

3.2.4 Transmission Electron Microscopy (TEM)

Three transmission electron microscopes were used to inspect the as-received and heat-treated material. Two of them belong to Centro Nacional de Microscopía Electrónica (CNME), located at Complutense University of Madrid: a TEM-JEM 2100HT, which operates at 120 kV, and a JEOL JEM 3000F, which operates at 300 kV. The latter one is a high-resolution TEM (HRTEM) and it is equipped with a scanning unit (STEM), high and low angle dark field detectors (HAADF and LAADF) and a XEDS detector for compositional analysis. The third microscope is a Tecnai-G2-F20 FEI-TEM that operates at 200 kV and allows high performance in S/TEM imaging and nanoanalysis. It is located at the Department of Materials Science and Engineering of the National Taiwan University in Taipei.

In TEM only thin samples can be studied, since they allow a fraction of the incident electron beam to go through them. Therefore, thin foils were prepared from 3 mm diameter discs, previously heat-treated in the furnace of the DT1000 dilatometer. The discs were thinned by mechanical grinding, to a thickness of ~ 30 μm, and subsequently electropolished by using a twin-jet Struers Tenupol-5, in a solution of 10 % perchloric acid and 90 % acetic acid at 17 °C and an operating voltage of 38 V by using a twin-jet Struers Tenupol-5.

3.2.5 X-Ray Diffraction (XRD)

Phase identification of the as-received cold-rolled state was performed by using a Siemens D5000 X-ray diffractometer, which operates with Co K_α radiation ($\lambda \approx 1.7903$ Å). Scans were taken from 30 to 110° 2θ and using a steps size of 0.030. The peaks indexation for phase identification was done by using the software Match! (Crystal Impact). Metallographic preparation was done as explained for

Diffraction patterns were recorded on the cross section, along the rolling direction. Due to the low thickness of the steel sheets (0.45 mm), up to ten samples of 12 mm in length and 4 mm in width were mounted together in transparent EPOXI resin in order to have a large enough material surface to inspect the cross section. The metallographic preparation was carried out in the same way as for EBSD measurements.

3.2.6 Electron Probe Microanalysis (EPMA)

As it will be shown later, the as-received microstructure, presents a profound chemical banding along the transversal section. The microsegregation of alloying elements (Cr, Ni, Mo, Cu and Ti) was investigated by means of EPMA. The measurements were performed using a JEOL JXA 8900 M microprobe with a wavelength dispersive spectrometer (WDS) at the ICTS National Centre for Electron Microscopy (CNME), located at the Universidad Complutense de Madrid (UCM). The metallographic preparation of the samples is the same as for EBSD or XRD. Two-dimensional (2D) EPMA maps were recorded using a step size of 1 μm over an area of approximately 450 x 200 μm^2. In order to find out the evolution of the chemical banding detected in the initial microstructure with the heat-treatment, EPMA measurements were also done on homogenized samples.

3.2.7 Thermoelectric Power (TEP)

Due to its sensitivity in detecting variations in the concentration of atoms in solid solution, the thermoelectric power (TEP) is a powerful method to study microstructural changes in steels such as recovery, recrystallization or dissolution/precipitation processes. For this reason, in combination with other experimental techniques, TEP turned out to be a very valuable tool in this work to study the aging behavior of this steel, as well as to gain insight about the processes that take place during continuous heating and accompany the reaustenitization.

It is based on the Seebeck coefficient (S) and on the appearance of a voltage gradient, ΔV, when a temperature difference, ΔT, is applied along a sample. The TEP is then defined by:

$$S = \lim_{\Delta T \to 0} \left(\frac{\Delta V}{\Delta T} \right) \qquad [3.1]$$

Physically, the phenomenon arises because charge carriers at higher temperature region of the sample diffuse into available states of lower energy in the lower temperature region of the sample. The accumulation of charge carriers at the cold side sets up an electric potential difference of electric field along the material. This electric field builds up until

To conduct TEP measurements, the sample is pressed between two blocks of a reference metal (pure copper, 99.99 wt.%, in this work). One of the blocks is held at 15 °C, while the other is at 25 °C, and given the temperature gradient, ΔT, of 10 °C (with a tolerance of ± 0.1 °C), the response in voltage, ΔV, is recorded. The Seebeck coefficient or thermoelectric power (S) measured by this equipment is not the absolute TEP value of the sample (S^*), but a relative one (S) in comparison to the TEP of pure copper reference blocks (S^*_{Cu}) at 20 °C ($S^*_{Cu} = 1.91\ \mu V K^{-1}$) [96; 97], and is given by:

$$S = S^* - S^*_{Cu} = \frac{\Delta V}{\Delta T} \qquad [3.2]$$

The TEP value does not depend on the shape of the sample, which is a great advantage of this technique. Moreover, the measurement is performed very quickly (less than 1 min) and precisely (about ± 0.5 %). The resolution is of the order of 0.001 μV/°C.

Thermoelectric power (TEP) measurements were performed on samples of 30 mm length and 5 mm width, using a TechLab-GEM-PPM INSA Lyon model. Heat-treatments for such machined samples were done in the LK02 dilatometer.

3.3 Magnetization measurements

A quantum design MPMS-XL SQUID magnetometer was employed for the magnetization measurements. This technique allows acquiring very accurate volume fraction measurements of ferromagnetic phases in steels (error of ± 0.01 pct). The SQUID can detect minute variations (of order of 1 x 10^{-14} T) of a sample response to an applied magnetic field. Measurements have been carried out at room temperature on 3 mm length square-shaped samples previously subjected to interrupted heating by quenching experiments in the DT1000 dilatometer. Magnetization curves were recorded by varying the external applied magnetic field from 0 to 5 T in steps of 0.2 T. The system takes two measurements at each incremental field step, and the average data point is noted. As austenite is a paramagnetic phase (small and positive susceptibility) and martensite is ferromagnetic (large and positive susceptibility); if both phases are present in the microstructure of this steel, the total magnetization, as a result of an applied magnetic field, can be regarded as proportional to the volume fraction of martensite (the contribution of the paramagnetic austenite can be discarded as long as the applied magnetic field is not very large [21]). To determine the volume fraction of martensite from these measurements, a reference value of a sample containing 100 % martensite ($M_{sat}^{\alpha'}$) is needed. The $M_{sat}^{\alpha'}$ value is set as a standard to normalize the saturation magnetization of all heat-treated samples (M_{sat}). Since M_{sat} value is directly obtained from the magnetization curve and $M_{sat}^{\alpha'}$ is known, the **volume fraction of martensite** can be calculated through:

$$f_{\alpha'} = {}^{M_{sat}}\!\big/_{M_{sat}^{\alpha'}} \qquad [3.3]$$

and, therefore, the volume fraction of austenite is obtained from:

$$f_{\gamma} = 1 - \left({}^{M_{sat}}\!\big/_{M_{sat}^{\alpha'}} \right) \qquad [3.4]$$

3.4 Mechanical testing

3.4.1 Micro-hardness Vickers

The micro-hardness Vickers was measured in the as-received state and in the heat-treated samples with two main purposes: 1) to characterize the evolution of the microstructure (precipitation, austenite formation and grain growth) under continuous heating (in combination with other techniques) and 2) to characterize the precipitation kinetics of the material during isothermal aging. For this purpose a WILSON

WOLPER 401 MVA equipment with a load of 1 Kg was used. For each sample, an average value was obtained after undertaking five indentations in the cross-section using an indentation time of 15 s.

3.4.2 Tensile testing on sub-size specimens

In addition to micro-hardness Vickers measurements, the influence of processes such as precipitation, austenite formation and austenite grain growth on the strength and ductility of the steel was characterized by tensile testing experiments.

Sub-size specimens were machined by wire erosion along the steel sheets transverse section (perpendicular to the rolling direction) with a gage length of 7 mm and a width of 2 mm Figure 3.2 (a). In this case, heat-treatments were carried out in the furnace the LK02 dilatometer. Two specimens were tested per condition in a 10 kN universal tensile testing, at room temperature and applying a strain rate ($\dot{\varepsilon}$) of 5 x 10^{-4} s^{-1} until fracture occurred. All mechanical characterization results presented in this work has been performed on this type of samples using the heat treatment conditions presented in *Section 3.5.3*.

For TEM inspection larger samples where designed with a wider gauge width so as to extract discs of 3 mm in diameter. Therefore, sub-size specimens of 11 mm gage length and 4 mm width were used for this aim Figure 3.2 (b).

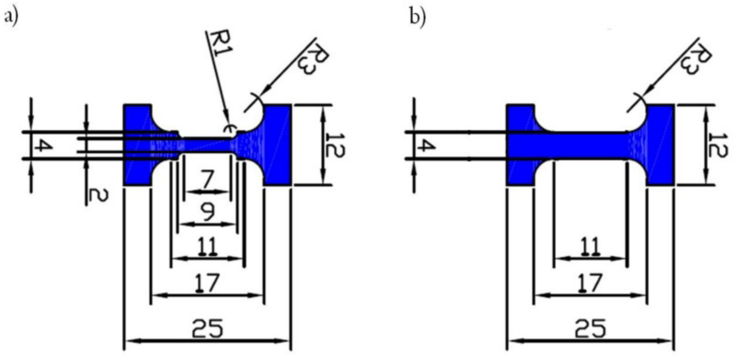

Figure 3.2. (a) Schematic drawings of sub-size specimens used for tensile testing, where the gage length is 7 mm and the width is 2 mm. (b) Schematic drawing of sub-size specimen used for tensile testing in case TEM inspection is needed, where the gage length is 11 mm and the width is 4 mm.

With the aim of studying the TRIP effect (formation of α'-martensite from austenite during straining), interrupted tensile tests at different strain levels were performed on materials presenting ultrafine-grained and a coarse-grained austenitic microstructures. For this purpose, and using the furnace of the LK02 dilatometer, sub-size tensile test samples Figure 3.2 (a) were isochronally heated at 0.1 and 10 °C/s up to different target temperatures where the desired microstructure was obtained. Interrupted tensile tests were subsequently performed at room temperature on these heat treated samples using a strain rate of 5 x 10^{-4} s^{-1} to different strain levels (including fracture) as summarized in Table 3.3. Finally, magnetization measurements were undertaken on these interrupted samples to estimate the amount of transformed martensite in the steel microstructure.

Table 3.3. Summary of the interrupted tensile test performed on samples previous isochronal heat-treatment at 0.1 and 10 °C/S up to 825 and 1000 °C and 950 and 1075 °C

HR (°C/s)	0.1		10	
*T*γ (°C)	825	1000	950	1075
Interrupted at strain (%)	–	2	–	1
	5	5	4	7
	10	12	12	–
	15	15	19	20
	27	30	29	34
	fracture			

3.5 Heat treatments

All heat treatments of this thesis work were carried out in two different high resolution dilatometers: an Adamel Lomargy DT1000 and an Adamel Lomargy LK02. Both dilatometers present similar characteristics, but the DT1000 is computerized and the LK02 is not. The dilatometers are equipped with high precision radiation furnace. The power radiated by two tungsten filament lamps is focused on the specimen of small dimensions (12 mm in length – 4 mm in width in the DT1000 and LK02; in addition, the LK02 has been adapted to heat treat also samples of 30 mm in length – 5 mm in width for thermoelectric power measurements (TEP)) by means of a bi-elliptical reflector. The temperature is measured with a 0.1 mm diameter Chromel-Alumel (type K) thermocouple welded to the specimen. The low mass of the specimen allows an excellent efficiency of heat transmission and a very low thermal inertia, which ensures actual heating rates from 0.01 °C/s to 100 °C/s. Cooling is done by blowing helium gas directly onto the specimen surface and cooling rates from 0.01 °C/s up to 300 °C/s can be reached. To minimize oxidation problems during heat-treatments at high temperatures, samples are treated under vacuum conditions (10^{-1} – 10^{-2} mbar) or in an inert atmosphere.

3.5.1 Continuous heating experiments

The evolution of the as-received cold-rolled microstructure during continuous heating was studied by a number of experimental techniques, some of them requiring specimens with different morphologies and dimensions. Therefore, depending on the specimen size, either the furnaces of the DT1000 or the LK02 dilatometer were used.

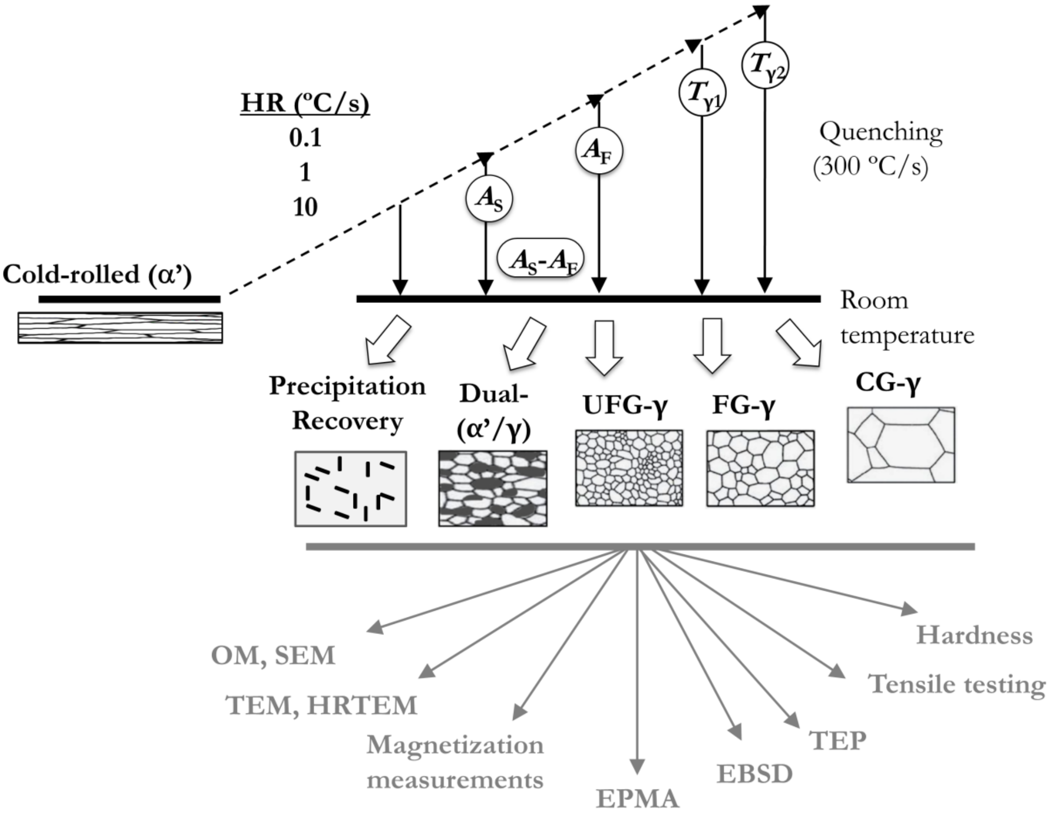

Figure 3.3. Schematic chart displaying the critical temperatures up to which isochronal heat-treatments have been performed at heating rates (HR) of 0.1, 1 and 10 °C/s. This figure points out the number of complimentary techniques needed to study the different processes taking place and the microstructural evolution.

As it will be shown in *Chapter 5*, to study the processes that take place in the microstructure under isochronal heating conditions, such as recovery, α'→γ phase transformation, precipitation or dissolution of particles and austenite grain growth, a great number of different heat-treatments were carried out in this research. Figure 3.3 in combination with Table 3.4 shows a schematic chart in which all these heat treatments have been summarized. A_S and A_F stand for the starting and finishing martensite to austenite transformation temperatures, $T_{\gamma 1}$ and $T_{\gamma 2}$ refer to annealing temperatures higher than A_F. All samples were helium gas quenched to room temperature immediately after reaching the target temperature. Heat-treatments below A_S result in recovered and precipitated martensitic microstructures. Between A_S and A_F the α'→γ transformation takes place, so that dual microstructures with different volume fractions of α' and γ have been obtained. At the exact temperature of A_F ultrafine-grained austenitic microstructures (UFG-γ) with some χ-phase precipitates are expected, whereas if the target temperature is increased aboveA_F, the austenite grains will growth and fine (FG-γ) and coarse-grained (CG-γ) microstructures will be obtained at $T_{\gamma1}$ and $T_{\gamma2}$, respectively. Table 3.4 displays critical transformation temperatures obtained after heating at 0.1, 1, 10 °C/s for the studied heating rates, to which we will refer throughout this thesis work.

Table 3.4. Isochronal heat treatments to study the evolution of the UFG austenitic microstructures with the temperature.

Heating Rate (°C/s)	Ctitical temperatures (°C)			
	A_S	A_F	$T_{\gamma1}$	$T_{\gamma2}$
0.1	600	825	900	1000
1	650	900	—	—
10	680	950	1000	1075

3.5.2 Precipitation hardening effect

To study the aging behavior of the steel under investigation (*Chapter 7*) the following heat-treatments were performed.

Table 3.5. Aging treatments for the study of the precipitation hardening of the as-received cold-rolled steel under investigation. All possible combination aging temperature-aging time were conducted.

Heating rate	Aging temperature
(°C/s)	T_a (°C)
30	300
	400
	425
	450
	475
	500
	550

Aging time, t_a			Cooling rate	Final T
(s)	(min)	(h)	(°C/s)	(C)
1			30	25
15				
30				
60	1			
120	2			
300	5			
900	15			
3600	60	1		
10800	180	3		
32400	540	9		
86400	1440	24		
259200	4320	72		

3.5.3 Mechanical behavior

Table 3.6. Isochronal heat-treatments performed on tensile test samples of the as-received material to evaluate the evolution of mechanical properties with the microstructure as the heat-treatment changes.

HR (°C/s)	0.1	1	10	Structure
T_γ (°C)	645	680	715	Dual (α'/γ)
	670	700	725	
	680	718	740	
	690	730	750	
	725	790	765	
	770	820	835	
	800	850	900	
	825	900	950	UFG-γ
	900	–	1000	FG-γ
	950	–	1025	
	1000	–	1050	CG-γ
	1050	–	1075	
t_γ (s)	–	–	–	
CR (°C/s)		300		
T_F (°C)		25		

To investigate the mechanical behavior (*Chapter 6*) of the different microstructures obtained isochronally different heat-treatments were performed on sub-size tensile test specimens in the precision furnace of the LK02 dilatometer. To generate dual (α'/γ) microstructures temperatures were selected in the range A_S-A_F for each heating rate, whereas to induce fully austenitic microstructures the A_F, $T_{\gamma 1}$ and $T_{\gamma 2}$ were reached. Table 3.6 gathers together all temperatures to obtain a certain structure depending on the heating rate.

3.5.4 Homogenization heat treatments

As it will be shown in *Chapter 4*, a profound chemical banding has been observed in the as-received microstructure along the transversal section. For this reason, high temperature homogenization heat treatments were performed to find out their effectiveness on reducing or eliminating this chemical banding. The main concern when designing the heat treatments was to avoid the formation of δ-ferrite phase. For this reason, a temperature of 1100 °C and times between 4 and 96 h were studied, as summarized in **Error! Not a valid bookmark self-reference.**. Treatments up to 24 h were carried out using the precision furnace of the Adamel Lhomargy DT1000 dilatometer in a vacuum atmosphere of 10^{1} mbar using samples of similar dimensions as described before (12 mm in length and 4 mm in width), while heat treatments longer than 24 h were done using a Carbolite tube furnace (using square samples of 10 x 10 mm^2), able to reach temperatures as high as 1200 °C. The samples were cooled down to room temperature (RT) by water quenching (WQ).

Table 3.7. Homogenization heat-treatments. RT, HGQ and WQ stand for room temperature, helium gas quenching and water quenching respectively

HR (°C/s)	*T* (°C)	*t* (h)	*CR*	T_f
5	1100	4	HGQ	RT
		12		
		18		
		24		
—		48	WQ	
		72		
		96		

3.6 Experimental limitations

It is important to mention that, as it will be shown in the following chapters, the experimental procedures have been limited in many cases by inherent features that the material under investigation exhibits. The chemical banding along the steel sheet cross-section, the stability of the sheet or the small sheet thickness have precluded the use of some experimental techniques. For instance, the presence of a pronounced chemical banding in the steel-sheet cross-section gives rise to an inhomogeneous behavior among the different bands. Therefore, in order to obtain representative results of the whole material, the need to perform the characterization on the cross-section rather than on the normal-section of the sheets is mandatory. Measurements on the longitudinal section by techniques that give surface information, such as X-ray diffraction, may lead to unreliable results if the surface normal to the rolling direction is analyzed, since these would depend on the band on which the measurements have been done. On the other hand, the low thickness of the sheets (about 0.45 mm.) make also difficult to perform X-ray diffraction on the cross-sectional area since a minimum surface of 1 cm^2 is required. Although this issue may be sorted out by mounting together some sheet pieces, it has to be born in mind the problem of the texture resulting from the cold-rolling. A strong texture, as the one this steel presents, will mask the signal from other minor phases and, hence, further investigation with complementary techniques will be required. As a consequence, the characterization by bulk-volume measurements techniques, such as magnetization measurements, micro-hardness Vickers or thermoelectric power, have been preferred to surface area measurements. These kinds of bulk-volume measurements are much more reliable and representative of the whole material but sometimes require be supporting and interpreting along with other experimental techniques.

In a similar way, the microstructural inspection by TEM should have been performed on the cross-section of the sheets, but the low thickness makes impossible the preparation of thin foils from this section. TEM specimens where then prepared parallel to the sheet normal section, which in consequence leads to the inspection of a microstructure that may not be representative of the sample, but dependent on the chemical banding. On the other hand, the stability of the steel-sheets also hinders the preparation of TEM thin foils. Particularly, the preparation of samples with a high volume fraction of austenite is tedious. Due to its metastability, the austenite phase may transform into martensite during grinding and electropolishing. Moreover, the martensitic transformation is enhanced as the thickness of the samples is reduced.

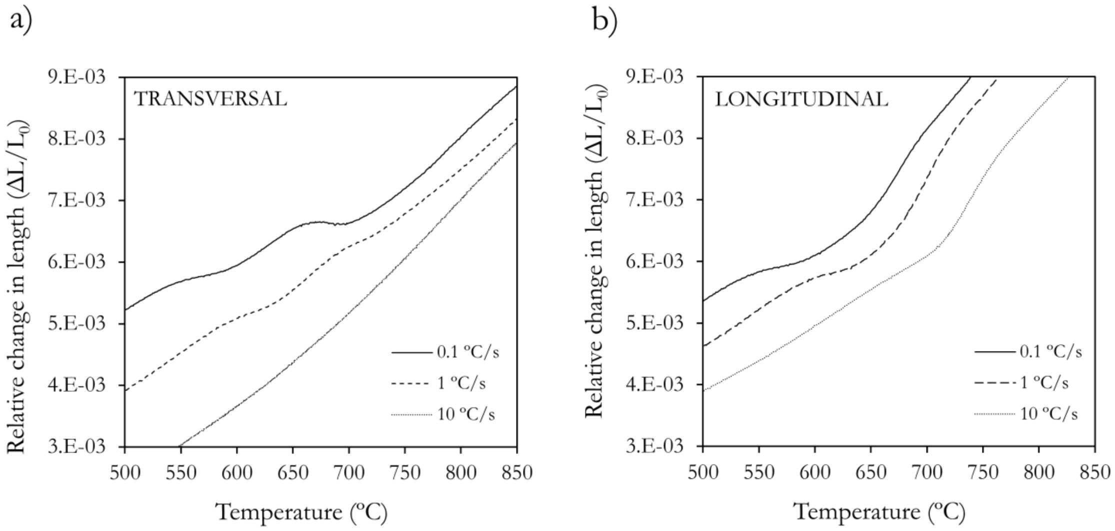

Figure 3.4. Dilatometric curves obtained during continuous heating at heating rates of 0.1, 1 and 10 °C/s of samples machined: (a) perpendicular to the rolling direction (from the transversal section) and (b) longitudinal to the rolling direction.

It has turned out that experimental techniques generally used to characterize and investigate steels similar to the one studied in this work do not give reliable information or even the results cannot be successfully interpreted. This is the case of the high-resolution dilatometry to study phase transformations upon continuous heating. It was found that the dilatometry was not able to detect precisely the contraction associated to the α'→γ transformation at none of the heating rates. Figure 3.4 shows the dilatometric curves obtained during continuous heating of samples machined with their axial length perpendicular (a) and parallel (b) to the rolling direction. As Figure 3.4 (a) displays, only the curves obtained at 0.1 and 1 °C/s exhibit the contractions related to the expected phase transformations: the first one is due to the precipitation and partial recovery and the second contraction is related to the α'→γ transformation, as seen in similar steels [43]. By heating at 10 °C/s the curve does not give any information. To discard a problem of texture the same experiments were performed on samples machined along the longitudinal section. As Figure 3.4 (b) shows, these curves present a dilatation instead of a contraction, an anomalous behavior we could not be able to explain.

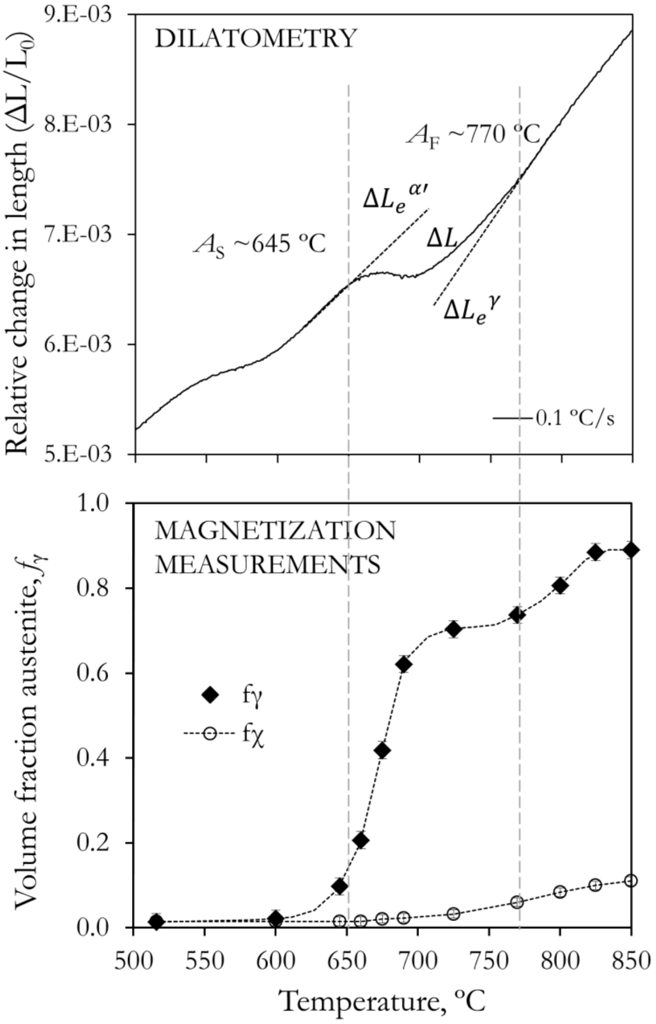

Figure 3.5. Comparison between dilatometry and magnetization measurements to study the evolution of the austenite phase during α'→γ transformation upon continuous heating at 0.1 °C/s.

On the other hand, an attempt was done to estimate the evolution of the austenite volume fraction from the dilatometric curve obtained at 0.1 °C/s in a transversal specimen by using the lever-rule method. Austenite (FCC crystal structure) and low-carbon martensite or ferrite (BCC crystal structure) have very different atomic volumes [19]. When steel transforms from one phase to the other the atomic volume of the sample changes and, thus, gives rise to a shape change which can be detected using high resolution dilatometry. In the absence of a transformation one should expect a linear behavior which a slope given by the coefficient of thermal expansion of the phase or phases present in the microstructure. As shown in Figure 3.5 dotted lines are the extrapolated austenitic length change ΔL_e^{γ} and martensitic length change $\Delta L_e^{\alpha'}$. The f_γ will be given by the ratio of the contraction $(\Delta L_e^{\alpha'} - \Delta L)$ to the maximum possible contraction at each temperature $(\Delta L_e^{\alpha'} - \Delta L_e^{\gamma})$. The location of A_S and A_F temperatures were estimated by dilatometry around 645 and 770 °C, respectively. However, when these results are compared with those of the magnetization temperature, one realizes that the dilatometry does not detect neither the first 10 % nor the last 20 % of the α'→γ transformation. As magnetization measurements predicts the transformation upon heating at 0.1 °C/s starts around 600 °C and finishes at 825 °C.

Dilatometry is able to detect phase changes among phases that possess different atomic volumes or changes in the atomic volume of a single phase due to precipitation reactions of deformation/recovery/recrystallization of those phases since the atomic volume depends on the lattice parameters of the crystal structure. Therefore, a process or transformation resulting in a dilatation that counteracts the contraction due to the α'→γ transformation must be taking place. On the other hand, Christien *et al.* [67] have observed similar results after studying the continuous heating (0.28 °C/s) behavior of 17-4 PH SS. While high-resolution dilatometry measurements located A_F around 810 °C, neutron diffraction experiments clearly showed that the transformation finished at 970 °C. To explain their observations, the evolution of the austenite and martensite dislocation densities during heating were determined by using the experimental lattice parameters obtained with neutron diffraction. They concluded that at high temperatures, the dislocation the specific volumes of these two phases are so similar that it becomes very difficult to differentiate them to the eyes of dilatometry. Something similar must be occurring in the steel under investigation for high temperatures. However, it does not explain why the dilatometry does not detect either the first 10 % of transformation. In an alternative way, in situ high energy X-ray diffraction experiments at a synchrotron source were planned to determine the evolution of the volume fraction and, specially, the lattice parameters of austenite and martensite with the aim of comparing them with the results obtained in this work.

Chapter 4

Microstructural characterization of the cold-rolled state

C. Celada, I. Toda-Caraballo, B. Kim, D. San Martín. *Chemical banding revealed by chemical etching in a cold-rolled metastable stainless steel.* Mater. Char., 82 (2013) 142-152.

This chapter describes the metallographic characterization of the initial microstructure (cold-rolled) of the stainless steel investigated in this work. It is shown that the use of the Lichtenegger - Blöch (L-B) color etching solution not only reveals the phases present in the microstructure, but also the existence of a pronounced chemical banding along the rolling direction. The L-B reagent has been found to color the microstructure in bands depending on what alloying elements have segregated to each band. Two-dimensional electron probe microanalysis (EPMA) maps have shown that Ni, Cu and Ti segregate together in the bands, while Cr has an opposite behavior. Mo has a mixed segregation behavior although weaker than the other elements and more prompt to segregate like Ni does. A comparison of the light optical micrographs with the EPMA maps has enable to establish a direct relationship between the alloying element band concentration and the resulting etching color contrast obtained with the L-B reagent.

4.1 Introduction

Microstructural banding occurs quite commonly in high-strength high-alloyed steels [98; 99]. Its presence is attributed to the segregation of alloying elements during solidification. In this process, alloying elements are rejected from δ-ferrite dendrites, leading to a high solute content in the interdendritic regions. In subsequent processing operations, such as extrusion or rolling, areas in the microstructure exhibiting segregation align along the material flow direction in the form of bands, resulting in the so-called chemical banding. Band width and pattern vary with the degree of inhomogeneity and the mechanical processing history [100]. This inhomogeneous solute distribution might give raise to a microstructural banding during solid-solid phase transformations [101].

The segregation of alloying elements can produce different etching responses, which can lead to the disclosure of regions of different composition. To the author's knowledge, one of the first to reveal the presence of microsegregation was Stead, as stated in [102]. His Cu based etchants (Stead's reagents), are extremely effective at revealing the relative phosphorous concentration in steels or phosphorous segregation to eutectoid cells in grey cast iron [103]. In the same sense, a large number of etchants that reveal chemical banding/segregation have been reported afterwards [101-104]. It is worthwhile to point out the difference between etchants that indirectly reveal chemical banding, as the bands consist of different phases resulting from a previous microsegregation [101; 102]; and etchants which vary the coloration according to the alloying element content in monophasic microstructures [103; 104], as has been investigated in this study.

It has been shown that the microsegregation of alloying elements can be removed or slightly reduced by annealing for several hours at high austenitization temperature [98]. The temperatures and times needed to chemically homogenize the microstructure depend on the element that appears segregated, the high temperature matrix phase (austenite, martensite, and ferrite) and steel composition. Using chemical etching procedures, chemically banded structures and their evolution with homogenization treatments have been studied by means of electron probe microanalysis (EPMA) by other authors [101]. In general, this technique has been proven very useful to investigate the composition of different phases in steels and thus help in the study phase transformations or assess the quality of steel products [105; 106].

4.2 Results

4.2.1 X-Ray Diffraction

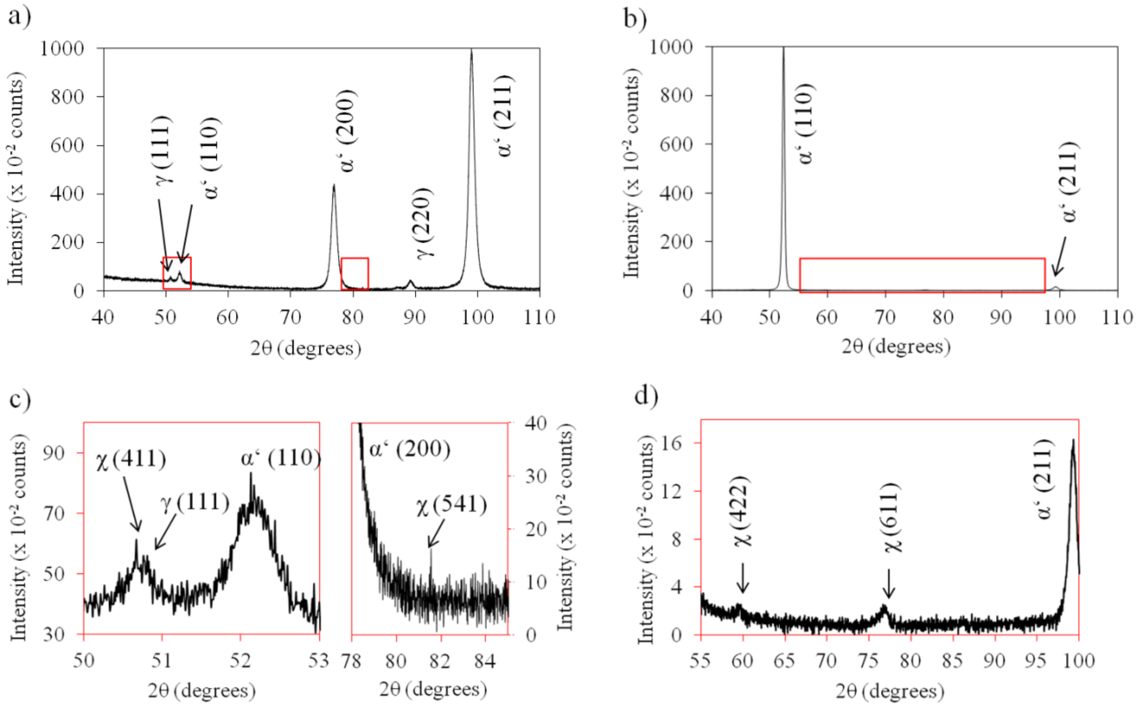

Figure 4.1. X-Ray diffraction patterns recorded along the longitudinal-rolling section (a), and cross section (b) of the steel sheets; (c) and (d) zoom in angle ranges framed in red of (a) and (b) respectively. The indices α', γ, and χ stand for martensite, austenite and chi-phase, respectively.

Figure 4.1 (a) and (b) show XRD patterns undertaken on surfaces normal and perpendicular to the rolling direction of the as-received steel sheets, respectively. Figure 4.1 (c) and (d) zoom in a specific angle range of Figure 4.1 (a) and (c) (framed in red), where the positions of specific χ-phase diffraction peaks have been pointed out by arrows. These diffractograms show that martensite is the main phase present in the cold-rolled, as-received microstructure. As expected, the martensite phase shows a very strong preferential texture induced by the severe cold-rolling: (110) along the cross section and (211) along the longitudinal section. There is also a small amount of χ-phase precipitates and retained austenite. The χ-phase is a hard and brittle intermetallic phase whose basic composition is $Fe_{36}Cr_{12}Mo_{10}$, although it usually contains other elements like Ti or Ni [49; 107; 108]. Peaks associated with austenite have only been detected perpendicular to the normal direction (Figure 4.1 (c) and (d)). This could be explained because the analyzed section may contain locally a larger amount of austenite phase compared to the bulk of the material (Figure 4.1 (b) and (d)). Since the peaks corresponding to the austenite have not been detected in Figure 4.1 (a), and because the detection limit of XRD measurements is around a volume fraction of ~0.02-0.03, it could be concluded that the volume fraction of austenite in this cold-rolled material is below this amount (0.02-0.03). In addition, the presence of a strong texture in the material could also make more difficult the detection of austenite peaks in the cross section.

4.2.2 Light optical and Scanning Electron Microscopy

Figure 4.2 shows optical and secondary electron SEM micrographs of the as-received microstructure. Figure 4.2 (a) displays the microstructure after electrolytic etching for 10 seconds with a 10 % oxalic acid solution at 17 °C and 15 V dc. This etching method reveals second phases and leaves the martensitic matrix basically unetched. The big, cubic shaped particles are titanium nitride (TiN) precipitates. Titanium has a high affinity for nitrogen, as well as for carbon, and thus it binds the residual nitrogen and/or carbon present in the steel leading to the formation of both, nitrides TiN and carbo-nitrides Ti(CN) [3]. On the other hand, the smaller and brighter particles are χ-phase. As observed in Figure 4.2 (a), a number of holes are present in the microstructure because some χ-phase precipitates were partially consumed/extracted from the matrix as a result of the chemical etching. The formation of χ-phase precipitates results in an impoverishment of the matrix in Cr content around them, which gives rise to an extremely localized corrosion in the course of the electrolytic etching.

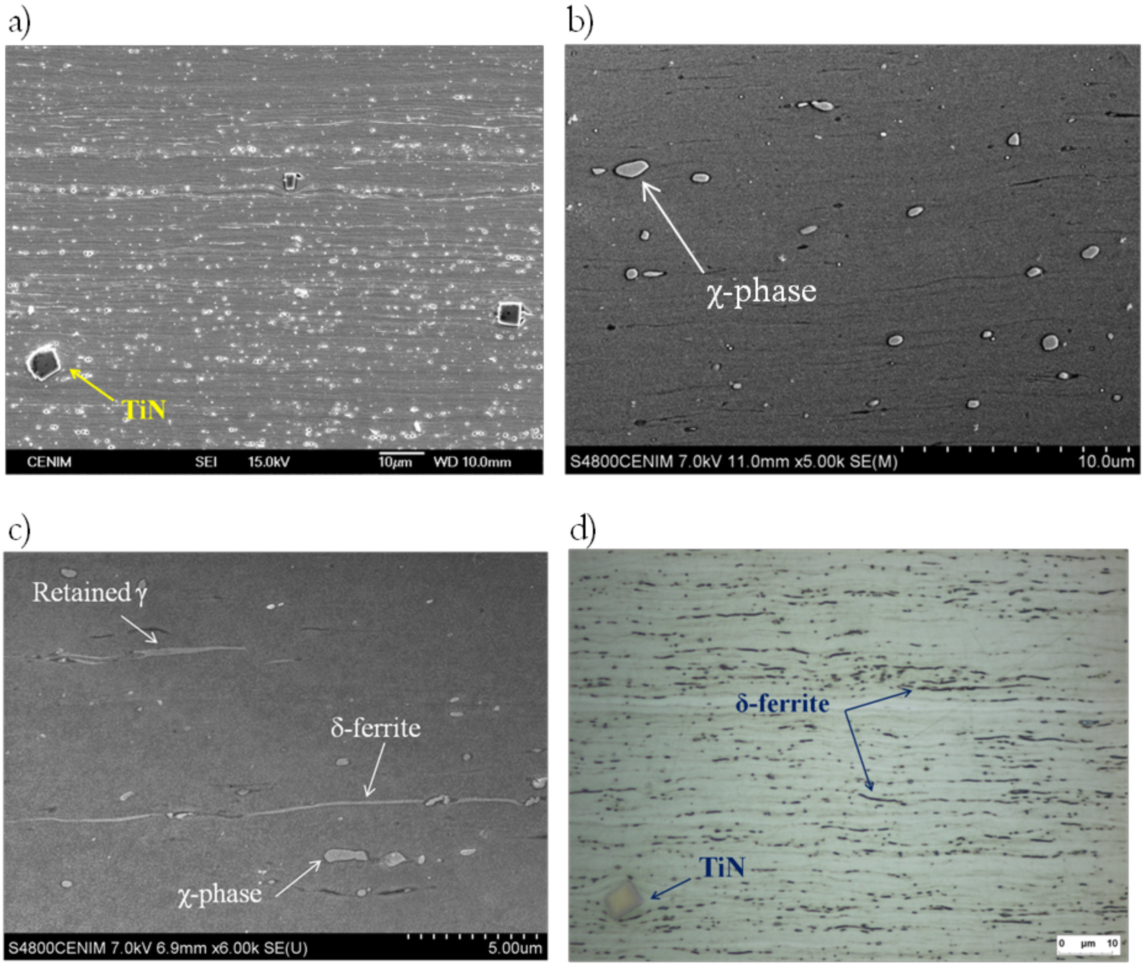

Figure 4.2. Secondary electron SEM micrographs of the as-received material after revealing the microstructure with different etchants: (a) electrolytic etching at 15 V for 6 s with an oxalic acid solution (10 %); (b)-(c) etching with hot Lichtenegger-Blöch at 60 °C for 10 s; and (d) electrolytic etching at 15 V for 10 s with a NaOH (10 %) aqueous solution.

The microstructure displayed in Figure 4.2 (b) was etched with L-B etching solution (Table 3.2). Although most chemicals, when dissolved in water, generate heat and produce an exothermic reaction, ammonium bifluoride absorbs heat, so the reaction is endothermic. If the distilled water is at room temperature, the solution gets colder, and the ammonium bifluoride will not dissolve. Consequently, one must heat the water before dissolving the ammonium bifluoride. This etchant is generally used at approximately 25 to 30 °C, rather than at room temperature [109; 110]. However, it has been found that when this etching solution is used hot, around 60 - 80 °C, more features of the microstructure are revealed in this kind of stainless steels [49]. On the other hand, when using ammonium bifluoride ($NH_4F{\cdot}HF$), one should take in account that in contact with water it will decompose to ammonium fluoride (NH_4F) and hydrofluoric acid (HF). The HF content of the resulting solution makes it very corrosive, toxic and hazardous. Therefore, this solution must be handled with care.

After etching with L-B for 10 seconds at 60 °C, χ-phase precipitates are made visible and appear as elongated or rounded white particles (Figure 4.2 (b)-(c)). In addition, retained austenite and δ-ferrite stringers, as identified by energy dispersive X-ray microanalysis (SEM-EDS), were also visualized (Figure 4.2 (c)).

The volume fraction of these phases was estimated by using the systematic manual point count method [111], in more than 10 SEM representative micrographs. The results showed a volume fraction of around 0.01 both for the δ-ferrite phase and retained austenite, and around 0.02 for the χ-phase. It should be borne in mind that these numbers might be slightly underestimating the real volume fraction as smaller particles below 50-100 nm are not being considered in the estimation of the χ-phase. The identification of the phases was done by SEM - EDS. The recognition of the χ-phase is rather straightforward since the Mo content of these precipitates is higher than 8 wt. %, which is much larger than that of the matrix (~4 wt. %). Ni is an austenite stabilizer; therefore, it tends to diffuse away from δ-ferrite and enrich austenite. For this reason, the detection of the retained austenite and δ-ferrite phases can be based on the Cr and Ni content. The following results (in wt. %) were obtained for retained austenite: 11.2 (0.7)-Ni and 11.4 (0.4)-Cr; for δ-ferrite: 6.1 (0.8)-Ni and 13.1 (0.5)-Cr; and for the martensitic matrix: 8.8 (0.6)-Ni and 11.9 (0.6)-Cr.

Figure 4.2 (d) displays an optical micrograph where the microstructure was electrolytically etched with NaOH (10 %) at 15 V dc for 10 seconds. After etching, δ-ferrite stringers are clearly revealed, appearing as the black-etching phase. Small black spots are also distinguishable, and are attributed to the χ-phase. In addition, the TiN particle is etched in light yellow whereas the matrix remains unetched.

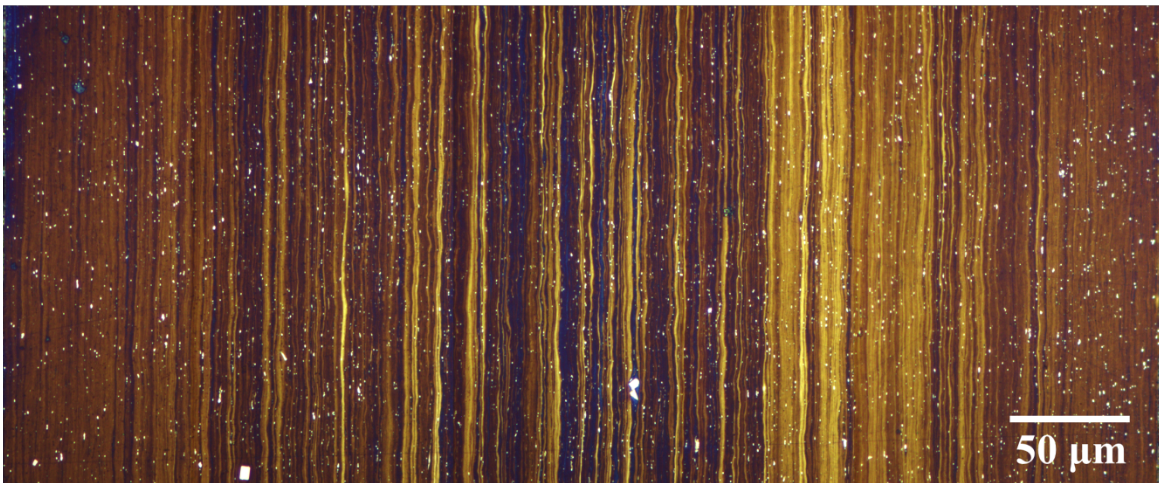

Figure 4.3. Optical micrograph of the complete steel sheet cross section in the as-received state. The sample was etched 30 s with the hot Lichtenegger-Blöch (60 °C) color etching solution.

The complete cross section of the as-received material is shown in the optical micrograph presented in Figure 4.3. In this case the sample was etched with L-B solution at 60 °C for 30 s. Titanium nitrides and χ-phase precipitates remain white, while the martensitic matrix is etched in different colors from yellow and light-brown to dark-brown and dark-blue.

4.2.3 Electron Probe Microanalysis (EPMA)

EPMA maps of the alloying elements Cr, Ni, Mo, Cu and Ti are shown in Figure 4.4 (b)-(f). All of them correspond to the same area of 450 x 200 µm^2 shown in Figure 4.3. However, in order to avoid some undesirable edge effects, the maps have been trimmed up to 447 x 173 µm^2. Each EPMA map contains the concentration of each element by means of an intensity parameter that can be easily processed to represent the content of each element per recorded pixel. This computation is under the assumption that the analyzed area has the same average composition than the nominal composition of the steel (Table 3.1), which is reasonable as no significant compositional variations were observed along the rolling direction.

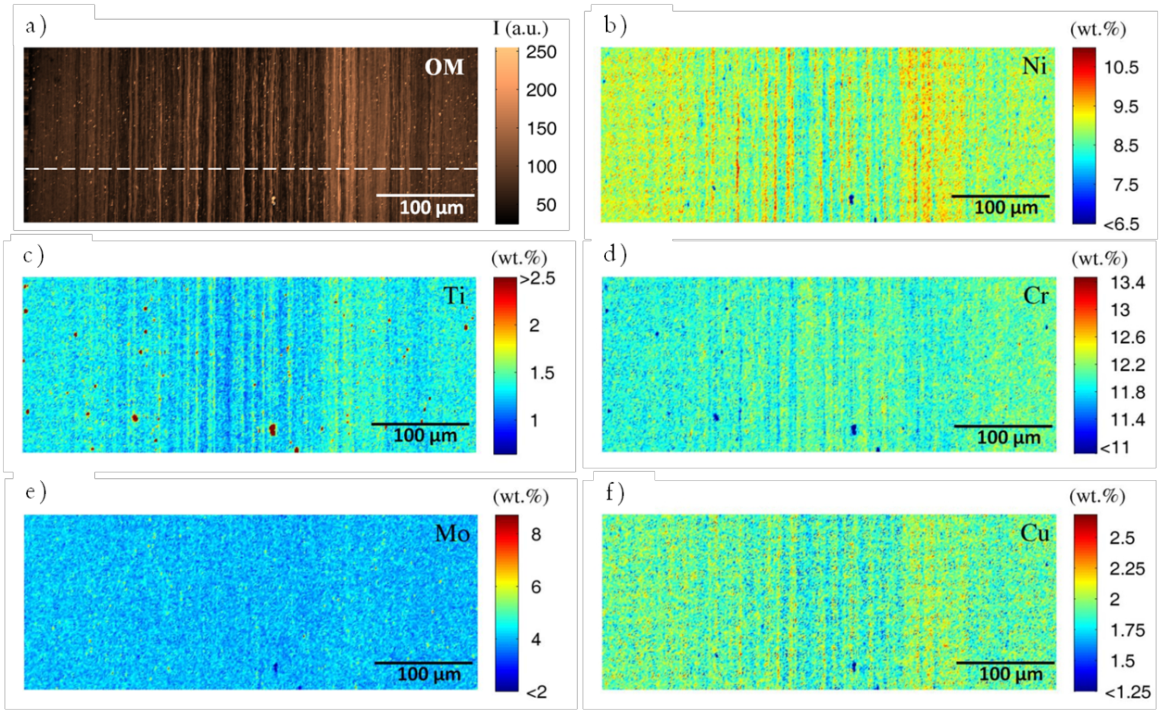

Figure 4.4. (a) Optical micrograph shown in Figure 4.3 transformed to brown scale that corresponds to exactly the same area where EPMA maps of the alloying elements were measured; (b)-(f) EPMA maps of the main alloying elements recorded over the same area of the steel sheet cross section.

Figure 4.4 (a) represents the optical micrograph shown in Figure 4.3 after transforming to brown scale. There is a clear correlation between the brighter bands in the optical image and the bands with higher content of Ni, Cu and Ti, while low concentration of Cr corresponds to darker bands in the optical image. That means that the L-B reagent is sensitive to the segregation of elements like Ni, Cu, Ti or Cr. However from these results it is not possible to disclose which influences most the etching response.

The presence of intermetallic precipitates in the steel may mask compositional variations of the matrix, as these will appear as very large concentration peaks of a certain alloying element in the maps. The scale of titanium map (Figure 4.4 (c)) is performed to display such compositional variation. It has to be borne in mind that, stoichiometrically, the calculated Ti concentration in TiN is much higher (77.37 wt.%) than the average chemical composition of the steel (1.35 wt. %). For this reason, in order to disclose the titanium segregation behavior, in the EPMA map the maximum threshold value for this element has been set to 2.5 wt. %. TiN precipitates appear thereby as dark-red cubic phases. In the other concentration maps, the presence of a TiN causes the opposite effect: very low or null concentration values of the corresponding alloying element. Different minimum threshold values were set in each map so as to disclose the segregation behavior, and that is why TiN particles appear as dark-blue cubic phases in Figure 4.4 (b) and Figure 4.4 (d)-(f). Regarding the concentration maps for chromium and molybdenum, the presence of fine particles (< 1 µm) of χ-phase ($Fe_{36}Cr_{12}Mo_{10}$) in the microstructure may also influence peak concentration values in the maps. According to the stoichiometry of χ-phase, the concentration of Mo (27.7 wt. %) and Cr (17.4 wt. %) is expected to be much higher than their average matrix content (4.05 and 12.00 wt. %, respectively). However, and contrary to the TiN precipitates (size ~3-10 µm), the size of χ-phase precipitates is smaller than the interaction volume excited by the beam (spatial resolution 1-2 µm). This means that the microanalysis spot covers at the same time matrix and χ-phase precipitates. Thus, maximum concentration values of Cr and Mo in the maps due to the presence of these precipitates are lower than it could be expected.

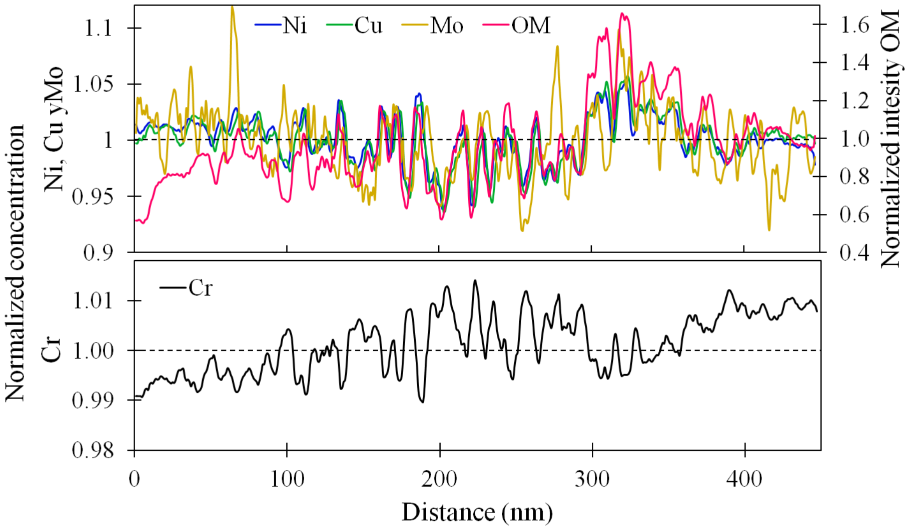

Figure 4.5. Line scans along the complete steel sheet cross section related to Ni, Cu, Mo, Cr obtained from the 2D EPMA maps shown in Figure 4.4.

The results shown in Figure 4.4 demonstrate that there is a clear chemical banding of Cr, Ni, Cu, and Ti along the thickness of the steel sheets. It is observed that Ni, Cu and Ti segregate in a similar fashion, while Cr has an opposite behavior. Mo shows a weaker segregation pattern than these other elements and slightly similar to Ni, Cu or Ti. Although this is not clearly visible in the maps from Figure 4.4, it can be easier concluded from results shown in Figure 4.5. In this figure, compositional variations of Ni, Cu, Mo and Cr are compared with intensity variations observed in the optical micrograph after etching with L-B solution. These line scans represent variations measured along the white dashed line drawn in Figure 4.4 a. In the concentration maps a line scan going through the same path has been considered. All intensity and concentration data points were normalized by dividing each value by the mean value in addition to a noise reduction by a curve smoothing. The curve smoothing was done by using the five-point moving average, disclosing the underlying trend of the data and leaving out noise or other fine scale structures, such as sharp maximum and minimum. It has been found that Ni, Cu and Mo follow the same trend than the intensity of the optical micrograph, while Cr trend is opposite. Moreover, Cr shows a less pronounced segregation pattern than the other alloying elements. For each maximum or minimum of Cr there is a minimum or maximum of Ni, Cu, Mo and LOM intensity, respectively. It is remarkable the good agreement observed in the trends of Ni, Cu (and Mo to a lesser extend) with respect to the intensities of the optical micrograph.

Several heat-treatments were performed with the aim of eliminating or reducing the chemical banding from the initial microstructure. The main concern was to avoid the formation of the high-temperature δ-ferrite phase. It was observed that at 1100 °C it started forming after 24 h. For this reason the treatment was reduced to 18 h. Figure 4.6 shows 2D EPMA maps of the main alloying elements for the cross section of a sample after homogenization at 1100 °C for 18 h.

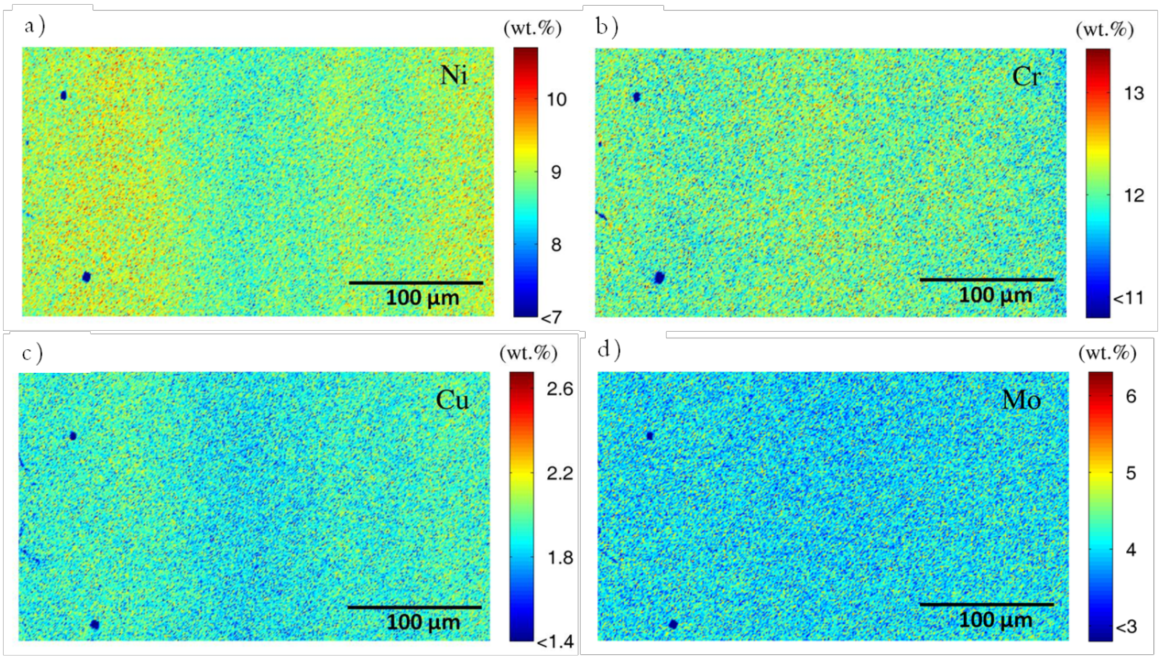

Figure 4.6. 2D EPMA maps done on the steel sheet cross section over an area of 350 x 200 µm^2 after an homogenization heat-treatment at 1100 °C for 18 hours.

Although the heat-treatment was carried out under vacuum conditions (10^{-1} mbar), holding the sample at high temperature for long times damaged the sample surfaces. Due to this slight modification of the microstructure caused by the heat-treatment, the borders of these maps (~ 60 µm of each side) have been cropped. Again, in order to avoid the influence of TiN precipitates on disclosing the microsegregation, the minimum cut-off values were set so as to reveal it properly, as was done in Figure 4.4. As expected, this homogenization heat-treatment causes the dissolution of the χ-phase precipitates, since Mo contents higher than 4 wt. % were not detected (Figure 4.7). After 18 h at 1100 °C the chemical banding is substantially reduced. Locally (~1-10 µm), chemical element distribution is significantly homogenized and most micro-bands disappear. However, some big macro-segregation bands (~100-200 µm in width) remain present, especially evident for Cr, Ni and Cu maps.

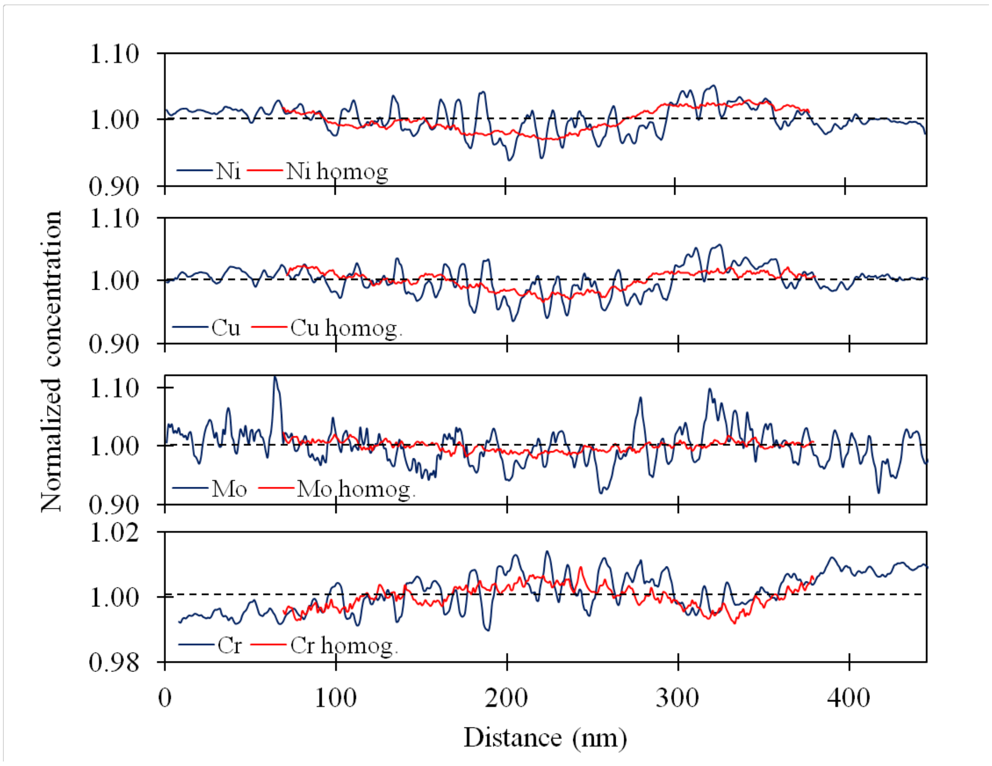

Figure 4.7. Comparison between line scans related to the alloying elements Ni, Cu, Cr and Mo before (blue line) and after (red line) the homogenization treatment.

4.3 Discussion

4.3.1 Revealing segregation by color etching

Color metallographic etchants react with the specimen surface to form what appears as stable films or tints. Contrary to standard chemical acid etchants, where the corrosion products caused by etching dissolve into the etchant and phase boundaries are generally the only features revealed, the surface is, generally, not physically altered. Common tint etchants used for steels are aqueous solutions of sodium metabisulfite ($Na_2S_2O_5$) or potassium metabisulfite ($K_2S_2O_5$) and/or sodium thiosulfate ($Na_2S_2O_3 \cdot 5H_2O$). In this solutions metabisulfite ($S_2O_5^{2-}$) and the thiosulfate ($S_2O_3^{2-}$) ions are the active ingredients. In aqueous or acidic solutions, in contrast to a metallic surface, these ions decompose into sulphur dioxide (SO_2), hydrogen sulphide (H_2S), sulphur, and hydrogen. The SO_2 depassivates surfaces, particularly stainless steel surfaces, promoting film formation. The H_2S provides the sulphur ion (S^{2-}) that creates a sulphide film on the steel surface when ions of iron, nickel, or cobalt are present [110; 112]. The colors observed by LOM depend on the thickness of the non-metallic film, result of the chemical reaction between the steel specimen and the reagent, and on the etching conditions and crystallographic orientation of the particular phase [113]. Several color etching solutions used in stainless steels were developed in the last decades; the most popular one is probably Behara and its variations [110; 114; 115]; but others like Murakami, L-B or Groesbeck's etching solutions are found also useful to differentiate phases such as ferrite, austenite, sigma phase or carbides in this type of steels [110]. The L-B color etching solution has been frequently used in duplex stainless steels to differentiate δ-ferrite from austenite. Some authors have used it in the past to differentiate martensite, austenite and χ-phase in stainless steels, in annealed condition [108]. In their seminal work [115], Lichtenegger and Blöch studied the usefulness of Behara etching solution and variations to the composition of this etchant. Their results seem to show that increasing the content of potassium metabisulphite and/or changing the hydrochloric acid by ammonium diflouride ($NH_4F{\cdot}HF$) helps revealing chemical banding in austenitic steels. They propose a reagent, become to be known as L-B etching solution, which was able to differentiate clearly ferrite from austenite and also chemical segregation within austenite in austenitic-ferritic welded materials. Besides, Di Schino et al. [100] found that, in low-Ni austenitic stainless steels, the L-B reagent etches yellow the Ni-rich austenite and blue the Ni-poor austenite. After etching the steel under investigation in this work with the hot L-B color etching solution (Figure 4.3), it is clearly observed that the martensitic matrix exhibits a similar etching contrast than the austenite described by Di Schino et al. [100]. Martensite is etched in different shades of brown, from yellow and light-brown to dark-brown or dark-blue, and different intensity variations. The comparison of the optical micrograph (Figure 4.3) with the EPMA maps (Figure 4.4) establishes a clear relationship between the content of Ni, Cu, Mo and Ti in solid solution and the color and brightness resulting after etching. Alloying elements Ni, Cu, Mo and Ti segregate together, whereas the Cr has an opposite behavior. Ni-rich bands are colored in bright yellow, whereas those depleted in Ni (consequently enriched in Cr) are colored dark-brown or dark-blue.

Thus, it is concluded that the higher the Ni content, the lighter the etching. As the Ni content decreases, the darkening by the etching increases, so that the darkest bands correspond to the lowest Ni contents. This effect is more noticeable in those bands located in the centre of the steel sheet cross section.

In addition to the tint etchant, many authors find electrolytic etching the easiest and most effective way of phase identification in stainless steels. The process is rather simple; the specimen becomes the anode and the cathode consists of a non-dissolving material such a stainless steel or pure iron. A simple battery with a direct current is applied at room temperature to activate the etching process. Thus, metal ions are conducted away from the anode into the electrolyte solution (the etching solution). A 10 % aqueous oxalic acid solution is widely used to reveal carbides, second phases and grain structures in austenitic stainless steels. If it is present, this etch will also outline δ-ferrite [112; 113], although in our investigation it turned out to be more effective the use of a 10 % solution of NaOH. This later reagent is commonly used to disclose uniquely the δ-ferrite phase in duplex stainless steels [116]. This electrolytic etchant can also help revealing phases such as the sigma (σ) and χ-phase [117], as it has been show in this work in Figure 4.2 d.

4.3.2 Effect of homogenization on chemical banding

Figure 4.7 shows four charts, in which compositional variations of Ni, Cr, Cu and Mo are compared before and after the homogenization treatment. Figure 4.7 was obtained following the same procedure as for Fig. 5. As previously discussed, the sample exhibits not only a local chemical banding, but also a big macro-segregation of about 150 – 200 nm. Figure 4.7 reveals that, the local chemical banding is substantially reduced with the homogenization at 1100 °C for 18 hours; however, the macro-segregation persists and is especially noticeable in Ni, Cu and Cr. In the case of Mo, it is less evident. On the other hand, possible maximum peaks related to the χ-phase precipitates also disappeared, since at 1100 °C the temperature is high enough to dissolve completely this phase.

4.3.3 The solidification mode: the origin of the chemical banding:

It is well known that the presence of chemical banding originates during the solidification and subsequent processing involved in the manufacturing process of the steel. For austenitic stainless steels, the solidification path followed by the melt during cooling was related in the past to Ni equivalent (Ni_{eq}) and Cr equivalent (Cr_{eq}) of the steel , which are used to simplify a multi-composition system into the Fe-Cr-Ni ternary system [100; 105; 118]. Depending on the ratio of Ni equivalent an Cr equivalent (Cr_{eq}/Ni_{eq}), the solidification modes of austenitic stainless steels can be divided into the four types that appeared summarized in Table 4.1, namely austenitic (A mode), austenitic – ferritic (AF mode), ferritic – austenitic (FA mode) and ferritic solidification (F mode) [105; 118]:

Table 4.1. Summary of the solidification modes of austenitic stainless steels as function of the Cr_{eq}/Ni_{eq} ratio [105; 118].

Solidification mode	Reaction	Cr_{eq}/Ni_{eq}
A mode	$L \rightarrow L + \gamma \rightarrow \gamma$	$Cr_{eq}/Ni_{eq} < 1.25$
AF mode	$L \rightarrow L + \gamma \rightarrow L + \delta + \gamma \rightarrow \gamma + \delta \rightarrow \gamma$	$1.25 < Cr_{eq}/Ni_{eq} < 1.48$
FA mode	$L \rightarrow L + \delta \rightarrow L + \delta + \gamma \rightarrow \gamma + \delta \rightarrow \gamma$	$1.48 < Cr_{eq}/Ni_{eq} < 1.95$
F mode	$L \rightarrow L + \delta \rightarrow \delta \rightarrow \gamma$	$Cr_{eq}/Ni_{eq} > 1.95$

Ma *et al.* [118] used the following equations for estimating Ni_{eq} and Cr_{eq}:

$$Ni_{eq} = (\%Ni) + 30\,(\%C) + 30\,(\%N) + 0.5\,(\%Mn) \quad [4.1]$$

$$Cr_{eq} = (\%Cr) + (\%Mo) + 1.5\,(\%Si) + 0.5\,(\%Nb) \quad [4.2]$$

With equations [4.2] and [4.1] Cr_{eq} and Ni_{eq} were calculated for the steel under investigation in this work, resulting 16.75 wt. % and 9.85 wt. %, respectively; and a ratio Cr_{eq}/Ni_{eq} of 1.70. So, the solidification mode of the steel falls into FA mode, which consists of the primary δ-ferrite precipitation stage and the three-phase reaction stage. At the stage, δ-ferrite dendrites form directly from the melt. As the solidification goes on, it reaches the three-phase reaction stage when eutectic colonies appear among the primary δ-ferrite dendrites [118]. Thermodynamic calculations carried out with ThermoCalc software [119], using TCFE6 (version 6.2) database, predict also that solidification would develop forming, first of all, δ-ferrite at 1437 °C and, later on, austenite at 1397 °C.

Guo *et al.* [105] studied the solidification process in a commercial metastable austenitic stainless steel type 316, which solidifies under a FA mode similarly to the stainless steel under investigation in this work. The equilibrium partitioning coefficients of Ni and Cr during the solidification of the alloy through δ-ferrite were predicted to be lower and larger than unity, respectively, for the 316 alloy. Therefore, Ni would tend to partition to the untransformed melt while the amount of Cr would increase in δ-ferrite. This would be expected since Cr and Ni stabilize ferrite and austenite phases, respectively. In the same way, the partitioning coefficient of Mo was calculated as lower than unity, which would imply the partitioning of Mo to the melt during the formation of δ-ferrite, as for Ni. In this sense, both Ni and Mo would appear segregated together after solidification at room temperature. If the sample is not quenched, the δ-ferrite would transform subsequently to metastable austenite, and some vermicular δ-ferrite would be likely retained. Their predictions were in good agreement with the experimental results. Using ThermoCalc, similar calculations were done in this work for alloy 316 and also the steel under investigation considering δ-ferrite as the primary phase (Table 4.2). A good agreement is found between calculations for Ni and Cr, but not for Mo. This discrepancy is not clear but could be due to the use of different thermodynamic databases.

Table 4.2- Equilibrium partitioning coefficients calculated for Cr, Ni, Mo, Cu and Ti during the initial stages of δ-ferrite formation in alloy 316 and the alloy under investigation in this work.

Alloy	Cr	Ni	Mo	Cu	Ti
316 (Guo *et al.*)	1.02	0.78	0.97		
316 (this work)	1.03	0.76	1.09		
This steel	1.04	0.73	1.06	0.56	0.33

Equilibrium partitioning coefficients for the steel investigated in this work predict a strong partitioning of Ni, Cu and Ti to the melt during the formation of δ-ferrite, while Cr and Mo would show an opposite but much weaker behaviour. These predictions would explain the segregation pattern results shown in Figure 4.4 and Figure 4.5, except for Mo, which exhibits a weak segregation behaviour but more similar to Ni, Cu or Ti than for Cr (Figure 4.5). The lack of reliable thermodynamic databases for novel high alloyed steels could be the origin of discrepancies between experiments and calculations. In addition, one should also bear in mind that experimental results are generally far from thermodynamic equilibrium conditions.

Finally, some retained δ-ferrite was detected at room temperature in this alloy (Figure 4.2), also observed in the scientific literature for similar alloys like 316 [118]. All these observations would corroborate that as for alloy 316, used here as a reference, solidification would take place in this steel through de FA mode.

4.4 Conclusion

- The microstructure of the as-received steel under investigation was characterized metallographically by using different chemical and electrolytic etching solutions. The use of the Lichtenegger and Blöch (L-B) colour etching solution was shown to reveal not only the phases present in the microstructure, but also the existence of chemical banding perpendicular to the rolling direction. The L-B reagent was found to color the microstructure in bands depending on what alloying elements have been segregated to each band.
- Two-dimensional electron probe microanalysis (EPMA) maps showed that Ni, Cu and Ti segregate together in the bands, while Cr has an opposite behaviour. Mo has a mixed segregation behaviour but more prompt to segregate like Ni does. On the other hand, EPMA also revealed that in addition to the local micro-chemical banding (lateral spacing of 1-10 μm) there is also a macro-segregation (100-200 μm).

- A comparison of the light optical micrographs with the EPMA maps enabled to establish a direct relationship between the alloying element band concentration, especially Ni content, and the resulting etching colour contrast obtained with the L-B reagent.
- Homogenization heat treatment at 1100 °C for 18 h substantially reduces the banded structure. However, this treatment does not seem to affect much the macro-segregation.

Chapter 5

Phase transformations upon isochronal heating: Reversion-induced ultrafine-grained microstructures and evolution with the temperature.

C. Celada-Casero, D. San Martín. *Austenite formation in a cold-rolled semi-austenitic stainless steel.* Metal. Mater. Trans. A, 45 (2014) 1767-1777.

C. Celada-Casero, B-M. Huang, J-R. Yang, D. San Martín. *Mechanisms of sub-micrometer size austenite formation under different isochronal conditions in a cold-rolled metastable stainless steel*, Mater. Char. (in preparation).

A primary objective of this chapter is to obtain fundamental insights on the reaustenitization (α'→γ transformation) process and microstructural evolution of the cold-rolled (CR) material under investigation upon different isochronal treatments (0.1, 1 and 10 °C/s). LOM, SEM, TEM, micro-hardness Vickers tests, TEP measurements, magnetization measurements EBSD and EPMA were used for microstructural characterization. All microstructural changes upon continuous heating shift to higher temperatures when the heating rate increases, which is characteristic of diffusional processes. The α'→γ transformation occurs in a wide range of temperatures and in two-steps regardless the heating rate. The two-step transformation is due to the chemical banding present in the as-received microstructure, which does not change significantly after heating slowly at 0.1 °C/s. The α'→γ transformation appears to be a interface-controlled reaction for all studied heating rates. The morphology of the initial martensite is responsible for the grain refinement experienced at all heating rates. Mean austenite grain sizes in the range 350-410 nm are obtained at the end of the transformation (A_F). Heating above A_F causes the austenite grains to grow, although it appears to be impeded by the presence of the intermetallic χ-phase at grain boundaries. The thermal stability of fully austenitic microstructures is affected by the AGS and the formation/dissolution of χ-phase.

5.1 Introduction

It is clear from the literature that the idea of controlled annealing of heavily cold-rolled metastable ASS to produce nano/submicron austenite grain structures is gaining wide acceptance [76; 78; 81; 89-91; 120-123]. Tomimura, Takaki and co-authors [89-91] were pioneers in obtaining for the first time ultrafine-grained (UFG) austenitic microstructures (1.8 μm and finer) in 18Cr-9Ni and 16Cr-10Ni stainless steels by reversion of the microstructure to the austenitic state after 90 % cold-rolling reduction. They established that the key to success of grain refinement lies is the volume fraction and the morphology of the strain-induced martensite generated during rolling. Since then, several works in low-carbon steels and Fe-Cr-Ni alloys have pointed out that high cold reductions produce a crystallographic distortion in the strain-induced lath-type martensite, which results in a much more dislocated microstructure, named dislocation-cell-type martensite. For instance, Misra *et al.* [78] studied the effect of different degrees of cold-deformation (45, 62 and 77 %) on the nature of the strain-induced martensite in a 17Cr-7Ni-N stainless steel and they found that, under the same annealing conditions, lower percentages of cold deformation resulted in grater austenite grain sizes. Weidner *et al.* [81] obtained AGS of 0.89, 1.20 and 2.55 μm after annealing a 90, 70 and 50 % cold-deformed high-alloyed austenitic TRIP steel, respectively. Therefore, it appears that the success of the phase-induced reversion to obtain NG/UFG structures lies in the predominance of a dislocation-cell-type structure in the severely deformed martensite. This morphology provides an increased number of nucleation sites for the austenite phase, improving thereby the attainment of NG/UFG structures [78; 121-123].

The mechanism of the reverse ($\alpha' \rightarrow \gamma$) transformation has been extensively studied [76; 79; 120-123]. Recently, several works have arisen, especially in AISI 301, 301LN and 304 SS grades, explaining that the $\alpha' \rightarrow \gamma$ transformation may occur either by diffusional or by diffusionless mechanism. Whereas a diffusional transformation occurs in a wide range of temperatures and results in defect-free equiaxed austenite grains with a wide grain size distribution, the diffusionless mechanism takes place in a narrow range of temperatures, similarly to the martensitic shear transformation, and leads to a defect laden lath-type austenite although, as Coleman and West [124] proposed, this lath-type austenite can undergo a subsequent recovery with further annealing, resulting in a completely recrystallized UFG austenite. From previous works it appears that the mechanism governing the α'→γ transformation is related to the chemical composition of the steel [90], the martensite morphology of the initial microstructure [78; 91], and by the heating rate [43; 125-129]. Apple and Krauss [125] noted considerable differences in the morphology of the reverted austenite in Fe-Ni-C(0.05-0.3 wt.%) alloys when varying the heating rate between 3 °C/s and 1500 °C/s. Lower heating rates provide sufficient time for short range diffusion, resulting in equiaxed grains by a diffusion-controlled transformation, whereas diffusion is not possible at higher heating rates, which instead leads to lath-austenite formed through a shear-type mechanism. D-S. Leem *et al.* [126], Kapoor and Batra [43], and more recently Han and co-authors [127] also found a diffusion-type reversion for heating rates lower than 10 °C/s, and a diffusionless reversion for higher heating rates in different stainless and precipitation hardening steels.

5.2 Results

5.2.1 Characterization of the initial microstructure by TEM

Although a complete characterization of the cold-rolled state of the steel was already presented in *Section 4.1* (by OM, SEM, X-Ray diffraction and EPMA), the great influence the morphology of the initial martensite has on the reversion process also requires its study by TEM.

Figure 5.1 illustrates bright-field (BF) TEM micrographs of the as-received microstructure. Selected area electron diffraction patterns (SADP) from different regions indicate the presence of two distinct martensite structures, namely, lath-type and dislocation-cell-type martensite. The former one (Figure 5.1 (a)), gives a spot-like diffraction pattern, while the second one produces a ring-like diffraction pattern (Figure 5.1 (b)) due to its higher dislocation density. Dislocation-cell type martensite has been, nevertheless, the main phase observed, being the presence of the lath-type occasional.

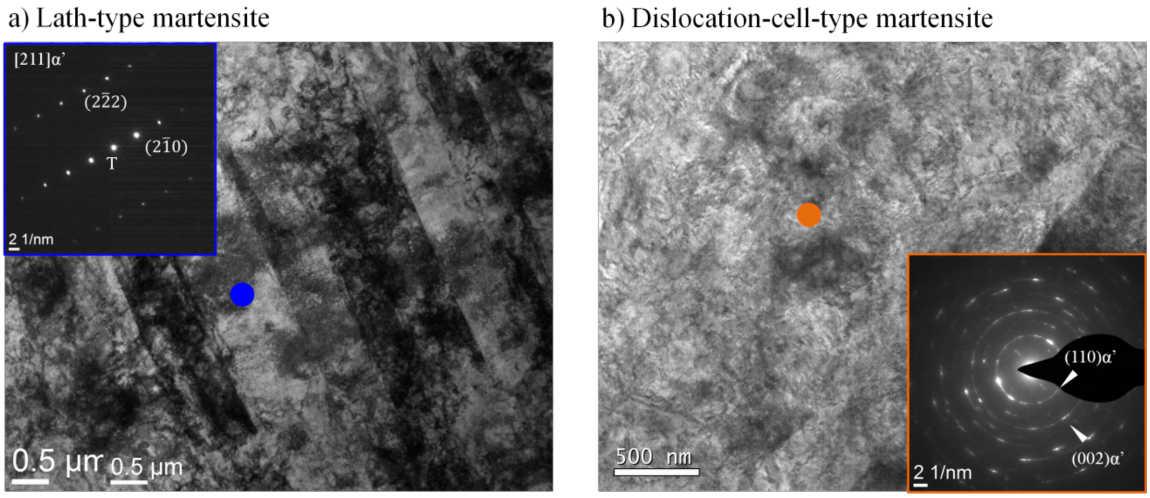

Figure 5.1. Bright-field TEM micrographs and their corresponding diffraction patterns illustrating different types of martensite in the as-received cold-rolled microstructure: (a) Lath-type martensite and (b) Dislocation-cell-type martensite.

5.2.2 Microstructural evolution during continuous heating

5.2.2.1 Magnetization, micro-hardness Vickers and TEM measurements

For this steel and under continuous heating, high-resolution dilatometry has been proven to be not sensitive to the whole contraction caused by the α'→γ transformation and, therefore, to the detection of the A_S and A_F transformation temperatures (*see Section 3.5*) [130]. For this reason, other experimental techniques were used.

Due to its high precision and reliability, magnetization measurements allow an accurate determination of the martensite volume fraction ($f_{\alpha'}$) during the reaustenitization. Additionally, micro-hardness Vickers tests and TEP measurements were performed in order to strengthen and support these data and to obtain information about the processes involved below the A_S temperature. The dependence of the $f_{\alpha'}$, the micro-hardness Vickers and the TEP with the temperature are plotted in Figure 5.2 (a)-(c). The range of temperatures at which the reaustenitization takes place ($A_S - A_F$) was determined from the magnetization measurements as follows for the different heating rates: 600-825 °C (0.1 °C/s); 650-900 °C (1 °C/s) and 680-950 °C (10 °C/s). It can be observed that A_S and A_F shift to higher temperatures with increasing heating rate. Moreover, from Figure 5.2 (a), it is observed that the α'→γ transformation proceeds in two consecutive steps in the same extent for all heating rates.

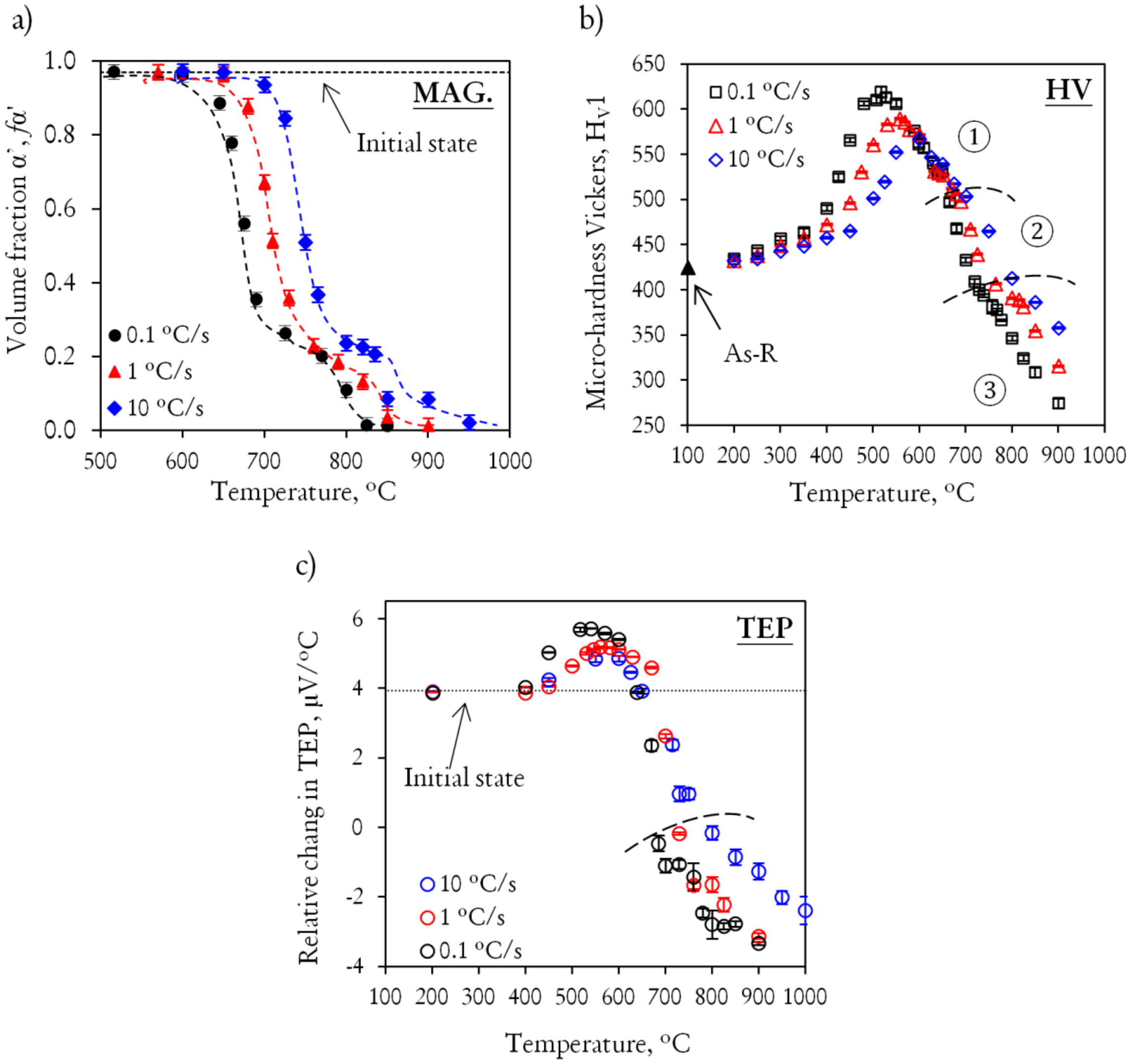

Figure 5.2. Temperature evolution of: (a) martensite volume fraction ($f_{\alpha'}$) obtained by magnetization measurements (MAG.); (b) micro-hardness Vickers (HV); and (c) the thermoelectric

power (TEP) as a function of the heating rates. Dotted lines indicate initial state values. As-R stands for as-received state. Dashed lines have been drawn as a guide to the eye.

The temperature evolution of the micro-hardness Vickers (Figure 5.2(b)) shows that the hardness increases monotonically from the as-received state (425 Hv) until a hardness peak is reached at the following pairs of temperature- hardness peak values and heating rates: 520 °C-620 Hv (0.1 °C/s), 560 °C–590 Hv (1 °C/s) and 600 °C-570 Hv (10 °C/s). As in other precipitation hardening steels [40], the rise of the hardness in this steel is achieved through the precipitation of intermetallic nanometric phases, type $Ni_3(Ti,Al)$, within the martensite phase. During heating up to the peak hardness, two distinct hardening steps have been observed: first, the hardness increases weakly below 400 °C and then accelerates abruptly, highlighting that the precipitation kinetics are greatly enhanced above this temperature. Once the peak hardness is reached the hardness starts decreasing and three regions can be distinguished as the slope changes, labeled with ①, ② and ③ and separated by dashed lines. The slope changes clearer for the slow rate. Region ①, the decrease after the hardness peak, it is thought to be related to the coarsening of the precipitates, the recovery of the martensite phase and growth of retained austenite islands. Then, ② presents a faster drop, that coincides with the range of temperatures at which the first step of the α'→γ transformation is detected in Figure 5.2 (a). This faster drop is hence associated with the rapid decrease in martensite volume fraction (80 % of the transformation). Eventually, the hardness falls in ③ due to the last 20 % of the transformation and due to austenite grain growth, once temperature A_F is exceeded.

Finally, Figure 5.2 (c) displays the evolution of the TEP with the temperature and the heating rate. The TEP value of the initial microstructure (~ 3.394 μV/°C) depends on the chemical composition, the phases present in the microstructure, the content of alloying elements in solid solution and the degree of deformation [97; 131-133]. It is observed that, from 400 °C on, the TEP increases for all heating rates, reaching a maximum at the following TEP (μV/°C)- temperature (°C) values: 5.72-540 (0.1 °C/s), 5.18-560 (1 °C/s) and 4.86-600 (10 °C/s). There are three main processes taking place before the α'→γ transformation: precipitation/dissolution of second phases and recovery. The maximum value is obtained at the slow heating rate, as observed for the hardness in Figure 5.2(b) and decreases as the heating rate is increased. The precipitation decreases the content of alloying elements in solid solution and, as a consequence, the TEP increases. Afterwards, there is a decrease of the TEP that is characterized by a change in the slope (marked with a dashed line) that occurs in a range of temperatures similarly than the one observed between ② and ③ in the evolution of the hardness. This decrease is related with the α'→γ transformation. The change of a BCC crystalline structure to a FCC causes a change in the electrical properties of the material, which are translated in a decrease of the TEP. The change in the slope must be related to the second step of the transformation, as observed in Figure 5.2(a) and (b).

5.2.2.2 Scanning Electron Microscopy (SEM)

Figure 5.3 presents SEM micrographs of the microstructure after isochronal heating up to different temperatures before, during and after the α'→γ transformation. A similar microstructural evolution is observed among heating rates. Figures (a1), (b1) and (c1) show the microstructure before the reaustenitization has started. The microstructure has undergone some recovery and the shear bands of the martensite and the retained austenite are visible. At the beginning of the transformation (Figure 5.3 (a2), (b2) and (c2)), apart from the large austenite (γ-) islands, small austenite nuclei along the shear bands (pointed with green arrows) are observed. The γ'-islands grow or coarsen from the retained-γ present in the initial microstructure. As an approach, the stability of austenite and martensite phases has been studied based on Ni and Cr contents by Energy Dispersive X-Ray Spectroscopy (SEM-EDS). The following results have been obtained in wt. %: γ-islands present 11.0 (0.8)-Ni and 11.5 (0.5)-Cr; whereas the martensitic matrix has 8.7 (0.5)-Ni and 11.5 (0.3)-Cr, similarly to the nominal composition of the steel (8.87-Ni and 12.00-Cr). Figure 5.3 (a3) shows a microstructure partially reaustenitized at 0.1 °C/s up to 680 °C ($f_\gamma \sim 0.50$) and large islands of untransformed martensite (α'-island) surrounded by on-growing austenite nuclei are observed. However, these α'-islands are no longer observed in partially reaustenitized microstructures with higher amount of austenite, as microstructures in Figure 5.3 (3b) and (3c). The untransformed martensite surrounds the small austenite grains and is barely noticeable.

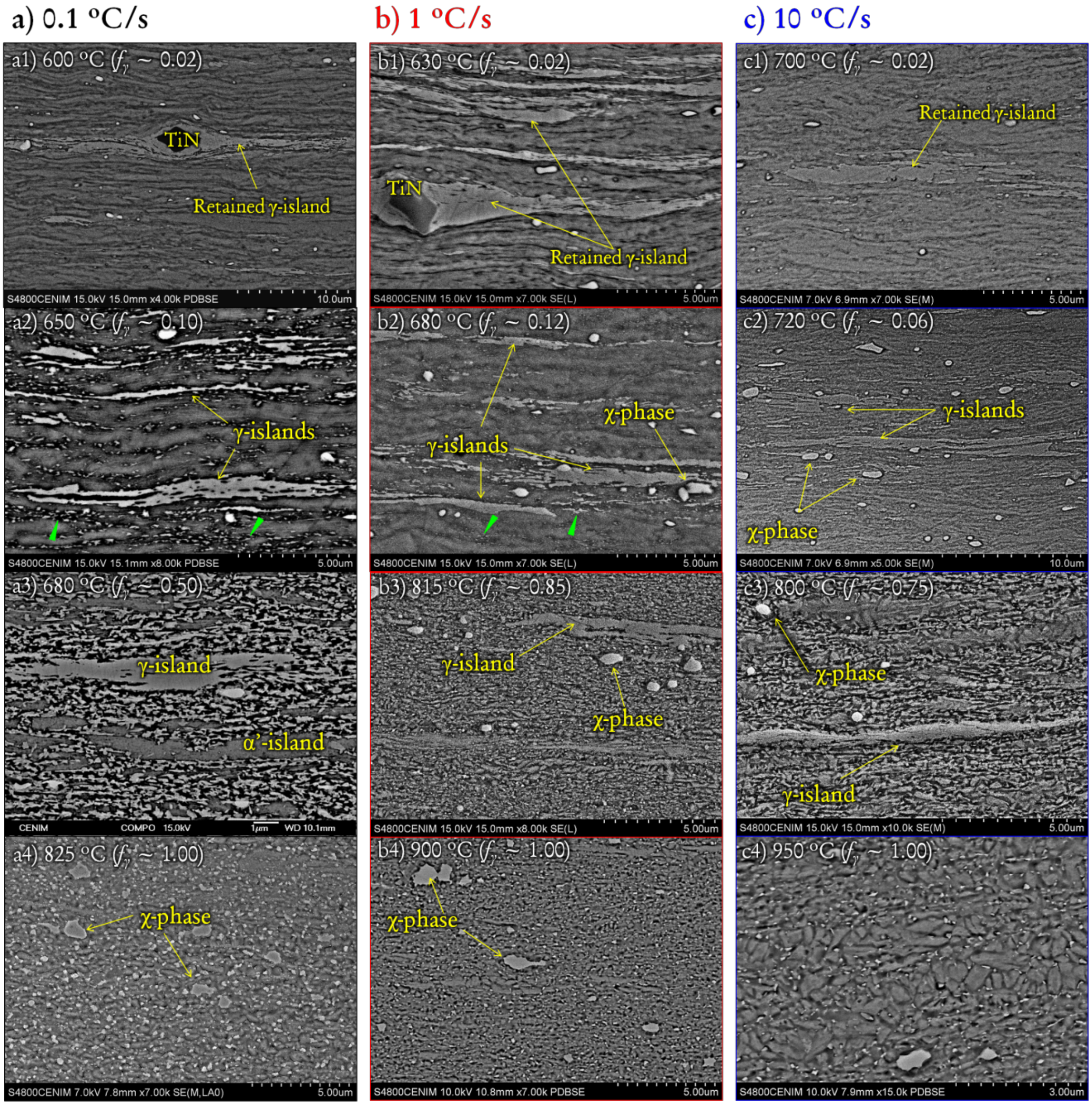

Figure 5.3. SEM micrographs of the microstructure after continuous heating up to different temperatures at heating rates of : (a) 0.1 °C/s; (b) 1 °C/s and (c) 10 °C/s. Temperature and volume fraction of austenite (f_γ) are noted above each micrograph. Phases present in the microstructure are labeled and highlighted by arrows. Green arrows point out the presence of austenite nuclei.

EDS analysis (wt. %) obtained at this stage showed: 11.0 (0.6)-Ni and 10.9 (0.4)-Cr for α'-islands, very similar to that obtained for the initial stage; 7.6 (0.6)-Ni and 12.1 (0.4)-Cr for α'-islands; and 10.2 (0.8)-Ni and (11.9 ± 0.5) Cr for the matrix. As expected, the Ni content in the untransformed α'-island is lower than that of the matrix (austenite and martensite) and α'-islands. Eventually, fully austenitic microstructures are obtained at A_F (Figure 5.3 (4a)-(4c)). It is evident that the austenite grain size (AGS) is below 1 μm for all heating rates and that the volume fraction of χ-phase (f_χ) has increased, especially at 0.1 °C/s. Two different χ-phase size distributions can be observed: large and globular χ-phase precipitates, which were already present in the initial microstructure, and very small χ-phase precipitates located at austenite grain boundaries, which have originated during the heating. Due to their small size of these latter precipitates, an estimation of f_χ and size will be more accurate by means of TEM micrographs.

5.2.3 Reaustenitization: Transmission Electron Microscopy (TEM)

The study of the α'→γ transformation was investigated by TEM. For this study, it is convenient to divide the transformation into two regimes: 1) nucleation, which corresponds to the first appearance of new austenite grains in the martensitic matrix; and 2) growth, during which the new austenite nuclei grow and replace the martensite phase.

A) Initial stages of the transformation: Austenite Nucleation

Figure 5.4 shows TEM micrographs and their corresponding SADPs of the first stages of the transformation. The microstructures contain f_γ ~0.10 and ~0.06 after heating up to 650 °C at 0.1 °C/s and up to 725 °C at 10 °C/s, respectively. Two different nucleation modes were detected. For a slow heating rate (0.1 °C/s), the austenite was found to nucleate at two different locations: 1) at dislocation-cell-type martensite (Figure 5.4 (1a)), which has formed a sub-grain structure made of dislocation-walls due to recovery, and 2) at martensite-lath boundaries (Figure 5.4 (1b)). In this latter case, the austenite coarsens within the lath, giving rise to nanometric defect-free crystals of austenite. For a heating rate of (10 °C/s), the austenite was observed to nucleate randomly ar the dislocation-cell-type marteniste, which is highly dislocated (Figure 5.4 (1c)). The austenite phase nucleates with a Kurdjumov-Sachs orientation relationship (KS OR), as generally reported [90].

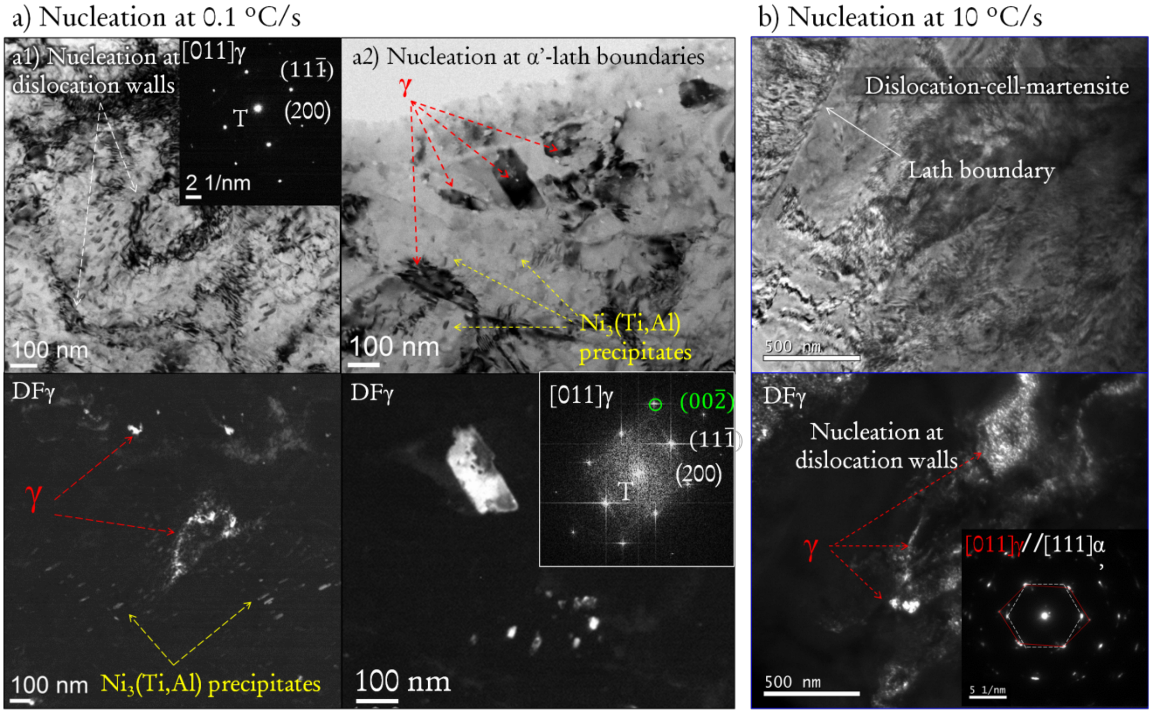

Figure 5.4. TEM micrographs illustrating the austenite nucleation process after heating to 650 °C at 0.1 °C/s (a) and to 725 °C at 10 °C/s (b). Each BF micrograph is accompanied by the SADP of the austenite and the corresponding DF of austenite phase (DFγ). (a1) Austenite (γ) nucleation at dislocation-walls of a recovered martensite, (a2) austenite nucleation at marteniste (α')-lath boundaries. (b) Austenite nucleates randomly at dislocation-walls of the dislocation-cell-type martensitic matrix. The double SADP shown reveals the existence of a KS OR between austenite and martensite. The presence of $Ni_3(Ti,Al)$ precipitates is highlighted in yellow.

The different dislocation density and distribution suggests that the recovery process occurs more significantly by heating at 0.1 °C/s than at 10 °C/s, which influences the nucleation of the austenite. The different recovery state is pointed out by the contrast in BF, since a bright contrast indicates a low density of dislocations and the way round. On the other hand, attention should be drawn to the presence of rod-shape nanometric $Ni_3(Ti,Al)$ precipitates, which appear brighten in DFγ images. This is not surprising, since the interplanar spacings of the {220} reflections of the austenite (highlighted in green in the SADP of Figure 5.4 (a) coincide with the $\{22\bar{4}0\}$ reflections of the hexagonal $Ni_3(Ti,Al)$ phase [39].

B) Austenite Growth Process

The austenite growth process is summarized through Figure 5.5 - Figure 5.8. Figure 5.5,Figure 5.6 and Figure 5.7 illustrate the microstructure after heating at 0.1, 1 and 10 °C/s to 680, 725 and 750 °C, respectively. These microstructures contain f_γ ~0.50-0.60.

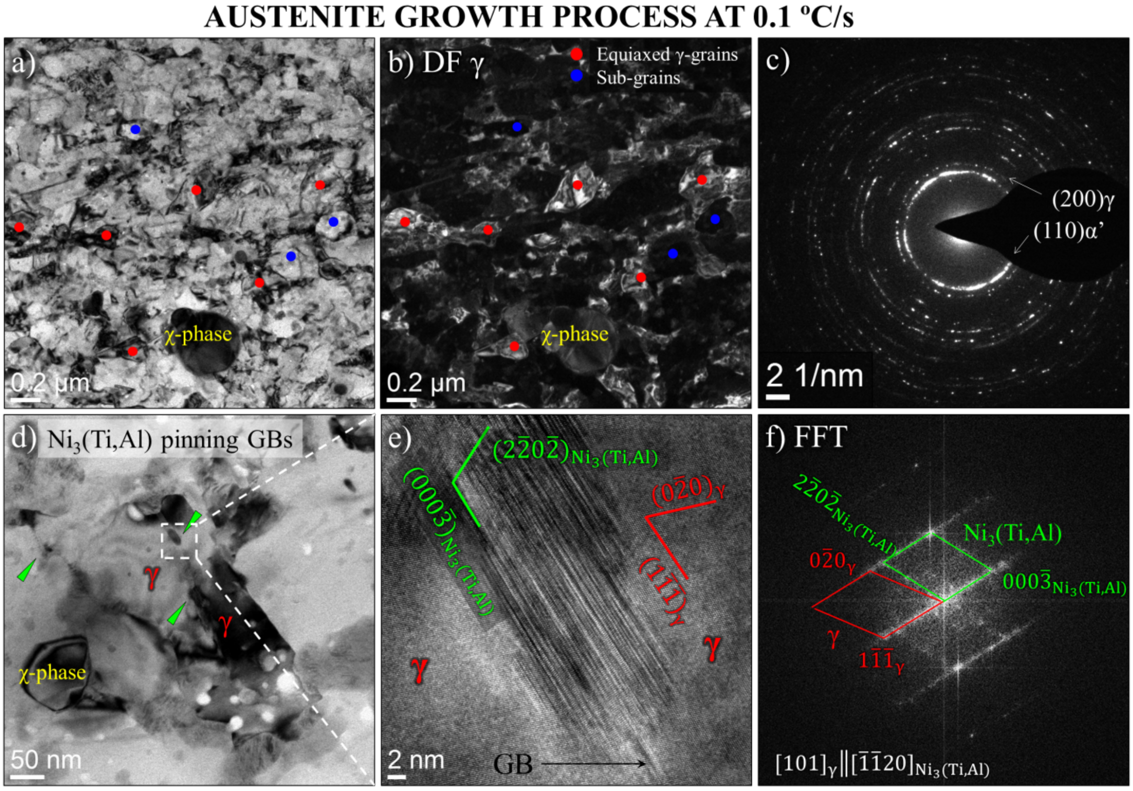

Figure 5.5. TEM micrographs of a sample after continuous heating at 0.1 °C/s up to 680 °C, so that it contains a f_γ ~ 0.50. (a) BF micrograph showing a general overview of the microstructure. (b) DF recorded using a reflection of austenite (γ) phase. (c) SADP of (a) showing the presence of martensite and austenite phases. (d) BF image pointing with green arrows the presence of $Ni_3(Ti,Al)$ precipitates located at γ grain boundaries (GBs). (e) High-resolution image of a $Ni_3(Ti,Al)$ precipitate at an γ grain boundary (area framed with a white dashed line in (d)). (f) Fast Fourier Transform (FFT) image of (e). The chi-phase (χ-phase) has been labeled in yellow. In (a) and (b) equiaxed γ-grains have been marked with red spots, and austenite nucleating at dislocation-walls with red and blue spots.

Figure 5.5 (a)-(c) shows a BF, the DFγ and the SADP of the overall microstructure after heating at 0.1 °C/s up to 680 °C. The microstructure comprises recovered martensite and some well-formed and relatively defect-free austenite grains with an average size of ~200 nm (marked with red spots). The recovery of the high dislocated martensite causes the rearrangement of dislocations, which results in the formation of cell-type structures (marked with blue spots). These cell-type structures consist of dislocation-walls surrounding quite defect-free areas or sub-grains (marked with blue spots). Dislocation-walls act as nucleation sites for the austenite and their dark contrast in BF is due to their high dislocation content and the presence of austenite phase, which has a different crystalline structure than the martensitic matrix. Therefore, the DFγ image points out that nucleation at dislocation-walls and growth of well-formed austenite grains occurs simultaneously. Figure 5.5 (d) shows a BF of a region where $Ni_3(Ti,Al)$ precipitates are located at austenite grain boundaries. The high-resolution (HR) TEM image, displayed in Figure 5.5 (e) and its Fast Fourier Transform (FFT) in Figure 5.5 (f), reveals a $(0001)\eta \| (01\bar{1})\gamma$; $[2\bar{1}\bar{1}0]\eta \| [011]\gamma$ orientation relationship.

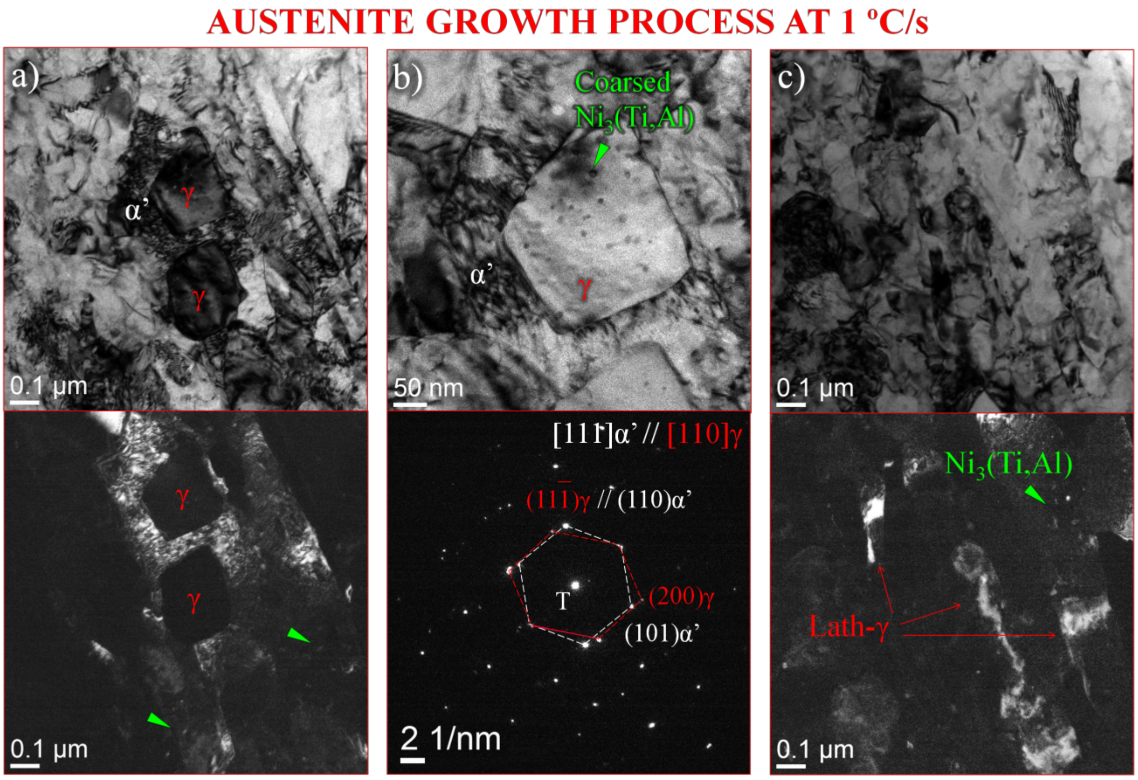

Figure 5.6. TEM micrographs illustrating the austenite grain growth in a sample which contains a f_γ ~ 0.60 after heating at 1 °C/s up to 725 °C. (a) BF and the corresponding DF from martensite phase displaying two austenite grains with globular morphology immersed in the martensitic matrix; (b) BF micrograph showing a higher magnification of image (a) and the SADP revealing a KS OR at the austenite/martensite (γ/α') grain boundary; (c) BF and DF of austenite phase showing an area where austenite presents a lath morphology. Ni_3(Ti,Al) precipitates are pointed by green arrows.

Figure 5.6 illustrates a microstructure with a f_γ ~ 0.60 obtained after heating the material at 1 °C/s up to 725 °C. Figure 5.6 (a) shows a BF and its corresponding DFγ that points out the globular growth of the austenite phase in a dislocated martensite matrix. As for 0.1 °C/s, the DFγ reveals the presence of Ni_3(Ti,Al) precipitates in the martensite. However, these precipitates appear to coarsen and dissolve within the austenite phase, as shown in Figure 5.6(b). The double SADP obtained from the α'/γ grain boundary reveals a KS OR, which agrees with the literature [79; 90]. Apart from globular austenite, lath-like austenite was also observed, as displayed in Figure 5.6 (c). It is worth mentioning that this lath-type morphology was very rarely detected, being the globular-type the most common.

Figure 5.7 shows a partially reaustenitized microstructure (f_γ ~ 0.50) after heating at 10 °C/s up to 750 °C. Figure 5.7 a presents a highly dislocated microstructure with some recovered areas. The DFγ highlights the presence of small austenite nuclei located at dislocation tangles, similarly to the nucleation process observed at the initial stages of the reaustenitization at 10 °C/s in Figure 5.4 (b). However, as Figure 5.7 (b) shows, other regions have undergone a more important recovery process, leading to the formation of sub-grains and dislocation-walls where austenite nucleates and grows (pointed by red arrows). As for lower heating rates, Ni_3(Ti,Al) precipitates are disclosed in the martensite phase by the DFγ. Regarding the growth mechanism, similarly to the growth observed at 1 °C/s, two different morphologies were distinguished: highly dislocated lath-like (Figure 5.7 (c)) and defect-free globular-like (Figure 5.7 (d)). This latter morphology was the most common. As revealed by the SADP in Figure 5.7 (d), a KS OR was also found to coexist between the parent and the new phases.

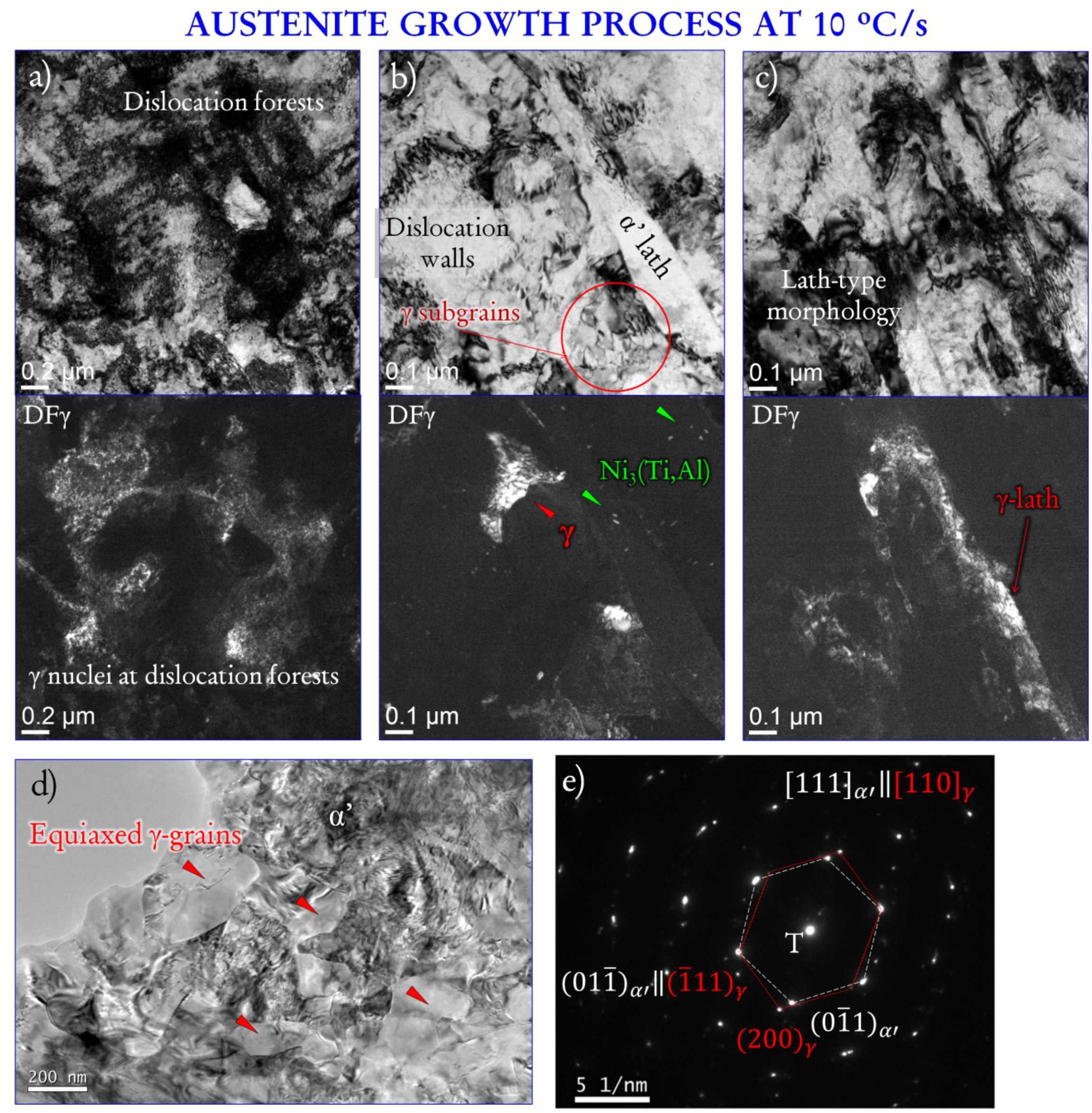

Figure 5.7. TEM images pointing out the austenite growth process in a microstructure at 10 °C/s up to 750 °C (f_γ ~ 0.50). (a) BF and DF of austenite (DFγ) of dislocation-cell-type martensitic matrix where austenite (γ) nucleates at dislocation forests and tangles. (b) BF and DFγ of recovered martensite (α') where dislocations have rearranged in dislocation-cells and austenite nucleates at dislocation-walls. (c) BF and DFγ displaying lath-type austenite with high dislocation content. (d) BF showing austenite growing equiaxed and defect-free inside a deformed martensitic matrix. (f) Double SADP from (d) revealing KS OR between austenite and martensite. All DF images are related to austenite phase. $Ni_3(Ti,Al)$ precipitates are visible in DF presented in (b).

Eventually, after heating up to the A_F temperatures (825, 900 and 950 °C at 0.1, 1 and 10 °C/s, respectively) fully-austenitic microstructures were obtained (Figure 5.8). Based on a statistical evaluation of several TEM images, an austenitic grain size (AGS) distribution is shown in Figure 5.9 for each heating rate. The mean AGS value, expressed as the average and its standard deviation, was estimated in 410 (110) nm, 410 (110) nm and 340 (90) nm for the heating rates of 0.1, 1 °C/s, and 10 °C/s, respectively.

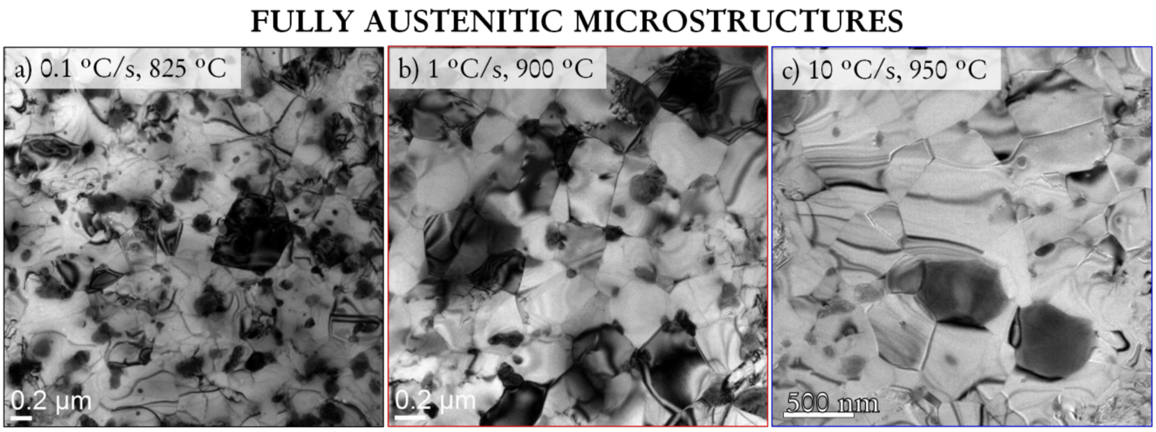

Figure 5.8. BF-TEM images of fully austenitic microstructures obtained after continuous heating up to the finishing transformation temperature (A_F) at studied heating rates: (a) 825 °C at 0.1° C/s; (b) 900 °C at 1 °C/s and (c) 950 °C at 10 °C/s.

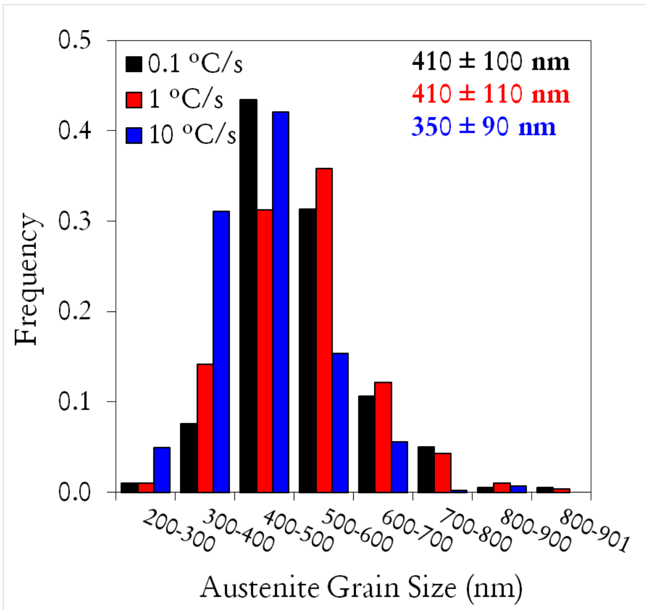

Figure 5.9. Statistics of austenite grain size (AGS) distribution obtained from Figure 5.8 for the studied heating rates. Average grain sizes and their standard deviations are noted in color black, red and blue for 0.1 and 1 °C/s and 10 °C/s, respectively.

As mentioned before, two χ-phase particle size distributions were observed in these microstructures. The estimation of the mean size χ-phase particle and its volume fraction (f_χ) was done from SEM and TEM micrographs as described in *Section 3.2.1*. The χ-phase ($Fe_{36}Cr_{12}Mo_{12}$) is an intermetallic that precipitates in the range of 600-900 °C [49], which nucleates at grain boundaries, but also intra-granularly on dislocations. On the one hand, larger particles (as large as 1 μm) were originated during the solidification process of the steel and, thus, were present in the as-received material. On the other hand, smaller particles have precipitated during the reaustenitization both inter and intra-granularly, and their size and volume fraction depends on the heating rate. A summary of these results is shown in Table 5.1.

Table 5.1. Summary of the volume fraction of χ-phase (f_χ) estimated in the initial state ($f_{\chi\ \mathrm{initial}}$), induced during the heating rate ($f_{\chi\ \mathrm{HR}}$) and total after complete reaustenitization ($f_{\chi\ \mathrm{total}}$). The average particle size ($\bar{d}_\chi$) in included for each case.

Heating rate	0.1 °C/s	1 °C/s	10 °C/s
$f_{\chi\,\mathrm{initial}}$		0.02 ± 0.01	
$\bar{d}_{\chi\,\mathrm{initial}}$ (nm)		400 ± 200	
$f_{\chi\,\mathrm{HR}}$	0.09 ± 0.02	0.05 ± 0.01	0.03 ± 0.01
$\bar{d}_{\chi\,\mathrm{HR}}$ (nm)	150 ± 50	100 ± 40	< 10
$f_{\chi\,\mathrm{total}}$	0.11 ± 0.02	0.07 ± 0.01	0.04 ± 0.01

5.2.4 Microstructural evolution after complete reaustenitization

The evolution with temperature and heating rate of the UFG austenitic microstructures were studied for the slowest and fast heating rates considered in this work: 0.1 and 10 °C/s. The aim is to modify the austenite grain size (AGS) to study its influence in the mechanical behavior (as it will be showed in *Chapter 6*). For this purpose, two temperatures were chosen above A_F, named $T_{\gamma 1}$ and $T_{\gamma 2}$ (details of heat-treatments in *Section 3.5.1*).

Figure 5.10 shows HAADF STEM, BF-TEM and OM micrographs and band contrast (BC) EBSD maps of fully austenitic microstructures obtained after isochronal heating at 0.1 and 10 °C/s up to A_F, $T_{\gamma 1}$ and $T_{\gamma 2}$. In addition, the grain size distribution obtained for each grain size group is included. Grain sizes and volume fractions of χ-phase were estimated as explained in *Section 3.2.1.* Values are expressed in µm as the mean value and the standard deviation in brackets in Table 5.2.

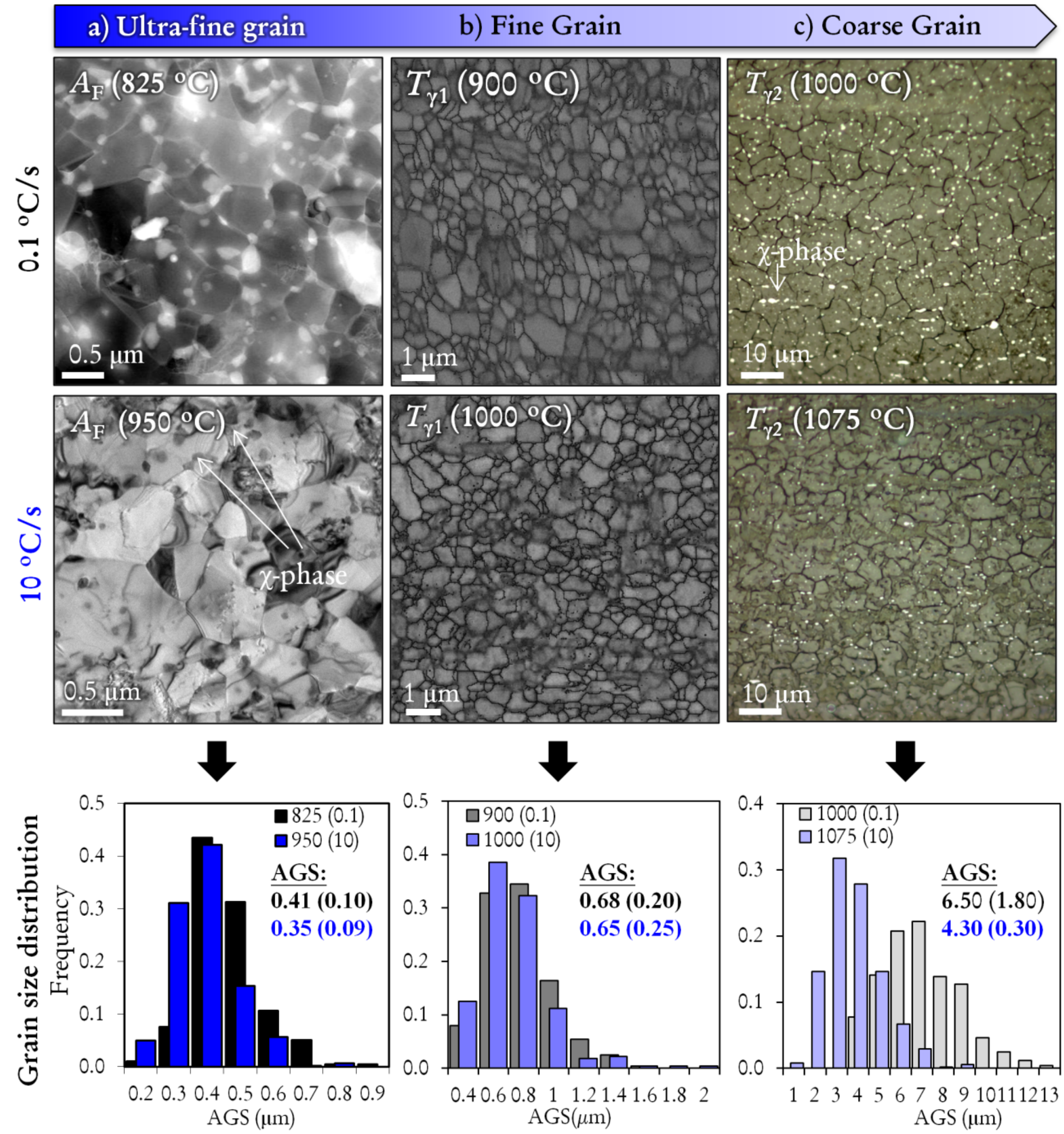

Figure 5.10. Evolution of austenitic microstructures with the temperature during isochronal heating at 0.1 and 10 °C/s. The corresponding austenite grain size (AGS) distribution and the mean grain size values are included for each scale: (a) BF-TEM and HAADF-STEM micrographs of UFG microstructures obtained at the A_F temperature, which have been included for comparison; (b) Optical micrographs of the fine-grained (FG) microstructures obtained at 900 °C and 1000 °C at 0.1 and 10 °C/s, respectively; and (c) Optical micrographs of the CG microstructures obtained at 1000 °C and 1075 °C after heating at 0.1 and 10 °C/s, respectively.

As observed from Figure 5.10, a homogeneous distribution of grains is obtained for all conditions, indicating that normal grain growth does take place. As expected, the AGS increases with the annealing temperature from ultrafine (a) to fine (b) and coarse scales (c). The grain growth is, however, much more important from $T_{\gamma1}$ to $T_{\gamma2}$ than from A_F to $T_{\gamma1}$, which may be related with the different fraction of χ-phase precipitates.

Table 5.2. Summary of the results obtained for austenite grain size (AGS) and volume fraction of χ-phase in microstructures reaustenitized at temperatures above A_F at heating rates of 0.1 and 10 °C/s. Errors in brackets.

	HR= 0.1 °C/s			HR= 10 °C/s		
T (°C)	**825 (A_F)**	**900 ($T_{\gamma1}$)**	**1000 ($T_{\gamma2}$)**	**950 (A_F)**	**1000 ($T_{\gamma1}$)**	**1075 ($T_{\gamma2}$)**
AGS (μm)	0.41 (0.11)	0.68 (0.20)	6.50 (1.80)	0.35 (0.09)	0.65 (0.25)	4.25 (1.30)
f_χ	0.11 (0.01)	0.13 (0.01)	0.06 (0.01)	0.04 (0.01)	0.01 (0.01)	0.02 (0.01)

As the HAADF STEM micrograph of the sample heated at 0.1 °C/s up to 825 °C shows, there is a compositional contrast between the austenitic matrix and the χ-phase, which present a distribution of sizes and, mainly, appears at austenite grain boundaries and triple junctions. In the BF-TEM micrograph of the sample heated at 10 °C/s up to 950 °C, instead, the χ-phase gives a darker contrast than the matrix and its location is either intergranular or intragranular. The fraction of χ-phase is quite important in samples reaustenitized up to A_F and $T_{\gamma1}$ at 0.1 °C/s and an increase from 0.11 (0.02) to 0.13 (0.01) have been detected from one to another. Further heating to $T_{\gamma2}$ leads to a decrease to half, though. On the contrary, for the heating rate of 10 °C/s, the fraction of χ-phase is maximum for the UFG structure and falls to about 0.02 when the material is further heating.

To study the influence of these microstructural changes, AGS and volume fractions of χ-phase, on the thermal stability of these microstructures, magnetization measurements were performed after different holding times at room temperature, varying from 1 to 375 days. The volume fraction of martensite was determined from the magnetization measurements, in the same manner than previously explained by using Eq. [3.3]. In addition, the microstructure was inspected using a LOM. It was found that the less thermally stable microstructure was the one obtained at 1000 °C-0.1 °C/s followed by the 1075 °C-10 °C/s condition, which presented $f_{\alpha'}$ ~0.07 and ~0.04, respectively, after 375 days at room temperature. The rest of the microstructures appeared to be quite stable, since they reached a maximum value of $f_{\alpha'}$ ~0.03 or lower after 100 days.

5.3 Discussion

5.3.1 Influence of alloy composition on the α'→γ transformation.

As observed from Figure 5.2 (a), the α'→γ transformation kinetics is very similar for the three heating rates. It takes place in a rather wide range of temperatures and splits into two consecutive steps. Similar splitting behaviors during the α'→γ transformation have been reported by other authors in maraging and precipitation hardening steels. For instance, Kapoor and Batra [43] observed this behavior during continuous heating of an 18 wt. % Ni maraging steel (M350), of a PH 13-8 Mo steel and of a PH 17-4 steel. Upon heating rates below 0.56 °C/s, the double step in the M350 steel was attributed to a change in the transformation mechanism from long-range diffusion to diffusionless. In the case of PH steels and heating of 5.6 °C/s or lower, both steps were diffusion-controlled and its origin was ascribed to the partitioning of alloying elements, enhanced by a prior precipitation reaction. In Ni and Mn-maraging alloys [134; 135], the splitting of the α'→γ transformation is also explained in terms of partitioning during precipitation, since it leads to Ni (or Mn) rich and depleted regions which will present different A_S temperature. Zones enriched in Ni (or Mn) start to transform at lower temperatures than zones depleted in Ni (or Mn) and, consequently, two stages are obtained. Thus, it is clear that partitioning considerably affects the α'→γ transformation in maraging steels, however, it is not completely clear whether it is sufficient to explain the pronounced splitting behavior found in this work. In the steel under investigation, the fact that the two steps of the transformation are almost identical for all heating rates means that same fraction of martensite transforms into austenite at each one of the steps. As observed from the evolution of the hardness and TEP with temperature in Figure 5.2 (b) and (c), the strongest hardening effect is found at 0.1 °C/s, since there is more time for the diffusion of alloying elements and a larger volume fraction of precipitates forms. In turn, different heating rates result in regions that are depleted or enrich in alloying elements in different extents. Thus, if partitioning was the origin of the splitting, it would be reflected in different extents as a function of the heating rate. This implies that the splitting must be related to something present in the initial microstructure. As explained in *Chapter 4*, significant compositional variations associated to a chemical banding were detected by Electron Probe Microanalysis (EPMA) across the thickness of the as-received steel sheets, especially in Ni, Cu, Ti and Cr: 6.50-11.00 wt. % Ni, 1.25-2.50 wt. % Cu, 1.00-2.00 wt. % Ti and 11.00-13.50 wt. % Cr.

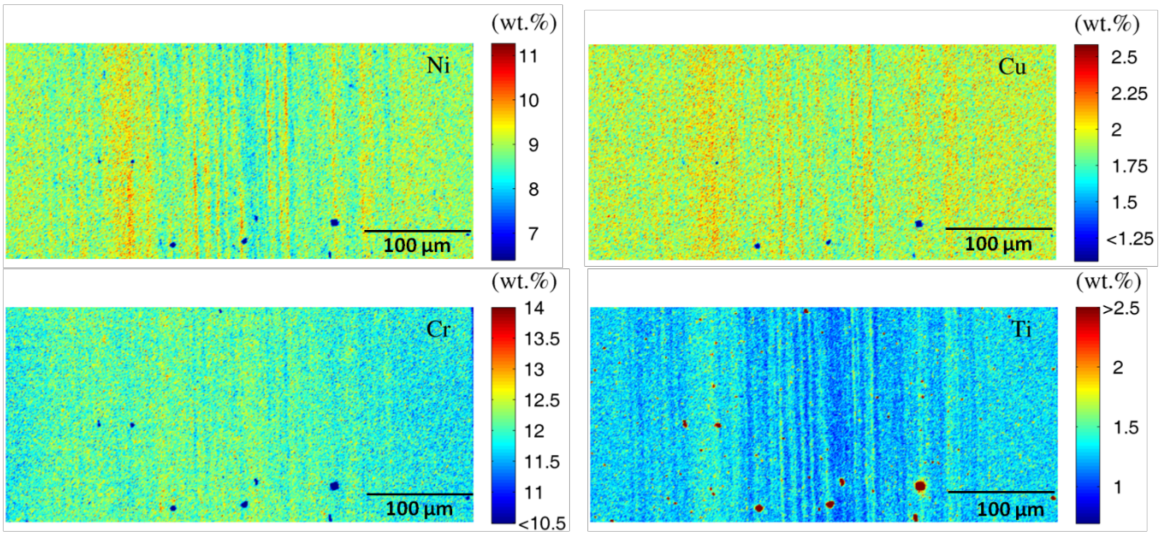

Figure 5.11. EPMA maps of the complete steel sheet cross section after reaustenitization at 0.1 °C/s up to 850 °C. Each scan corresponds to a certain alloying element and gives qualitative and quantitative information about the local concentration of alloying elements.

Figure 5.11, a similar microanalysis by EPMA is presented after fully reaustenitizing at 0.1 °C/s up to 850 °C for those alloying elements that presented a strong segregation behavior. It is observed that the continuous heating at 0.1 °C /s up to temperatures even higher than A_F does not reduce the initial chemical banding, being particularly strong for Ni. These results support that the chemical banding sets the pace of the α'→γ transformation under continuous heating, even at the slowest heating rate. Therefore, regarding the very low bulk diffusion rate of substitutional elements [136] and the low carbon concentration in the steel under investigation, it is reasonable to consider that long-range diffusion processes are not involved in the α'→γ, but a redistribution of substitutional elements through the α'/γ-interface. In other words, the reaustenitization in this steel is an interface-controlled reaction.

It is clear that EPMA gives precise information about the evolution of the chemical banding during heating; however, it is not possible to obtain information about the chemical composition of the phases present in the microstructure. In this sense, EDS microanalyses have provided localized information of the austenite and marteniste phases. The high Ni content detected in elongated γ-islands indicate that they originate from Ni-rich bands on the initial microstructrue. At higher temperatures, a slow heating as 0.1 °C/s enhances the diffusion of elements, especially of Ni, which results in the formation of small areas (few micrometers) with different thermal stabilities, such as α'-islands. However, for the fast heating rate the diffusion of alloying elements is hindered and transformation behavior can only be explained based on features present in the initial state of the material.

Therefore, it is reasonable to conclude that the chemical banding has a dominant effect on the transformation and it is reflected in the same magnitude at all heating rates. Bands enriched in γ-stabilizers, such as Ni and Cu, present low A_S temperature and transform first, which results in approximately the 75-80 % that constitutes the first step of the transformation. Instead, bands depleted in γ-stabilizers present a higher As temperature and, thus, transform later and givie rise to the second step of the tranformation kinetics (20-25 %).

5.3.2 Influence of the heating rate on the α'→γ transformation

As it has been reported by several authors [78; 89-91; 121-123], the dislocation cell-type martensite initial microstructure is a prerequisite for obtaining UFG austenite by reversion. Its higher dislocation density, compared to lath-type martensite, provides a higher number of heterogeneous nucleation sites. In this work it is shown that UFG austenite (350-410 nm) can be obtained by continuous heating at very different heating rates (0.1, 1 or 10 °C/s). It appears that the heating rate does not influence significantly the average final AGS, but the precipitation of χ-phase and η-Ni_3(Ti,Al) phase and the martensite recovery process. It is important to mention that no recrystallization has been observed in the martensitic matrix, just a recovery. According to literature [137], the recovery is a complex process that lowers the stored energy of the material, involving some stages that may overlap. On annealing of polycrystalline materials, excess dislocations of two or more Burgers vectors react to form two-dimensional networks that result in lower energy configurations such as cell-structures. Cell-structures are made of sub-grains, inside which the dislocation density is minimal and whose walls are made of complex dislocation tangles. Graphically illustrates the various stages in the recovery process of a plastically deformed material.

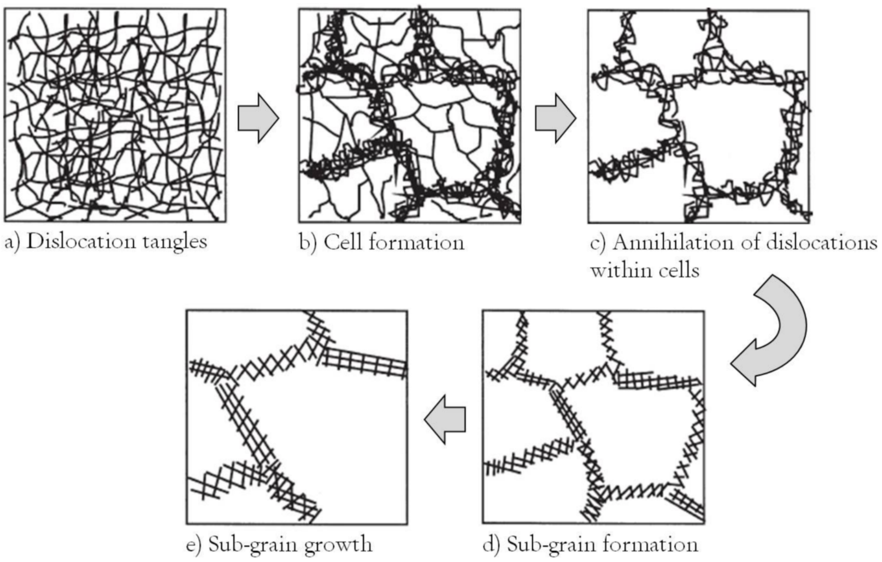

Figure 5.12. Schematic illustrations of the different stages involved in the recovery process of a plastically deformed materiall [137].

Dislocation-walls act as nucleation sites for the austenite phase as previously detected by other authors [121-123]. However, the recovery process is highly influenced by the heating rate, as pointed out in Figure 5.4 by the different contrast of BF images obtained at 0.1 and 10 °C/s at the initial stages of the transformation. The heating at 0.1 °C/s causes a rearrangement of dislocations in defect-free martensite areas and dislocation-walls. Instead, higher temperatures are needed to obtain such cell-structures at 10 °C/s, as Figure 5.7 (b) demonstrates. In the same manner as the recovery, the $\alpha' \rightarrow \gamma$ phase transformation is also affected by the hating rate, as indicates the shift of A_S and A_F shift to higher temperatures when increasing the heating rate, which is characteristic of diffusional transformations [90; 125-128]. Besides, both recovery and transformation processes are influenced by $Ni_3(Ti,Al)$ nanoprecipitates formed during heating, which may act as pinning obstacles for the movement of dislocations and grain boundaries. Although the recovery at 0.1 °C/s is more extensive than at 10 °C/s, it does not remove all the storage deformation of the initial stage and, thus, it does not make a significant difference on the final AGS. Nucleation and growth are competing processes and the extent to which they occur will depend on the heating rate. If it is increased, the nucleation rate is enhanced and the growth competition is decreased, whereas slow heating rates facilitate the growth. This would explain why the average AGS obtained at 10 °C/s is slightly finer than that at 1 or 0.1 °C/s. On the other hand, the effect of $Ni_3(Ti,Al)$ precipitates at α'/γ boundaries can effectively retard their migration and, hinder the austenite grain growth [40; 134]. To summarize, it is the great amount of dislocations present in the microstructure, which continuously provides new nucleation sites for the austenite, together with the pinning effect exerted by the nanoparticles, what leads to a distribution of ultrafine austenite grains, regardless the heating rate. Apart from the shift to higher temperatures of diffusional processes, increasing heating rates also lead to morphological differences during the growth. Whereas at 0.1 °C/s just austenite globular growth was observed, at 1 and 10 °C/s globular and lath-type growth were detected (Figure 5.6 and Figure 5.7). It is worth mentioning that this lathy morphology is scarce compared to the mayor presence of the globular one. In any case, a KS OR between the parent martensite and the new austenite was found.

5.3.3 Mechanism of the α’→γ transformation

There are three evidences that imply a predominant diffusional mechanism: 1) The α’→γ transformation occurs over a rather wide range of temperatures; 2) A_S and A_F shift to higher temperatures when increasing the heating rate; and 3) the final fully austenitic structure consists of equiaxed defect-free austenitic grains [90; 125-128]. Besides, EPMA map from Figure 5.11 demonstrates that long-range diffusional processes do not take place even at the slow heating rate and suggest an interface-controlled transformation, which is in good agreements with what other authors have found for phase transformations with sufficient overheating ($\Delta T = T_{onset} - T_0$, at T_0 the Gibbs energy of the product (γ) and the parent (α’) phases for the same composition are equal) [134; 136].

In order to understand how this transformation occurs, the most important features of the microstructural evolution while heating are described here bellow:

The nucleation site of austenite depends on the initial martensitic morphology, as Figure 5.4 illustrates. On the one hand, austenite nucleates at recovered martensite lath-boundaries, as observed at 0.1 °C/s. On the other hand, austenite nuclei appear randomly at dislocation-walls and tangles of the dislocation-cell-type martensite, observed for 0.1 and 10 °C/s. Regarding the growth, globular-growth predominates at all heating rates, but lath-growth was also detected at 1 and 10 °C/s. At 0.1 °C/s, a globular growth is enhanced irrespective of the nucleation site lath-boundaries or dislocation-walls. At 1 or 10 °C/s, however, the growth mechanism changes as a function of the marteniste morphology: nucleation at cell-structure entail a diffusional globular-growth from the very beginning of the transformation, whereas nucleation at lath-boundaries promotes a diffusionless lath-growth, as detected at intermediate stages of the transformation (Figure 5.6 and Figure 5.7). A summary of these observations is presented in Table 5.3.

Table 5.3. Summary of the transformation mechanisms detected during the reaustenitization as a function of the heating rate and the morphology of the starting martensitic microstructure.

Heating rate	Nucleation sites	Transformation mechanism
0.1 °C/s	α'-lath boundaries	Diffusional
	Dislocation walls	Diffusional
1 °C/s	Dislocation-cell-α'	Diffusional
	Lath-type α'	Diffusionless
10 °C/s	Dislocation-cell-α'	Diffusional
	Lath-type α'	Diffusionless

The results are in good agreement with other works [90; 91; 123]. Particularly, it was Takaki *et al.* [91] who studied the effect of pre-cold working on isothermally reversed austenite in an Fe-18.08%Cr-8.65%Ni alloy and found that the lath-type martensite led to austenite laths and blocks, whereas the dislocation-cell-type gave rise to small equiaxed austenite grains bounded by large angle boundaries due through the recovery of dislocation-cells. The lath-austenite morphology and its high dislocation content suggest that it has been formed through a diffusionless mechanism, similar to the shear martensitic transformation. However, its high dislocation density promotes a recovery process with further heating, similarly to that undergone by the parent martensite. This recovery causes a sub-grain structure inside the laths that, eventually, coalesce and leads to a completely recrystallized UFG austenite microstructure, as observed by other authors [79; 120; 123; 128]. The scarce presence of lath-martensite, in the as-received microstructure, and lath-austenite, in partially reaustenitized microstructure, leads to consider that lath-austenite arises from lath-martensite via a diffusionless mechanism at 1 and 10 °C/s. On the contrary, dislocation-cell-type martensite, rapidly leads to globular and defect-free austenite grains through a diffusional mechanism, in a similar fashion as Shakhova *et al.*[79] detected in S304H steel.

The degree of metastability and the alloy composition play a determining role on the diffusional or diffusionless nature of the α'→γ transformation. Tomimura and co-authors [89; 90] have earlier discussed the reaustenitization mechanism in metastable 16Cr-10Ni and 18Cr-9Ni steels. They explained that an increase in Ni/Cr ratio causes an increase in the Gibbs free energy change between BCC (α') and FCC (γ) structures ($\Delta G^{\alpha\rightarrow\gamma}$), which results in a decrease of the shear reversion temperature. In their work, the critical driving force for complete shear reversion was estimated in −500 J/mol. The following equation was derived using the thermodynamic data reported by Kaufman *et al.* [138] for the ternary Fe-Cr-Ni system. It has been used as criteria in other works [76; 84; 126]:

$$\begin{aligned}\Delta G^{\alpha\rightarrow\gamma}(J/mol) = {} & 10^{-2}\Delta G_{Fe}^{\alpha\rightarrow\gamma}(100 - Cr - Ni) - 97.5Cr + 2.02Cr^2 - 108.8Ni \\ & + 0.52Ni^2 - 0.05CrNi + 10^{-3}T(73.3Cr - 0.67Cr^2 + 50.2Ni \\ & - 0.84Ni^2 - 1.51CrNi)\end{aligned} \quad [5.1]$$

Where $\Delta G^{\alpha\rightarrow\gamma}$ is the free energy difference in pure iron, T is temperature in Kelvin and Ni and Cr represent the chemical composition of each element (mass %). Somani *et al.* [120] extended the criteria to include the effects of other alloying elements with strong influence on the microstructure. It was considered appropriate to use Ni_{eq} or Cr_{eq} instead of just Ni and Cr in equation [5.1:

$$Ni_{eq} = Ni + 0.6Mn + 20C + 4N - 0.4Si \quad [5.2]$$

$$Cr_{eq} = Cr + 4.5Mo \quad [5.3]$$

Values of $Ni_{eq}=12.28$ and $Cr_{eq}=30.22$ have been obtained for the steel under investigation. Substituting these values in equation [[5.1] it is obtained that the diffusionless transformation can occur above an estimated temperature of 1004 K (731 °C), provided that the steel is quickly heated. Although the influence of other alloying elements present in the composition of this steel is not taken into account in the equations, the result is in good agreement with the experimental observations, which detected diffusionless transformation after heating to 725 °C and 750 °C at 1 and 10 °C/s, respectively.

Summarizing, it is concluded that the nature of the transformation depends on: 1) the initial martensite morphology, which affects the number of nucleation sites for the austenite; 2) the heating rate and 3) the composition, since the higher the Ni/Cr ratio, the higher the $\Delta G^{\alpha \to \gamma}$ is. This decreases the shear reversion temperature, enhancing a shear transformation provided that the material is sufficiently fast heated.

5.3.4 Validation of experimental techniques for the characterization of the α'→γ transformation

In view of the experimental limitations, different experimental techniques were combined to obtain accurate information about the α'→γ transformation. As shown in *Section 5.2.1*, magnetization, micro-hardness Vickers and TEP measurements were performed. Although magnetization measurements are the most accurate and sensitive technique for this purpose, it is a technique that is not always available and whose measurements are time-consuming. In view of results presented in Figure 5.2, it appears that micro-hardness and TEP measurements are also sensitive to the α'→γ transformation, although the micro-hardness evolution is not able to differentiate clearly the two-step transformation behavior. It is interesting, though, to compare magnetization results with the ones obtained with these other techniques, which are more affordable and easy-to–use. Assuming that the A_S and A_F temperatures have been reliably determined by magnetization measurements, the evolution of the TEP and hardness within this range of temperatures can be converted to the transformed volume fraction of austenite (f_γ) using the following expression:

$$f_\gamma = \frac{X - X_i}{X_f - X_i} \qquad [5.4]$$

where X_i and X_f represent the values of Hv or TEP at the A_S and A_F temperatures, respectively, and X is the value of the Hv or TEP at each measured temperature within this range. The results obtained for each of the heating rates are displayed in Figure 5.13. The Hv or TEP measurements give reasonable estimations of f_γ when compared with magnetizations results at the slow rate of 0.1 °C/s. The match is particularly good for TEP measurements at 0.1 and 1 °C/s. This technique even reveals the two-steps transformation behavior. However, as the heating rate increases the data points scatter. This is not surprising since both Hv and TEP are techniques sensitive to the deformation in the microstructure and the presence of precipitates, which are influenced by the heating rate.

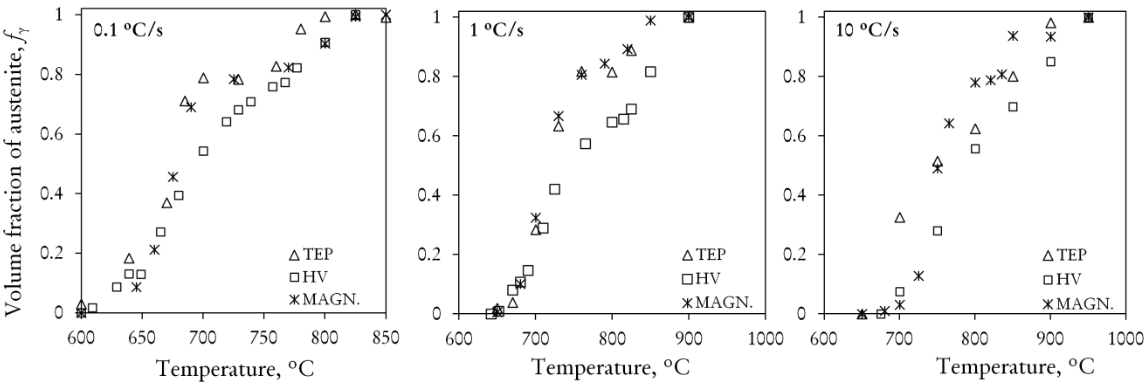

Figure 5.13. Comparison of the temperature evolution of the austenite volume fraction estimated using three different experimental techniques: thermoelectric power (TEP), hardness Vickers (HV) and magnetization measurements (MAGN.)

To summary, although magnetization measurements appear as the most accurate and reliable technique to follow-up the evolution of f_γ with the temperature in this type of steels, it is possible to use other experimental techniques as Hv and TEP to gain insight about the reaustenitization process upon slow continuous heating.

5.3.5 Austenite grain growth and effect on the thermal stability

The driving force for grain growth results from the decrease in the free energy of the system. The grain boundary area is the main source of energy for grain growth process; therefore, the system will evolve to reduce its grain boundary area [139]. Larger grains will grow at the expense of smaller ones. Austenite grain growth is theoretically explained taking as a basis the model proposed by Zener [140], which has been adapted for non-equilibrium kinetics, taking into account the alteration of microalloyed and interstitial elements in austenite solid solution due to isothermal and/or continuous heating. Microalloying elements like V, Nb and Ti are employed to produce fine precipitation in the matrix. The austenite grain boundaries and dislocations are pinned by these precipitates, inhibiting their movement during the thermal and thermo-mechanical processing of steels. This pinning force is governed by the thermodynamic stability of second-phase precipitates in austenite [141] and their effect of the grain growth has been investigated in numerous works, especially in microalloyed steels [142-145].

The influence of the heating rate on the AGS has also been pointed out in previous works [142; 146-149]. In plain carbon steels, it has been suggested that the final AGS depends on the heating rate through the transformation region and on the annealing temperature (via the competition between nucleation and growth) with further annealing [147]. In microalloyed steels containing Ti and V [149], specific austenitization conditions of temperature and heating rate have been found to produce bimodal grain size distributions as a result of austenite abnormal grain growth. San Martín *et al.* [142] observed that the austenite grain coarsening in a microalloyed steels containing Nb occurs in two stages due to the existence of niobium carbonitrides. They found out that as the heating rate increases, the grain size at that temperature decreases.

In the steel under investigation a similar behavior is observed, since the grain growth is much more pronounced between A_F and $T_{\gamma 1}$ than from $T_{\gamma 1}$ and $T_{\gamma 2}$ for both heating rates, as observed from Figure 5.14. The austenite grain growth appears to boost at 0.1 °C/s for annealing temperatures higher than 900 °C, which is explained by the dissolution of χ-phase particles (Table 5.2) that reduces pinning forces at higher temperatures and, thereby, promotes grain growth. In the case of the fast heating rate the grain growth is also boosted above $T_{\gamma 1}$ but the AGS at $T_{\gamma 2}$ is smaller than at 0.1 °C/s, even though a higher annealing temperature is reached and pinning effect of the χ-phase particles is much lower. Therefore, it appears that at slow rates the pinning effect of the χ-phase precipitates controls the grain growth until they are dissolved, whereas in a rapid heating at 10 °C/s the annealing temperature plays the important role.

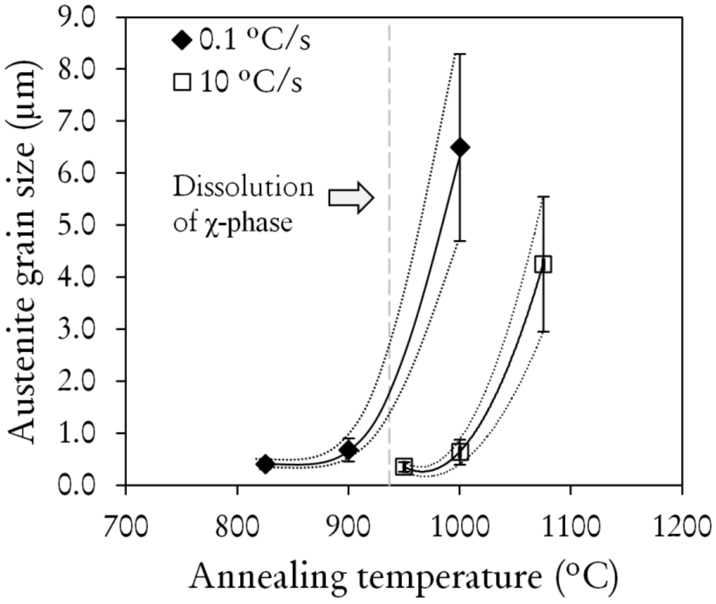

Figure 5.14. Evolution of the heating rate and annealing temperature on the mean austenite grain size.

Regarding the stability of the austenite phase, the time-dependent formation of martensite at a constant temperature has been subsequently investigated in Fe-Ni-Cr and Fe-Ni-Mn alloys and maraging alloys [20; 31; 150-153]. The isothermal transformation of austenite into martensite phase is associated with an experimental C-curve kinetics with a maximum transformation rate at the so-called nose temperature. Whereas athermal martensitic transformation is not expected for this steel, even after quenching down to -196 °C (4 K); the nose temperature at which the isothermal transformation is faster was detected in -40 °C by Holmquist *et al.* [31]. In their work they found that the nose temperature was about -40 °C and that the martensitic transformation rate increased rapidly with the grain size. Moreover, recent investigations by San Martin *et al.* [20; 21] have pointed out that it is possible to accelerate the isothermal transformation by applying external magnetic fields.

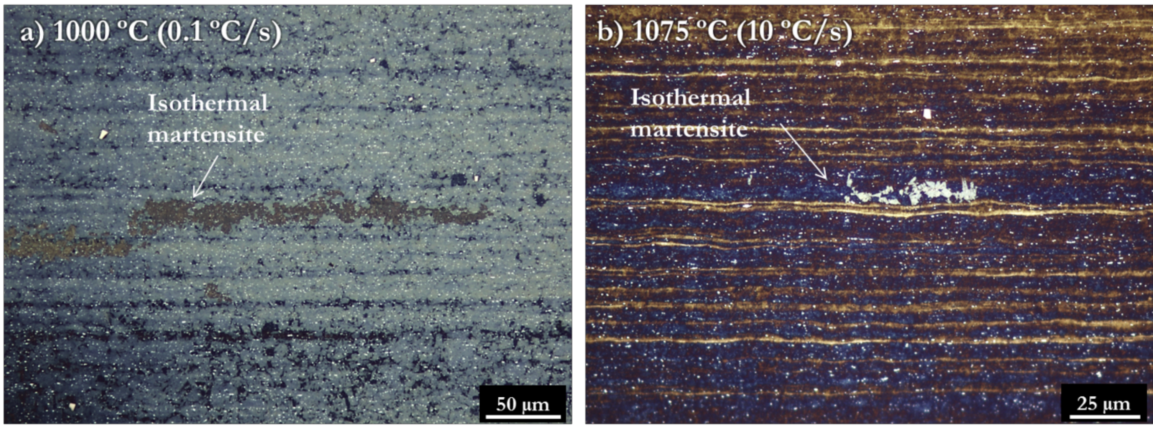

Figure 5.15. Optical micrographs showing the presence of isothermal martensite formed after two weeks in fully austenitic microstructures obtained by continuous heating at: (a) 0.1 °C/s up to 1000 °C and (b) 10 °C/a up to 1075 °C.

Figure 5.15 (a)-(b) displays two optical micrographs of the less stable conditions according to the results presented in *Section 0* (1000 °C-0.1 °C/s and 1075 °C-10 °C/s respectively). The microstructure was revealed after holding the samples for two weeks at room temperature. In order to disclose the isothermal martensite formed over this time, an aging heat-treatment consisting 30 min of at 500 °C was applied. Such a heat-treatment does not induce changes in the overall microstructure but causes the precipitation of nano-intermetallic particles in the martensite phase, making easier to distinguish it from the austenite by etching with the hot L-B etching solution. As usual, the color of the etching is very sensitive to the temperature ant time of etching. In this case, the time varied from 20 to 35 s. It is observed from the micrographs that some isothermal martensite has formed preferentially along some bands, presumably rich in Cr. This is not surprising since, as a consequence of the chemical banding, it is expected that the austenite has different thermal stabilities across the steel-sheet cross section. In addition, studies and thermodynamic calculations point out that up to a 20 % of isothermal martensite can be expected to be formed at room temperature for AGS around 5-10 µm [154]. As detected from the magnetization measurements over the time, the austenitic microstructure with the largest grain (1000 °C-0.1 °C/s) size turned up to be the less stable ($f_{\alpha'}$ ~0.07 after 357 days), followed by the microstructure with second largest grain size (1075 °C-10 °C/s and $f_{\alpha'}$ ~ 0.04). Instead, microstructures with sub-micron grain sizes appeared to be more stable, which is in good agreement with the literature [90].

5.4 Conclusions

- The evolution of the cold-rolled microstructure present in the as-received state of the steel investigation has been studied under continuous heating at different rates (0.1, 1 and 10 °C/s). The combination of magnetization and micro-hardness Vickers measurements showed a shift to higher temperatures in the critical transformation temperatures and a two-steps $\alpha'\rightarrow\gamma$ transformation due to the chemical banding and, thus, to martensitic regions with different thermal stability.
- The isochronal heating up to the finishing transformation temperature leads to ultrafine-grained austenite in the range 350 – 410 nm, regardless the heating rate. The volume fraction of χ-phase is, nevertheless, considerably high (~ 0.10) in the microstructure obtained at 0.1 °C/s and may result in a decrease of the corrosion resistance.
- Regarding the $\alpha'\rightarrow\gamma$ transformation, the following conclusions are obtained from TEM observations: for a certain chemical composition, the transformation may proceed with or without diffusion depending on the heating rate and the martensite morphology. During the heating at 0.1 °C/s, austenite nucleates both at martensite lath-boundaries and dislocation tangles and grows globularly. The finely dispersed $Ni_3(Ti,Al)$ precipitates pin the migration of the α'/γ interfaces, hindering the austenite grain-growth and leading to ultrafine and equiaxed defect-free austenite phase. During the heating at 1 or 10 °C/s, the dislocation-cell-type martensite leads to globular and defect-free austenite grains via a diffusional mechanism, whereas the lath-type results

in highly dislocated lathy austenite through a diffusionless mechanism. However, this latter mechanism is negligible due to the low fraction of lath-type martensite present in the initial microstructure. Besides, further heating enhances recovery processes inside the austenite laths, being replaced by ultrafine and equiaxed defect-free austenite.

- From the previous observations it can be concluded that the α'→γ transformation presents the following characteristics independent the heating rate: (i) it is a interface-controlled reaction, (ii) it occurs in a wide range of temperatures, and (iii) via a two-step process due to the chemical banding present in the initial microstructure; this banding influences the thermal stability of the martensite phase.

Chapter 6

Mechanical behavior of reaustenitized microstructures

C. Celada-Casero, J. Chao, D. San Martín. *Mechanical stability and properties of dual (α'/γ) and fully γ microstructures obtained by controlled isochronal heating*, Mater. Sci. Eng. A (in preparation).

The goal of this chapter is the study of the mechanical behavior of different microstructures obtained by controlled isochronal heating with the purpose of establishing a linkage annealing route – microstructure - mechanical properties. The mechanical characterization has been performed by tensile testing at room temperature on ultrafine-grained dual (α'/γ) microstructures as well as on fully austenitic microstructures with different grain sizes (from the ultrafine to the coarse scale). Additionally, the mechanical stability of the austenite phase has been studied by measuring the magnetization of tensile specimens after fractured and interrupted at certain strain level. It has been found that the mechanical response of mixed (α'/γ) microstructures depends on the austenite volume fraction, its mechanical stability and the presence of $Ni_3(Ti,Al)$ precipitates. These dual (α'/γ) microstructures exhibit strengths of 2.10 - 1.21 GPa and elongations of 3 -25 %. In fully γ-microstructures the strength can drop to 0.87 GPa and the elongation increase to 44 % depending on the grain size, which has been observed to vary from 0.40 to 6.50 µm. The TRIP effect (formation of strain-induced martensite during tensile testing) has been found to produce an increment in the strain-hardening rate of dual and fully austenitic microstructures, leading to a simultaneous increase of ductility and strength.

6.1 Introduction

Austenitic stainless steels meet requirements such as high corrosion and oxidation resistance, relatively high strength and excellent ductility that make them attractive for a number of industries. It is clear from the literature that the “severe plastic deformation and subsequent annealing” leads to NG/UFG microstructures that are very interesting from the point of view of mechanical properties [82-91]. Previous researches have demonstrated that nano-crystalline materials show much higher strength than their coarse-grained counterparts, as expected from the well-known Hall-Petch relationship [77-81]. Although the strength is significantly enhanced by grain refinement, the elongation of the most nano-crystalline materials is greatly decreased due to little work hardening ability [155]. To overcome the restricted ductility of UFG materials some strategies have been proposed, such as the fabrication of a bimodal grain size distribution [156]. The bimodal distribution allows significant strain-hardening since the preferential accommodation takes place in large grains. In fact, most of NG/UFG metals showing some strain hardening and respectable ductility consist of a distribution of grain sizes, even though the number fraction of the larger grains may be low. However, if larger uniform elongations are required, then the strain-hardening ability is needed as a stabilizing mechanism [157]. The outstanding mechanical properties of NG/UFG ASSs stem from the instability of the austenite phase, which can easily transform into strain-induced martensite (SIM) during plastic deformation due to the Transformation-Induced Plasticity (TRIP) effect. The remarkable properties of ductility and toughness of TRIP steels results from the plastic strain accompanying martensitic transformation and the internal stress field emerging from this phase change leading to an additional plastic flow known as TRIP effect.

It is well established that the mechanical stability of austenite is strongly dependent on the chemical composition of the alloy, the temperature and the strain rate. In this respect, numerous works are found in metastable ASSs [81; 157-165]. The stacking fault energy (SFE), which is also strongly dependent on the chemical composition and the temperature, plays a crucial role in the austenite stability, since it controls the formation of shear bands and thus the formation of nucleation sites for the martensite [163; 166-168]. Due to a high SFE and numerous slip systems, the plastic deformation of the ferrite phase (BCC) is mainly dominated by dislocation glide [169]. However, plastic deformation of austenite (FCC) is rather complex. In the literature, the dependence of the active deformation mechanism in high-alloyed ASSs appears strongly correlated to the chemical composition through different expressions for the SFE. Some of the most common equations have been used to calculate the SFE of the steel under consideration, as Table 6.1 shows.

Table 6.1. Comparison of SFE values calculated with compositional equations presented in the literature.

Reference	Equation for SFE	SFE (mJ/m^{-2})
Schramm and Reed [166]	$\gamma = -53 + 6.2\%Ni + 0.7\%Cr + 3.2\%Mn + 9.3\%Mo$	49.24
Rhodes and Thompson [167]	$\gamma = 1.2 + 1.4\%Ni + 0.6\%Cr + 17.7\%Mn - 44.7\%Si$	10.60
Brofman and Ansell [170]	$\gamma = 16.7 + 2.1\%Ni - 0.9\%Cr + 26\%C$	24.83

It is clear that the results vary significantly from one to another. However, in this manner many authors have related the deformation mechanism to the SFE [163; 171]. For instance, Frommeyer *et al.* [171] concluded that SFE < 16 mJ/m^2 favors the transformation induced plasticity (TRIP), while SFE > 25 mJ/m^2 and 60 mJ/m^2 lead to twinning induced plasticity (TWIP) and deformation mediated by dislocation slip, respectively. Additionally, it is reported that SFE of about 20 mJ/m^2 promote a direct $\gamma_{FCC} \rightarrow \alpha'_{BCC}$ transformation, while lower SFE leads to a TRIP effect via $\gamma_{FCC} \rightarrow \varepsilon_{HCP} \rightarrow \alpha'_{BCC}$ transformation [24; 158; 159; 162; 164], where the ε-martensite is a transition phase that is formed at the shear bands intersections and acts as nucleation site of the α'-martensite. On the other hand, recent studies have shown that both transformation routes (γ→ε→α' or γ→α') are possible for the same stainless steel [172; 173]. Byun *et al.* [174] hold that not only the SFE, but also the applied stress play a crucial role on the deformation mechanism in ASSs [174]. Indeed, a variety of deformation microstructures can be developed in low SFE material, such as ASSs, as a result of local variations of the effective shear stress acting on dislocations. These variations might be induced by any stress concentrator such as dislocations pile-ups, irregular grain boundaries, precipitates, etc. Mishra *et al.* [175] also observed that martensitic transformation may occur during deformation in parallel with twinning. These variations in the deformation mechanism are translated into different mechanical properties. For instance, high-manganese TRIP steels (Fe-15Mn-3Al-3Si at. %) exhibits a pronounced strain-hardening behavior with tensile strength of ~1100 MPa and improved elongations of 55 %, whereas a TWIP steel (Fe-20Mn-3Al-3Si at. %) shows relatively low flow stress (~280 MPa) and moderate tensile strength (650 MPa) but extremely high elongations (95 %). This extremely high elongation to failure and the specific energy absorption is more than twice that of the conventional high strength deep-drawing steels [171].

It is important to bear in mind that, besides the SFE, the temperature, the strain rate or the applied stress, the grain size strongly influences the austenite stability. It is generally accepted that the smaller the AGS, the more stable the austenitic structure is. Kisko *et al.* [161] showed, for an ASSs type 204Cu (15Cr-9Mn-Ni-Cu, wt. %), that the rate of the formation of SIM in tensile straining decreases on refining the grain size from 18 to 1.5 µm. Y-S. Jung *et al.* [160] studied the effect of grain size on the M_d temperature (temperature above which the austenite is stable, even when plastic strain is applied) in an UFG metastable ASS (Fe-0.01C-8.05Ni-9.85Cr-7.80Mn, wt. %) and observed that M_d was linearly lowered with a decrease in the AGS from 12 to 0.25 µm. This result was attributed to an increase in the austenite stability brought about by the grain refinement.

6.2 Results

6.2.1 Mechanical behavior of ultrafine-grained dual (α'/γ) and austenitic microstructures

Figure 6.1 shows the engineering stress-plastic strain $(\sigma - \varepsilon)$ curves of microstructures obtained after partial (heating between A_S and A_F) and complete reaustentitization (to A_F) under continuous heating at 0.1, 1 and 10 °C/s. Two tensile tests were conducted per heat-treatment condition to study the reproducibility. It is observed that the strength decreases and the elongation increases as the annealing temperature increases. The strength-ductility balance depends mainly on the martensite/austenite volume fractions and on the state of precipitation of the martensite.

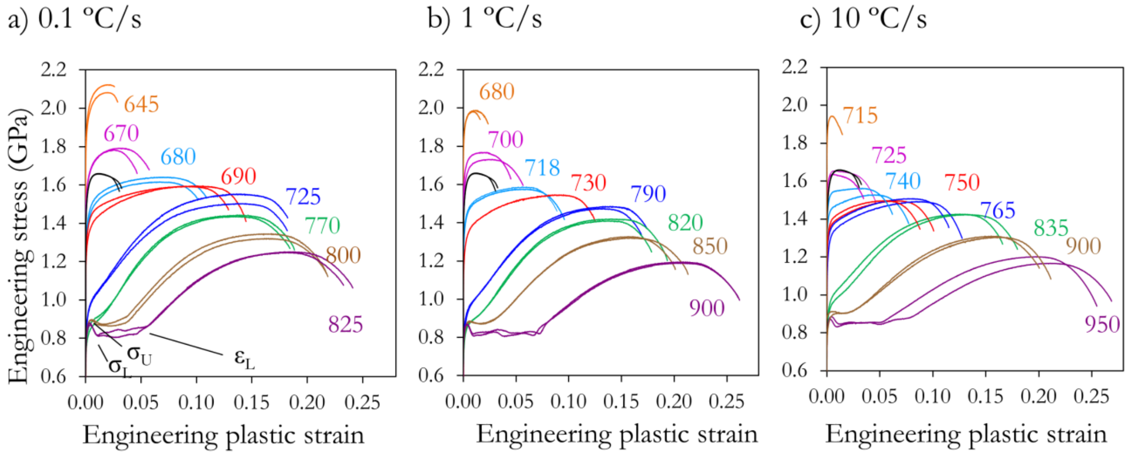

Figure 6.1. Engineering stress-plastic strain curves of partially and fully microstructures reaustenitized at (a) 0.1 °C/s; (b) 1 °C/s and (c) 10 °C/s to temperatures ranging A_S -A_F. The curve obtained for the CR state (black) has been included for comparison.

The overall trend is very similar for all heating rates. For comparison, the stress-strain curve of the initial microstructure has been also included (black curve). The as-received material presents a very high ultimate tensile strength (σ_{UTS}) of 1.66 (0.01) GPa, but its elongation is only 0.03 (0.01). It is noticed that there is a significant increment in the strength in those samples annealed slightly above A_S, exhibiting the highest σ_{UTS} values: 2.10 (0.03), 2.00 (0.01) and 1.95 (0.25) GPa after heating at 0.1, 1 and 10 °C/s, respectively. As expected, the maximum strengthening response is experienced at 0.1 °C/s since the lower the heating rate, the greater the formation of $Ni_3(Ti,Al)$ precipitates is. As the material is heated up, the volume fraction of austenite (soft phase) increases and that of martensite (hard phase) decreases, leading to a softening. The coarsening and dissolution of $Ni_3(Ti,Al)$ precipitates in the austenite, as presented in the previous chapter, also contributes to a significant decrease in the yield strength ($\sigma_{y0.2}$). This is clearly observed in the curves obtained at 750 °C-0.1 °C/s, 790 °C-1 °C/s and 765 °C-10 °C/s, whose $\sigma_{y0.2}$ is almost the half than that obtained at the previous temperature.

It has to be highlighted that partially re-transformed microstructures with a high austenite volume fraction ($f_\gamma \sim 0.8 - 0.9$) or fully austenitic microstructures present a very low strain-hardening (almost a plateau after yielding) for small plastic strains ($< 0.06 - 0.08$), which is attributed to the Lüders band formation. The deformation occurring at this stage is heterogeneous and is characterized by the appearance of discrete localized and visible bands of plastic deformation at approximately 45° to the tensile axis, being hence undesirable in metalworking operations. This effect is more pronounced in fully austenitic microstructures (curves at 825, 900 and 950 °C). These curves exhibit a sudden drop of strength just after the yield point, resulting in the formation of an upper (σ_U) and lower (σ_L) yield stress. Then, the deformation proceeds at a constant σ_L stress level, giving rise to a plateau called yield-point elongation, after which an inflection point in the stress-strain curve sets the onset of homogeneous deformation of the tensile sample and the strain-hardening. Once the strain-hardening is not able to counteract the reduction of cross-sectional area in the specimen, necking develops and leads to fracture. UFG austenite microstructures exhibit the largest total elongation ($\varepsilon_t \sim 0.26$ (0.03)) for σ_{UTS} values of 1.25 (0.01), 1.19 (0.01) and 1.18 (0.02) GPa after heating at 0.1, 1 and 10 °C/s, respectively.

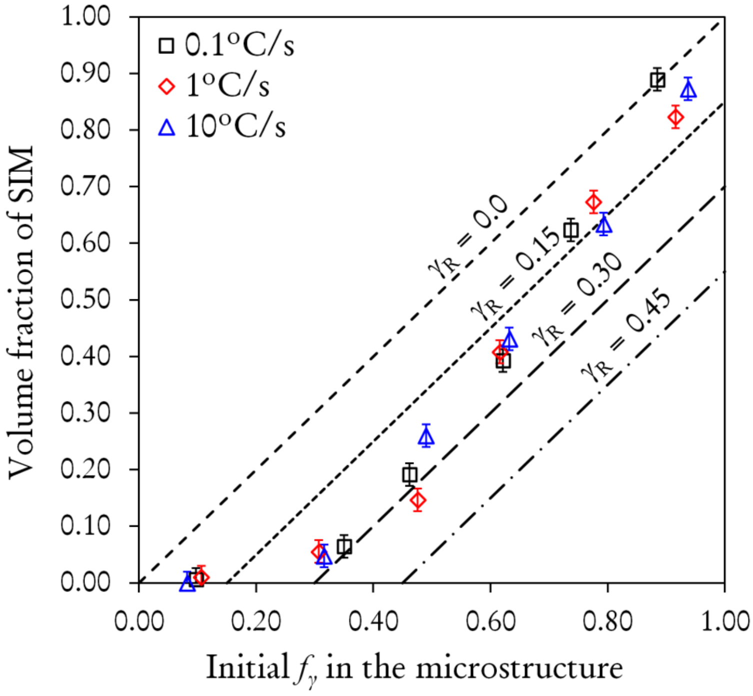

Figure 6.2. Volume fraction of strain-induced martensite (SIM) after fracture versus initial volume fraction of austenite (f_γ) present in microstructures after heating at 0.1, 1 and 10 °C/s. Dotted and dashed lines represent fixed volume fractions of retained austenite (γ_R) in the microstructure after testing.

In order to disclose the role of TRIP effect on the mechanical behavior of these microstructures, magnetization measurements were performed on the complete gage length of some tensile tests specimens after fracture. These measurements provided information about the formation of SIM and, thus, about the mechanical stability of the austenite as a function of the annealing heat-treatment. The results are displayed in Figure 6.2 in terms of the volume fraction of strain-induced martensite (SIM) versus the austenite volume fraction (f_γ) present in the initial microstructure before tensile testing. Dashed and dotted lines at fixed volume fractions of retained austenite (γ_R) were outlined as a guide to the eye. The overall trend between heating rates is quite similar. Microstructures containing f_γ ~0.10 do not present TRIP effect, since the volume fraction of austenite after tensile testing remains the same; no SIM has been formed. This fraction of austenite is the most stable. Microstructures with $f_\gamma > 0.10$ do exhibit TRIP effect. The larger the initial volume fraction of austenite, the less stable the austenite is (observed for the three heating rates). A $\gamma_R < 0.15$ is observed after tensile testing for those samples obtained after heating at 1 and 10 °C/s to A_F (initial f_γ~0.90), whereas γ_R =0 for that obtained after heating at 0.1 °C/s. Therefore, the UFG austenitic microstructure obtained at the heating rate of 0.1 °C/s appears to be the less stable.

6.2.2 Mechanical behavior of fully austenitic microstructures with UFG-CG sizes

Figure 6.3 (a) and (b) shows the $\sigma - \varepsilon$ curves of fully austenitic microstructures obtained isochronally at 0.1 and 10 °C/s to different annealing temperatures: A_F, $T_{\gamma 1}$ and $T_{\gamma 2}$, being $T_{\gamma 1}$ and $T_{\gamma 2}$ the same temperatures above A_F studied in *Chapter 5*, for which the AGS and volume fraction of the second phase (χ-phase) was determined. As a consequence of the austenite grain growth, the increase in the annealing temperature results in a decrease of $\sigma_{y0.2}$ and σ_{UTS} accompanied by an increase of ε_{un} and ε_t. A summary of these parameters is presented in Table 6.2 in terms of mean values and their standard deviations.

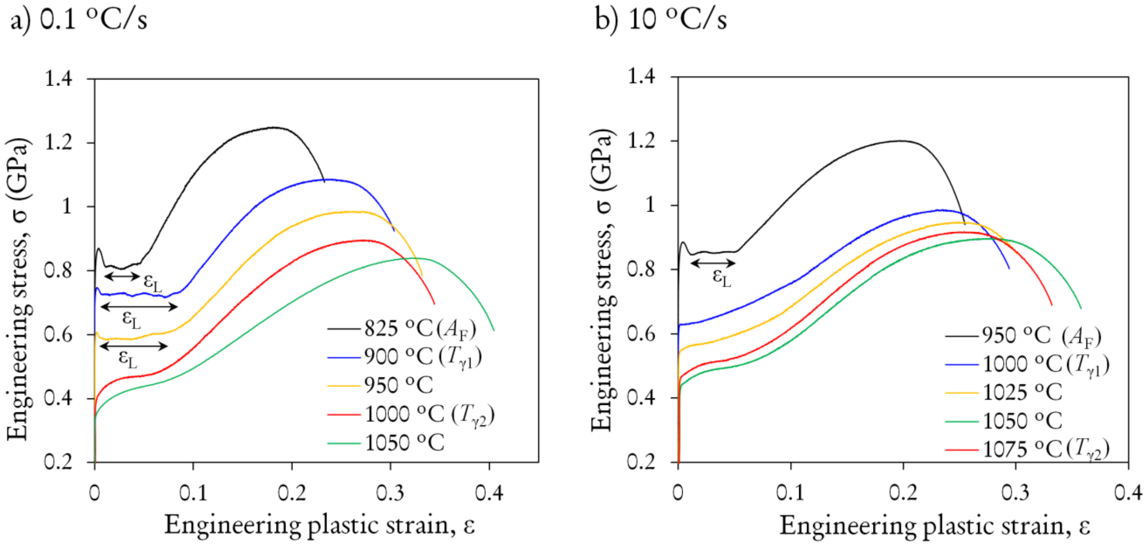

Figure 6.3. Engineering stress – plastic strain curves of fully austenitic microstructures obtained upon isochronal heating at 0.1 °C/s (a) and 10 °C/s (b) to A_F and higher temperatures.

As observed from Figure 6.3, all curves are characterized by an inflection point that gives rise to an increase of the strain-hardening rate. This kind of "S-shape" curve is characteristic of steels exhibiting TRIP effect. The increase in the strain-hardening rate originates from: 1) the transformation of the metastable austenite into martensite during plastic deformation, and 2) the hardening of the martensite phase. It is important to highlight some features of the curves and their evolution with the grain size. On the one hand, UFG microstructures (heated to A_F) show the greater yield-drop (σ_U-σ_L increment). In the case of samples heated at 0.1 °C/s the yield-drop becomes smaller and smaller as the AGS increases until it disappears, while for samples heated at 10 °C/s it is observed at none of the others annealing temperatures. On the other hand, apart from samples treated to A_F, a wavy Lüders bands plateau (ε_L) is also observed for microstructures obtained at 0.1 °C/s to 900 and 950 °C, being the 900 °C-curve the one with the largest ε_L. In samples annealed at 0.1 °C/s to 1000 and 1050 °C, the Lüders band plateau is not so clearly observed. Instead, these curves exhibit continuous yielding and an ideal "S-shape" curve. This is also the case for samples heated at 10 °C/s to 1025, 1050 and 1075 °C. The microstructure obtained rapidly at 10 °C/s to 1000 °C shows a sharp change at the yield-point inflexion, leading to a short and flat plateau and a progressive transition to the uniform elongation regime.

Table 6.2. Tensile properties of fully austenitic microstructures with different grain sizes obtained after heating at 0.1 and 10 °C/s. The standard deviation of strength and elongation values is not larger than 0.045 GPa and 0.01, respectively.

HR (°C/s)	T_γ (°C)	AGS (μm)	$\sigma_{y0.2}$ (GPa)	σ_{UTS} (GPa)	ε_{un}	ε_t
0.1	**825**	0.44 (0.11)	0.858	1.250	0.19	0.24
	900	0.68 (0.20)	0.761	1.099	0.23	0.30
	950	—	0.611	0.992	0.25	0.33
	1000	6.48 (1.87)	0.395	0.896	0.27	0.35
	1050	—	0.385	0.861	0.31	0.40
10	**950**	0.35 (0.09)	0.867	1.185	0.20	0.26
	1000	0.65 (0.25)	0.620	0.984	0.24	0.30
	1025	—	0.510	0.943	0.24	0.31
	1050	—	0.447	0.912	0.26	0.34
	1075	4.25 (1.30)	0.420	0.885	0.28	0.36

To quantify the contribution of the TRIP effect (amount of martensite transformed) to the mechanical behavior and its dependence with the AGS, selected annealing conditions were chosen in order to compare the mechanical behavior of UFG and CG structures obtained after slow (0.1 °C/s) and rapid (10 °C/s) heating. Therefore, the annealing temperatures of A_F and $T_{\gamma 2}$ were compared. *Ex-situ* magnetization measurements were performed on the complete gage length of tensile specimens tested to fracture and interrupted at different strain levels. Figure 6.4 shows the true plastic strain (ε_T) versus the true stress (σ_T) and versus volume fraction of SIM (f_{SIM}) for the UFG and CG structures. The σ_T-ε_T curves were calculated from the engineering curves shown in Figure 6.3. Filled black and blue squares correspond to the evolution of the f_{SIM} during uniform elongation for UFG microstructures obtained after heating at 0.1 and 10 °C/s, respectively. Unfilled black and blue squares represent the evolution of f_{SIM} for CG structures obtained after heating at 0.1 and 10 °C/s, respectively. Red filled and unfilled squares correspond to maximum f_{SIM} obtained after fracture for UFG and CG structures, respectively. From a global comparison it can be concluded that both UFG and CG structures exhibit a pronounced TRIP effect. The martensitic transformation appears to be, however, faster for UFG than for CG structures and, in both cases, it is faster for microstructures heated at 0.1 than for those obtained after heating at 10 °C/s, which results in slightly higher elongations for microstructures obtained rapidly at 10 °C/s. It is also important to notice that the f_{SIM} increases during the Lüders plateau. To minimize the influence of SIM formation during isothermal holding at room temperature, samples were measured immediately after straining. However, f_{SIM} of 0.14 (0.1 °C/s) and 0.08 (10 °C/s) were detected after the yield-drop in UFG structures. Since the magnetization measurements were done *ex-situ*; after stopping the experiment; it is not possible to discern whether some stress-induced martensite was transformed before undertaking the magnetic measurement, due to accumulated stresses or not.

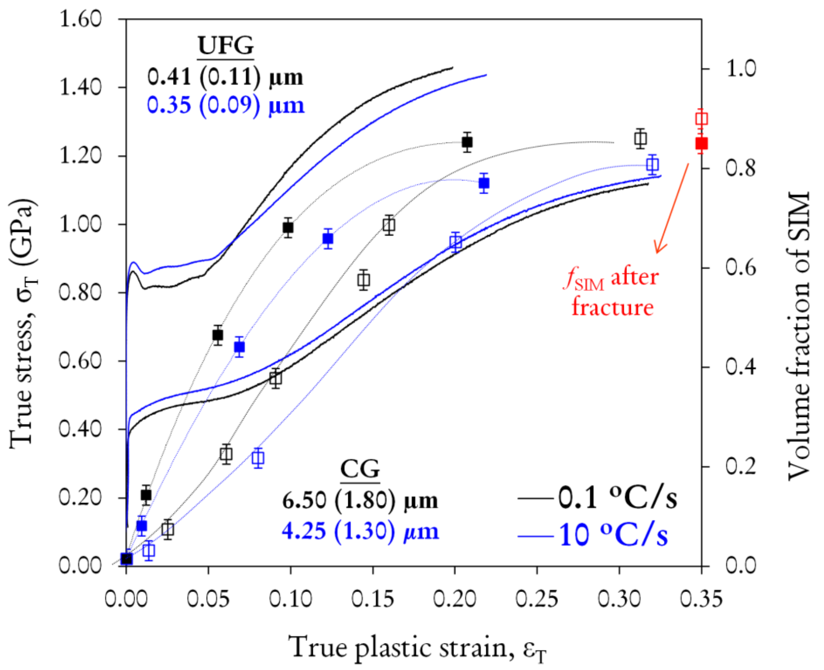

Figure 6.4. Evolution of the volume fraction of strain-induced martensite (SIM) with the plastic strain during tensile testing for the ultrafine-grained (a) and coarse grained (b) austenitic microstructures obtained isochronally at 0.1 °C/s and 10 °C/s. Dotted lines were drawn as a guide to the eye.

To distinguish between *stress-* or *strain-assisted* martensite these interrupted tensile tests were repeated to the same strain level and the samples were heat-treated at 500 °C for 20 minutes before measuring the magnetization. This heat-treatment does not produce changes in the volume fraction of austenite or martensite, but stabilizes them by inducing the precipitation of nano-intermetallic phases within the martensite and by relieving the stress accumulated in the austenite in form of dislocations during the tensile test (responsible for the formation of of stress-induced martensite). Magnetization measurements gave f_{SIM} of 0.17 (0.1 °C/s) and 0.07 (10 °C/s), which are similar or slightly higher volume fractions compared to the unaged ones. Therefore, one could conclude that this martensite was formed during the *in-situ* plastic deformation and that the formation of *stress-assisted* martensite after stopping the experiment is not significant. For CG structures, a f_{SIM} of 0.07 and 0.03 are detected immediately after yielding (at strain levels of 0.025 and 0.014) for heating rates of 0.1 and 10 °C/s, respectively. By the end of the plateau, a f_{SIM} of 0.47 (0.1 °C/s) and 0.44 (10 °C/s) are found in UFG microstructures, whereas just a f_{SIM}~ 0.38 (0.1 °C/s) and

0.22 (10 °C/s) for the CG ones. Finally, the UFG structure obtained at 0.1 °C/s reaches its maximum f_{SIM} at the uniform elongation strain level, whereas the rest of microstructures do it after fracture. A summary of these data is presented in Table 6.3, where $f_{SIM}(\varepsilon_{un})$ and $f_{SIM}(\varepsilon_t)$ represents the volume fraction of martensite detected at the maximum tension and at fracture, respectively.

Table 6.3. Summary of parameters that characterize the mechanical behavior of UFG and CG microstructures. Errors for strength and ductility are not longer than 0.05 GPa and 0.01, respectively. Errors for f_{SIM} are of 0.02.

HR (°C/s)	T_γ (°C)	AGS (µm)	$\sigma_{y0.2}$ (GPa)	σ_{UTS} (GPa)	ε_{un}	$f_{SIM}(\varepsilon_{un})$	ε_t	$f_{SIM}(\varepsilon_t)$
0.1	825	0.41 (0.11)	0.86	1.25	0.19	0.85	0.26	0.85
	1000	6.50 (1.80)	0.39	0.90	0.27	0.86	0.44	0.95
10	950	0.35 (0.09)	0.87	1.18	0.20	0.77	0.27	0.85
	1075	4.25 (1.30)	0.42	0.88	0.29	0.81	0.42	0.90

6.2.3 Microstructural characterization of the martensitic transformation during the yield-point elongation in UFG-γ microstructures

TEM characterization was performed on UFG austenite microstructures strained to levels corresponding to the middle and to the end of the Lüders strain plateau. Sub-size tensile tests specimens annealed at 825 °C (0.1 °C/s) and 950 °C (10 °C/s) were strained to ~0.03 and ~0.06, respectively. TEM discs were extracted from the gage length of the specimens by using a puncher and TEM foils were prepared as described in *Section 3.2.4*. The results are displayed in Figure 6.5 and Figure 6.6, respectively.

Figure 6.5 displays TEM images of the UFG structure obtained after heating at 0.1 °C/s to 825 °C and after introducing a plastic strain of 0.06. Figure 6.5 (a) shows a BF micrograph where the plastic deformation of austenite is pointed out by the presence of slip bands and dislocations, which appear to accumulate near grain boundaries and close to the corners of triple junctions. The DFγ in (b) reveals the presence of high dislocation content in the austenite. A narrow lath of martensite is also distinguishable in the BF (a) and is characterized by the presence of micro-shear bands or twins that form by the pileup dislocations. The presence of twins within the martensite lath is revealed by the DP of Figure 6.5 (c), where the BF image points out the presence of a sub-microstructure within the martensitic lath. In Figure 6.6 TEM images of the UFG austenite microstructure obtained at 10 °C/s to 950 °C after introducing a plastic strain of 0.03 (which is approximately the strain level in the middle of the Lüders plateau).

Figure 6.6 (a) is a BF micrograph of an austenite grain of about 200 nm in size surrounded by strain-induced martensite, as revealed by the DPs and the DFα' in (b). Figure 6.6 (c) presents a higher magnification of the area framed in red in (a) where the austenite grain does not appear to be highly dislocated. However, the dislocation density appears to be greater at the grain boundary adjacent to the martensite phase. Figure 6.6 (d) shows a BF micrograph of strain-induced martensite and strained austenite. The martensite region exhibits some parallel micro-shear bands that go from a grain boundary to another. Some χ-phase precipitates are visible due to their darker contrast. The austenite grain presents the typical pattern of dislocations structure in strained austenite. DPs of each phase are shown in Figure 6.6 (e).

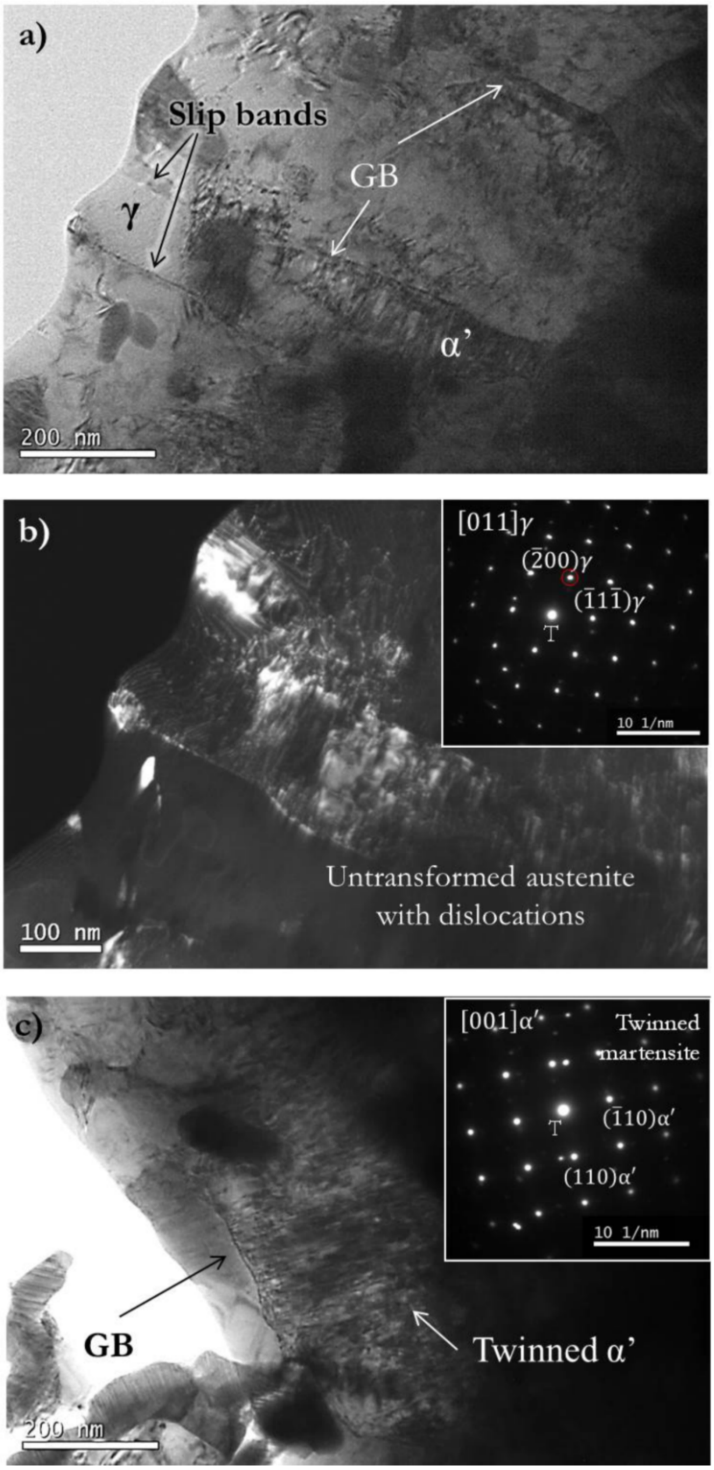

Figure 6.5. TEM micrographs of UFG austenitic microstructure obtained after heating at 0.1 ºC/s up to 825 ºC introducing a plastic strain of 0.06 (strain corresponding to the ε_L magnitude). (a-b) BF and DFγ with its corresponding DP of plastic deformed austenite phase, which exhibits slip bands, and some strain-induced martensite. The DFγ micrograph reveals the presence of dislocation in the untransformed austenite; (c) BF TEM and DP of a martensite lath showing parallel micro-shear bands.

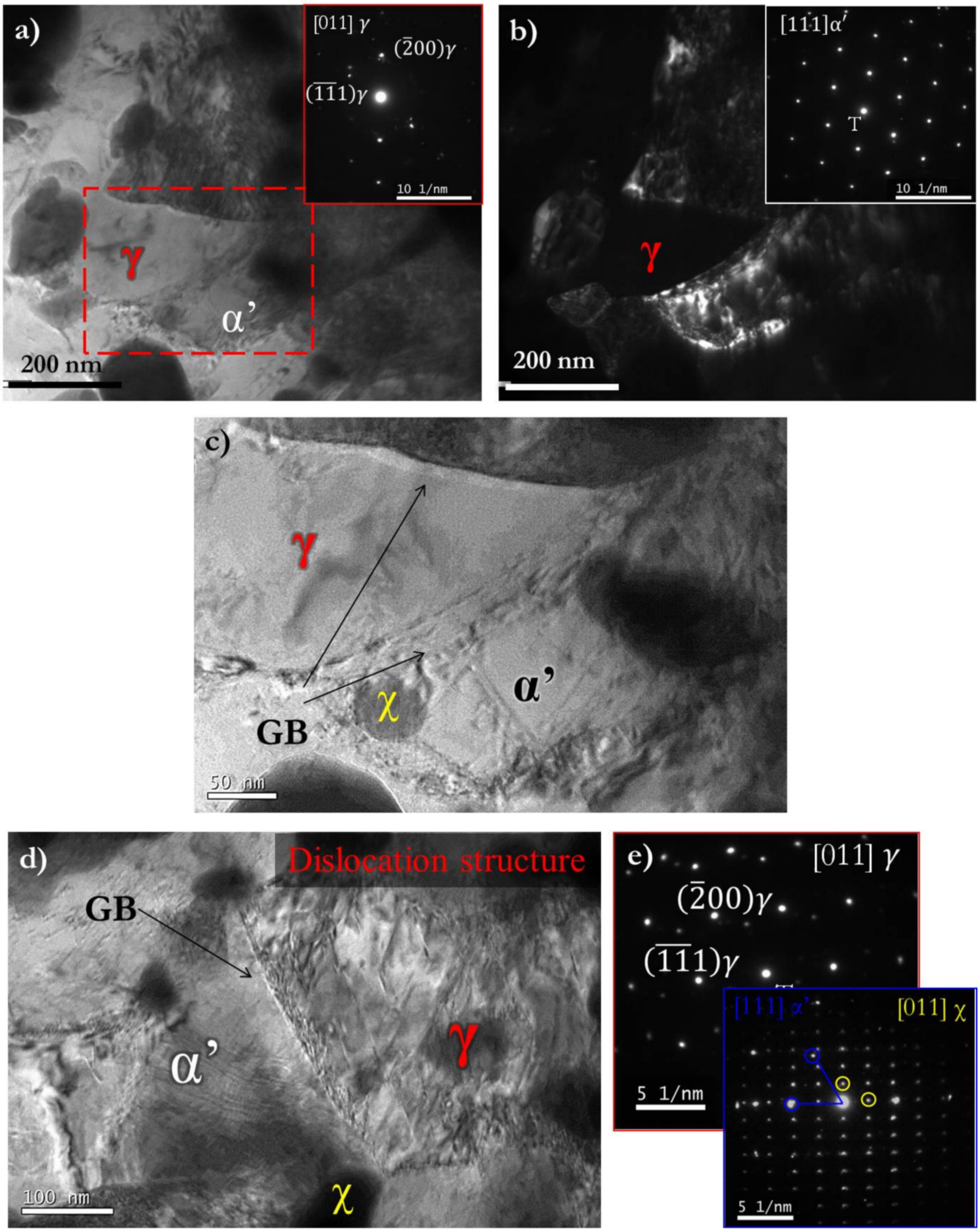

Figure 6.6. TEM micrographs of the UFG austenite microstructure obtained isochronally after heating at 10 °C/s up to the A_F temperature (950 °C) and after applying a plastic strain of 0.03 (strain corresponding to the middle of the Lüders strain plateau region). (a-b) BF and DF showing an austenite grain of about 200 nm in size, surrounded by strain-induced martensite; (c) BF magnification of area framed in red in (a), in which the dislocation density in the martensite phase does appears to be rather low, although some pileup dislocations are visible at the grain boundary (BG); (d) BF micrograph of strain-induced martensite and austenite phase with a high dislocation density; (e) Corresponding DP of the austenite and martensite phases. The presence of χ-phase has been also highlighted.

6.3 Discussion

6.3.1 Understanding the microstructure-mechanical properties relationship in UFG-(α'/γ) microstructures

Figure 6.7 shows the evolution of σ_{UTS} and $\sigma_{y0.2}$ (a) and ε_{un} and ε_t (b) with the volume fraction of austenite (f_γ) for UFG-(α'/γ) dual and UFG austenitic microstructures obtained isochronally at 0.1, 1 and 10 °C/s between A_S and A_F. The values of the cold-rolled microstructure (CR) have been included for comparison. The evolution of the strength can be divided in three regions. In region ①, in spite of having some small amount of austenite in the microstructure (f_γ ~ 0.1), there is an increase in the strength compared to the initial microstructure (IM). After heating at 0.1, 1 and 10 °C/s up to A_S, $\sigma_{y0.2}$ increases from 1.57 (0.01) GPa in IM to 1.95 (0.03), 1.87 (0.01) and 1.74 (0.01) GPa, respectively. And σ_{UTS} increases from 1.66 (0.01) GPa (in the CR) to 2.10 (0.03), 2.00 (0.01) and 1.95 (0.25) GPa, respectively. As for the hardness evolution shown in Figure 5.2 (b), the largest increment of strength is experienced at 0.1 °C/s and decreases when the heating rate is increased.

One of the most important strengthening mechanisms in this steel is the precipitation of the nano-intermetallic particles in the martensite during heating (Figure 6.8). The BF image shows finely dispersed rod-shaped particles of about 20 nm of axial length. The high dislocation density present in the initial microstructures is the responsible of such a fine distribution. The TEM-EDS microanalysis of these particles shows a higher content in Ni, Ti and Al compared to the surrounding matrix, which suggests that these precipitates correspond to the stoichiometric phase $Ni_3(Ti,Al)$. The HRTEM image discloses a preferential growth parallel to <011> directions of the martensite. Similarly, in other maraging and precipitation hardening steels, the optimum mechanical properties have been achieved through the precipitation of nano-intermetallic phases such as Ni_3Mo, Ni_3Ti, Fe_2Mo, FeTi or Fe_2Ti, in the martensite at temperatures in the range of 300-550 °C [40; 52; 94].

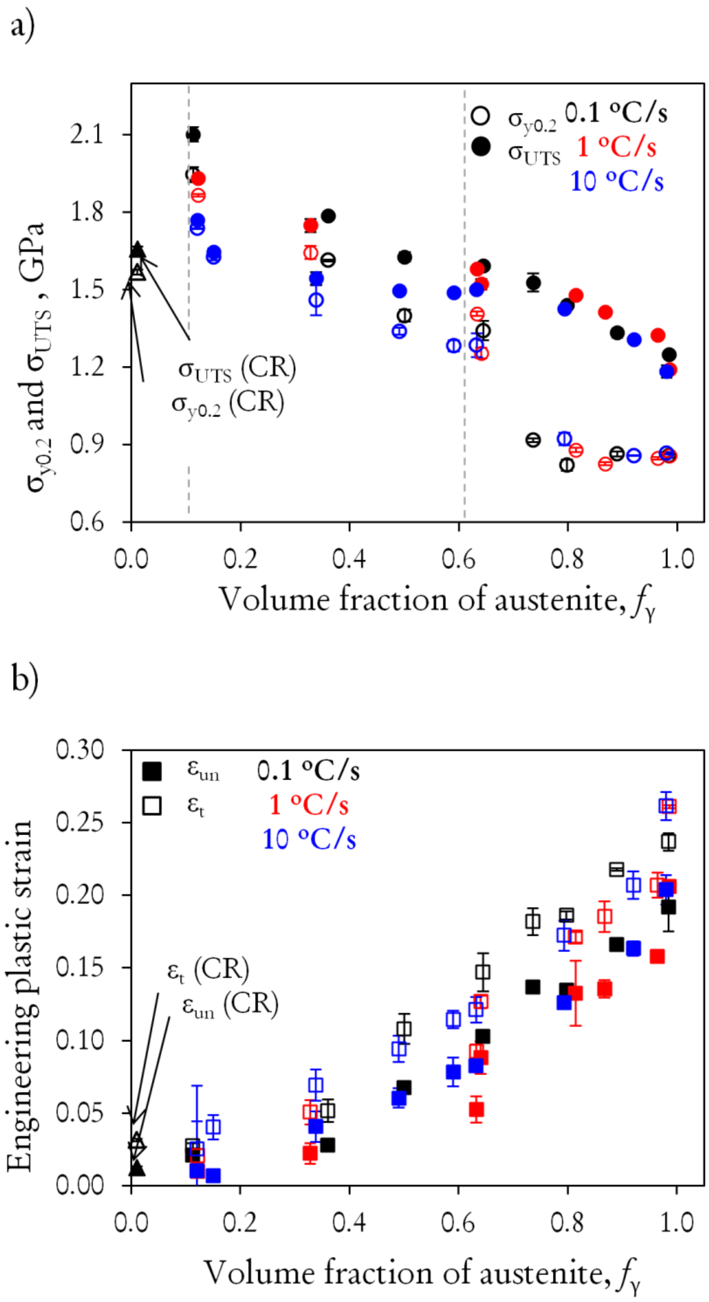

Figure 6.7. Evolution of the mechanical properties with the volume fraction of austenite (f_γ) and the heating rate: (a) Evolution of the uniform elongation (ε_{un}) and total elongation (ε_t), (b) Evolution of the 0.2 % offset yield strength ($\sigma_{y0.2}$) and ultimate tensile strength (σ_{UTS}). Values of the initial microstructure (CR) have also been plotted for comparison.

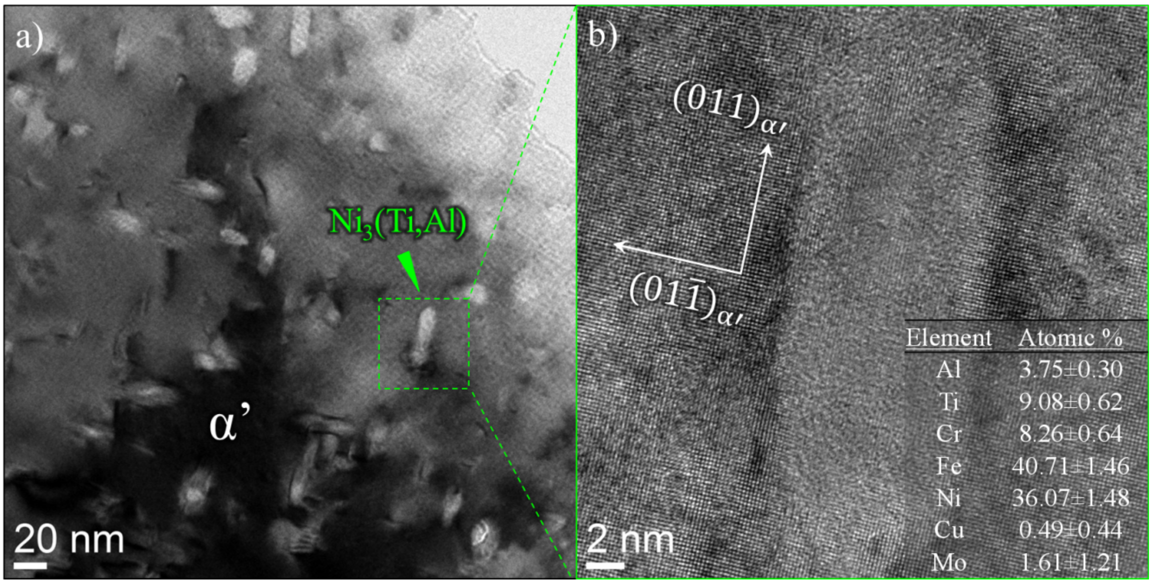

Element	Atomic %
Al	3.75±0.30
Ti	9.08±0.62
Cr	8.26±0.64
Fe	40.71±1.46
Ni	36.07±1.48
Cu	0.49±0.44
Mo	1.61±1.21

Figure 6.8. (a) BF TEM micrograph showing the presence of nanometric rod-shape particles in the martensitic matrix after heating at 0.1 °C/s up to 650 °C. (b) HRTEM micrograph of the area framed in green in (a). The TEM-EDS microanalyses support a stoichiometry $Ni_3(Ti,Al)$ for the rod-shape precipitates, which grow within the martensite (α') with their axial length parallel to the <011> directions.

As it is well known, the strengthening contribution due to precipitation hardening depends on the particle size, its volume fraction, the distribution and coherency with the matrix. Assuming a similar precipitate size for all heating rates [94], the contribution is expected to be higher for the lowest heating rate, since it leads to a higher volume fraction of precipitates, as observed in the evolution of $\sigma_{y0.2}$, σ_{UTS} (Figure 6.7) and the hardness (Figure 5.2 (b)). In addition to the nanoprecipitates, the dislocation density in the martensite matrix is also important for the strength. It is noteworthy that a dense dislocation arrangement prevailed even after the first 50 % of the reaustenitization process. Then, after the strengthening peak is achieved, region ② shows a decay due to the increase of the volume fraction of austenite (soft phase) and decrease of martensite (hard phase). It is important to mention that, due to the dissolution of $Ni_3(Ti,Al)$ precipitates in the austenite, differences in $\sigma_{y0.2}$ and σ_{UTS} between heating rates become smaller and smaller until the f_γ reaches a value of about 0.7. In region ③, further annealing does not produce significant differences in $\sigma_{y0.2}$ and σ_{UTS}, values between heating rates. The $\sigma_{y0.2}$ exhibits a remarkable drop from ~1.30 GPa to ~0.85 GPa when f_γ is increased from 0.63 to 0.74. Then, this value remains more or less constant until the end of the reaustenitization, which indicates that plastic yielding starts in the soft austenite, while the hard untransformed martensite remains in the elastic region. On the other hand, the σ_{UTS} decreases linearly when increasing f_γ, which indicates that in region ③ the mechanical behavior is governed by the austenite phase and the TRIP effect. These changes experienced by the $\sigma_{y0.2}$ and σ_{UTS} values for volume fractions of austenite above 0.7 are associated with the complete and probably quite sudden dissolution of remaining $Ni_3(Ti,Al)$ precipitates, as the reduction in the volume fraction of martensite cannot explain these results alone. Once the precipitates dissolve, the evolution of σ_{UTS} and $\sigma_{y0.2}$ with the volume fraction of austenite appears to be very similar among the microstructures obtained at different heating rates. Fully austenitic microstructures lead to the following values of σ_{UTS}: 1.25 (0.01) GPa at 0.1 °C/s, 1.19 (0.01) GPa at 1 °C/s and 1.18 (0.02) GPa at 10 °C/s (Figure 6.7). Magnetization measurements after tensile testing (Figure 6.4) have pointed out that the microstructure heated at 0.1 °C/s transforms completely to stain-induced martensite, whereas in those obtained after heating at 1 or 10 °C/s a fraction of austenite slightly lower than 0.15 remains untransformaed. Moreover, this fully austenitic microstructure contains a greater volume fraction of χ-phase than those obtained after heating at 1 or 10 °C/s (Table 5.1).Therefore, it might be the presence of small and dispersed intra-granular χ-phase particles along with a greater TRIP effect what would explain why the σ_{UTS} is slightly larger for austenitic structures obtained after heating at 0.1 °C/s.

Figure 6.7 (b) illustrates the variation of the uniform (ε_{un}) and total elongation (ε_t). These two parameters increase almost linearly with the volume fraction of austenite, appearing heating rate independent. The partial reaustenitization influences the ductilization, since the volume fraction of austenite increases. Besides, except for microstructures with f_γ ~0.10, the TRIP effect also contributes to an enhanced ductility. It is also important for the plastic properties that the (nearly) carbon-free martensite matrix is rather ductile.

6.3.2 Influence of the grain size on fully austenitic microstructures

Previous research demonstrates that nano-crystalline materials show much higher strength than their CG counterparts, as expected from the well-known Hall-Petch relationship [74-81]. Shino *et al.* [75; 77] reported a Hall-Petch behavior for AISI 304 SS and AISI 301 SS down to 0.8 - 0.3 µm grain sizes, respectively, and it was found that the relation seemed to break down below 3 µm grain size for AISI 301 SS [75]. On the contrary, Shakhova *et al.* [79] illustrated the link between conventional and nanoscale grains with the offset yield stress for Cr-Ni austenitic stainless steels, including AISI 301LN, AISI 301, 316L and S304H grades, and showed that Hall-Petch relationship was satisfied, being $\sigma_0 = 205$ MPa and $k_{HP} = 395$ MPa µm$^{0.5}$, as generally reported [74; 75; 80].

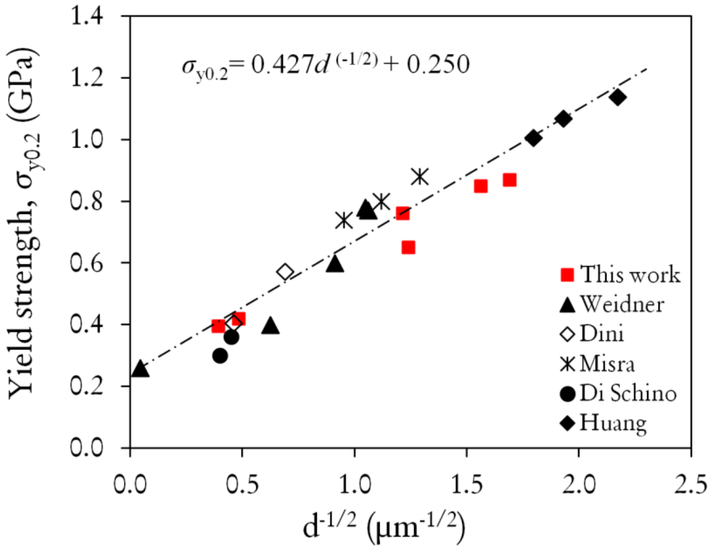

Figure 6.9. Relationship between the offset yield strength and the grain size in different Cr-Ni austenitic stainless steels subjected to different thermo-mechanical treatments.

Figure 6.9 illustrates the dependence of $\sigma_{y0.2}$ with inverse square of the grain size ($d^{-(1/2)}$) for fully austenitic microstructures obtained isochronally in this work. Data available in the literature for similar steels such as AISI 301, 301LN, 304, 316L and high-alloyed austenitic steels have been included for interpretation [77; 78; 80; 81; 176]. In Figure 6.9, the grain size varies from 0.212 to 6.50 µm and conventional micrometer grain scale of 500 µm has been included for comparison. Despite some differences in chemical composition and phase content, all data points obey the Hall-Petch relationship ($\sigma_y = \sigma_0 + k_{HP} d^{-1/2}$) where $\sigma_0 =$ 250 MPa and $k_{HP} = 427$ MPa $\mu m^{-0..5}$. Similar values of σ_0 and k_{HP} are found in the literature, especially, when the austenite grain size lies in the ultrafine – submicron scale [78; 80].

6.3.3 Inhomogeneous yielding in UFG austenitic structures

Apart from the present case, the yield point phenomenon, i.e. the presence of an upper (σ_U) and lower (σ_L) yield point and Lüders banding, occurs in a surprisingly large range of materials [177], including NG/UFG steels [157; 178; 179], TRIP steels, shape memory alloys or Al [180-182]. The inhomogeneous flow is usually the result of interactions dislocations-solute atoms; however, in the case of the interstitials-free stainless steel under investigation, it may arise from the lack of mobile dislocations needed for the plastic deformation [179]. As observed in Figure 6.1, the yield-drop and Lüders-like deformation show up in UFG-γ and dual UFG-(α'/γ) in an advanced annealing state ($f_\gamma \geq 0.80$). On the contrary, dual microstructures in a previous reaustenitization state ($f_\gamma < 0.80$), have enough mobile dislocation during the tensile deformation and, consequently, do not exhibit the yield-drop behavior.

As generally proposed [181-184], the yield-drop in pure metals can be attributed to a shortage of mobile dislocations in the specimen to fulfill the applied strain rate, and the presence of Lüders banding is associated to a relatively low work hardening rate due to the rapid dynamic recovery, respectively. The shear strain is proportional to the number of mobile dislocation per unit volume (N) and the area swept by these moving dislocations (A) through: $\gamma = bNA$; where b is the Burgers vector. Mobile dislocations that carry the plastic strain rate are produced by two different mechanisms: dislocation multiplication inside the grains and dislocation emission at grain boundaries. The extent in which these mechanisms occur depend on the grain size [185]. In CG metals, Frank-Read sources are the well-known intragranular dislocation sources, in which a dislocation segment on an active slip plane, whose ends are strongly pinned by the other parts of dislocation lying outside the plane, bows out under an applied stress. At a critical stress, this dislocation segment generates dislocation loops that results in dislocation multiplication. These dislocation structures formed in the grains gives rise to a large number of interactions between each other and govern the mechanical properties of CG structures [186; 187]. On the contrary, in UFG metals, dislocations in the grains do not form easily and, therefore, grain boundaries are activated as dislocation sources. Since UFG microstructures are characterized by an increased surface area of grain boundaries, more dislocations are emitted but also blocked or annihilated by the grain boundaries [188]. This reduces the number of mobile dislocation, the area swept and thus a greater number of dislocations are required to carry out the imposed strain rate. If the mobile dislocation density is lower than the required value, then the dislocation must increase their velocity to maintain the strain rate. In turn, a high stress results from the increased velocity and a yield peak appears (an upper σ_U and lower σ_L yield point). Therefore, in UFG materials it is the increased dislocation sink effect of grain boundaries the responsible for the yielding phenomenon [185]. The creation or activation of mobile dislocations from grain boundaries is needed and requires a higher stress compared to the one needed to propagate dislocations through the matrix [189]. For this reason the grain refinement increases the yield strength. Coincident with the formation of the yield peak, the first Lüders band appears as a result of the extremely rapid increase in mobile dislocation density within the microstrained region (the first band). The remaining gage length of the specimen may still require dislocation source activation. Therefore, the deformation proceeds at σ_L stress level, giving rise to the yield-point elongation. Lüders bands propagate along the length of the specimen until the entire surface is covered and all areas have been strained by an amount ε_L. A schematic view of the Lüders bands propagation along the gage length of the specimen during the tensile test is displayed in Figure 6.10 (a), after Schwab [177]. In (b) a sub-size sample reaustenitized at 10 °C/s up to A_F displays the presence of Lüders bands propagating fronts after applying a plastic strain of 0.02.

Regarding the Lüders strain magnitude (ε_L), it has been observed from the engineering stress-plastic strain curves in Figure 6.3 that ε_L changes as a function of the annealead temperature and heating rate. In the case of the material raustenitized at 10 °C/s, the Lüders strain plateau disappears above A_F. However, in materials heated at 0.1 °C/s, there is an increase of ε_L from 825 to 900 °C and, then, again a decrease from 900 to 950 °C. Table 6.4 displays a summary of the AGS, volume fraction of χ-phase (f_χ) and ε_L values obtained for materials reaustenitized at 0.1 °C/s, whose σ-ε curves are shown in Figure 6.3. It appears to be a relationship between the volume fraction of precipitates and ε_L, similar to that found by Varin *et al.* [178]. They studied the deformation behavior of UFG 316 ASS and observed that ε_L increased either with a decrease in the test temperature or with an increase of the strain rate. Additionally, they also discussed that a high number of particles per grain boundary surface increases ε_L, since it implies a larger number of sources locked and fewer mobile dislocations available. These observations by Varin suggest that a higher f_χ result in longer ε_L. The mobile dislocations are pinned by the precipitates and, consequently, an increase in the Lüders magnitude is detected. Moreover, it was observed by Hall [190] that the transition from the Lüders plateau to the uniform elongation sharpens as the precipitation density increases, which would explain why materials reaustenitized at 10 °C/s exhibit smoother transitions than materials annealed at 0.1 °C/s.

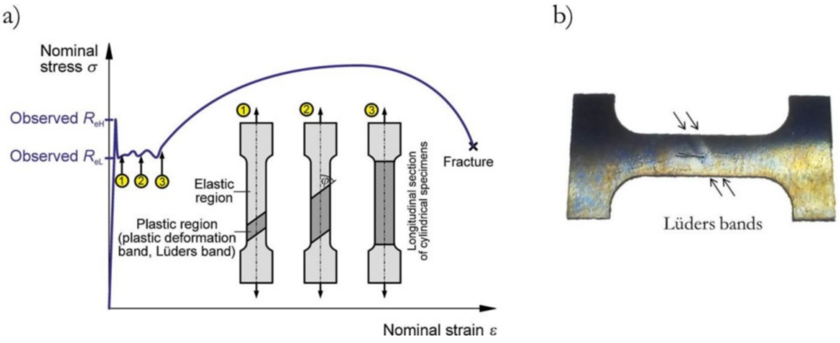

Figure 6.10. (a) Schematic representation of stress-strain behavior and plastic deformation band of a typical structural steel in a tensile test, after Schwab *et al.* [177]. (b) Sub-size tensile test sample of the material reaustenitized at 10 °C/s up to 950 °C (*A*F) showing the presence of Lüders banding after plastic straining a 0.02.

On the other hand, no stacking faults or dislocation pile-ups have been observed by TEM in UFG samples strained to 0.03 and 0.06. Instead, laths of strain-induced martensite and austenite grains with different dislocation densities and almost dislocation free were detected. This is not surprising since the formation of dislocation pile-ups is difficult in small grains. Moreover, dislocation glide and twinning are competitive mechanisms of plastic deformation: the second comes into play when the first exhausts and cease to accommodate the imposed strains [171]. As reported by Shimokawa *et al.* [191] dislocations emitted from grain boundaries to small grains exert a back-stress to the grain boundary that hinders the generation of successive dislocations, which results in the activation of other sources rather than in the pile-ups formation. Yamakov *et al.* [188] also discussed in nanocrystalline aluminum that dislocations nucleate at grain boundaries and may be absorbed by the opposite boundaries, especially in the early stages of plasticity. Something similar must be occurring in the early stages of deformation of the UFG material obtained in this work, as pointed out by the presence of nanometric defect free austenite grains as seen in Figure 6.6 (c).

Table 6.4. Evolution of the Lüders strain magnitude (ε_L) with microstructural modifications (AGS and f_χ) undergone during reaustenitization at 0.1 ºC/s.

HR = 0.1 ºC/s			
T_γ (ºC)	**825 (A_F)**	900 ($T_{\gamma1}$)	1000 ($T_{\gamma2}$)
AGS (μm)	0.41 (0.11)	1.65 (0.40)	6.50 (1.80)
f_χ	0.11 (0.01)	0.13 (0.01)	0.06 (0.01)
$\boldsymbol{\varepsilon_L}$	0.05	0.08	0.06

Cheng *et al.* [185] studied the mechanical behavior transition from ultrafine and traditional regime. Whereas ultrafine regime should be dominated by grain boundary dislocation sources, the traditional regime will deform both by boundary and intragranular sources. It was found that the transition grain size varies 200 nm and 1 μm depending on the material and its processing history. This suggests that CG structures studied in this work may deform through in traditional regime. Besides, the fact that the yield-drop disappears as the austenite grain size increases suggests that the sink effect of grain boundaries is counteracted by a more rapid multiplication of dislocations from intragranular sources, which means that plastic deformation occurs through dislocation interactions.

Therefore, it can be concluded that, during inhomogeneous deformation, grain growth from UFG to CG scale leads to a change in the dominant operating deformation mechanism. Whereas UFG is characterized by dislocation emission from grain boundary sources, CG materials appear to plastically deform through dislocation interactions inside the grains [185].

6.3.4 Strain-hardening behavior of austenitic microstructures: TRIP effect and mechanical properties

It has been observed in the previous section that, similarly to UFG-dual microstructures with high f_γ (Figure 6.1), fully austenitic microstructures (Figure 6.3) also exhibit an inflection point in the σ-ε curve after the Lüders plateau that leads to an increase of the stress at intermediate levels of strain. This means that the strain-hardening rate (SHR) increases, which is a consequence of the martensitic transformation and the hardening of the martensite (TRIP effect). The interplay between strain-hardening, deformation mechanism and mechanical properties in conjunction with the grain size has been previously investigated in austenitic TRIP steels from nanograined/ultrafine-grained (NG/UFG) to coarse-grained (CG) regime [81; 157; 161; 163; 165; 192; 193].

The relationship between microstructural evolution and mechanical properties can be further discussed with empirical equations. One of the best-known is the Hollomon analysis. After yielding the stress-strain relationship in the uniform deformation stage is expressed by the Hollomon Eq. [6.1]; where σ_T and ε_T are the true stress and true strain, respectively, n is the strain-hardening exponent and K is the strength coefficient.

$$\sigma_T = K\varepsilon_T^n \tag{6.1}$$

$$ln\,\sigma_T = lnK + nln\varepsilon_T \tag{6.2}$$

A logarithmic plot of σ_T and ε_T up to the maximum stress (plastic instability) will result in a straight-line if the power law is satisfied. The slope of this line is the strain hardening exponent (n), and the strength coefficient (K) is the true stress at $\varepsilon_T = 1$ ($\ln\varepsilon_T = 0$). The Hollomon analysis was applied in this work to reaustenitized microstructures with different grain sizes. These results are shown in Figure 6.11 (a). As it can be seen, the Hollomon analysis failed to show the linearity of ln σ_T-ln ε_T over the strain ranges. Instead, the plot exhibits two slopes. The hardening exponent n increases with the grain size, while the maximum value of K decreases.

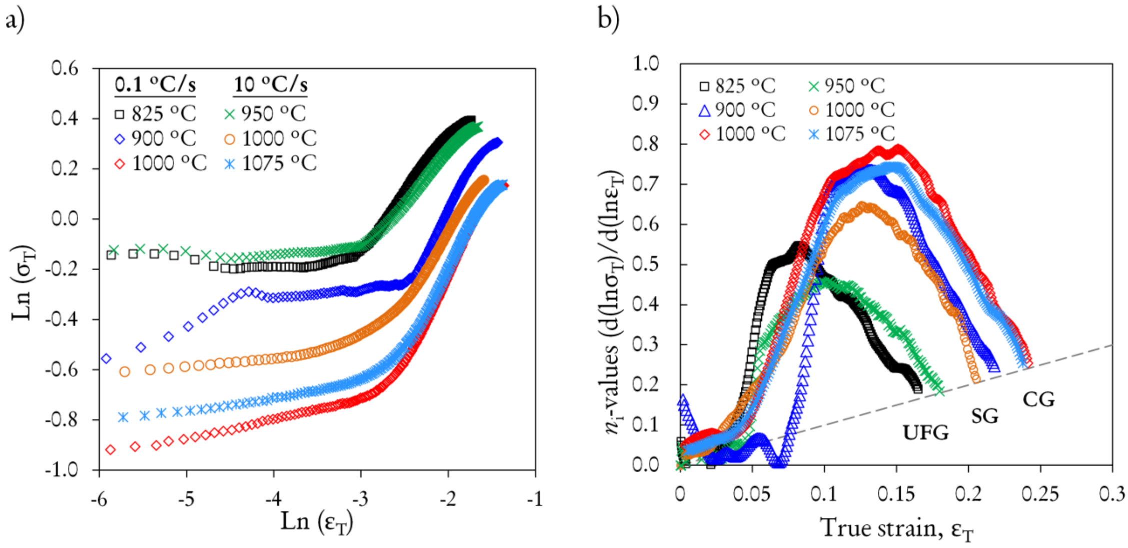

Figure 6.11. (a) Hollomon analysis (ln σ_T-ln ε_T) and (b) instantaneous n_i-values ($d(\ln\sigma_T)/d(\ln\varepsilon_T)$) vs. ε_T for the reaustenitized samples with different austenite grain sizes.

The deviation from the linearity of the n-value leads to the concept of instantaneous n-value (n_i) [176; 194; 195]. The n_i is the first derivative of the ln σ_T-ln $\varepsilon_T$plot. Figure 6.11 (b) shows the n_i-value as a function of plastic strain for the same reaustenitized conditions. As it can be seen, samples with the largest grain size have the highest n_i-values, which decrease with increasing the grain size. It has to be noted that the n_i-value is not the same as the strain-hardening rate ($d\sigma_T/d\varepsilon_T$). A higher n_i-value does not necessarily mean a higher instantaneous work hardening rate. For a given n_i-value, a higher K_i-value will give the higher work hardening. The uniform elongation can be explained by the instability condition, given by the Considères criterion ($d\sigma_T/d\varepsilon_T \leq \varepsilon_T$) [33]. When the strain hardening ($d\sigma_T/d\varepsilon_T$) is equal to ε_T, the uniform elongation stops and necking is initiated (grey dashed line in Figure 6.11 (b)). At this point, the σ_T-ε_T and SHR ($d\sigma_T/d\varepsilon_T$) vs. ε_T curves intersect each other at the uniform true strain.

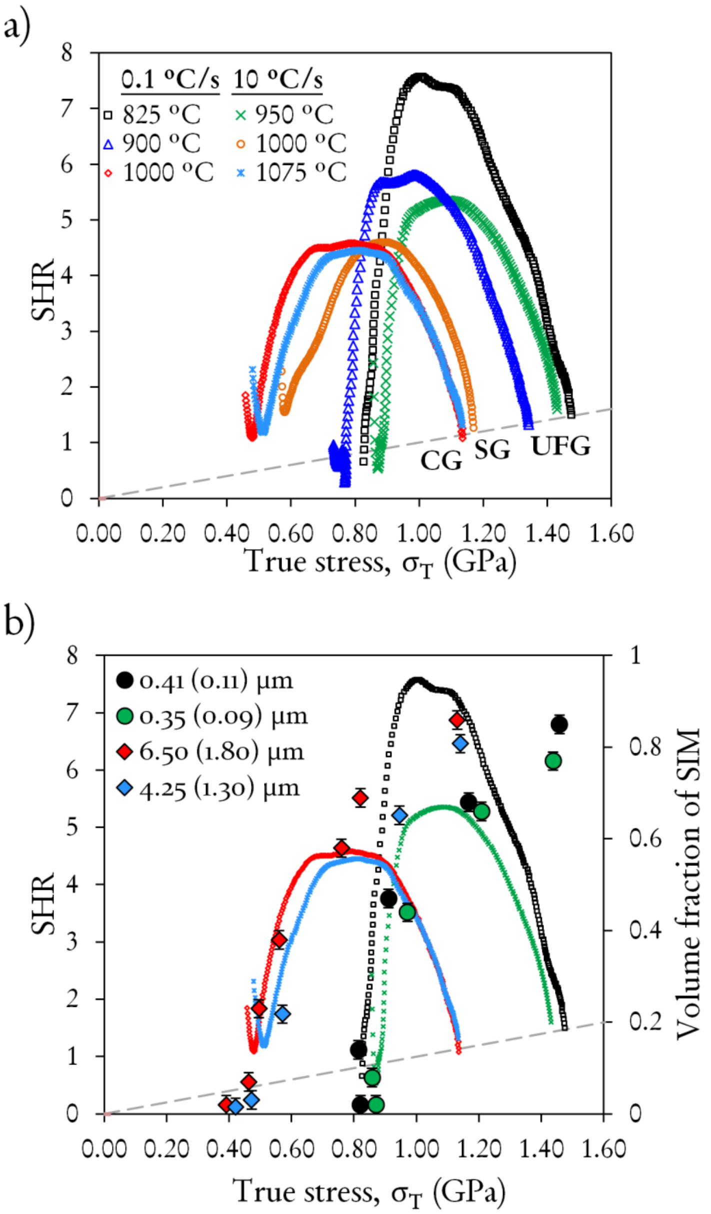

Figure 6.12. (a) Strain-hardening rate (SHR) vs. true stress (σ_T) and; (b) Strain-hardening rate (SHR) vs. true stress (σ_T) including the evolution of volume fraction of strain-induced martensite (SIM) for UFG and CG austenitic microstructures.

Generally, the SHR is determined from the σ_T-ε_T curve. Figure 6.12 (a) shows the SHR against true stress (σ_T). The SHR curves have been truncated at the onset of plastic instability, as established by the Considère's criterion. As observed in Figure 6.12 (a), the SHR decreases with increasing the grain size. This is because the greater the grain size, the lower the stress level at which SIM starts forming. This is highlighted in Figure 6.12 (b), which basically presents the same plot as in (a) for the UFG and CG microstructures, along with the evolution of the strain-induced martensite during plastic straining (see Figure 6.4). From this plot it is clearly observed that there is a relationship between the stress level at which the martensitic transformation is initiated and the stress level at which the SHR starts increasing. The grain refinement causes an increase in the yield strength and, thus, higher SHR will be required to initiate the plastic deformation. Whereas the transformation for CG structures starts at about 0.40 GPa, it does it for UFG around 0.80 GPa. In turn, this means that the mechanical stability of austenite in the UFG structures is greater than in the CG ones, as generally reported [26].

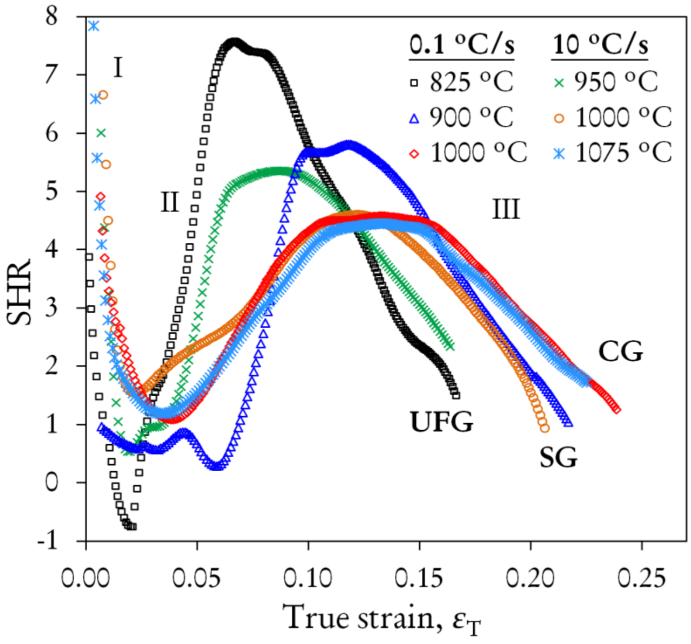

Figure 6.13. Strain-hardening rate (SHR) vs. true strain (ε_T).

In Figure 6.13 the evolution of the SHR with ε_T is presented. Three different regions are distinguished as the slope changes. This three-stage hardening behavior has already been reported in ultrafine duplex Mn-TRIP steels [165], in commercial type 301LN ASS [157] or in 304, 316 and 316LN grades [168]:

- Stage I. The SHR drops and reaches a minimum at relatively low strains (0.02 - 0.06). The rapid SHR decrease in UFG structures in stage I indicates a lower strain hardening than for CG structures (relative slow decrease). This may be related with the stronger dynamic recovery of dislocations in UFG materials, while in CG structures intragranular dislocation sources lead to their rapid multiplication and storage, in other words, to a higher dislocation density.
- Stage II. The SHR increases rapidly to a maximum (or a plateau in CG structures) that is related to the martensitic transformation. For some conditions (950 °C-10 °C/s or 900 °C-0.1 °C/s.) a plateau before the SHR increase is observed. This plateau is related to the Lüders bands formation and does not exhibit a significant strain-hardening. This can be ascribed to a continuous dynamic recovery of dislocations due to an increased grain boundary area. Therefore, this phenomenon is expected to be pronounced in those conditions with small grain sizes and high volume fraction of χ-phase precipitates, as it is the case of UFG microstructures and those annealed at 0.1 °C/s to a temperature below the dissolution temperature of the χ-phase. It is not surprising that the 900 °C-0.1 °C/s condition (with a grain size of 0.68 (0.20) μm and a f_χ ~0.13 presents the most pronounced Lüders band formation [190].
- Stage III. The SHR decreases slowly with increasing tension until the material fractures.

6.3.5 Design and mechanical properties

Steels combining properties of ultra-high strength (above 1 GPa) and good ductility (elongations of 15 – 20 %) are of great importance in automotive, aerospace, nuclear, gear or bearing industries. They are future key materials for lightweight engineering design strategies and corresponding CO_2 savings. For this reason, both academia and industry have made great efforts to develop a large variety of steel grades and processing technology. In applications of UHS steels, the materials are usually subjected to extreme mechanical loads and harsh environmental conditions in which corrosion is an important issue. Therefore, a stainless steel with equivalent mechanical properties but not requiring a corrosion protective coating would be an attractive alternative.

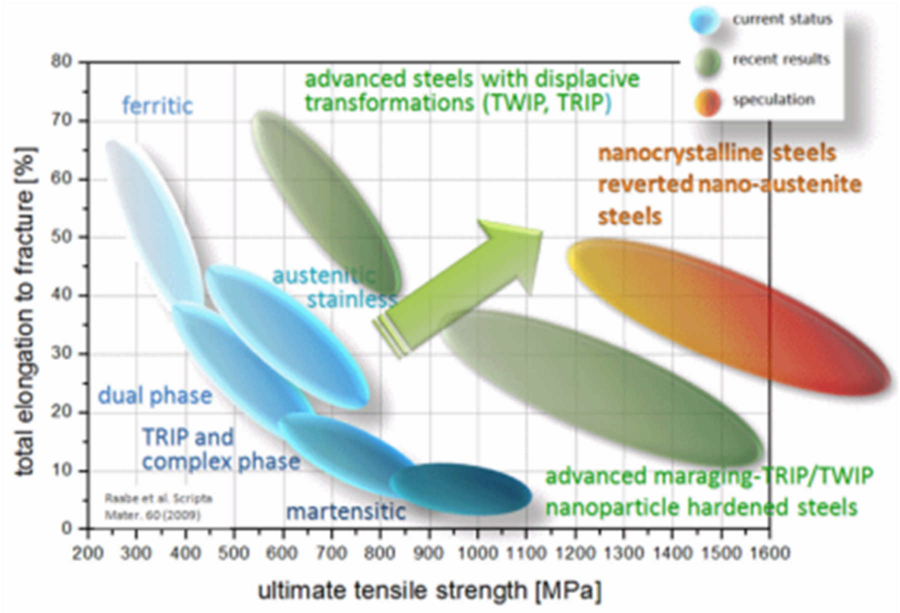

Figure 6.14. Typical strength-ductility profile of steels after Raabe *et al.* [196]: TRIP: transformation-induced plasticity; TWIP: twinning-induced plasticity; maraging TRIP: steel concept that uses hardening mechanisms based on transformation-induced plasticity and the formation of intermetallic nanoprecipitates in the martensite during aging.

Conventionally produced bulk high strength steels are known as high-strength low-alloy (HSLA) or microalloyed (MA) steels. This family of steels usually has a strength not exceeding 700 – 800 MPa and can be manufactured under relatively simple processing conditions. In order to further enhance the combination of strength and ductility, more alloying elements have been added and more sophisticated alloy systems have been designed such as dual phase (DP) steels, TRIP, TWIP and maraging steels. Characteristic strength-ductility profiles are presented in Figure 6.14, after Raabe *et al.* [196]. As observed, there is a trend towards increasing strength and ductility simultaneously via stimulating transformation during deformation such as martensite formation (TRIP) of twinning (TWIP) in unstable austenite, or, alternatively, by introducing nanoprecipitates in a wide range of grain size regimes, from NG/UFG to CG [81; 157; 161; 163; 165; 192; 193; 197].

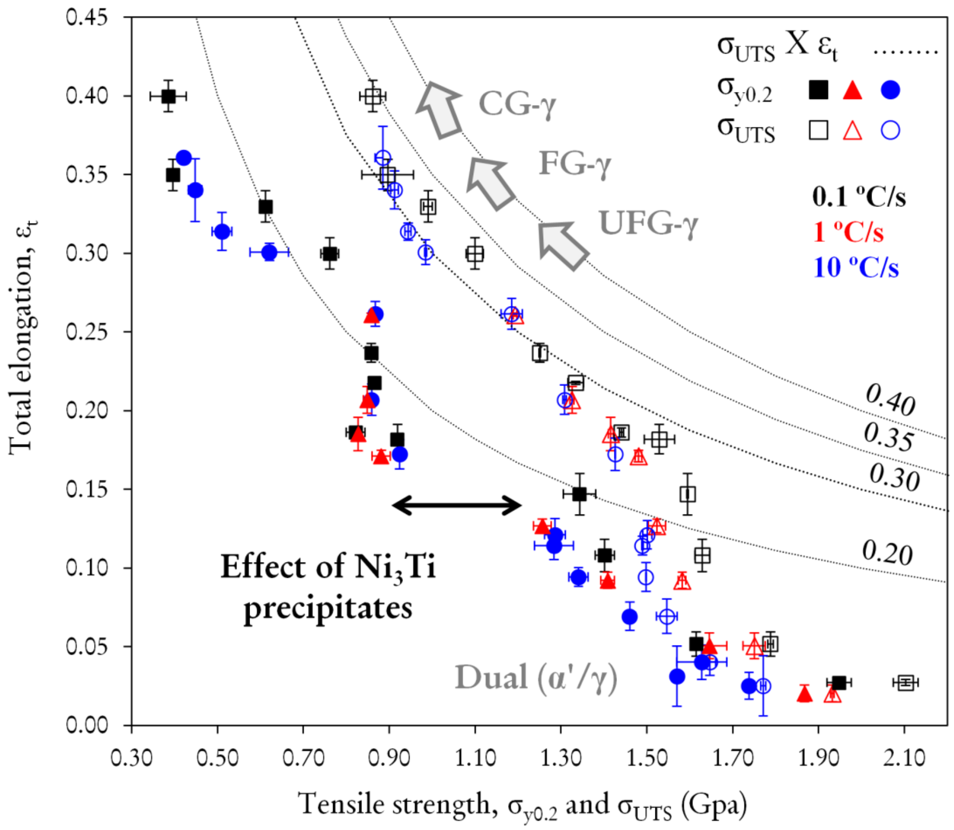

Figure 6.15. Summary of the strength-ductility combinations, represented in a typical banana-like plot, exhibited by the microstructures obtained isochronally at different heating rates: 0.1 (black), 1 (red) and 10 °C/s (blue). Filled and unfilled data points correspond to $\sigma_{y0.2}$ and σ_{UTS} values, respectively. Dotted lines represent fixed values (0.30, 0.35 and 0.40) of the product σ_{UTS} x ε_t.

In this thesis work, the interplay between the annealing route, the strain-hardening, deformation mechanism and the mechanical properties in conjunction with the grain size has been investigated for the metastable semi-austenitic SS under investigation. In a similar way than that presented by Raabe *et al.* [196], Figure 6.15 shows, in a banana-like plot the mechanical behavior of the different microstructures obtained isochronally by the processing routes designed in this work. Filled and unfilled data points correspond to $\sigma_{y0.2}$ and σ_{UTS} values, respectively. Starting from a martensitic severe cold-deformed state, it is possible to produce different microstructures: fully martensitic, fully martensitic with $Ni_3(Ti,Al)$ precipitation, dual (α'/γ) microstructures with different fractions of martensite, austenite and $Ni_3(Ti,Al)$ precipitates and fully austenitic microstructures with grain sizes ranging from UFG to CG (0.35 – 6.50 μm). Strength and ductility can be modified from 0.85 to 2.10 GPa and from 0.03 to 0.40, respectively, due to the great adaptability that this material exhibits. As the grain size grows the strength decreases and the ductility increases. For better comparison, fixed values of the product σ_{UTS} x ε_t have been drawn in Figure 6.15. As observed, the largest σ_{UTS} x ε_t value (almost 0.35 GPa) is obtained for the CG austenite microstructure obtained after heating at 0.1 °C/s, which exhibits a grain size of 6.50 μm. FG austenite structures obtained at 0.1 °C/s also show higher σ_{UTS} x ε_t value than those obtained at 10 °C/s, especially for smaller grain sizes. However, UFG austenite structures generated rapidly are above 0.30 GPa, whereas the one obtained slowly is below.

It is surprising that the heating rate does not appear to influence significantly the final mechanical properties. It is worth mentioning, though, that the great volume fraction of χ-phase in UFG structures obtained at 0.1 °C/s is not desirable at all. Since the Cr content of the steel under investigation is 12 wt. %, the precipitation of this Cr-rich intermetallic may have adverse effects on the corrosion resistance of the steel, as Cr is removed from the solid solution, making the steel less stainless. Besides, a more rapid heating not only is advantageous from the corrosion resistance point of view, but also from an industrial point of view. A faster heating consumes less energy and time, making the heat-treatment more convenient.

6.4 Conclusions

- Ultrafine-grained partially (α'/γ) and fully reaustenitized microstructures obtained by controlled isochronal heating have shown enhanced mechanical properties, with σ_{UTS} and ε_t ranging from 1.18 - 2.10 GPa and 3 – 26 %, respectively.

- When the austenite grain size is increased to the submicron and coarse scale the strength decreases and the elongation increases, as predicted by the Hall-Petch relation, due to a decrease in the grain boundary area.
- The mechanical behavior of partial (α'/γ) and fully reaustenitized microstructures is influenced by: (i) the volume fraction of austenite and its stability, (ii) the presence of nanometric Ni_3(Ti,Al) precipitates in the untransformed martensite, (iii) the TRIP effect, (iv) the austenite grain size and (v) the χ-phase content.

Chapter 7

Study of the precipitation aging processes

C. Celada-Casero, E. Urones-Garrote, S. Mato, J. Chao and D. San Martín. *Nano-precipitation hardening in a semi-austenitic metastable stainless Steel*, Mater. Sci. Eng. A (in preparation).

In this chapter the aging behavior of the CR steel under consideration has been studied in a wide range of aging temperatures (300-550 °C) for times not longer than 72 h. By combining the metallographic characterization, micro-hardness Vickers tests, TEP measurements and tensile testing, the linkage aging-microstructure-properties has been investigated. TEM and HR-TEM have shown that the hardening is due to the formation of $Ni_3(Ti,Al)$ nanoprecipitates, which exhibit a $(1\bar{1}0)_{\alpha'} \| (0001)_{Ni_3(Ti,Al)}$ and $[1\bar{1}1]_{\alpha'} \| [11\bar{2}0]_{Ni_3(Ti,Al)}$ orientation relationship with the martensitic matrix. It has been observed that the higher the aging temperature, the faster the hardening response of the material is. The maximum hardening effect (710 Hv) has been reached after 72 h aging in the range 425-475 °C and no peak-age has been detected in this time range. This continuous hardening over time and final ultra-high strength has been attributed to a particle shearing strengthening mechanism consequence of the resistance to coarsen of the precipitates, which remain below their critical size. However, high aging temperatures such us 500-550 °C and aging times of 24 h or longer induce the formation of the austenite phase, which along with the recovery of the microstructure and the precipitates coarsening lead to softening of the material and to slightly improved work-hardening ability. Finally, a reliable hardness-strength correlation has been found that enables the rapid evaluation of the strength from bulk hardness measurements.

7.1 Introduction

As in other precipitation hardening [7-17] and maraging [39-47; 51; 52] steels, the superior strength properties in the steel under investigation are achieved through the martensitic transformation followed by an aging (precipitation hardening) heat-treatment, which promotes the precipitation of nanometric particles in the martensitic matrix. These precipitates act as obstacles and hinder the movement of dislocations through the well-known Orowan and Kelly-Fine mechanism. Beside the strong effect of the nanoprecipitates, the high retained dislocation content in the deformed martensitic matrix is also responsible for the high strength. The dislocation density may also play an important role in the nucleation of precipitates and their high dispersion since the diffusion of alloying elements is enhanced by pipe-diffusion.

Whereas conventional carbon-based martensitic steels typically reveal very poor ductility, the nearly carbon-free martensitic matrix of maraging steels makes them rather ductile. Besides, the kinetics of re-transformation from martensite to austenite of these steels highly depends on the heating rate, temperature and holding time during aging, making ductility somewhat tunable [43; 198; 199].

Numerous works can be found in the literature on the precipitation sequence of the steel under investigation, presenting slight variations of composition: 12-13 Cr and 8.5-9 Ni in wt. % [51-53; 93-95; 200-203]. However, these studies have been mainly focused on the aging temperature of 475 °C and aging times as long as 1000 h in order to promote the formation of new phases such as the quasicrystalline *R*' phase. Different experimental techniques have been used to characterize the complex precipitation sequence in this steel, such as such as atom probe tomography (APT), three-dimensional atom probe (3-DAP), energy-filtered TEM (EFTEM) and conventional TEM [51; 52; 93-95]. It has been shown that the precipitation sequence involves different precipitate phases that form in direct contact with each other at different aging times. Stiller *et al*. [51; 93] found that at a very early aging stage (~5 min) a high number density of Cu/Ni/Ti/Al/Si-rich clusters containing 20 - 100 atoms appear, which develop within the following 4 h aging into multiphase Ni-rich precipitates, namely $Ni_3(Ti,Al)$ and $Ni_3(Ti,Al,Si)$, and Cu-rich 9R particles. Later, Cr-rich α' precipitates form on the Ni-rich precipitates and the γ'-$Ni_3(Ti,Al,Si)$ phase dissolves and is replaced by the G-$Ni_{16}Si_7Ti_6$ phase. Eventually, the Mo-rich quasicrystalline R' phase is formed in contact with other particles. The precipitation process at an aging temperature of 475 °C was summarized by Thunvander *et al.* [95] as Table 7.1 shows. As Thunvander observed, although the number density of precipitates decreases during 100 h of aging, likely due to coarsening, the hardness does not. This was explained by an increasing total volume fraction of precipitates as additional phases appear within the 100 h of aging. Hättestrand and co-authors [52] had earlier found that, in fact, the hardness of the steel increases continuously up to about 700 H_v during aging at 475 °C for 1000 h. They estimated the relative contribution to the strength based on 3-DAP measurements of particle densities and concluded that Ni-rich precipitates play the most important role up to about 40 h of aging after which, the effect of the quasicrystalline R' phase becomes increasingly important. On the other hand, aging for longer than 1 h at 475 °C induces the formation of a Mo-rich film in direct contact with Ni-rich precipitates, to which it has been attributed their resistance to coarse [94].

Table 7.1. Number density (10^{24} m^{-3}) of various precipitates phases found after aging at 475 °C the steel under investigation after certain aging times [95].

Precipitate phase		Crystalline structure	Aging time			
Stoichiometry	Symbol		5 min	4 h	40 h	100 h
Cu-clusters	9R	Coherent BCC	3.7±1.5	2.2±0.2	0.82±1.0	0.30±0.0.5
	η + γ'		3.7±1.5	–	–	–
η-$Ni_3(Ti,Al)$	η	HCP	–	0.9±0.4	0.25±0.05	0.12±0.05
$Ni_3(Ti,Al,Si)$	γ'	FCC ($L1_2$)	–	1.4±0.5	0.52±0.1	–
$Ni_{16}Si_7Ti_6$	G		–	–	–	0.17±0.06
Cr-rich	α'	Coherent BCC	–	–	0.86±0.20	0.21±0.06
Mo-rich	R'	Quasicrystalline	–	–	–	0.03±0.02

This research, rather than focusing on one single temperature for very long aging times, has focused on a wider temperature range for times which are more valuable from an industrial point of view. Moreover, there is a lack of work explaining the relationship between microstructure and mechanical properties or the mechanisms contributing to the strengthening in this steel. In this sense, this chapter provides new and valuable information that will help to improve an important manufacturing step of this steel: the aging.

7.2 Results

A series of heat-treatments were designed in order to study the effect of different temperatures (300, 400, 425, 450, 475, 500 and 550 °C) and holding times (from 1 s to 72 h) on the aging behavior of the as-received material. See Table 3.5 in *Section 3.5.2* for heat-treatments details.

7.2.1 Evolution of the micro-hardness Vickers and thermoelectric power

A direct method to study the aging process of the heat-treated material is by micro-hardness Vickers measurements. The variation in hardness as a function of aging time at different temperatures is shown in Figure 7.1 (a). As observed, aging at 300 °C does not have a significant effect on the hardening of the material. The maximum hardness (710 Hv) is reached after 72 h of isothermal holding in the range 425-475 °C, after which the as-received material experiences a hardness increment of almost 300 Hv (from 425 Hv to 710 Hv). Higher aging temperatures, such as 500 and 550 °C, do not show a hardness improvement as spectacular as the one obtained at 425-475 °C. However, it is remarkable the fast aging response of the material at 550 °C, which increments the hardness in 130 Hv after heating at 30 °C/s and isothermal holding for 1 s. However, the hardness does not increase much more with further aging at 550 °C since, after 15 s, the hardness reaches a plateau around 605 Hv and then, after 900 s, decreases. The overaging is also observed in the material treated at 500 °C after 24 h.

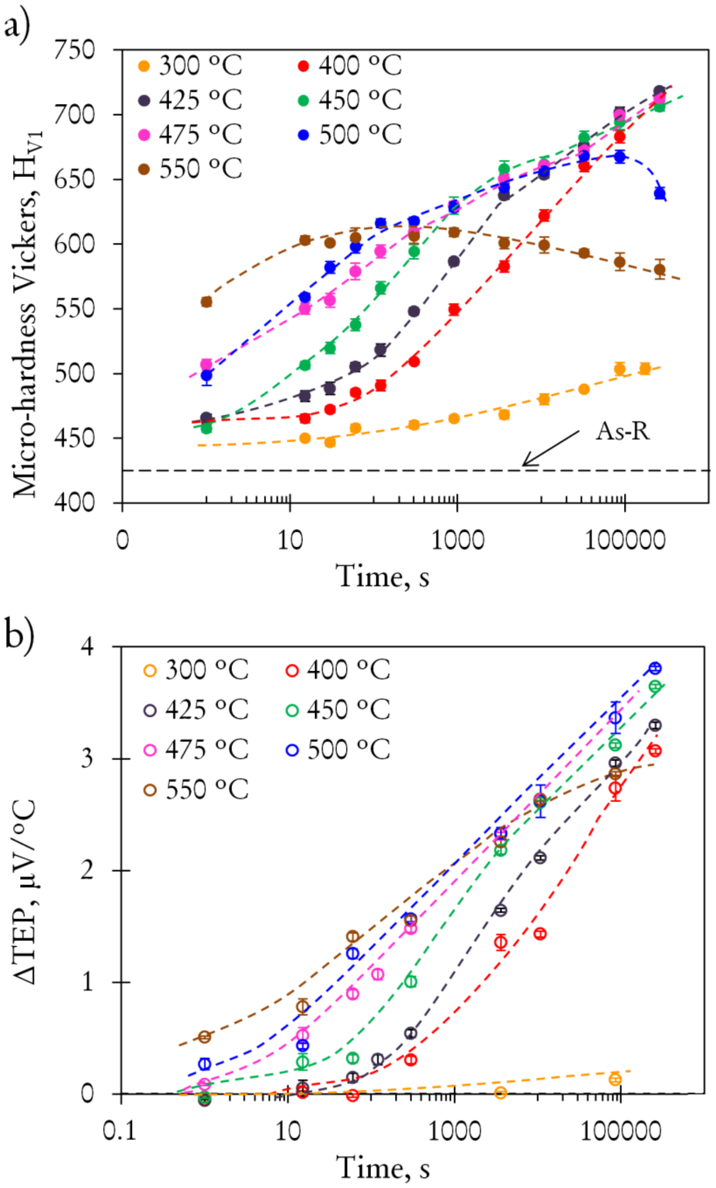

Figure 7.1. (a) Effect of aging time on micro-hardness Vickers and (b) thermoelectric power (TEP) at given temperatures.

TEP measurements were performed on samples aged under the same conditions than for micro-hardness Vickers measurements. Three TEP measurements were noted per condition and final values have been expressed as the mean value and standard deviation. Figure 7.1(b) displays the relative TEP variation with respect to the as-received state. The reference value obtained for the CR material (3.94 μV/°C) depends on the electrical transport properties of the steel. In this case, the reference value was set as zero, due to the interest in the TEP variation more than in the absolute value. As observed, the TEP increment (ΔTEP) is positive over time for all aging temperatures. As expected, this variation is insignificant at 300 °C, since the diffusion processes at this temperature are quite hindered, whereas it is maximum after 72 h aging at 450-500 °C. The largest ΔTEP is detected for the highest aging temperature, 550 °C. In general, TEP and Hv behaviors are very similar to each other, except for the curves at 500 and 550 °C. The hardness plateau observed at 550 °C is reflected in a slope change in the ΔTEP curve. On the other hand, the hardness-peak detected after 24 h aging at 500 °C is not observed in the ΔTEP curve, which increases steadily giving rise to the largest TEP increment (3.8 μV/°C).

7.2.2 Microstructural characterization: LOM, SEM, and magnetization measurements

To study the microstructural evolution during aging, i.e., recovery and precipitation processes, formation of austenite, evolutions of precipitates, etc., different characterization techniques were used. As observed in Figure 7.1, the most interesting hardness properties were found to range the aging temperatures 400-500 °C. For this reason, the microstructural characterization was done in this range of temperatures.

Figure 7.2 shows optical micrographs of the material cross-section aged at 400 and 500 °C for 3 and 24 h. The microstructure was revealed using the L-B color etching solution at 60 °C for times ranging 15–30 s. As mentioned in *Section 4.3.1*, both temperature and etching time are factors influencing the resulting etching color. Shorter etching times (15 s) lead to yellowish colors, whereas longer times (20–30 s) result in bluish tones. For this reason, and in addition to the effect of the chemical banding on the resulting etching color, the martensitic matrix appears etched in different shades of blue, green and yellow. However, both retained and new formed austenite are etched in pale yellow or white and the χ-phase remains white. The volume fraction of austenite appears to increase after 24 h aging at 500 °C, as the greater number of white islands in Figure 7.2(d) indicate, compared to the counterpart at 400 °C (Figure 7.2(d)).

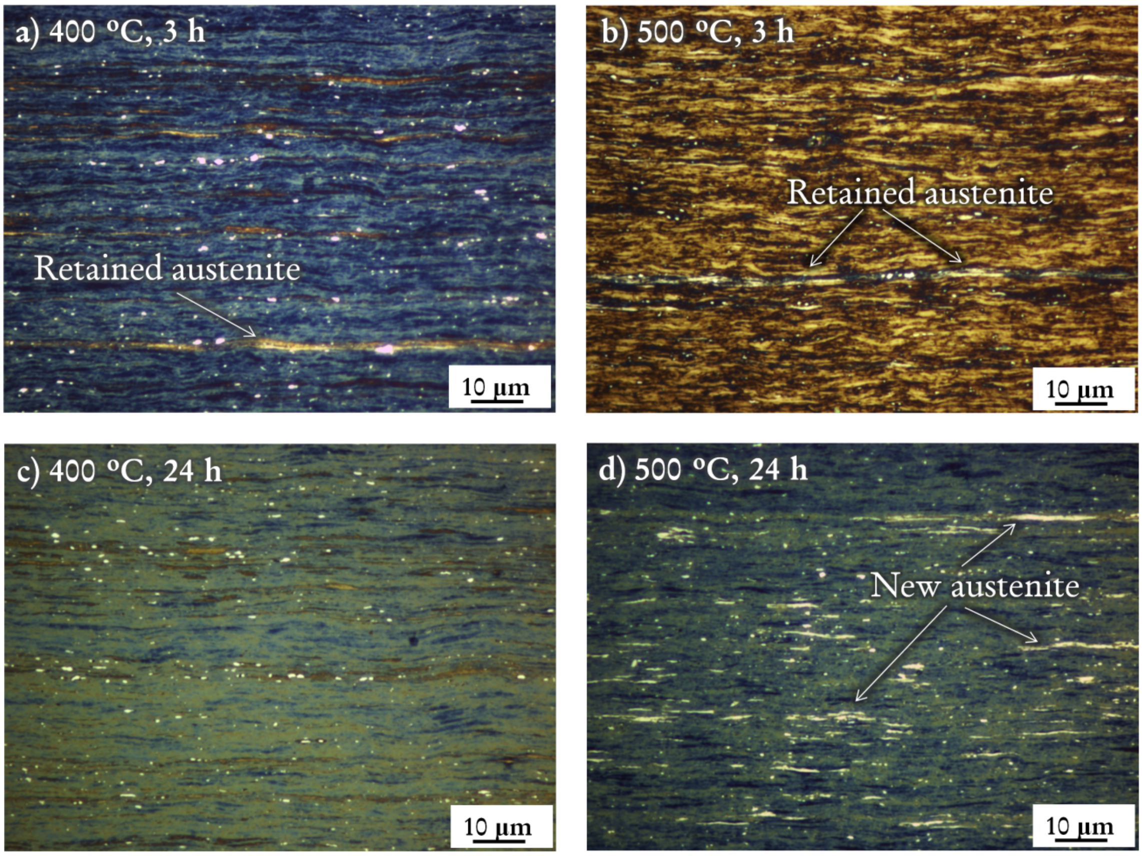

Figure 7.2 – Optical micrographs of samples aged: (a) 400 °C. 3 h; (b) 500 °C, 3 h; (c) 400 °C, 24 h and (d) 500 °C, 24 h. The microstructure was revealed with the hot L-B color etching solution.

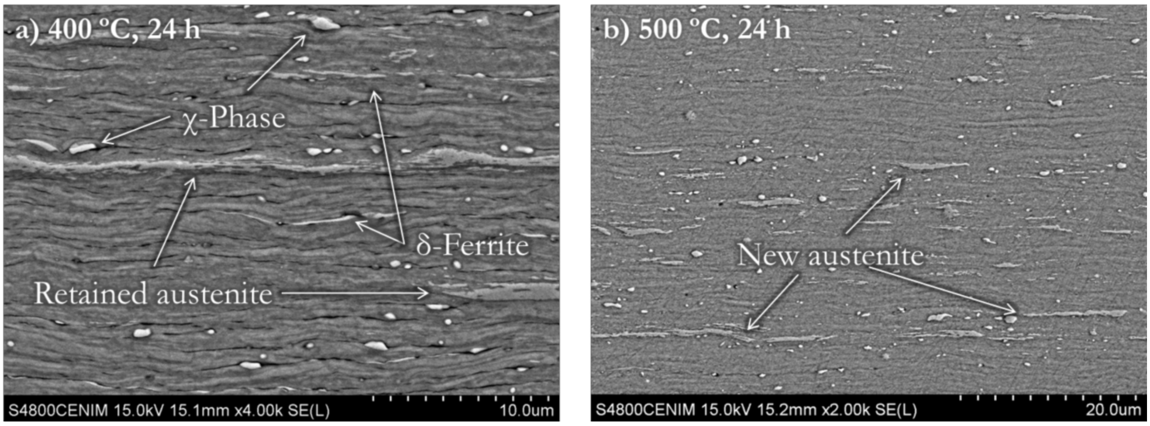

Figure 7.3. Scanning electron micrographs of the material after aging at: (a) 400 °C, 24 h and (b) 500 °C, 24 h. The microstructure was revealed with the hot L-B color etching solution.

Figure 7.3 displays SEM micrograph of specimens aged for 24 h at 400 and 500 °C. The recovery the material undergoes during aging discloses the shear bands (parallel to the rolling direction) and highlights the presence of δ-ferrite and austenite phase. The combination of the OM and SEM helps to clarify whether the austenite phase is forming upon long isothermal holding times or not. After 24 h aging at 400 °C (Figure 7.2(c) and Figure 7.3(a)) the austenite appears forming elongated bands in the rolling direction, similarly as observed in the CR state. However, the specimen aged at 500 °C shows a great number of new austenite islands randomly distributed in the matrix and exhibiting different sizes (Figure 7.2(d) and Figure 7.3(b)). Although the studied range of aging temperatures is below the austenite starting transformation temperature detected upon heating at 0.1 °C/s (A_S ~600 °C), optical and scanning electron microscopy point out that long aging treatments seem to enhance the kinetics of the α'→γ transformation at temperatures as low as 500 °C.

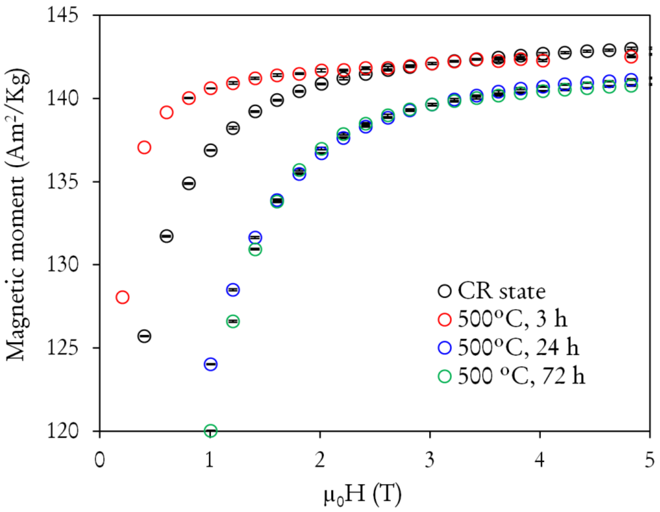

Figure 7.4. Evolution of the magnetic moment as a function of the applied magnetic field (μ₀H) of the material aged at 500 °C for 3, 24 and 72 h. The CR magnetization curve is included for comparison.

In order to quantify the volume fraction of new austenite phase, magnetization measurements were done on samples aged for 3, 24 and 72 h at 500 °C. Figure 7.4 displays the magnetization curves as function of the applied magnetic field (μ_0H). As explained in *Section 3.3*, the volume fraction of austenite was estimated using equation [3.3] and taking into account that the volume fraction of χ-phase remains close to the initial value (~0.02). A summary of these results is shown in Table 7.2. Whereas no austenite forms after 3 h aging, the isothermal holding for 24 h results in a volume fraction of about 0.04 that remains constant with further aging to 72 h. However, it is important to bear in mind that the precipitation during aging modifies the composition of the matrix, which in turn alters the magnetization of the alloy. The higher the volume fraction of precipitates, the larger the depletion in alloying elements in the matrix becomes and the higher the relative Fe content is [204]. In consequence, the magnetization saturation of the precipitated matrix may be larger than that of the CR material ($M_{sat}^{\alpha'} = 147$ Am^2/Kg). Therefore, the volume fractions of austenite may be larger than 0.04.

Table 7.2. Summary of the results of volume fraction of austenite, f_γ, obtained from the magnetization measurements performed on the cold-rolled (CR) state and samples aged at 500 °C for 3, 24 and 72 h.

Sample	$(\mu_0 H)_{sat}$ (T)	M_{sat} (Am^2/Kg)	f_γ
CR-state	3.82	142.59	0.02 (0.01)
500 °C, 3 h	1.21	141.89	0.02 (0.01)
500 °C, 24 h	3.62	140.18	0.04 (0.01)
500 °C, 72 h	3.62	140.20	0.04 (0.01)

Additionally, it is possible to extract some information from the approach to the saturation values $(\mu_0 H)_{sat}$ since it is representative of the interaction microstructure-movement of magnetic domains as an external magnetic field is applied. It has been demonstrated that the greater the amount of stored deformation, i.e. dislocation density, the higher the magnetic field needed to reach M_{sat} in a sample is [205]. On the other hand, precipitates have been found to act as pinning sites for the movement of magnetic domain walls [206]. For this reason, the 3 h-aged specimen reaches the saturation more easily ($(\mu_0 H)_{sat}$ ~1.21 T) than the as-received material ($\mu_0 H$ ~3.82 T), since the recovery in the initial stages of aging is significant. However, stronger magnetic field is needed to saturate the long-aged specimens, since the more important precipitation of nanometric particles obstruct the magnetic domains wall movement.

7.2.3 Characterization of the $Ni_3(Ti,Al)$ nano-precipitates by TEM and HRTEM

Due to their small size, the transmission electron microscopy could not resolve the precipitates of specimens aged at 400 °C, even after 72 h of aging. The precipitates become distinguishable at 450 °C and 24 h aging and at 500 °C after 3 h aging. TEM micrographs at different stages of aging at 450 and 500 °C are shown in Figure 7.5–Figure 7.8. In order to understand phase transformations and their kinetics, e.g. precipitate growth and coarsening, it is necessary to quantitatively determine microstructural parameters such as volume fraction, size distribution and number density using stereological methods. Attempts to use conventional TEM to determine such quantitative data for fine features have generally not been very successful. Even with a HRTEM it is difficult to distinguish the precipitates since the diffraction contrast used for imaging introduces a number of contrast effects that do not reflect the microstructure itself but rather thickness and orientation variations in the specimen. In practice, such phenomena (thickness and bend fringes, strain contrast including contrast from dislocations, orientation dependent contrast from the same phase, etc.) make automatic evaluation very difficult and manual evaluation very uncertain. Instead of using diffraction contrast for imaging, inelastic scattered electrons may be used. This means that contrast is produced by variations in composition rather than in crystal structure and orientation, which gives rise to a high contrast essentially free from diffraction phenomena. This is done in annular dark field (ADF) or high angle annular dark field (HAADF) imaging. Contrast in HAADF arises from the difference in mean atomic number of the phases (Z contrast).

a) 450 °C, 24 h

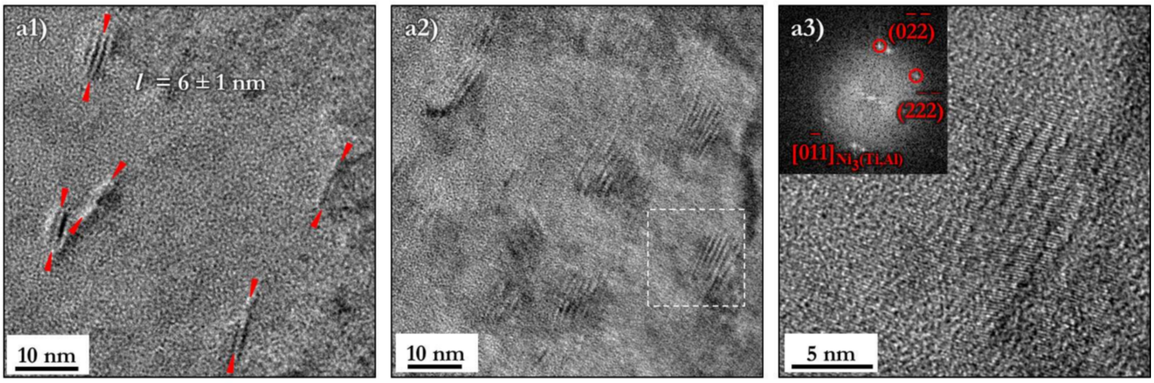

b) 450 °C, 72 h

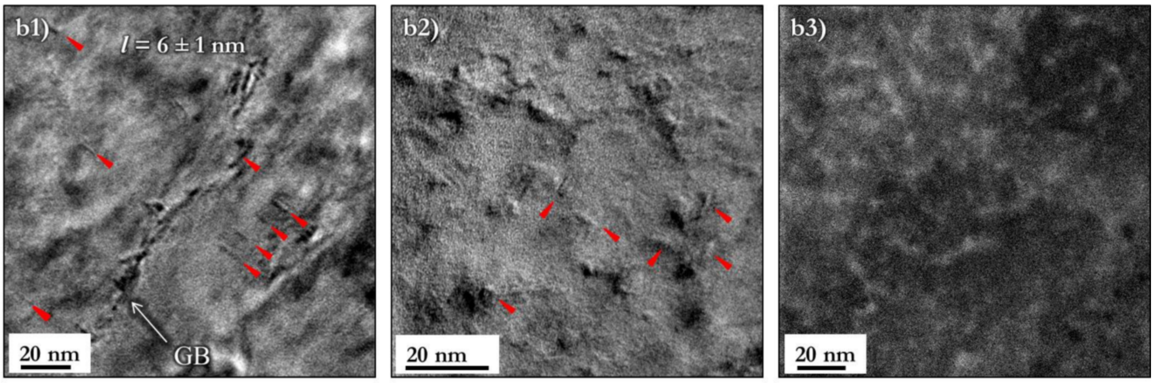

Figure 7.5. HRTEM images of a sample aged at 450 °C for (a) 24 h and (b) 72 h. (a1) and (a2) show rod-like precipitates of *l* ~6 ± 1 nm pointed by red arrows. Figure (a3) shows a magnification of the precipitate in the area framed in (a2) and the its FFT indexed as Ni_3(Ti,Al) phase. (b1) and (b2) highlight rod-like precipitates of of *l* ~6 ± 1 nm aligned along two preferential directions. (b3) STEM image obtained with an annular dark field (ADF) detector where precipitates appear brighter than the matrix due to their different composition.

Figure 7.5 presents HRTEM images of the material after aging at 450 °C for 24 h (a) and 72 h (b), in which the presence of rod-like precipitates is observed. The contrast from these precipitates is weak and, to a large extent, obliterated by contrast from the highly dislocated martensite. Therefore, no estimation of their volume fraction could be done. It was possible, however, to estimate the long axis size of the nano-rods in more than five HRTEM images, resulting in 6 ± 1 nm in terms of the mean value and its standard deviation (Figure 7.5 (a1)). Figure 7.5 (a2) displays another HRTEM where the precipitates seem to be wider and present a more rounded shape. However this image is misleading since the dislocation pile-ups where the precipitates nucleate and grow are also visible. Figure 7.5 (a3) is a magnification of the precipitate framed with white dashed line in (a2), and its corresponding FFT (Fast Fourier Transform) pattern. The diffraction spots marked in green were indexed as reflections $(0\bar{2}2\bar{2})$ and $(2\bar{2}0\bar{2})$ of the $[0\bar{1}1]$ zone axis of the Ni$_3$(Ti,Al) phase (hexagonal, $a = 0.511$ nm, $c = 0.823$ nm) [47]. Figure 7.5 (b1)-(b2) display HRTEM micrographs in which it is difficult to detect the precipitates due to the diffraction contrast used for imaging. Some precipitates were marked with red arrows. In the same manner as for the 24 h-aged sample, the long axis of the rods (l) was estimated in 6 ± 1 nm. It is surprising that the mean size of these precipitates remains essentially constant with increasing aging times at 450 °C. A better contrast is obtained in Figure 7.5 (b3), which shows an STEM image generated with an annular dark field (ADF) detector. In this image the diffraction contrast is minimized and the mass-thickness contrast is enhanced. The image, however, is quite noisy since the specimen is thin and, thus, the number of picked-up back-scattered electrons is small. Although it is not possible to estimate the volume fraction of precipitates from the STEM image, it gives an idea of their distribution.

Figure 7.6 and Figure 7.7 show TEM BF and HRTEM images of samples aged at 500 °C for 3 and 24 h, respectively. In these cases not only the long axis (l), but also the diameter (d) of the particles was measured, since they appear to be well defined in the images. For this purpose, more than five representative HRTEM images were used per condition and values of $l = 12 \pm 4$ nm and $d = 3 \pm 2$ nm were obtained after 3 h aging and values of $l = 29 \pm 5$ nm and $d = 6 \pm 1$ nm, after 24 h aging. The particle long axis of the 24 h-aged specimen at 500 °C is, therefore, five times greater the particle length of its counterpart at 450 °C. Figure 7.6 (d)-(e) display a magnification of the framed area in Figure 7.6 (c) and its corresponding FFT, respectively. The FFT pattern shows some additional spots, likely generated by the matrix. In order to attribute the origin of spots to specific regions of the high-resolution image in (d), Fourier filtering was applied. The inverse FFT (IFFT) image of Figure 7.6 (f) was obtained by extracting the strong signal of the FFT (circled in red) using filtering mask on the reflections $(\bar{2}000)$, $(0\bar{2}2\bar{2})$ and $(2\bar{2}0\bar{2})$ of the Ni$_3$(Ti,Al) phase. When applying a Fourier filter over the precipitates reflections, the martensitic matrix contribution is removed and the structure of the precipitates is shown more clearly. Figure 7.6 (f) points out that the selected spots are related to the $Ni_3(Ti,Al)$ phase.

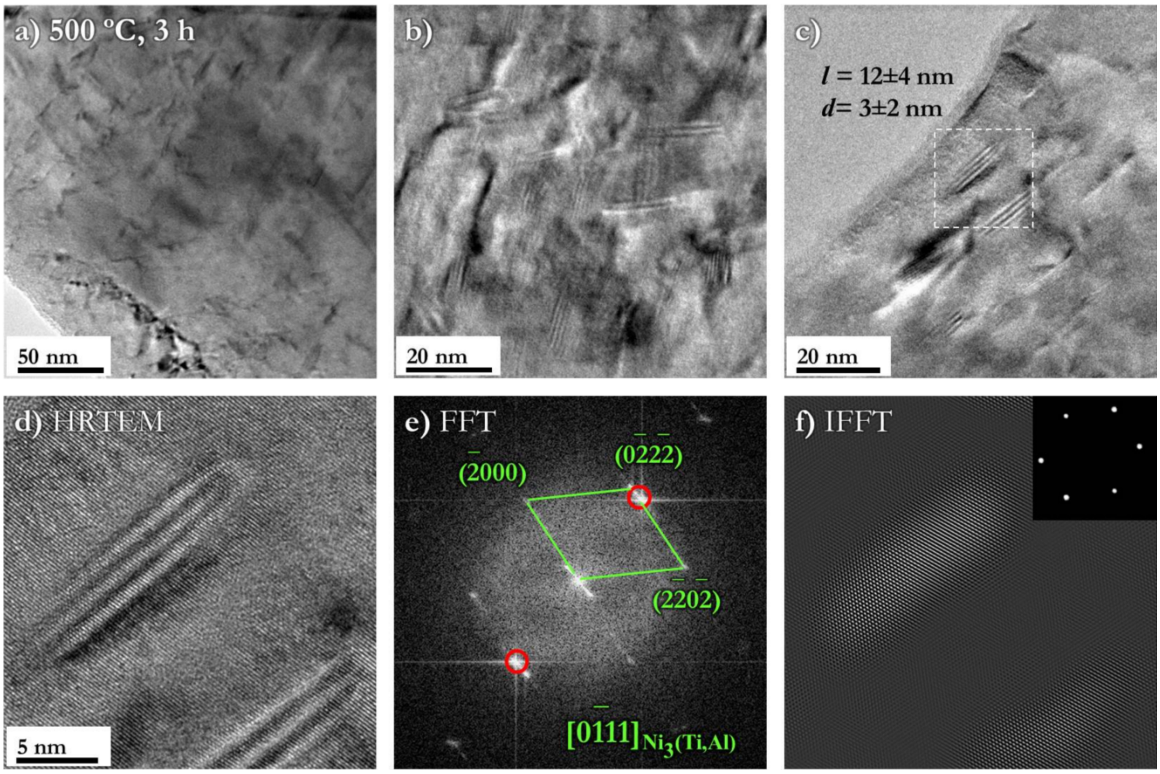

Figure 7.6. TEM images of a specimen aged 3 h at 500 °C. (a) BF TEM image; (b-c) HR TEM images; (d) magnification of area framed in (c); (e) fast Fourier transforms (FFT) patterns; and (f) Inversed FFT (IFFT) of selected spots supporting reflections indexed in (e) as $Ni_3(Ti,Al)$ phase. Average length (*l*) and diameter (*d*) of the rods have been indicated in (c).

TEM images of a sample aged at 500 °C for 24 h are displayed in Figure 7.7. From the comparison of Figure 7.7 (a)-(b) and Figure 7.6 (a)-(b), the 3 h-aged condition, it is apparent that the volume fraction of precipitates has increased significantly. The mean long axis and diameter values were estimated in 29 ± 5 nm and 6 ± 1 nm, respectively. Figure 7.7 (c) displays the DP of b, where the $Ni_3(Ti,Al)$ reflection used to generate the DF in Figure 7.7 (b) have been circled in green and the martensitic matrix presents a [111] orientation. The HRTEM image in Figure 7.7 (d) shows two $Ni_3(Ti,Al)$ particles whose long axis have grown parallel to two preferential directions of the matrix. Their long axes are oriented ~70° to each other. The corresponding FFT pattern is displayed in Figure 7.7 (e) and reveals the existence of the well-known orientation relationship between the martensite and the $Ni_3(Ti,Al)$ precipitates: $(1\bar{1}0)_{\alpha'} \| (0001)_{Ni_3(Ti,Al)}$ and $[1\bar{1}1]_{\alpha'} \| [11\bar{2}0]_{Ni_3(Ti,Al)}$ [95].

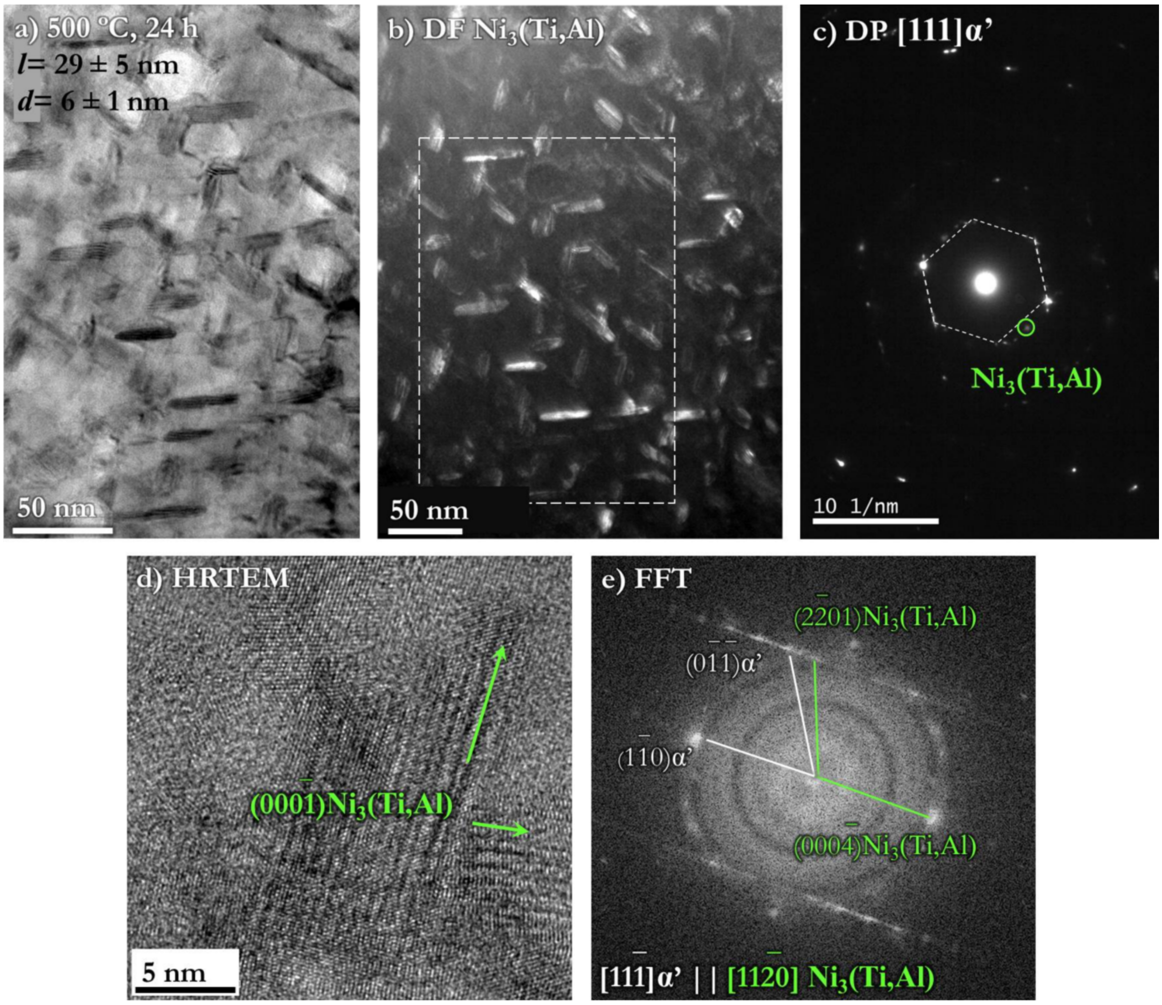

Figure 7.7. TEM images of a specimen aged for 24 h at 500 °C. (a-c) BF, corresponding DF and DP. The $Ni_3(Ti,Al)$ reflection marked in green was used to generate the DF in (b); (d) HRTEM image of two $Ni_3(Ti,Al)$ precipitates aligned along preferential directions. (f) FFT pattern from (d) pointing out the existence of a $[1\bar{1}1]_{\alpha'} \| [11\bar{2}0]_{Ni_3(Ti,Al)}$ OR between the martensite and the $Ni_3(Ti,Al)$ precipitates.

Finally, Figure 7.8 (a)-(c) show STEM images generated using incident convergent beam and a BF on-axis detector, which picks up the direct beam and, thus, electrons scattered at low angles. This means that the main contrast comes from diffraction instead of from composition. A good contrast is obtained since the crystalline structure of precipitates and matrix is different. Figure 7.8 (a) displays the corresponding BF of the area where the STEM image (b) was taken. Figures (c) and (d) show magnifications of areas framed in red in (b) and numbered as ① and ②.

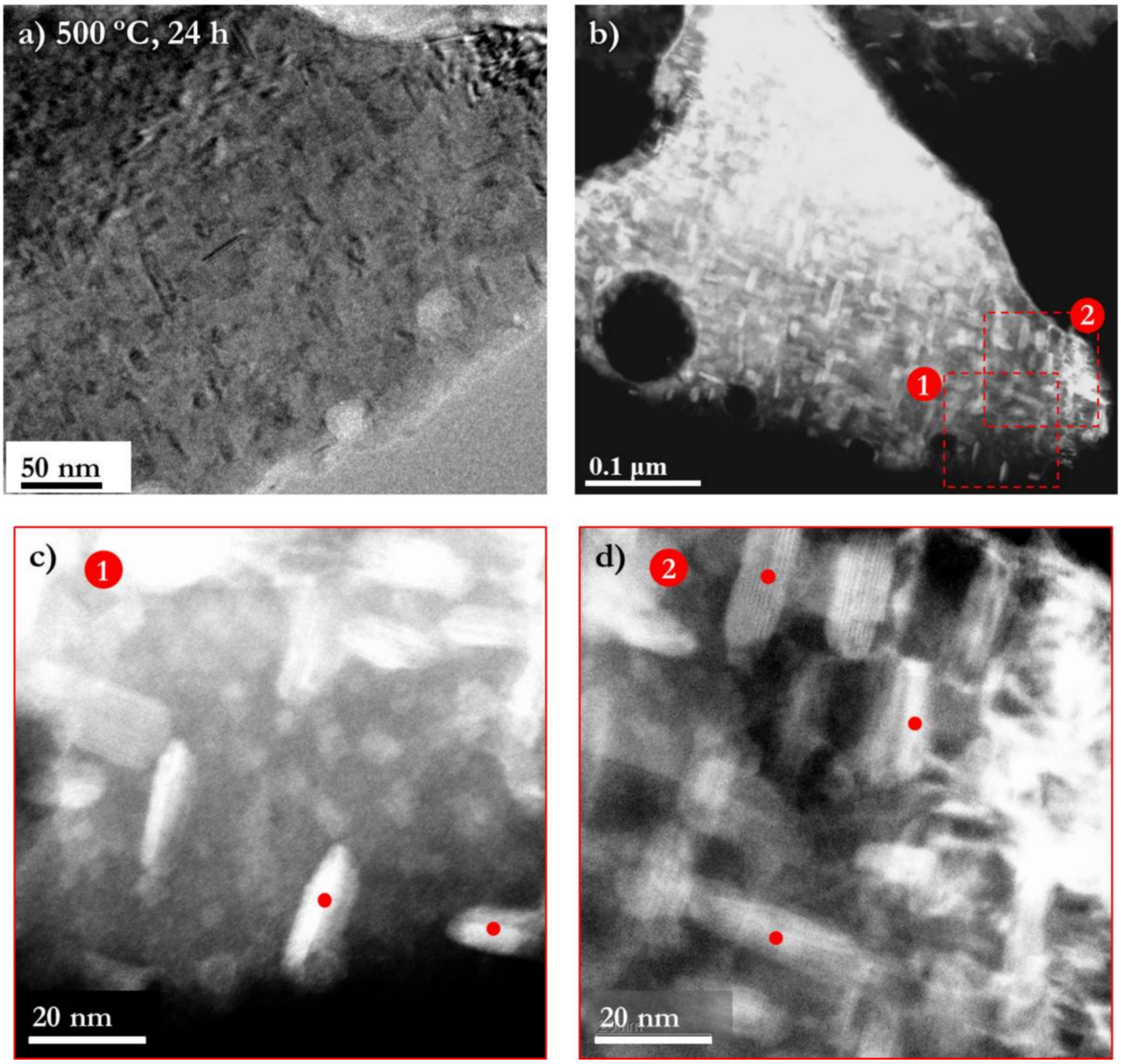

Figure 7.8. Sample aged at 500 °C for 24 h. (a) BF image, (b) BF STEM image and (c, d) magnifications of areas framed in (b). TEM-EDS microanalyses of precipitates (marked with a red spot) and matrix are summarized in Table 7.3.

TEM-EDS microanalyses were performed on the rod-like precipitates marked with a red spot and the matrix. The results in terms of mean value and standard deviation are summarized in Table 7.3 and compared with the nominal composition of the steel. These results suggest a stoichiometry similar to the one of $Ni_3(Ti,Al)$. The high Cu content is not surprising since the nucleation and growth of the $Ni_3(Ti,Al)$ precipitates takes place at Cu-clusters that form at the very beginning of the precipitation sequence. However, this Cu is not integrated in the crystalline structure of the precipitates and remains next to them [51]. On the other hand, the relative high content of Cr is not surprising either. As $Ni_3(Ti,Al)$ the precipitates grow, a distribution of the Ni, Ti and Al occurs within the precipitates and other elements as Cr and Mo are rejected into the matrix and the precipitate-matrix interfaces [95]. In addition to the rod-like particles, round-shaped precipitates of about 5 nm are also observed in Figure 7.8 (c). Due to their small size, no fair TEM-EDS microanalyses could be done on them, but on the matrix. As expected, and as a result of the rejection of Cr and Mo from the $Ni_3(Ti,Al)$ precipitates to the matrix, the matrix EDS microanalysis detected an enrichment in Cr and Mo and a depletion in Cu, Ni, Ti and Al.

Table 7.3. TEM-EDS microanalyses results (in at. % and wt. %) of the $Ni_3(Ti,Al)$ precipitates and the matrix obtained from a sample aged at 500 °C for 24 h. The nominal composition of the steel is included for comparison.

Element	$Ni_3(Ti,Al)$ (at. %)	$Ni_3(Ti,Al)$ (wt. %)	Matrix (wt. %)	Nominal composition (wt. %)
Al	3.6 ± 2.1	1.8 ± 1	–	0.39
Ti	5.5 ± 1.9	4.8 ± 1.7	0.2 ± 0.3	1.35
Cr	10.5 ± 2.5	9.7 ± 2.3	15.1 ± 1.1	12.00
Fe	49.3 ± 8.6	49.2 ± 8.8	74.3 ± 2	70.74
Ni	22.1 ± 5.1	23.2 ± 5.6	3.9 ± 0.8	8.87
Cu	6.6 ± 6.3	7.5 ± 7	0.8 ± 0.9	1.91
Mo	2.3 ± 1.3	4 ± 2.2	5.9 ± 2.7	4.05

7.2.4 Tensile characterization

Typical effects of the influence of aging temperature and time on the ultimate tensile strength (σ_{UTS}), yield strength ($\sigma_{y0.2}$) and uniform and total elongation (ε_u and ε_t, respectively) are shown in Figure 7.9. As for the microstructural characterization, just the aging temperatures of 400, 450 and 500 °C were studied under uniaxial tensile testing on sub-size specimens. Two tests were done per condition to study the reproducibility. For comparison, the stress-plastic strain curve of the CR material (black curve) was included. At first sight, it is observed that the material aged at 400 and 450 °C behaves similarly, whereas at 500 °C it behaves somewhat differently.

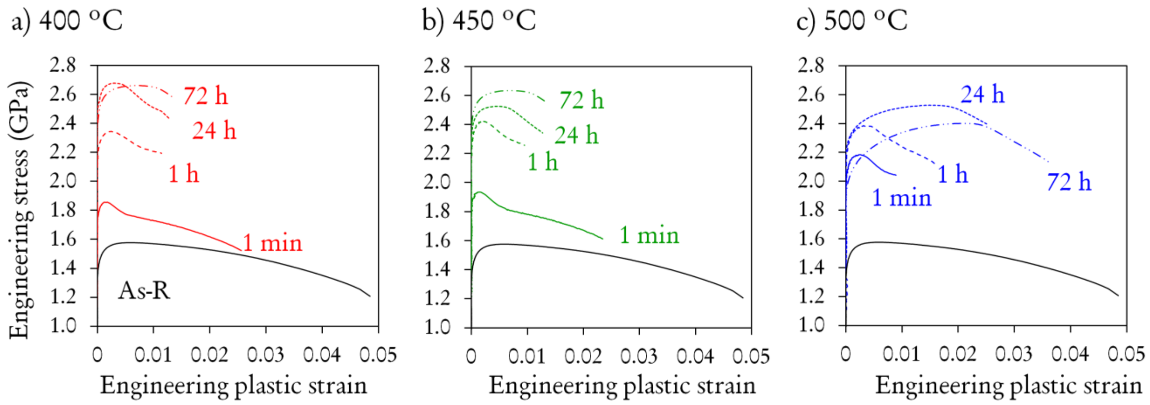

Figure 7.9. Engineering stress-plastic strain curves obtained for the aging times of 1 min, 1 h, 24 h and 72 h at the aging temperatures: (a) 400 °C, (b) 450 °C and (c) 500 °C. The curve obtained in the as-received material (black line) is included in all graphics as a reference.

Table 7.4. Values of the 0.2 % offset yield strength ($\sigma_{y0.2}$), which appears shaded, and the ultimate tensile strength (σ_{UTS}) obtained for the as-received state and at various aging conditions. All values are given in GPa.

As-received state	T, °C	Aging time			
		1 min	1 h	24 h	72 h
	400	1.88 ± 0.21	2.34 ± 0.02	2.63 ± 0.05	2.61 ± 0.02
		1.88 ± 0.04	2.35 ± 0.01	2.64 ± 0.05	2.66 ± 0.01
$\sigma_{y0.2}$: 1.56 ± 0.04 GPa	450	1.93 ± 0.01	2.43 ± 0.01	2.59 ± 0.1	2.61 ± 0.01
		1.94 ± 0.01	2.43 ± 0.01	2.61 ± 0.12	2.65 ± 0.02
σ_{UTS}: 1.58 ± 0.01 GPa	500	2.16 ± 0.02	2.36 ± 0.02	2.36 ± 0.01	2.13 ± 0.01
		2.17 ± 0.02	2.37 ± 0.02	2.51 ± 0.02	2.4 ± 0.01

Values of 0.2 % offset yield strength ($\sigma_{y0.2}$) and ultimate tensile strength (σ_{UTS}) extracted from the stress-plastic strain curves are summarized in Table 7.4. It is observed that σ_{UTS} values are very close to $\sigma_{y0.2}$ values or are even the same. This is indicative of a very low work-hardening ability of the material, as expected from the aged state. As observed in Figure 7.9, the engineering stress-plastic strain curves, except aging conditions beyond 24 h, exhibit a peak-stress at relatively small plastic strains followed by a continued decrease of stress. The low $\sigma_{UTS}/\sigma_{y0.2}$ ratio indicates that the tolerance to plastic overload is small as the work hardening after yielding is minimal and after the maximum stress peak is non-existent [33]. As expected, the strength increment at 400 and 450 °C for aging times below 1 h involves a significant reduction in the total elongation. However, aging times longer than 1 h result in the increment of both strength and, slightly, the total elongation. Besides, a change in the shape of the engineering stress-strain curve is obtained after 72 h aging: there is no early stress peak, but a continuous yielding until the maximum stress is reached. This results in a higher work hardening ability, as the higher tensile to yield strength ratio indicates. This effect is more pronounced at 500 °C, where, in addition to the change in the curve shape, a decrease in strength is detected after 72 h aging.

7.3 Discussion

7.3.1 Aging kinetics and thermodynamic calculations

The classical analyses of phase-transformation kinetics was formulated in the late 1930s by several researchers: Johnson and Mehl [207], Avrami [208-210] and Kolmogorov [211]. Since then, it has been referred to Johnson-Mehl-Avrami-Kolmogorov (JMAK), Johnson-Mehl-Avrami (JMA) or simply the Avrami kinetic equation. This model pertains to isothermal transformations and assumes homogeneous/random nucleation in the parent phase, which allows relating the real transformed fraction of a specimen with the hypothetical, so-called extended transformed fraction, which is defined as the volume fraction of all growing grains if they could nucleate and growth isotropically in an infinitely large parent phase in the absence of other nuclei. The JMAK equation is formulated as follows:

$$f(t) = 1 - e^{-k(T)t^n} \qquad [7.1]$$

where $f(t)$ is the fraction transformed as function of time, n is the Avrami exponent and $k(T)$ is a temperature-dependent factor: $k(T) = k_0 e^{(-Q/k_B T)}$, where k_0 is the preexponential factor, k_B is the Boltzman constant and Q is the activation energy associated to the transformation. The Avrami exponent is given as $n = ab + c$, where the parameters a, b and c are related to the nucleation and growth processes as follows [212-214]. The parameters a and b are related to the dimensionality of the growth (1, 2 or 3) and the type of growth (1 for interface-controlled growth and ½ for diffusion-controlled growth), respectively. The parameter c is related to the type of nucleation rate (it takes 0 for site saturation, 1 for a constant nucleation rate, between 0 and 1 for decreasing nucleation rate and higher than 1 for autocatalytic nucleation processes).

Although the JMAK equation has been used in the analysis of precipitation reactions of maraging and precipitation hardening steels [9; 11; 16; 40; 42; 215], it has also been proved that this approach is only correct when nucleation is random and growth is linear, but no such proofs exists for diffusion-controlled growth. This relation ignores the fact that the growth of precipitates slows down before the physical interaction between precipitates takes place due to the saturation of untransformed regions with the elements diffusing away from the interface. In this sense the JMAK relation underestimates the impingement effect. Hence, the approximation can be expected to hold only for limited transformed fractions [216; 217]. The phenomenological Austin-Rickett (AR) equation has been found to provide a better fit for nucleation and growth reactions like bainite formation in shape-memory alloys [218] and precipitation reactions in aluminum alloys [214] and Fe-Cr-Al ferritic alloys [219]. In the AR relation $f(t)$ is written as:

$$\frac{f(t)}{1 - f(t)} = k(T)t^n \tag{7.2}$$

where the kinetic parameters have the same meaning that those in the JMAK relation.

In this section, the ability of the JMAK equation to fit the experimental data is compared with the AR equation. For this purpose the fraction precipitated, $f(t)$, is taken to be proportional to the hardness change according to:

$$f(t) = \frac{H_t - H_0}{H_{max} - H_0} \quad [7.3]$$

where H_t is the hardness at a certain isothermal aging time t and H_{max} and H_0 are the peak-hardness and the initial hardness values obtained for each aging temperature shown in Figure 7.1. It is important to bear in mind that this leads to $f(t) = 1$ at the peak-hardness, which is not necessarily the case. Particularly, for the steel under investigation, the precipitation reactions near the peak condition is quite complex as different precipitate reactions occur simultaneously with coarsening and austenite reversion. Thus, the relationship between hardness and precipitated fraction is difficult to be evaluated experimentally and the calculated value from equation [7.3] is, therefore, approximate. Rewriting the JMAK and AR equations by using logarithms, equations [7.4] and [7.5] are obtained.

$$\ln \ln \left[\frac{1}{(1 - f(t))}\right] = \ln k(T) + n \ln t \quad [7.4]$$

$$\ln \left[\frac{f(t)}{(1 - f(t))}\right] = \ln k + n \ln t \quad [7.5]$$

Table 7.5. Evolution of *n* and *k*(T) values for JMAK and AR equations for the aging temperatures tested.

T (ºC)	T (K)	JMAK			AR		
		n	ln *k*(T)	R^2	*n*	ln *k*(T)	R^2
400	673	0.53	-4.59	0.986	0.69	-5.29	0.986
425	698	0.42	-3.52	0.973	0.58	-4.14	0.992
450	723	0.38	-2.48	0.964	0.53	-2.86	0.989
475	748	0.34	-2.33	0.968	0.43	-2.48	0.961
500	773	0.35	-1.33	0.920	0.65	-1.84	0.959

According to these equations, Figure 7.10 (a) and (b) show respectively the evolution of $\ln \ln[1/(1 - f(t))]$ and $\ln[f(\mathrm{t})/(1 - f(\mathrm{t}))]$ as a function of aging time for the aging temperatures between 400 and 500 ºC. The data points were fitted to straight lines. The slopes and intercepts of these lines represents the Avrami exponent n and $\ln k(T)$, respectively, which are summarized along with the corresponding correlation factor

(R^2), is shown in Table 7.5. As observed, the fitting provided by both JMAK and AR models is quite good, although some deviations are found in the values of n exponent. Those n values obtained from AR model are closer to theoretical values predicted by the Cottrel and Bilby [220] or Harper [221] models for precipitation on dislocations ($n \sim 1/3 - 2/3$) than n values obtained from JMAK model.

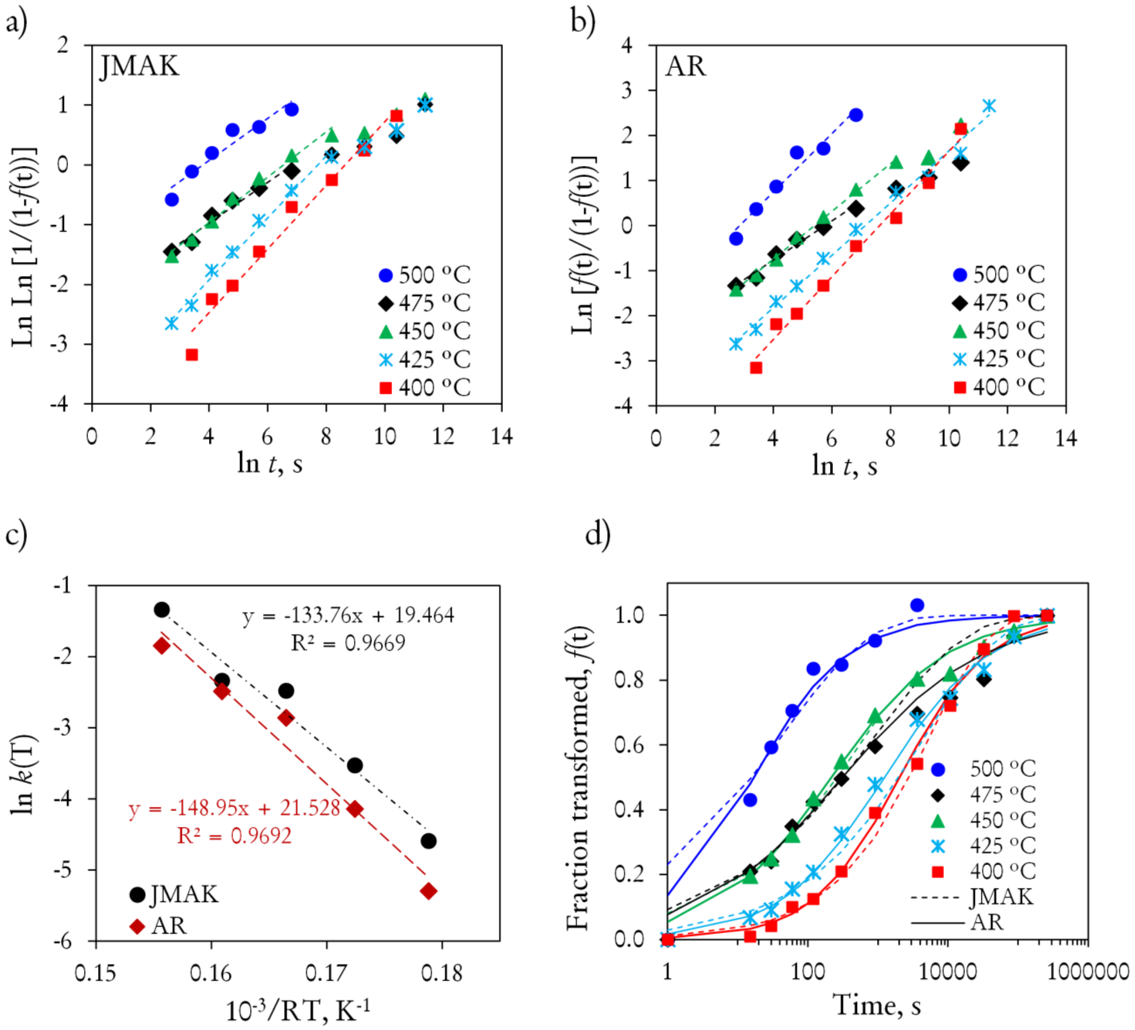

Figure 7.10. Kinetic analyses of aged material at 400, 425, 450, 475 and 500 ºC. (a) Plot of lnln[1/(1-*f*(t))] vs. ln *t* (JMAK equation); (b) Plot of ln[α/(1-α)] versus ln *t* (AR equation); (c) plot of ln *k*(T) vs. 1/*T* derived from the linear fits obtained from (a) and (b); and (d) comparison between experimental data and calculated evolution of the precipitated fraction according to the kinetic constants obtained by JMAK and AR models

Regarding the activation energy of the process (Q), it has been derived from the slope of the $\ln k(T)$ vs. $1/RT$ plot presented in Figure 7.10 (c) and obtained from the values listed in Table 7.5. As indicated by the linear regressions, values of 134 kJ/mol and 149 kJ/mol were obtained from the JMAK and AR relations, respectively. Similar values are reported by Sinha *et al.* [42] in maraging stainless steel, and it is associated to the Cu/Ni diffusion in dislocations, which is approximated half the value of bulk diffusion (260-280 kJ/mol). Either the JMAK or AR model provide a good fit of the evolution of precipitated fraction over the aging time, as presented in Figure 7.10 (d). The estimation of the activation energy for the precipitation process in the steel under investigation is, therefore, in good agreement with previous experimental observations [52; 94]. Although the precipitation sequence in this steel is complex, it is well-known from the literature that Cu-clusters form within the first minutes of aging that act as nucleation sites for the $Ni_3(Ti,Al)$ phase, as identified in this work by TEM-EDS microanalysis in *Section 7.2.3*. Only after long aging times (100 h) other phases contribute significantly to the hardness [94].

For comparison with the experimental observations, thermodynamic calculations using the ThermoCalc package with the SSOL4 database were carried out. Driving forces ($\Delta G/RT$, where ΔG is the Gibbs energy change, R is the universal gas constant and T is the temperature) were computed for various phases in a BCC matrix (Table 7.6). A positive driving force indicates a tendency for the phase to be formed. It has to be mentioned that, among all the possible equilibrium phases predicted for this steel, just those similar to the experimental observations were allowed to become equilibrium phases. Phases such as Laves (Fe_2Mo) and μ (Fe_7Mo_6) phases were excluded since they appeared as equilibrium when included in the calculations but presumably do not form due to slow nucleation and growth. The precipitation of the predicted phases in Table 7.6 is commented as follows: copper is the most unstable element in solid solution and readily precipitates forming clusters; subsequently, the Ni_3Ti phase precipitates, apparently enriched in Al, as experimentally observed. Regarding the formation of FCC austenite, it has been observed on conventional maraging steels that long holding times influence the kinetics of re-transformation from martensite to austenite [43], so it is not surprising that heat treatments longer than 24 h at 500 °C entail the formation of austenite in the steel under investigation (Table 7.2). Increasing nickel levels generally tend to accelerate austenite formation rate. In the steel under investigation, the presence of a chemical banding (especially pronounced for Ni) makes possible the transformation of those bands leading to elongated austenite islands along the rolling direction plane, as shown in Figure 7.3. In addition to the formation of austenite, it was observed in *Section 5.2.3* that $Ni_3(Ti,Al)$ precipitates dissolve within this phase. This chain of events reduces the strength and increases the uniform elongation.

Table 7.6. Equilibrium phases and driving forces ($\Delta G/RT$) of different phases in the BCC martensitic matrix at different temperatures. Calculations were done with the software ThermoCalc and the SSOL4 database.

Phase	300 °C	400 °C	500 °C	600 °C
HCP (Cu-rich)	8.59	6.60	3.81	3.79
Ni_3Ti	3.38	2.37	1.02	0.96
Al_3Ni_5	2.29	1.44	0.76	0.18
Sigma (Cr,Mo)(Fe,Ni)	1.13	1.05	0.02	0.15
R-Phase (Mo-rich)	0.78	0.44	0.14	-
χ-phase ($Fe_{36}Cr_{10}Mo_{12}$)	0.56	0.33	0.17	0.05
FCC	8.74	6.73	5.17	3.89

7.3.2 Microstructural evolution during aging: impact on hardness and thermoelectric power

When the as-received state of the steel under investigation is aged in the range of temperatures 300–550 °C, precipitation hardening occurs, as shown in *Section 7.2.* Whereas for aging temperatures of 500 °C or higher overaging is observed, between 300 and 475 °C the hardness increases continuously up to 72 h. Actually, the maximum precipitation hardening effect was found in the range 400-475 °C after 72 h, causing an increment of 300 Hv in hardness and more than 1000 MPa in strength, compared to the CR state. The strengthening is attributed to:

- The formation of very small Cu-clusters within the first 5 min of aging. As reported by Thuvander [95] and Stiller [51], the aging of the steel under investigation at 475 °C produces the formation of clusters rich in Cu, Ni, Ti and Al in the very early stages of aging. The study of the microstructure at this nanometric scale requires the use of powerful techniques such as APT or 3-DAP. They found by APT that Cu clustering was the most pronounced, which is not surprising since the solubility of Cu in ferrite or martensite is very low at temperatures below 500 °C [222]. This may be the reason of the important hardening observed after just 1 s of isothermal aging at 450 and 550 °C, which causes a hardness increment of 18 % and 30 %, respectively. Besides, the surfaces of those Cu-clusters act as nucleation sites for Ni-rich precipitates, such as $Ni_3(Ti,Al)$ and $Ni_3(Ti,Al,Si)$, as Hättestrand *et al.* [52] and Thuvander *et al.* [95] demonstrated, which would explain the high Cu content detected by TEM-EDS in the rod-like $Ni_3(Ti,Al)$ phase (Figure 7.8, Table 7.3)
- The homogeneous and fine distribution of nanosized $Ni_3(Ti,Al)$ precipitates, as observed from TEM images (Figure 7.5–Figure 7.7), plays a crucial role in the hardening. This fine distribution of precipitates stems from the high dislocation density in the CR microstructure, which provides a great number of nucleation sites for precipitation [52].
- The effect of the mean particle size. It was estimated to be about 6 nm after 24 h aging at 450 °C, without significant variations after 72 h. Even after 24 h aging at 500 °C the mean particle size was about 30 nm.
- The resistance to coarsen of precipitates. This has been attributed by other authors to the segregation of Mo at the precipitate/matrix interface [51] and to the orientation relationship of the precipitates with the matrix [47]. However, it is believed that the strengthening mechanism plays also a crucial role.

As introduced in *Section 1.5.3*, depending on the particle size either the shearing or Orowan bowing may be the active strengthening mechanism (Figure 1.8). It is accepted for maraging steels that the critical radius at which the change in the mechanism occurs takes place is about 15*b*, being *b* the Burgers vector [47]. For a α-Fe system the critical radius is about 3.8 nm, which can be translated in a diameter value of 7.6 nm. Therefore, the particle size for aging treatments at 450 °C remains below its critical radius over the studied aging times, being the particle shearing the active strengthening mechanism. This would explain the continuous hardening for aging temperatures in the range 400 – 475 °C. Instead, the 500 °C/3 h-condition may exhibit a mixed mechanism, while in the case of 500 °C/24 h, the particle size is clearly larger than the critical radius and the Orowan mechanism is the responsible of the strengthening. For aging condition, the overaging might be explained by a combined effect of the change in the strengthening mechanism, formation of austenite phase and coarsening of precipitates. A summary of the evolution of the particle size with aging and the predicted strengthening mechanism is presented in Table 7.7.

Table 7.7. Summary of mean particle lengths (*l*) and diameter (*d*) of the rod-like precipitates for different aging times and temperatures.

Aging condition		**Particle size**		**Strengthening mechansim**
T (°C)	**t (h)**	***l* (nm)**	***d* (nm)**	
450	24	6 ± 1	—	Shearing
450	72	6 ± 1	—	
500	3	12 ± 4	3 ± 2	Shearing/Orowan
500	24	29 ± 6	5 ± 1	Orowan

TEP measurement is an effective method for evaluating microstructural changes during thermal aging of stainless steels [96; 97; 133]. In metal or alloys, the resistance arises from the lattice scattering, i.e. defects scattering from external impurities, dislocations, boundaries and interfaces. This experimental technique is very sensitive to the amount of atoms in solid solution, since they act as scattering centers for the electrons flowing through the material and, thus, decrease the final TEP signal [133]. The evolution of TEP with aging time is governed by two effects [219]. The first one is attributed to the gradual decrease in solute content as precipitation proceeds. This effect is determined by the specific TEP of the solute atom in the matrix and its contribution is generally divided into two terms: a diffusion component and a phonon drag component, where the first term is usually taken as a linear function of temperature and includes the solute content, and the second term depends on electron and phonon scattering. Solute atoms can have a positive or negative influence on the TEP of the matrix. In particular, it is well known that solutes decrease the TEP of iron. The second effect is ascribed to the intrinsic effect of the precipitates formed during aging, which depends on the volume fraction, type, size and morphology of the precipitates. A summary of the effect that different processes have on the hardness and on the TEP is presented in Table 7.8.

Table 7.8. Effect on hardness and TEP of different processes that may take place during aging.

Process	Hv	TEP
Precipitation	↑	↓
Recovery	↓	↑
Precipitates coarsening	↓	↑
Formation of γ	↓	↓
Dissolution of precipitates	↓	↓
Spinodal decomposition	↑	↑

Taking into account that in the CR state alloying elements are in solid solution, except for the small initial fraction of χ-phase (~0.02), the strong TEP increment observed in Figure 7.1 (b) after the shortest aging time (especially at 500 and 550 °C) suggests that the incubation time for age-hardening is zero. As it has been already commented, the formation of Cu-clusters takes place at very early aging times. This has been attributed by Peters and Cupp [223] to the elimination of the free-energy barrier to nucleation under conditions of high supersaturation and precipitation at dislocations. As the Cu-clusters evolve to other Ni-rich precipitates, the matrix impoverishes in alloying elements and, thus, the TEP increases with aging time. Besides, TEM-EDS microanalyses (Table 7.3) support the enrichment of Cu, Ni, Ti and Al in the precipitates and its depletion in the matrix.

Considering that the mean particle size does not vary significantly with time at 450 °C (6 nm), it is reasonable to attribute the continued rise in hardness in the range 400–475 °C to an increase in the number density of precipitates, governed by a reduction in the amount of atoms in solid solution, which also explains the rise in TEP. However, the situation is different at 500 °C, where the particle size does increase (Table 7.7) and some austenite phase forms (~ 0.04) for aging times longer than 24 h (Table 7.2). As observed, from Table 7.8, the firs effect increases the TEP, while the second one decreases it. However a continuous TEP increase is observed in Figure 7.1 (a). It has been reported that coarse and incoherent precipitates have a negligible influence on the TEP, whereas coherent and semi-coherent precipitates may have a strong intrinsic effect of the TEP of the alloy [224]. Therefore, the coalescence of precipitates increases the TEP, as long as they remain coherent, and the formation of austenite causes a decrease [130]. The contribution to the TEP of the low fraction of austenite (~ 0.04) must be negligible and, thus, the rise in the TEP observed for long aging times must be governed by the coalescence of coherent precipitates.

On the other hand, the decomposition of the Cr-rich martensitic matrix into Cr-rich and Cr-poor phases after long-term aging must be also considered. Due to a larger Cr content in the nominal composition of this steel, the Cr enrichment in the matrix is more important than the enrichment in any other element rejected from the Ni-rich precipitates during aging leading. As Figure 7.8 (c) highlights, the presence of spherical and very small (~ 5 nm) phases were detected, similar to the Cr-rich (α) phase found previously by Thuvander and Stiller [93; 94]. These observations suggest that, in the sample aged at 500 °C for 72 h, this Cr-rich phase may have formed. This suggestion is strengthened by Kawaguchi and co-authors findings [96], who detected that, for very low carbon steels, microstructural changes leading to a Cr impoverishment in solid solution, increase the TEP.

As expected, the aging at 550 °C results in a strong precipitation process within the first 10 s of isothermal holding. The hardness plateau extends considerably in time, which means that counteracting processes are taking place simultaneously: precipitation and formation of austenite. This is reflected as a change in the slope of TEP in Figure 7.1 (b).

7.3.3 Relationship between precipitation hardening and mechanical properties

As observed in Figure 7.11, the strength increases and the elongation decreases with the aging time, as generally reported by authors in maraging steels [42]. The evolution of the yield strength ($\sigma_{y0.2}$) and ultimate tensile strength (σ_{UTS}) is approximately equal at the temperatures of 400 and 450 °C and indicates a continued strengthening, which is accompanied with the corresponding decrease in ductility. This is attributed to a permanent increment in the number density of precipitates and their resistance to coarsen, as discussed in the previous section. However, at 500 °C and long aging times the material overages and the strengthening decreases. The softening of the material may be caused by (i) the recovery of the martensitic microstructure, (ii) the coarsening or dissolution of the precipitates and (iii) the formation of austenite or (iv) a change in the strengthening mechanism resulting from the growth of the particles.

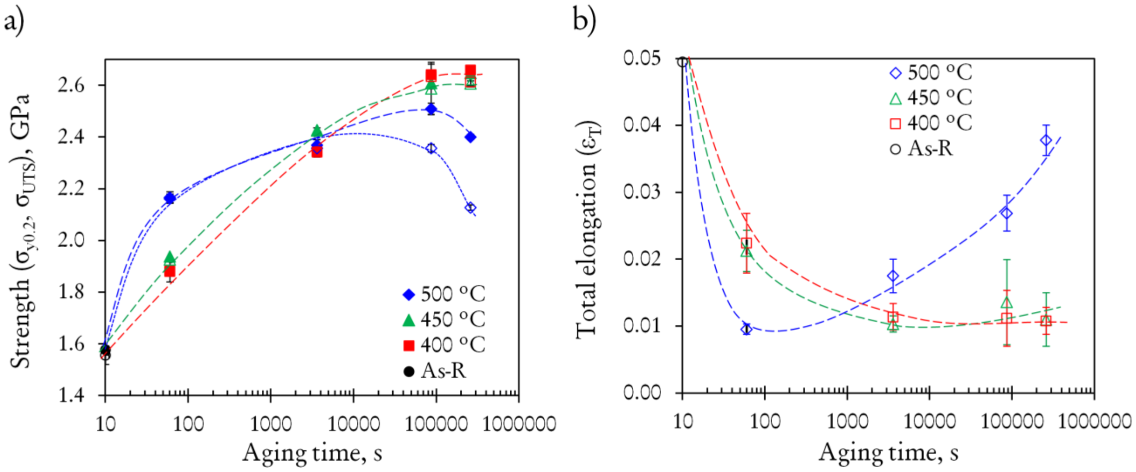

Figure 7.11. Evolution of the strength (a) and the total elongation (ε_T) (b) with the aging time. Open and full dots are related to the yield strength ($\sigma_{y0.2}$) and ultimate tensile (σ_{UTS}), respectively. Dashed lines have been drawn as a guide to the eye.

7.3.4 Correlation of yield and ultimate tensile strength with hardness in aged material

Figure 7.12 shows the fitting between yield ($\sigma_{y0.2}$) and ultimate tensile (σ_{UTS}) strength and hardness data in MPa. Both yield strength (a) and ultimate tensile strength (b) show a clear linear relationship with the diamond pyramid hardness (DPH) for the entire hardness range, as the coefficient of determination (R^2) from the least-squares linear regression indicates. The relation between the yield strength in MPa and hardness Vickers (H_V) in MPa has been theoretically determined to be $H_V \approx 3\cdot\sigma_y$ for metals that do not strain harden [225], being 3 the elastic constrain factor. As shown before, the work-hardening of the material under investigation is already very low in the CR state and decreases with aging treatments, leading to yield strengths $\sigma_{y0.2}$ approximately equal to σ_{UTS} (Table 7.4). Although the elastic constrain factor is slightly lower than expected, it is reasonable to say that these data obey the three-time relationship between hardness and strength. The microstructure plays an important role in this sense, since correlations for martensitic microstructures are slightly better than those for non-martensitic or more complex microstructures [226]. These fittings indicate that there is a reliable hardness-strength correlation that enables a rapid strength evaluation from a bulk hardness measurement for the material under investigation after aging.

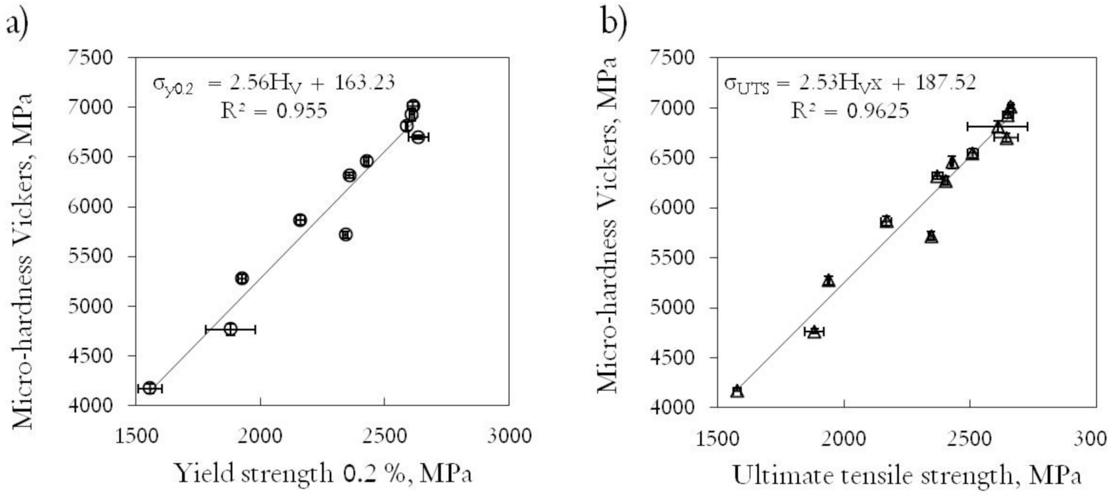

Figure 7.12. Plots of the yield strength (a) and the ultimate tensile strength (b) as function of micro-hardness Vickers (MPa) for the studied aging conditions at different temperatures. Dashed

lines represent the result of the linear regression analysis, whose equation and coefficient of determination (R^2) are noted.

7.4 Conclusions

The aging behavior of the steel under investigation has been studied in a wide range of aging temperatures (300-550 °C) and times (from 1 s to 72 h) by combining microstructural and mechanical characterization. The following conclusions have been extracted:

- All studied aging treatments lead to the hardening of the material, being the most interesting ones those performed between 400 and 500 °C, which exhibit a continuous increase of the hardness in the whole range of studied aging times. Hardness up to 710 H_V and strengths of 2.65 GPa are achieved after 72 h aging in the range 425–475 °C.
- The higher the aging temperature, the faster the hardening response of the material is. Just the fast heating up to 550 °C and 1 s of isothermal holding results in a hardness increment of about a 30 %.
- Aging times longer than 24 h at high aging temperatures such as 500 and 550 °C promote the formation/growth of austenite phase, which slightly improves the work hardening of the material, but also reduces the hardness/strength and increases the ductility.
- The nanoprecipitates responsible for the strengthening have been characterized by TEM and HRTEM. They present a rod-like morphology, have been identified as $Ni_3(Ti,Al)$, as suggested by EDS analysis and exhibit a $(1\bar{1}0)_{\alpha'} \| (0001)_{Ni_3(Ti,Al)}$ and $[1\bar{1}1]_{\alpha'} \| [11\bar{2}0]_{Ni_3(Ti,Al)}$ orientation relationship with the martensitic matrix. Axial lengths of 6 and 30 mm have been measured in samples aged for 24 h at 450 and 500 °C, respectively.
- A reliable correlation, close to the three-time relationship between hardness and strength, has been found for the aged conditions of the material investigated, which enables a rapid strength evaluation from a bulk hardness measurement.

Chapter 8

Conclusions

1. The chemical banding in cold-worked high-alloy stainless steels has turned up to be a thorny and difficult-to-solve problem that influences the stability and the microstructure of the material. The solidification mode of the steel under investigation has been predicted to occur through ferrite as primary phase and then austenite. The equilibrium partitioning coefficient calculations support the segregation patterns observed by 2D-EPMA maps. Alloying elements such as Ni, Cu and Ti segregates together, while Cr and Mo have an opposite and mixed behavior. The metallographic characterization with the Lichtenegger-Blöch etching solution has enable to establish a direct relationship between the alloying element band concentration and the resulting etching color contrast.

2. Phase transformations were studied upon isochronal heating at three different heating rates (0.1, 1 and 10 °C/s) in the cold-rolled state of the steel under consideration. The recovery, precipitation and reaustenitization were found to shift to higher temperatures as the heating rate increases, which is characteristic of diffusional processes.

3. The chemical banding strongly influences the reaustenitization process ($\alpha' \rightarrow \gamma$ transformation) since it leads to different thermal stabilities in the initial

martensite and, thus, different transformation temperatures. This results in a two-steps transformation of the same magnitude for the studied heating rates.

4. Regarding the α'→γ transformation mechanism it is concluded that, for a certain chemical composition, the transformation may proceed with or without diffusion depending on the heating rate and the initial martensite morphology.

   A. During the heating at 0.1 °C/s, austenite nucleates both at martensite lath-boundaries and dislocation tangles and grows globularly. The finely dispersed $Ni_3(Ti,Al)$ precipitates pin the migration of the α'/γ interfaces, hindering the austenite grain-growth and leading to ultrafine and equiaxed defect-free austenite phase.

   B. During the heating at 1 or 10 °C/s, the dislocation-cell-type martensite leads to globular and defect-free austenite grains via a diffusional mechanism, whereas the lath-type results in highly dislocated lathy austenite through a diffusionless mechanism. However, this latter mechanism is negligible due to the low fraction of lath-type martensite present in the initial microstructure. Besides, further heating enhances recovery processes inside the austenite laths, being replaced by ultrafine and equiaxed defect-free austenite.

5. The isochronal heating to the finishing α'→γ transformation temperature has been proven to be a good annealing route to obtain ultrafine-grained dual (α'/γ) and fully austenitic microstructures with AGS of 350–440 nm, regardless the heating rate. At slow rates of 0.1 °C/s, the high dislocation density in the initial martensite as well as the presence of an important amount on nanoprecipitates of $Ni_3(Ti,Al)$ play a crucial role in the grain refinement; however, their high volume fraction of χ-phase may reduce their corrosion resistance.

6. By controlled annealing routes proposed in this work, mechanical properties of 1.18-2.10 GPa of σ_{UTS} and ε_t of 3-26 % are achieved. The mechanical behavior of these microstructures is dependent on: (i) the volume fraction of austenite,

(ii) the presence of nanometric $Ni_3(Ti,Al)$ precipitates in the untransformed martensite, (iii) the TRIP effect, (iv) the austenite grain size and (v) the volume fraction of χ-phase.

7. Finally, the precipitation hardening investigation provides valuable information to improve this last processing step that provides the final mechanical properties in this steel. Aging temperature in the range 300 - 550 °C and holding times up to 72 h have been investigated. Hardness up to 710 H_V and strengths of 2.65 GPa are achieved after 72 h aging in the range 425–475 °C. The continuous hardening over time experienced by the material in this range is ascribed to a homogeneous distribution of nanometric sized precipitates, their resistance to coarsen and the active strengthening mechanism. Aging at higher temperatures, such as 500 or 550 °C, induces the formation of austenite phase, which results in a softening of the material.

Bibliography

[1] J.K.L. Lai, C.H. Shek, K.H. Lo, Stainless Steels: An Introduction and Their Recent Developments, Bentham Science Publishers, 2012.

[2] Outokumpu Stainless Corrosion Handbook, Outokumpu stainless steel Oy, 2004.

[3] E. Folkhard, G. Rabensteiner, Welding metallurgy of stainless steels, Springer-Verlag Wien, Wien ; New York 1988.

[4] H.K.D.H. Bhadeshia, S.R. Honeycombe, in: H.K.D.H.B.R. Honeycombe (Ed.), Steels (Third Edition), Butterworth-Heinemann, Oxford, 2006, pp. 71-93.

[5] J.A. Sedriks, Corrosion of stainless steels, John Wiley and Sons, New York, USA, 1979.

[6] O.D. Sherby, J. Wadsworth, D.R. Lesuer, C.K. Syn, MATERIALS TRANSACTIONS 49 (2008) 2016-2027.

[7] C. Servant, E. Gherbi, G. Cizeron, Journal of Materials Science 22 (1987) 2297-2304.

[8] U.K. Viswanathan, S. Banerjee, R. Krishnan, Materials Science and Engineering: A 104 (1988) 181-189.

[9] U.K. Viswanathan, P.K.K. Nayar, R. Krishnan, Materials Science and Technology 5 (1989) 346-349.

[10] M. Murayama, K. Hono, Y. Katayama, Metallurgical and Materials Transactions A 30 (1999) 345-353.

[11] H. Mirzadeh, A. Najafizadeh, Materials Chemistry and Physics 116 (2009) 119-124.

[12] K. Ozbaysal, O.T. Inal, Journal of Materials Science 29 (1994) 1471-1480.

[13] H.R. Habibi Bajguirani, Materials Science and Engineering: A 338 (2002) 142-159.

[14] V. Seetharaman, M. Sundararaman, R. Krishnan, Materials Science and Engineering 47 (1981) 1-11.

[15] D.V.V. Satyanarayana, G. Malakondaiah, D.S. Sarma, Materials Characterization 47 (2001) 61-65.

[16] C.V. Robino, M.J. Cieslak, P.W. Hochanadel, G.R. Edwards, Metallurgical and Materials Transactions A 25 (1994) 697-704.

[17] D.H. Ping, M. Ohnuma, Y. Hirakawa, Y. Kadoya, K. Hono, Materials Science and Engineering: A 394 (2005) 285-295.

[18] J. Post, H. Nolles, K. Datta, H.J.M. Geijselaers, Materials Science and Engineering: A 498 (2008) 179-190.

[19] D. San Martín, K.W.P. Aarts, P.E.J. Rivera-Díaz-del-Castillo, N.H. van Dijk, E. Brück, S. van der Zwaag, Journal of Magnetism and Magnetic Materials 320 (2008) 1722-1728.

[20] D. San Martin, E. Jimenez-Melero, J.A. Duffy, V. Honkimaki, S. van der Zwaag, N.H. van Dijk, Journal of Applied Crystallography 45 (2012) 748-757.

[21] D. San Martin, N.H. van Dijk, E. Jiménez-Melero, E. Kampert, U. Zeitler, S. van der Zwaag, Materials Science and Engineering: A 527 (2010) 5241-5245.

[22] H.K.D.H. Bhadeshia, S.R. Honeycombe, in: H.K.D.H.B.R. Honeycombe (Ed.), Steels (Third Edition), Butterworth-Heinemann, Oxford, 2006, pp. 95-128.

[23] C.M. Wayman, H.K.D.H. Bhadeshia, in: R.W.C. Haasen (Ed.), Physical Metallurgy (Fourth Edition), North-Holland, Oxford, 1996, pp. 1507-1554.

[24] G.B. Olson, M. Cohen, Journal of the Less Common Metals 28 (1972) 107-118.

[25] G.F. Bolling, R.H. Richman, Acta Metallurgica 18 (1970) 673-681.

[26] E. Jimenez-Melero, N.H. van Dijk, L. Zhao, J. Sietsma, S.E. Offerman, J.P. Wright, S. van der Zwaag, Acta Materialia 55 (2007) 6713-6723.

[27] S. Chatterjee, H.K.D.H. Bhadeshia, Materials Science and Technology 23 (2007) 1101-1104.

[28] D. Bancroft, E.L. Peterson, S. Minshall, Journal of Applied Physics 27 (1956) 291-298.

[29] H.K.D.H. Bhadeshia, S.R. Honeycombe, in: H.K.D.H.B.R. Honeycombe (Ed.), Steels (Third Edition), Butterworth-Heinemann, Oxford, 2006, pp. 259-286.

[30] J.-B. Seol, J.E. Jung, Y.W. Jang, C.G. Park, Acta Materialia 61 (2013) 558-578.

[31] M. Holmquist, J.O. Nilsson, A.H. Stigenberg, Scripta Metallurgica et Materialia 33 (1995) 1367-1373.

[32] M. Eskandari, A. Najafizadeh, A. Kermanpur, M. Karimi, Materials & Design 30 (2009) 3869-3872.

[33] G.E. Dieter, Mechanical metallurgy, 1961.

[34] H.K.D.H. Bhadeshia, S.R. Honeycombe, in: H.K.D.H.B.R. Honeycombe (Ed.), Steels (Third Edition), Butterworth-Heinemann, Oxford, 2006, pp. 209-234.

[35] G. Krauss, Materials Science and Engineering: A 273–275 (1999) 40-57.

[36] P. Winchell, M. Cohen, The strength of martensite, DTIC Document, 1962.

[37] S. Morito, H. Yoshida, T. Maki, X. Huang, Materials Science and Engineering: A 438–440 (2006) 237-240.

[38] P. Liu, Materials Characterization 44 (2000) 413-424.

[39] S.-J. Kim, C.M. Wayman, Materials Science and Engineering: A 128 (1990) 217-230.

[40] V. Vasudevan, S. Kim, C.M. Wayman, Metallurgical Transactions A 21 (1990) 2655-2668.

[41] W. Sha, A. Cerezo, G.D.W. Smith, Metallurgical Transactions A 24 (1993) 1251-1256.

[42] P. Shina, K. Tharian, K. Sreekumar, K. Nagarajan, D. Sarma, Materials Science and Technology 14 (1998) 1-9.

[43] R. Kapoor, I.S. Batra, Materials Science and Engineering: A 371 (2004) 324-334.

[44] E.V. Pereloma, A. Shekhter, M.K. Miller, S.P. Ringer, Acta Materialia 52 (2004) 5589-5602.

[45] Y. He, K. Yang, W. Sha, Metallurgical and Materials Transactions A 36 (2005) 2273-2287.

[46] J.M. Pardal, S.S.M. Tavares, V.F. Terra, M.R. Da Silva, D.R. Dos Santos, Journal of Alloys and Compounds 393 (2005) 109-113.

[47] W. Sha, Z. Guo, Maraging Steels: Modelling of Microstructure, Properties and Applications, Elsevier Science, 2009.

[48] A.F. Padilha, P.R. Rios, ISIJ International 42 (2002) 325-327.

[49] D. San Martin, P.E.J. Rivera Diaz del Castillo, E. Peekstok, S. van der Zwaag, Materials Characterization 58 (2007) 455-460.

[50] K.H. Lo, C.H. Shek, J.K.L. Lai, Materials Science and Engineering: R: Reports 65 (2009) 39-104.

[51] K. Stiller, M. Hättestrand, F. Danoix, Acta Materialia 46 (1998) 6063-6073.

[52] M. Hättestrand, J.-O. Nilsson, K. Stiller, P. Liu, M. Andersson, Acta Materialia 52 (2004) 1023-1037.

[53] R. Schnitzer, M. Schober, S. Zinner, H. Leitner, Acta Materialia 58 (2010) 3733-3741.

[54] H.K.D.H. Bhadeshia, S.R. Honeycombe, in: H.K.D.H.B.R. Honeycombe (Ed.), Steels (Third Edition), Butterworth-Heinemann, Oxford, 2006, pp. 307 - 334.

[55] S. Queyreau, G. Monnet, B. Devincre, Acta Materialia 58 (2010) 5586-5595.

[56] P.E.J. Rivera-Díaz-del-Castillo, K. Hayashi, E.I. Galindo-Nava, Materials Science and Technology 29 (2013) 1206-1211.

[57] H.K.D.H. Bhadeshia, S.R. Honeycombe, in: H.K.D.H.B.R. Honeycombe (Ed.), Steels (Third Edition), Butterworth-Heinemann, Oxford, 2006, pp. 17 - 38.

[58] Q. Lu, W. Xu, S. van der Zwaag, Acta Materialia 77 (2014) 310-323.

[59] Y. Nakada, A.S. Keh, Acta Metallurgica 16 (1968) 903-914.

[60] B. Kim, E. Boucard, T. Sourmail, D. San Martín, N. Gey, P.E.J. Rivera-Díaz-del-Castillo, Acta Materialia 68 (2014) 169-178.

[61] R.D.K. Misra, G.C. Weatherly, J.E. Hartmann, A.J. Boucek, Materials Science and Technology 17 (2001) 1119-1129.

[62] J. Syarif, K. Nakashima, T. Tsuchiyama, S. Takaki, ISIJ International 47 (2007) 340-345.

[63] J.P. Hirth, in: R.W.C. Haasen (Ed.), Physical Metallurgy (Fourth Edition), North-Holland, Oxford, 1996, pp. 1831-1875.

[64] Y.H. Kim, K.Y. Kim, Y.D. Lee, Materials and Manufacturing Processes 19 (2004) 51-59.

[65] B. Kim, C. Celada, D. San Martín, T. Sourmail, P.E.J. Rivera-Díaz-del-Castillo, Acta Materialia 61 (2013) 6983-6992.

[66] T. Shintani, Y. Murata, Acta Materialia 59 (2011) 4314-4322.

[67] F. Christien, M.T.F. Telling, K.S. Knight, Scripta Materialia 68 (2013) 506-509.

[68] A.I.H. Committee, ASM Handbook Volume 01: Properties and selection: Irons, Steels, and High Performance Alloys, ASM International, 1990.

[69] M. Huang, P.E.J. Rivera-Díaz-del-Castillo, O. Bouaziz, S.v.d. Zwaag, Materials Science and Technology 25 (2009) 833-839.

[70] J.W. Martin, Precipitation Hardening: Theory and Applications, Elsevier Science, 2012.

[71] T. Gladman, Materials Science and Technology 15 (1999) 30-36.

[72] A.J. Ardell, Metallurgical Transactions A 16 (1985) 2131-2165.

[73] J.S. Zhang, High Temperature Deformation and Fracture of Materials, Elsevier Science, 2010.

[74] B.P. Kashyap, K. Tangri, Acta Metallurgica et Materialia 43 (1995) 3971-3981.

[75] A. Di Schino, M. Barteri, J.M. Kenny, Journal of Materials Science Letters 21 (2002) 751-753.

[76] F. Forouzan, A. Najafizadeh, A. Kermanpur, A. Hedayati, R. Surkialiabad, Materials Science and Engineering: A 527 (2010) 7334-7339.

[77] A. Di Schino, I. Salvatori, J.M. Kenny, Journal of Materials Science 37 (2002) 4561-4565.

[78] R.D.K. Misra, S. Nayak, S.A. Mali, J.S. Shah, M.C. Somani, L.P. Karjalainen, Metallurgical and Materials Transactions A 41 (2010) 3-12.

[79] I. Shakhova, V. Dudko, A. Belyakov, K. Tsuzaki, R. Kaibyshev, Materials Science and Engineering: A 545 (2012) 176-186.

[80] C.X. Huang, G. Yang, C. Wang, Z.F. Zhang, S.D. Wu, Metallurgical and Materials Transactions A 42 (2011) 2061-2071.

[81] A. Weidner, A. Müller, A. Weiss, H. Biermann, Materials Science and Engineering: A 571 (2013) 68-76.

[82] Y. Ma, J.-E. Jin, Y.-K. Lee, Scripta Materialia 52 (2005) 1311-1315.

[83] F.Y. Dong, P. Zhang, J.C. Pang, D.M. Chen, K. Yang, Z.F. Zhang, Materials Science and Engineering: A 587 (2013) 185-191.

[84] J. Huang, X. Ye, J. Gu, X. Chen, Z. Xu, Materials Science and Engineering: A 532 (2012) 190-195.

[85] Y.F. Shen, X.M. Zhao, X. Sun, Y.D. Wang, L. Zuo, Scripta Materialia.

[86] H. Wang, I. Shuro, M. Umemoto, K. Ho-Hung, Y. Todaka, Materials Science and Engineering: A 556 (2012) 906-910.

[87] A. Belyakov, T. Sakai, H. Miura, R. Kaibyshev, Scripta Materialia 42 (2000) 319-325.

[88] W. Pachla, et al., Materials Science and Engineering: A 615 (2014) 116-127.

[89] K. Tomimura, S. Takaki, S. Tanimoto, Y. Tokunaga, Tetsu-to-Hagane 74 (1988) 1052-1057.

[90] K. Tomimura, S. Takaki, Y. Tokunaga, ISIJ International 31 (1991) 1431-1437.

[91] S. Takaki, K. Tomimura, S. Ueda, ISIJ International 34 (1994) 522-527.

[92] J. Post, J. Huetink, H.J.M. Geijselaers, R.M.J. Voncken, Journal de Physique IV (PROCEEDINGS) 112 (2003) 417-420.

[93] K. Stiller, H.O. Andrén, M. Andersson, Materials Science and Technology 24 (2008) 633-640.

[94] M. Thuvander, M. Andersson, K. Stiller, Ultramicroscopy 132 (2013) 265-270.

[95] M. Thuvander, M. Andersson, K. Stiller, Materials Science and Technology 28 (2012) 695-701.

[96] Y. Kawaguchi, S. Yamanaka, Journal of Alloys and Compounds 336 (2002) 301-314.

[97] C. Capdevila, T. De Cock, F.G. Caballero, D. San Martin, C.G. de Andres, Journal of Materials Science 44 (2009) 4499-4502.

[98] M. Ahmed, I. Salam, F.H. Hashmi, A.Q. Khan, Journal of Materials Engineering and Performance 6 (1997) 165-171.

[99] P.H.S. Cox, B.G. Reisdorf, G.E. Pellissier, Journal Name: Trans. Met. Soc. AIME, 239: 1809-17(Nov. 1967).; Other Information: Orig. Receipt Date: 31-DEC-68 (1967) Medium: X.

[100] A. Di Schino, M.G. Mecozzi, M. Barteri, J.M. Kenny, Journal of Materials Science 35 (2000) 375-380.

[101] S.E. Offerman, N.H.v. Dijk, M.T. Rekveldt, J. Sietsma, S.v.d. Zwaag, Materials Science and Technology 18 (2002) 297-303.

[102] J.D. Verhoeven, Journal of Materials Engineering and Performance 9 (2000) 286-296.

[103] J.M. Radzikowska, Materials Characterization 54 (2005) 287-304.

[104] P. Lichtenegger, R. Blöch, Practical Metallography 12 (1975) 567-673.

[105] J.Q. Guo, S. Tsukamoto, T. Kimura, H. Nakae, Acta Materialia 47 (1999) 3767-3778.

[106] A. Ray, S.K. Dhua, S. Jha, X-Ray Spectrometry 28 (1999) 41-50.

[107] J.S. Kasper, Acta Metallurgica 2 (1954) 456-461.

[108] W. Xu, D. San Martin, P.E.J. Rivera Díaz del Castillo, S. van der Zwaag, Materials Science and Engineering: A 467 (2007) 24-32.

[109] P.G. Bastien, Journal of Iron and Seel Institute 187 (1957) 281 - 291.

[110] G.F. Vander Voort, in, "Color metallography", *Metallography and Microstructures*, vol. 9 ASM International, 2004, pp. 493 - 512.

[111] A. International, ASTM E562-11, Standard Test Method for Determining Volume Fraction by Systematic Manual Point Count, ASTM International, West Conshohocken, PA, 2011.

[112] B.L. Bramfitt, A.O. Benscoter, in, ASM International, Metals Park, OH, 2002.

[113] G.F. Vander Voort, Metallography: Principles and practice, ASM International, New York, 1984.

[114] E. Behara, Pract. Metallogr. 7 (1970) 242-248.

[115] P. Lichtenegger, R. Blöch, Pract. Metallogr. 12 (1975) 567-573.

[116] G.F. Vander Voort, in, ASM Handbook Volume 9: Metallography and Microstructures, ASM International, 2004, pp. 1057-1066.

[117] J. Michalska, M. Sozańska, Materials Characterization 56 (2006) 355-362.

[118] J.C. Ma, Y.S. Yang, W.H. Tong, Y. Fang, Y. Yu, Z.Q. Hu, Materials Science and Engineering: A 444 (2007) 64-68.

[119] K.R.I.o.T. ThermoCalc Software AB, Stockholm, Sweden.

[120] M.C. Somani, P. Juntunen, L.P. Karjalainen, R.D.K. Misra, A. Kyröläinen, Metallurgical and Materials Transactions A 40 (2009) 729-744.

[121] D.L. Johannsen, A. Kyrolainen, P.J. Ferreira, Metallurgical and Materials Transactions A 37 (2006) 2325-2338.

[122] S. Rajasekhara, L.P. Karjalainen, A. Kyröläinen, P.J. Ferreira, Materials Science and Engineering: A 527 (2010) 1986-1996.

[123] R.D.K. Misra, Z. Zhang, P.K.C. Venkatasurya, M.C. Somani, L.P. Karjalainen, Materials Science and Engineering: A 527 (2010) 7779-7792.

[124] T.H. Coleman, D.R.F. West, Metals Technology 3 (1976) 49-53.

[125] C.A. Apple, G. Krauss, Acta Metallurgica 20 (1972) 849-856.

[126] D.-S. Leem, Y.-D. Lee, J.-H. Jun, C.-S. Choi, Scripta Materialia 45 (2001) 767-772.

[127] J. Han, Y.-K. Lee, Acta Materialia 67 (2014) 354-361.

[128] S.-J. Lee, Y.-M. Park, Y.-K. Lee, Materials Science and Engineering: A 515 (2009) 32-37.

[129] Y.-K. Lee, H.-C. Shin, D.-S. Leem, J.-Y. Choi, W. Jin, C.-S. Choi, Materials Science and Technology 19 (2003) 393-398.

[130] C. Celada Casero, D. San Martín, Metallurgical and Materials Transactions A 45 (2014) 1767-1777.

[131] F.G. Caballero, C. Capdevila, L.F. Alvarez, Garcı, amp, x, C. a de Andrés, Scripta Materialia 50 (2004) 1061-1066.

[132] F.G. Caballero, A. García-Junceda, C. Capdevila, C.G. de Andrés, Scripta Materialia 52 (2005) 501-505.

[133] J.P. Ferrer, T. De Cock, C. Capdevila, F. García Caballero, C. García de Andrés, Acta Materialia 55 (2007) 2075-2083.

[134] F. Moszner, E. Povoden-Karadeniz, S. Pogatscher, P.J. Uggowitzer, Y. Estrin, S.S.A. Gerstl, E. Kozeschnik, J.F. Löffler, Acta Materialia 72 (2014) 99-109.

[135] J.B. Lecomte, C. Servant, G. Cizeron, Journal of Materials Science 20 (1985) 3339-3352.

[136] Y.C. Liu, F. Sommer, E.J. Mittemeijer, Acta Materialia 58 (2010) 753-763.

[137] F.J. Humphreys, M. Hatherly, in: F.J.H. Hatherly (Ed.), Recrystallization and Related Annealing Phenomena (Second Edition), Elsevier, Oxford, 2004, pp. 169-213.

[138] L. Kaufman, E.V. Clougherty, R.J. Weiss, Acta Metallurgica 11 (1963) 323-335.

[139] H.V. Atkinson, Acta Metallurgica 36 (1988) 469-491.

[140] C. Zener, Trans. AIME 175 (1948) 15 - 51.

[141] T. Gladman, D. Dulieu, Metal Science 8 (1974) 167-176.

[142] D. San Martín, F. G. Caballero, C. Capdevila, C. García de Andrés, MATERIALS TRANSACTIONS 45 (2004) 2797 - 2804.

[143] K.A. AlOgab, D.K. Matlock, J.G. Speer, H.J. Kleebe, ISIJ International 47 (2007) 1034-1041.

[144] K. Banerjee, M. Militzer, M. Perez, X. Wang, Metallurgical and Materials Transactions A 41 (2010) 3161-3172.

[145] L.J. Cuddy, J.C. Raley, Metallurgical Transactions A 14 (1983) 1989-1995.

[146] J. Mizera, J.W. Wyrzykowski, K.J. Kurzydłowski, Materials Science and Engineering: A 104 (1988) 157-162.

[147] G. Sheard, J. Nutting, Metal Science 13 (1979) 131-135.

[148] N. Zavaleta Gutiérrez, M.I. Luppo, C.A. Danon, I. Toda-Caraballo, C. Capdevila, C. García de Andrés, Materials Science and Technology 29 (2013) 1254-1266.

[149] F. Peñalba, C.G. De Andres, M. Carsi, F. Zapirain, Journal of Materials Science 31 (1996) 3847-3852.

[150] T. Kakeshita, K. Kuroiwa, K. Shimizu, T. Ikeda, A. Yamagishi, M. Date, Mater. Trans. JIM 34 (1993) 423 - 428.

[151] G. Ghosh, G.B. Olson, Acta Metallurgica et Materialia 42 (1994) 3371-3379.

[152] A. Borgenstam, M. Hillert, Acta Materialia 45 (1997) 651-662.

[153] I.S. Golovin, J.O. Nilsson, G.V. Serzhantova, S.A. Golovin, Journal of Alloys and Compounds 310 (2000) 411-417.

[154] D.S. Martin, N.H. van Dijk, E. Brück, S. van der Zwaag, Materials Science and Engineering: A 481–482 (2008) 757-761.

[155] E. Ma, Scripta Materialia 49 (2003) 663-668.

[156] H. Azizi-Alizamini, M. Militzer, W.J. Poole, Scripta Materialia 57 (2007) 1065-1068.

[157] V.S.A. Challa, X.L. Wan, M.C. Somani, L.P. Karjalainen, R.D.K. Misra, Materials Science and Engineering: A 613 (2014) 60-70.

[158] L. Bracke, G. Mertens, J. Penning, B. De Cooman, M. Liebeherr, N. Akdut, Metallurgical and Materials Transactions A 37 (2006) 307-317.

[159] P. Haušild, V. Davydov, J. Drahokoupil, M. Landa, P. Pilvin, Materials & Design 31 (2010) 1821-1827.

[160] Y.-S. Jung, Y.-K. Lee, D. Matlock, M. Mataya, Metals and Materials International 17 (2011) 553-556.

[161] A. Kisko, R.D.K. Misra, J. Talonen, L.P. Karjalainen, Materials Science and Engineering: A 578 (2013) 408-416.

[162] K. Spencer, J.D. Embury, K.T. Conlon, M. Véron, Y. Bréchet, Materials Science and Engineering: A 387–389 (2004) 873-881.

[163] J. Talonen, H. Hänninen, Acta Materialia 55 (2007) 6108-6118.

[164] S.S.M. Tavares, J.M. Pardal, M.J.G. da Silva, H.F.G. Abreu, M.R. da Silva, Materials Characterization 60 (2009) 907-911.

[165] J. Shi, X. Sun, M. Wang, W. Hui, H. Dong, W. Cao, Scripta Materialia 63 (2010) 815-818.

[166] R.E. Schramm, R.P. Reed, Metallurgical Transactions A 6 (1975) 1345-1351.

[167] C. Rhodes, A. Thompson, Metallurgical Transactions A 8 (1977) 1901-1906.

[168] T.S. Byun, N. Hashimoto, K. Farrell, Acta Materialia 52 (2004) 3889-3899.

[169] N. Jia, P. Eisenlohr, F. Roters, D. Raabe, X. Zhao, Acta Materialia 60 (2012) 3415-3434.

[170] P.J. Brofman, G.S. Ansell, Metallurgical Transactions A 9 (1978) 879-880.

[171] G. Frommeyer, Br, uuml, U. x, P. Neumann, ISIJ International 43 (2003) 438-446.

[172] A. Das, S. Sivaprasad, M. Ghosh, P.C. Chakraborti, S. Tarafder, Materials Science and Engineering: A 486 (2008) 283-286.

[173] C.X. Huang, G. Yang, Y.L. Gao, S.D. Wu, S.X. Li, Journal of Materials Research 22 (2007) 724-729.

[174] T.S. Byun, Acta Materialia 51 (2003) 3063-3071.

[175] S. Mishra, K. Narasimhan, I. Samajdar, Materials Science and Technology 23 (2007) 1118-1126.

[176] G. Dini, A. Najafizadeh, R. Ueji, S.M. Monir-Vaghefi, Materials & Design 31 (2010) 3395-3402.

[177] R. Schwab, V. Ruff, Acta Materialia 61 (2013) 1798-1808.

[178] R.A. Varin, B. Mazurek, D. Himbeault, Materials Science and Engineering 94 (1987) 109-119.

[179] S.S. Hazra, E.V. Pereloma, A.A. Gazder, Acta Materialia 59 (2011) 4015-4029.

[180] D.J. Lloyd, L.R. Morris, Acta Metallurgica 25 (1977) 857-861.

[181] C.Y. Yu, P.W. Kao, C.P. Chang, Acta Materialia 53 (2005) 4019-4028.

[182] R.W. Hayes, D. Witkin, F. Zhou, E.J. Lavernia, Acta Materialia 52 (2004) 4259-4271.

[183] W.G. Johnston, J.J. Gilman, Journal of Applied Physics 30 (1959) 129 - 144.

[184] J.W. Wyrzykowski, M.W. Grabski, Materials Science and Engineering 56 (1982) 197-200.

[185] S. Cheng, J.A. Spencer, W.W. Milligan, Acta Materialia 51 (2003) 4505-4518.

[186] F.C. Frank, W.T. Read Jr, Physical Review 79 (1950) 722-723.

[187] in: D. Caillard, J.L. Martin (Eds.), Pergamon Materials Series, Pergamon, 2003, pp. 323-360.

[188] V. Yamakov, D. Wolf, S.R. Phillpot, A.K. Mukherjee, H. Gleiter, Nat Mater 1 (2002) 45-49.

[189] D.W. Moon, Materials Science and Engineering 8 (1971) 235-243.

[190] E. Hall, Yield Point Phenomena in Metals and Alloys, Springer US, 2012.

[191] T. Shimokawa, T. Hiramoto, T. Kinari, S. Shintaku, MATERIALS TRANSACTIONS 50 (2009) 2-10.

[192] R.D.K. Misra, V.S.A. Challa, P.K.C. Venkatsurya, Y.F. Shen, M.C. Somani, L.P. Karjalainen, Acta Materialia 84 (2015) 339-348.

[193] J.H. Ryu, J.I. Kim, H.S. Kim, C.-S. Oh, H.K.D.H. Bhadeshia, D.-W. Suh, Scripta Materialia 68 (2013) 933-936.

[194] Z.H. Cai, H. Ding, X. Xue, J. Jiang, Q.B. Xin, R.D.K. Misra, Scripta Materialia 68 (2013) 865-868.

[195] Y.-S. Jung, Y.-K. Lee, Scripta Materialia 59 (2008) 47-50.

[196] D. Raabe, D. Ponge, O. Dmitrieva, B. Sander, Scripta Materialia 60 (2009) 1141-1144.

[197] R.D.K. Misra, S. Nayak, P.K.C. Venkatasurya, V. Ramuni, M.C. Somani, L.P. Karjalainen, Metallurgical and Materials Transactions A 41 (2010) 2162-2174.

[198] M. Farooque, H. Ayub, A. Ul Haq, A.Q. Khan, Journal of Materials Science 33 (1998) 2927-2930.

[199] X. Li, Z. Yin, Materials Letters 24 (1995) 239-242.

[200] P. Liu, A.H. Stigenberg, J.O. Nilsson, Acta Metallurgica et Materialia 43 (1995) 2881-2890.

[201] K. Stiller, F. Danoix, A. Bostel, Applied Surface Science 94–95 (1996) 326-333.

[202] K. Stiller, F. Danoix, M. Hättestrand, Materials Science and Engineering: A 250 (1998) 22-26.

[203] M. Hättestrand, H.-O. Andrén, Materials Science and Engineering: A 318 (2001) 94-101.

[204] Y. Xin, Y. Li, Z. Liu, Scripta Materialia 63 (2010) 35-38.

[205] J.M. Makar, B.K. Tanner, Journal of Magnetism and Magnetic Materials 222 (2000) 291-304.

[206] Z. Akase, Y.-G. Park, D. Shindo, T. Tomida, H. Yashiki, S. Hinotani, MATERIALS TRANSACTIONS 46 (2005) 974-977.

[207] W.A. Johnson, K.E. Mehl, Trans Am Inst Min Met Eng 195 (1939) 416.

[208] M. Avrami, The Journal of Chemical Physics 7 (1939) 1103-1112.

[209] M. Avrami, The Journal of Chemical Physics 8 (1940) 212-224.

[210] M. Avrami, The Journal of Chemical Physics 9 (1941) 177-184.

[211] N. Kolmogorov, Ivz Akad Nauk SSSR Ser Mat 3 (1937) 355.

[212] J.W. Christian, "The Theory of Transformation in Metals and Alloys", 2nd Edn., Part 1, Pergamon Press, Oxford, UK, 1975.

[213] I. Gutiérrez-Urrutia, Journal of Materials Science 46 (2011) 3144-3150.

[214] M.J. Starink, Journal of Materials Science 32 (1997) 4061-4070.

[215] Z. Guo, W. Sha, E.A. Wilson, Materials Science and Technology 18 (2002) 377-382.

[216] M.J. Starink, Journal of Materials Science 36 (2001) 4433-4441.

[217] M.T. Todinov, Acta Materialia 48 (2000) 4217-4224.

[218] E.-S. Lee, Y.G. Kim, Acta Metallurgica et Materialia 38 (1990) 1669-1676.

[219] C. Capdevila, M.K. Miller, J. Chao, Acta Materialia 60 (2012) 4673-4684.

[220] A.H. Cottrell, B.A. Bilby, Proceedings of the Physical Society. Section A 62 (1949) 49.

[221] S. Harper, Physical Review 83 (1951) 709-712.

[222] M.K. Miller, K.F. Russell, P. Pareige, M.J. Starink, R.C. Thomson, Materials Science and Engineering: A 250 (1998) 49-54.

[223] D.T. Peters, C.R. Cupp, Trans. Met. Soc. AIME 236 (1966) 1420-1429.

[224] G.M. Raynaud, P. Guyot, Acta Metallurgica 36 (1988) 143-147.

[225] D. Tabor, The Hardness of Metals, OUP Oxford, 2000.

[226] E.J. Pavlina, C.J. Van Tyne, Journal of Materials Engineering and Performance 17 (2008) 888-893.

[227] J. Post, On the Constitutive Behaviour of Sandvik Nanoflex TM—Modelling Experiments and Multi-Stage Forming, University of Twente, 2004.

[228] J. Post, C. de Vries, J. Huétink, Journal of Materials Processing Technology 209 (2009) 5558-5572.

Appendix I

In-situ inductive measurements to study the martensitic transformation during tensile testing

Introduction

The experiments described in this section are the result of a short stay at the Advanced Technology Center (ATC) Philips, located in Drachten, the Netherlands. during a summer placement of two months. Philips is using this type of steels to produce the shaving heads of some of their electrical water-proof shavers. Researchers from this technology centre have accumulated a lot of knowledge throughout the years regarding the mechanical characterization of this type of steels.

As discussed throughout this thesis work, one of the key features of the metastable stainless steel under investigation is the TRIP effect, the formation of strain-induced martensite that enhances the strength and ductility of the steel. The austenite stability determines the transformation rate and, therefore, the final mechanical properties of the material. However, it is not easy to study the evolution of the volume fraction of martensite under straining. The determination of volume fraction of martensite through *ex-situ* measurements on tensile samples interrupted to certain strain levels and their subsequent quantification by metallographic methods or magnetization measurements requires a great number of experiments and long times of experimental procedure.

The evolution of the volume fraction of martensite during cryogenic treatments or upon straining has been studied *in-situ* in the last years by some authors by using a synchrotron radiation source [20]. Although the use of a synchrotron radiation source is becoming generalized, it is still difficult to get measurement time at a certain line and the analysis of the results is time-consuming. Philips ATC has recently developed an inductive sensor that enables *in-situ* measurements of the volume fraction of martensite during tensile testing [18; 92; 227; 228]. The use of this equipment would simplify the characterization of the martensitic transformation.

Therefore, the proposal for this short stay at Philips ATC arose from the need to study the martensitic transformation *in-situ* during plastic deformation in isochronally reaustenitized microstructures obtained of the steel under investigation. For this purpose, the work was focused on the study of the mechanical behavior at room temperature by tensile testing on standard specimens (ASTM E8/E8M-09) after isochronal reaustenitization at 0.1 °C/s (due to experimental limitation, it was not possible to study faster heating rates). In this way, two different goals can be accomplished:

1) To study the mechanical behavior of standard tensile specimens and to compare the mechanical parameters such as ultimate tensile and yield strength and uniform and total elongation, with the ones obtained on sub-size samples.

2) The *in-situ* characterization of the martensitic transformation during tensile testing.

Experimental procedure

For these experiments, standard tensile test specimens were machined perpendicular to the rolling direction. To this end, pre-forms of 300 mm length and 35 mm width were first cut from the steel sheet coil using a manual sheet metal shearing machine (GERVER). Then, a manual hydraulic press machine (Eoc Normalien GmbH + Co. KG) with a template was used to obtain the final machined specimens of 20 mm width and 120 mm gauge length.

These samples were subjected to isochronal treatments at 0.1 °C/s up to different temperatures (Table I) in a horizontal vacuum furnace (HLFC1218, CVE). Immediately after reaching the temperatures, the samples were cooled down by high pressure (850 mbar) inert gas quenching (HPIGQ)). Along with the selected heat-treatments, the volume fraction of austenite, martensite and χ-phase (as determined in *Chapter 5*) have been included as reference.

Table I. Summary of heat-treatments performed in the horizontal vacuum furnace. The volume fraction of the phases martensite, austenite and chi ($f_{\alpha'}$, f_γ and f_χ, respectively) the microstructure will present after heating to the temperature have been included for reference.

HR (°C/s)	T (°C)	CR	$f_{\alpha'}$	f_γ	f_χ
0.1	630	HPIGQ	0.97	0.02	0.02
	645		0.89	0.09	0.02
	660		0.78	0.20	0.02
	680		0.47	0.51	0.02
	690		0.36	0.62	0.02
	700		0.34	0.64	0.02
	725		0.26	0.70	0.03
	770		0.20	0.74	0.06
	800		0.11	0.81	0.08
	825		0.02	0.89	0.10
	900		0.01	0.87	0.12
	950		0.02	0.90	0.09
	1000		0.02	0.93	0.06
	1025		0.02	0.95	0.04
	1050		0.02	0.97	0.02

Two specimens were tested per condition to study the reproducibility using a universal testing machine Zwick-Roell-Z030 equipped with extensometers. All the tensile tests were carried out at room temperature and a strain rate of $5 \times 10^{-4}\ s^{-1}$. To monitor the strain-induced martensite formation during tensile testing the inductive sensor developed by ATC Philips was attached to the tensile sample as Figure I shows. This sensor is able to measure the formation of both, strain-induced and the stress-assisted types of transformation, as well as the combination of the two types. This sensor performs the measurement inductively, taking advantage of the difference of relative magnetic permeability (μ_r ~100) between the paramagnetic austenite and the ferromagnetic marteniste. To prevent the magnetic field from disturbing the transformation, a low field strength of 1.3 *T* was selected.

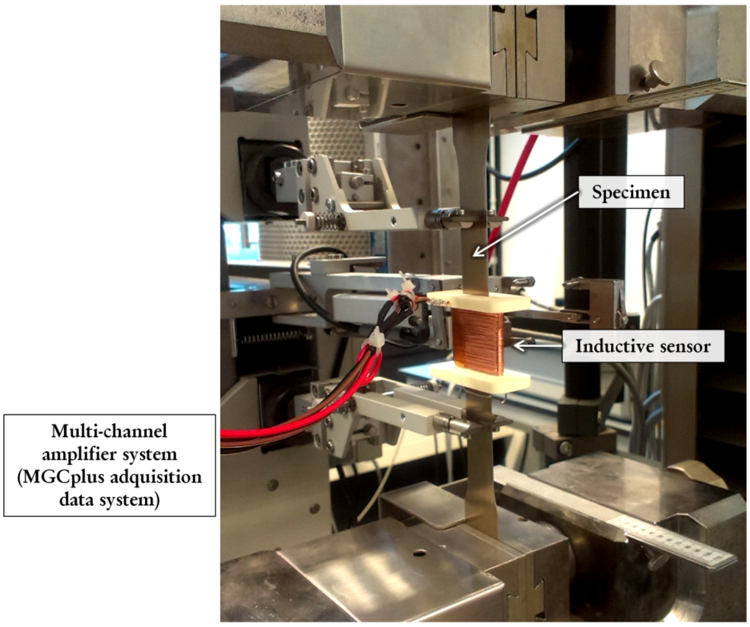

Figure I. Schematic plot of the tensile testing machine and the inductive sensor attached to the sample.

For the electronics, a standard integrated circuit (IC) was used. An alternating current (AC), in constant direct mode, is sent through two coils (the measurement and the reference coil) and the difference in voltage across the coils is measured and amplified. A constant AC excitation coil current of 55 mA at 7.5 kHz was used, which ensured a constant magnetic field of 1.3 *T*. The slit of the coils measures 31 mm length and

0.8 mm width and is surrounded by 1 mm of material. The coils are relatively thin, consisting of a single primary layer and single secondary later of windings measuring 30 mm in length. The coils were connected in series, since it is important that the same current flows through both excitation coils. The induction voltage, V_{out}, and the current measurement voltage are fed to a National Instruments 6251 data acquisition card. The signals are measured simultaneously in differential mode and ten RMS (Root Mean Squared) values are obtained every second. Besides the induction voltage, the data acquisition card can also record analog values representing the strain and force recorded by the tensile stage. A number of adjusting elements can be used to set the voltage, current, frequency and amplification factor. The IC contains an oscillator that generates voltage, a filter and an amplifier. The output signal is a signal in Volt. A frequency of 7.5 kHz was selected in order to avoid as much external electromagnetic interference as possible.

Results and discussion

Figure II (a) shows the engineerign stress vs. strain (%) obtained for the samples after heating to the different temeperatures. As expected, the heating of the material causes, first, an increase in the strength as a result of the precipitation hardening of the material and, then, a decrease of the strength and increase of ductility due to the austenite formation. Curves obtained for samples heated to 700 °C or higher show the "S-shape" typical of TRIP effect (the austenite transforms into martensite and this martensite hardens with the increase of stress). As also observed in sub-size samples, specimens annealed above 800 °C exhibit a yield-drop and Lüders band formation, which is translated in the apearance of an upper and lower yield strength and a subserquent plateau. This plateau is maximum for specimens heated to 875-925 °C. Austenitic microstructures obtained at 1000 °C or higher show continuous yielding and a smooth "S-shape" curve, similarly to the observation in sub-size samples.

Figure II (b) dislplays the evolution of the voltage with the strain, which was recorded simultaneously as the tensile testing proceeded. Different behaviors are observed depending on the annealing temperature and, thus, the microstructure. On the one hand, the voltage signal starts at high value for those samples with a essentially martensitic microstructure and drops as the stress rises to a certain voltage level. Then, the signal increases slightly until the material fractures. It is important to notice that the starting voltage signal decreases as the volume fraction of martensite decreases and that of austenite increases. This is not surprising since the initial voltage signal is related to the volume fraction of martensite in the microstructure. The larger the fraction of martensite, the strongest the stress dependency of the voltage is. However, it is not clear why of the initial voltage of the 630 °C-curves is higher than that of the cold-rolled (As-R). It is believed that the advance precipitation state of the 630 °C-condition is related with this behavior but it cannot be confirmed. On the other hand, it appears that the initial voltage of fully austenitic microstructures is approximately zero, which indicates that the volume fraction of martensite in these initial microstructrues is indeed negligible. Then as these microstructures are strained, the signal rises indicating that the martensitic transformation is taking place. However, there is no clear direct relationship between the final volume fraction of martensite and the final voltage signal. Although the volume fraction of SIM has been observed to be essentialy the same regardless the austenite grain size (about 0.90-0.95) in sub-size specimens (*Section 6.2.3*), differences up to 4 V are found between the samples annealed to 825 and 1025 °C. This suggest that other factors apart from the fraction of martensite are influencing the voltage signal. Additionally, a two-steps tranformation is detected for those samples exhibiting a Lüders strain plateu.

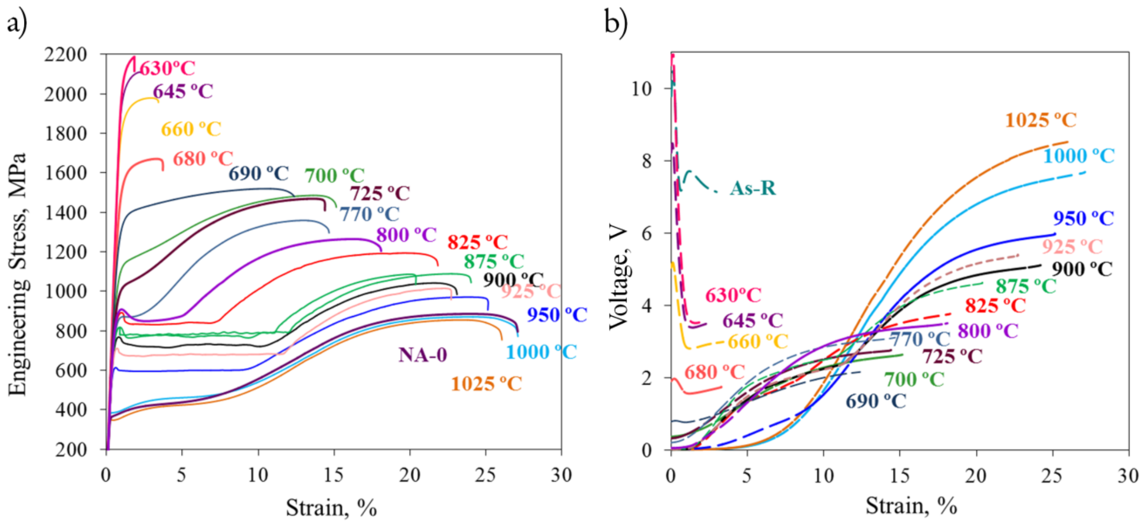

Figure II. (a) Engineering stress vs. strain (%) curves obtained after heating at 0.1 ºC/s to different temperatures; (b) Voltage vs. strain (%) curves obtained in-situ during the tensile testing. As-R and NA-0 stand for as-received microstructure (cold-rolled) and Nanoflex annealed, respectively.

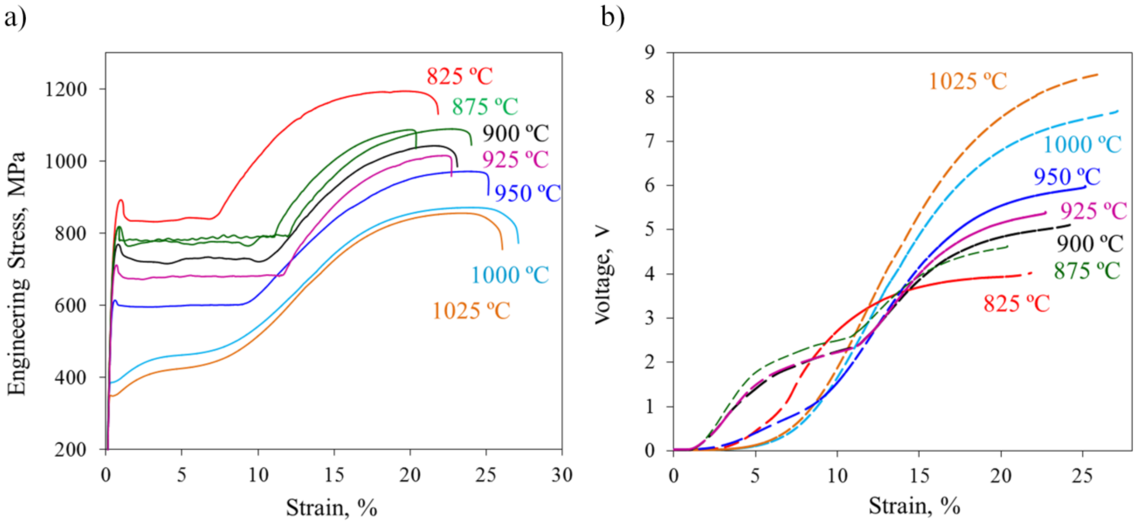

Figure III. (a) Engineering stress vs. strain (%) curves obtained after heating at 0.1 ºC/s to obtain fully austenitic microstructures; (b) Voltage vs. strain (%) curves obtained in-situ during the tensile testing.

Figure III presents the same plots as Figure II but only for fully austenitic conditions. In Figure III (b), it is clearly appreciated the two-step transformtaion behavior: the first step of the transformation coincides with the plateau magnitud, while the second step correspond to the hardening of the material. The formation of SIM due to the Lüders straining was also detected by *ex-situ* magnetization measurements in sub-size samples (Figure 6.4). However, as observed in Figure III (b), the signal voltage starts increasing at different strains depending on the condition. For instance, the signal of the curves at 875, 900 and 925 °C starts increasing at low strains (after the yiedl-drop), whereas those of the 825 and 950 °C do it around the middle of the Lüders bands plateau. Generally, Lüders bands initiate at one of the radius of the tensile specimen or simultaneously at both because these places accumulate all the stress at the beginning of the tensile test due to the change in cross-section. Then, the bands fronts propagate at the same velocity along the gage length of the specimen. During the propagation the austenite essentially remains intact until the passage of the band. Once the fronts coalesce the deformation turns homogeneous and the material starts strain hardening. It is important to recall that the length of the sensor used for this measurements is shorter than the gage length and that it is located at the center of the tensile specimen. Therefore, the sensor will not give any positive signal until the bands pass through it. However, Lüders bands may initiate at the centre of the gage length or at any other place induced, for instance, by surface defects. In this case the sensor would detect the signal associated to the martensite inmediately after the formation of the first Lüder band. To proof this theory an experiment was performed on a sample annealed to 875 °C in which the cross-section was slighly reduced in the centre by grinding in order to force the Lüders bands to initiate in the center of the gage length, just inside the sensor. The results are displayed in Figure IV.

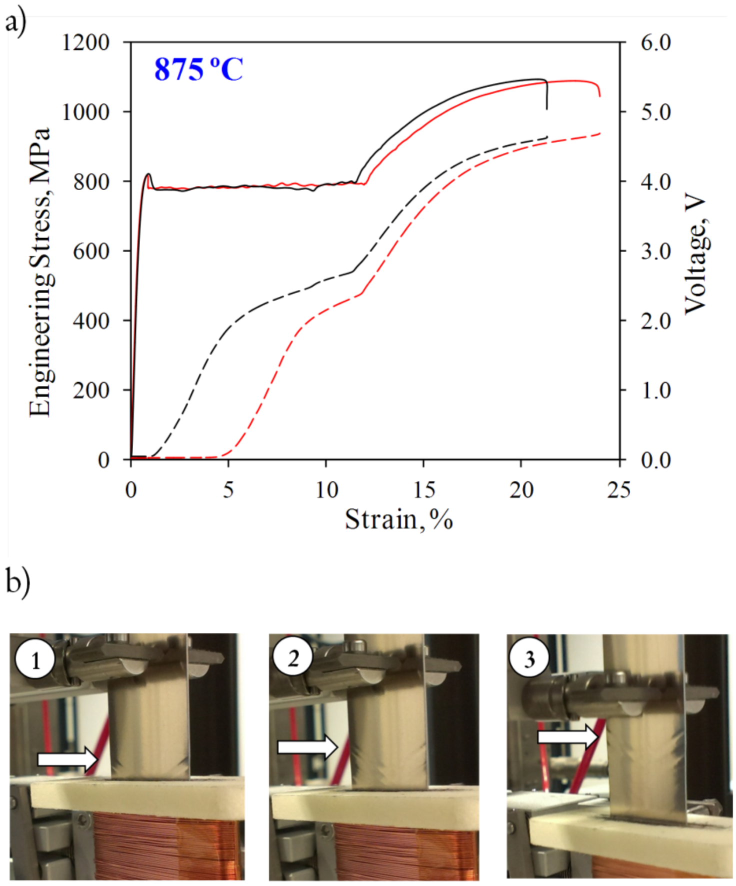

Figure IV. (a) Engineering stress vs. strain curve and voltage vs. strain for two samples annealed to 875 °C and tensile tested. Black curves correspond to the sample with the cross-section slighly reduced.

As observed in Figure IV (a), the martensitic transformation starts after the yield-drop in the sample with the cross-section sligthly reduced in the center (black), whereas in the unaltered sample (red curve) the transformation starts in the middle of the Lüders straining plateau. Figure IV (b) shows three photographs taken consecutively, in which the propagation of the Lüders bands has been pointed out with white arrows. It can be appreciate that Lüders bands have originated at the centre of the gage length (inside the sensor) and they propagate to the sides. These results point out that the martensitic transformation is strain-induced rather than stress-assisted. The voltage signal is not detected until the Lüders band (local deformation) sweeps the volume inside the sensor, plastically deforming the austenite phase and causing the martensitic transformation. The austenite in the region ahead of the Lüders band is stressed but remains unaltered.

Altough these results have turned up to be very helpful to gain insight about the martensitic transformation, there is still a great amount of valuable information that has not been analyzed and some question marks not anwered:

- How are the voltage signal and the volume fraction of martensite related to each other?
- How does the stress affect the voltage signal?
- How important is the heating of the specimen during tensile testing and how does it influence the martensitic transformation and the sensor?

Appendix II

Curriculum Vitae

Carola Alonso de Celada Casero

Dpt. Physical Metallugy, National Center for Metallurgical Research (CENIM-CSIC).
Av. Gregorio del Amo, 8, 28040 Madrid, Spain.
c.celada@cenim.csic.es; carola.celada@gmail.es

EDUCATION

02/2010 – 02/2012	**Master in Applied Physics**. Faculty of Physics, Universidad Complutense de Madrid (UCM).
10/2007 – 02/2010	**Bachelor in Materials Engineering with honors (1st)**. Faculty of Physics, UCM.
10/2003 – 02/2007	**First Cycle of Chemistry Degree** at the Faculty of Chemistry, UCM.

PUBLICATIONS

Publications related to this thesis work

1. C. Celada-Casero, E. Urones-Garrote, S. Mato, J. Chao and D. San Martín. *Nano-precipitation hardening in a semi-austenitic metastable stainless Steel*, Mater. Sci. Eng. A (in preparation).
2. C. Celada-Casero, J. Chao and D. San Martín. *Mechanical stability and properties of dual (α'/γ) and austenitic microstructures obtained by controlled isochronal heating*, Mater. Sci. Eng. A (in preparation).
3. C. Celada-Casero, B-M. Huang, J-R. Yang and D. San Martín. *Mechanisms of submicron austenite formation under different isochronal conditions in a cold-rolled metastable stainless steel*, Mater. Char. (in preparation).

4. C. Celada-Casero and D. San Martín. *Austenite formation in a cold-rolled semi-austenitic stainless steel*, Metal. Mater. Trans. A 45 (2014) 1767 – 1777.
5. C. Celada, I. Toda-Caraballo, B. Kim and D. San Martín. *Chemical banding revealed by chemical etching in a cold-rolled metastable stainless steel*, Mater. Char. 84 (2013) 142 – 152.

Publications related to other research projects

1. D. San Martin, C. Celada-Casero, J. Chao, S. Mato. *Heat treatment optimization in AISI 420: Microstructure and Properties.* Mater. Sci. Eng. A (in preparation).
2. D. Waanders, D. San Martin, C. Celada-Casero and H.J.M. Geijselaers. *Modeling Martensite Transformation: A novel carbide-dependent approach.* Mater. Sci. Eng. A (submitted).
3. D. Waanders, D. San Martin, C. Celada-Casero and H.J.M. Geijselaers. *Analysis of the ferrite to austenite phase transformation: an isokinetic approach.* Comp. Mater. Sci. (submitted).
4. H. Calvo, C. Celada-Casero, G. Alcalá and D. San Martin. *Thermal Stability of an Aluminum Matrix Composite Reinforced with NiTi Particulates at 495 °C*, Mater. Char. (in preparation).
5. B. Kim, C. Celada, D, San Martín, T. Sourmail and P.E.J. Rivera-Díaz-del-Castillo. *The effect of silicon on the nanoprecipitation of cementite,* Acta. Mater. 61 (2013) 6983 – 6992.
6. B. Kim, C. Celada, D. San Martín, J. Chao, J. Vara and P.E.J. Rivera-Díaz-del-Castillo. *Interrupted ageing in steels: Hardness improvement and microstructural stabilization*, Scripta Mater. 68 (2013) 945 - 948.

Conference papers

1. C. Celada-Casero, B-M. Huang, J. Chao, J-R. Yang and D. San Martín. *Phase transformations in a metastable stainless steel: microstructure evolution and mechanical properties*. Proceedings of the International Conference on Solid-Solid Phase Transformations in Inorganic Materials (PTM 2015).

2. C. Celada-Casero, J. Chao and D. San Martin. *Influence of Heating/Cooling Conditions on the Martensitic Transformation in a Stainless Steel AISI 420: Microstructure and Properties.* Proceedings of the International Conference on Solid-Solid Phase Transformations in Inorganic Materials (PTM 2015).

3. C. Celada and D. San Martín. *Study of the reaustenitization process in a cold-rolled metastable austenitic stainless steel* (in Spanish). Proceedings of the XII National Conference on Materials (2012), ISBN: 978-84-695-331-1.
4. J. M. Gómez de Salazar, M.I. Barrena, C. Celada, L. Matesanz Benito and A. Soria Muñoz. *Study of the oxidation kinetics in heat-treated magnesium alloys* (in Spanish).

Proceedings of the XII National Conference on Heat and Surface Treatments (TRATERMAT 2010) 205 – 214.

CONFERENCES

1. **C. Celada-Casero**, E. Urones-Garrote, S. Mato and D. San Martín. *Precipitation hardening in a metastable semi-austenitic stainless steel*. Advances in Materials & Processing Technologies Conference (AMPT), Madrid, Spain, 14-17 Dec., 2015. (Invited talk).
2. **C. Celada-Casero** and D. San Martin. *Phase Transformations in Nanoflex: Microstuture and mechanical behavior*. Solutions for Enhanced Product Quality in Stainless Steel. Workshop organized by Philips and Sandvik, Drachten, Netherlands, 8-9 Sept., 2015. (Oral communication).
3. **C. Celada-Casero**, B-M. Huang, J. Chao, J-R. Yang and D. San Martín. *Phase transformations in a metastable stainless steel: microstructure evolution and mechanical properties*. International Conference on Soli-Solid Phase Transformations in Inorganic Materials (PTM2015), Whistler, Canada, June 28 – July 3, 2015. (Oral communication)
4. **C. Celada-Casero**; J. Chao and D. San Martín. *Influence of heating/cooling conditions on the martensitic transformation in a stainless steel AISI 420: microstructure and properties*. International Conference on Soli-Solid Phase Transformations in Inorganic Materials (PTM2015), Whistler, Canada, June 28 – July 3, 2015. (Oral communication)
5. **C. Celada-Casero**, B-M. Huang, E. Urones-Garrote, J. Chao, J-R. Yang and D. San Martín. *Sub-micrometer austenite obtained by controlled heat treatments: microstructure and mechanical properties*. Advanced Steels 2014 Workshop, Madrid, Spain, 18-19 Sept., 2014. (Oral communication).
6. **C. Celada-Casero**, B-M. Huang, E. Urones-Garrote, J. Chao, J-R. Yang and D. San Martín. *Mechanical stability of reversed metastable austenite in a semi-austenitic stainless steel*. International Conference on Martensitic Transformations (ICOMAT), Bilbao, Spain, 6-11 July, 2014. (Poster).
7. **C. Celada-Casero**, B-M. Huang, E. Urones-Garrote, J. Chao, J-R. Yang and D. San Martín. *Mechanical stability of reaustenitized microstructures in a cold-rolled metastable stainless steel* (in Spanish). XIII National Conference on Materials, Barcelona, Spain, 18-20 June, 2014. (Oral communication).
8. **C. Celada-Casero**, M. Jiménez Amores, E. Urones-Garrote, S. Mato Díaz and D. San Martín. *Nano-precipitation hardening in a semi-austenitic stainless Steel* (in Spanish). XIII National Conference on Materials, Barcelona, Spain, 18-20 June, 2014. (Oral communication).
9. **C. Celada-Casero**, J-R. Yang and D. San Martín. *Obtaining ultrafine-grained austenite in a cold-rolled metastable stainless steel*. TMS Annual Meeting & Exhibition 2014, San Diego, USA, 16-20 Feb., 2014. (Oral communication).
10. D. San Martín, **C. Celada-Casero** and C. García de Andrés. *Ultra-high strength martensitic and austenitic metastable stainless steel*. International Symposium on Metallurgy: 50th Anniversary CENIM, Organized by CENIM-CSIC, Madrid, Spain, 25-25 Oct., 2014. (Poster).

11. **C. Celada-Casero**, I. Toda-Caraballo and D. San Martín. *Continuous heating transformations in a chemically banded cold-rolled stainless steel: Microstructural and mechanical characterization.* EUROMAT 2013, Seville, Spain, 8-13 Sept., 2013. (Oral communication).
12. **C. Celada-Casero** and D. San Martín. *Austenite formation in metastable cold-rolled stainless steel.* International Workshop on Materials Design Process: Thermodynamics, Kinetics and Microstructure Control (MDPTKM 2013). Organized by IMDEA Materials, Tecnogetafe, Madrid, Spain, 3-4 June, 2013. (Oral communication).
13. **C. Celada-Casero** and D. San Martín. *Study of the reaustenitization process in a cold-rolled metastable austenitic stainless steel* (in Spanish). XII National Conference on Materials, Alicante, Spain, 30 May – 1 June, 2012. (Poster).
14. J.M. Gómez de Salazar, M.I. Barrena, **C. Celada-Casero**, L. Matesanz Benito, and A. Soria Muñoz. *Study of the oxidation kinetics in heat-treated magnesium alloys* (in Spanish). XII National Conference on Heat and Surface Treatments (TRATERMAT 2010), Navarra, Spain, 20-22 Oct., 2010. (Oral communication)